Identification and Analysis of Key Parameters in Organic Solar Cells

Dissertation

zur Erlangung des akademischen Grades
des Doktors der Naturwissenschaften
(Dr. rer. nat.)
an der Universität Konstanz
Fachbereich Physik

vorgelegt von

Moritz K. Riede

Durchgeführt am Fraunhofer Institut für Solare
Energiesysteme (ISE), Freiburg im Breisgau,
und am Freiburger Materialforschungszentrum (FMF),
Freiburg im Breisgau

2006

Tag der mündlichen Prüfung: 27.10.2006

Referenten: Priv. Doz. Dr. Gerhard Willeke
Prof. Dr. Wolfgang Dieterich

Acknowledgements

First of all, I want to express my gratitude to PD. Dr. Gerhard Willeke at the Fraunhofer Institute for Solar Energy Systems ISE in Freiburg for giving me the opportunity to work on this exciting and fascinating topic of organic solar cells.

I am extremely grateful to PD. Dr. Andreas Gombert of the Fraunhofer Institute for Solar Energy Systems and Dr. Andreas Liehr of the Freiburger Materials Research Center for the 20 months of valuable supervision and guidance on this topic. I would like to express my gratitude to Dr. Rainer Kern who provided me with motivating support when the first topic turned out not to be practicable due to unforeseen reasons.

I would also like to thank the staff of the Dye- and Organic Solar Cell group at the Fraunhofer Institute for Solar Energy Systems ISE and the Freiburg Materials Research Centre FMF at the Albert-Ludwigs University of Freiburg. My special thanks go to Dr. Kristian Sylvester-Hvid for the fruitful discussions, the advice and his contribution to the absorption measurement. Nicholas Keegan is also gratefully acknowledged; without him and Dr. Kristian Sylvester-Hvid, the feat of manufacturing the large number of organic solar cells would have been difficult in the time the thesis had to be done.

For many interesting and exciting discussions about organic solar cells I want to thank Markus Glatthaar, Dr. Michael Niggemann and Birger Zimmermann.

Furthermore, I would like to thank all the other present and past members with whom I had the privilege to work: Udo Belledin, Florian Clement, Dr. Anneke Georg, Jan Haschke, Simon Hemming, Dr. Sharmimala Hore, Dr. Andreas Hinsch, Peter Lewer, Nichola Mingirulli, Marius Peters, Ronald Sastrawan, Melanie Schumann, Bas van der Wiel, Vera Walliser, Uli Würfel and Tobias Ziegler, who is acknowledged for measuring the optical constants of the used materials.

Many thanks also go to Michael Röttger in the group of Dr. Andreas Liehr for his kind support with Python and Matlab, to Florian Jäger for the technical drawings of the multiple mount and the XY-table, to Martin Hermle in the group of PD Dr. Gerhard Willeke for the discussions on the IV-curves, to Christian Wawrzinek and Sébastien Braun for the implementation of the web interface and to Martin Meier for the LabView program.
Finally, my deepest thanks go to both my family and Saskia for the strong and invaluable support.

Contents

Chapter 1

Introduction

Research in the field of organic semiconductors has attracted much interest in recent years. Organic semiconductors, i.e. carbon-based materials with semiconducting properties, have intriguing features, which make them interesting for both fundamental research and industrially made products.

The focus of scientific research is on the special electronic properties of organic semiconductors, which exhibit novel behaviour, making them an exciting system for fundamental research. From a commercial point of view the prospects of simple processing, e.g. processing from solution, and the mechanical flexibility of the devices made from organic semiconductors are very attractive. Some electronic devices made of organic semiconductors are already commercially available, e.g. displays with organic light-emitting diodes (OLEDs), whereas other devices, e.g. organic solar cells (OSCs), are still at the development stage. What is yet to be shown are OSCs, which satisfy the preconditions for commercialisation, i.e. with lifetimes >5 years, competitive cost ($<$€$1/\mathrm{W_p}$) and simultaneously a power conversion efficiency η $>5\%$ [1].

Conjugated polymers, which were discovered in 1976 by A. Heeger et al., belong to the group of organic semiconductors [2]. Due to their mechanical properties and the prospect of simple processing from solution, much research has been devoted to them since then. The research on polymer-based solar cells began in the 1980's. However, as in other organic semiconductors, the photogenerated electron-hole pair, i.e. exciton, is strongly bound ($>0.1e$V) and dissociation into free charge carriers is unlikely in a single material at room temperature. Consequently, the first OSCs had very poor power conversion efficiencies η ($\ll 1\%$). The discovery of the ultrafast photoinduced charge transfer at the interface between a conjugated polymer and the Buckminster

fullerene C_{60} was a milestone in the development of OSCs [3]. It turned out that the photogenerated excitons dissociate very effectively at the interface that forms between the polymer (electron donor) and the fullerene (electron acceptor) due to their difference in electron affinity. When the two immiscible materials are blended, a large interfacial area and an efficient exciton dissociation throughout the so-called bulk heterojunction can be obtained (see figure 1.1). For a sufficiently small phase separation between the donor and acceptor phase, the exciton dissociation in this interpenetrating network is not restricted by the short exciton diffusion length of a few tens of nanometres, which has severely limited OSCs with a planar heterojunction.

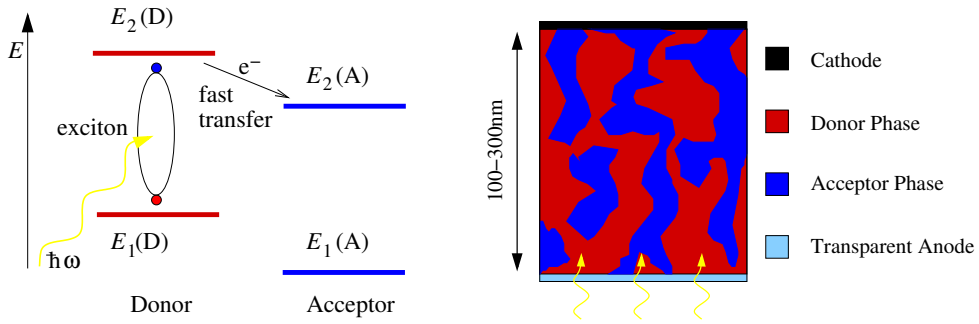

Figure 1.1: *The fast electron transfer from donor to acceptor (left) and an idealised cross-section through a bulk heterojunction solar cell (right). On the left-hand side, the simplified donor-acceptor principle is shown for two materials with each two energy levels, which are separated by an energy gap. The photogenerated exciton has high binding energies (>0.1eV) and dissociation into free charge carriers is unlikely within either material alone. However, the dissociation is very efficient at the interface to a second material. To ensure that every exciton is generated close to a heterojunction a fine phase separation with a length scale of a few nanometres is required between the electron donor and electron acceptor in the blend. This is obtained by blending donor and acceptor materials, leading to a bulk heterojunction the idealised structure, of which is shown on the right-hand side. Once the exciton has dissociated, the free charges have to move through the interpenetrating network to their respective electrodes, where they are collected.*

The morphology of this interpenetrating network has two significant effects on OSC performance. (1) It determines the efficiency of exciton dissociation on the nanometre scale by a phase separation with length scales on the same order of magnitude as the exciton diffusion length. (2) The efficiency of the charge carrier collection is significantly determined by the combination of the

effect of the morphology on the charge carrier mobility and the formation of a continuous path to the respective electrodes. Despite its importance for the OSC performance, the morphology has not yet been fully determined. Its dimensions require atomic force microscopy (AFM) and it is often not possible to infer from the AFM surface the morphology in the bulk.

The major limiting factor for the materials used in OSCs at the moment is the loss of nearly 1eV in energy during the dissociation of the exciton [4]. Additionally, the large optical band gap of $\approx$2eV of the semiconductor materials makes only a limited fraction of the solar spectrum available for harvesting. Thus much research is focused on optimising the morphology of donor and acceptor material and synthesising new materials with more appropriate energy levels and optical gaps. So far the highest power conversion efficiency reached at our laboratory is 3.5%. The highest certified η for an OSC is 3.0%, although values approaching 5% have been reported by other groups in the literature [5].

Despite the progress of the previous years in qualitatively understanding OSC behaviour, there are still many open questions regarding the fundamental physical understanding of the processes in an OSC as well as the relation between the production parameters and their effects on OSC characteristics. The experimental investigation of these issues is complicated by the fact that generally an intentional variation of one single production parameter is difficult to realise. Due to the nature of the production process there are generally other parameters with variations as well. These variations often affect the experimental results by the same order of magnitude as the intended variation. Thus the characteristics observed in the measured OSC data are difficult to attribute to a specific variation in the production process. Although only a few steps are necessary to produce an OSC, these steps have many degrees of freedom, which often exhibit a complex interdependence. This complicates both the optimisation of the production steps and the development of a statistically sound understanding of the physical processes in an OSC.

Even when considering the same material combination of donor and acceptor, there are many parameters during production with a potential influence on the OSC performance and always several differ from one substrate to the next. The effects of these variations have to be analysed simultaneously due to the complexity and sensitivity of the OSCs. This makes the application of

multivariate methodology essential, because only partial information about the OSC can be obtained when the effect of one parameter alone is considered. The creation of both an experimental infrastructure, which permits a statistically sound analysis, and the use of principal component analysis (PCA) as a multivariate statistical method is the primary new contribution of this thesis to research on organic solar cells.

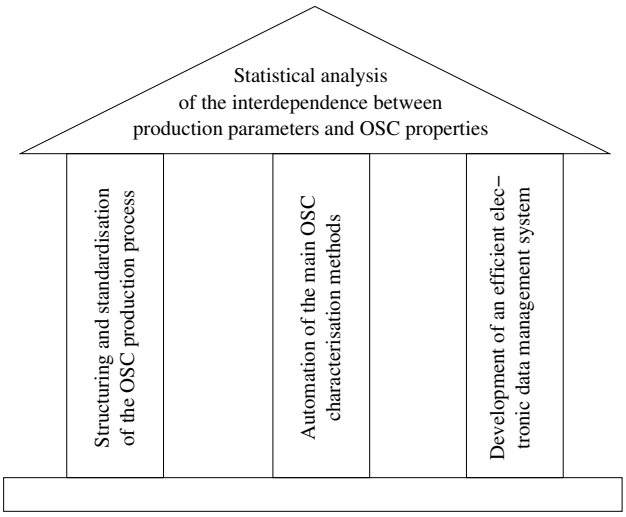

Figure 1.2: *The three requirements for the statistical analysis of the data. The structuring and standardisation of their production process allows organic solar cells (OSCs) to be produced with a set of comparable production parameters. Automation of the standard characterisation methods is necessary for reliable acquisition of measurement data with the required throughput. The large quantity of obtained data demands efficient data management, both for handling and analysing the data. These three requirements form the basis for statistical analysis of the interdependence between production parameters and OSC properties.*

Experimental Infrastructure

The prerequisite for sound statistical analysis is an adequate set of production and characterisation records. Both the quality of the record has to be ensured and there has to be sufficient data. This requires a reliable and fast method of data acquisition and efficient data management. The corresponding necessary experimental infrastructure has been developed during the work on this thesis. The production process was structured to allow comparative testing. The concept for a webinterface was developed, through

which the standardised logging of the production process is now carried out. The main OSC characterisation methods – current-voltage measurements, spectral response measurements and absorption measurements – were all integrated into one automated setup, which allows a reliable acquisition of measurement data with the necessary high throughput. This is essential, at the characterisation stage, to handle the many variations in production parameters – both intentional and caused by usual fluctuations – which lead to a large number of OSCs. The main hardware component of the automated setup is the multiple mount, which is shown in figure 1.3.

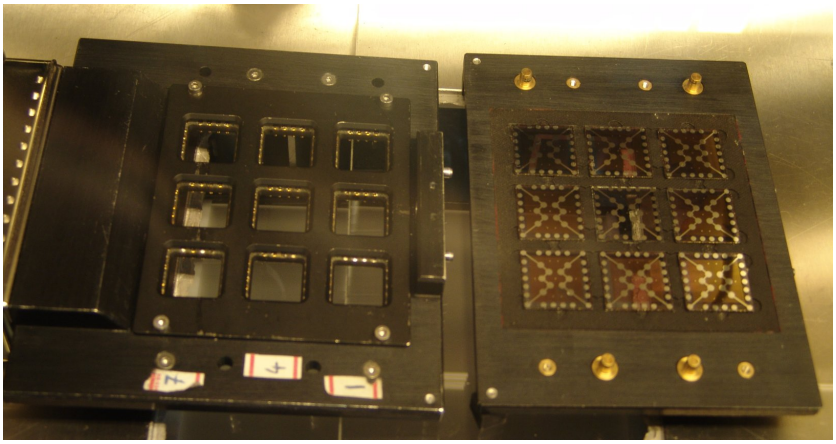

Figure 1.3: *The multiple mount opened for loading/unloading the substrates. The multiple mount is the main component of the automated characterisation setup. It can hold and simultaneously contact up to 90 OSCs on nine substrates. All the main measurements can be performed on the OSCs in the multiple mount.*

The data obtained from the production process and the OSC characterisation is managed with an electronic laboratory notebook (ELN), which provides structured access to all data obtained. The computational tools required for handling the data and for extracting OSC properties from the measured data were developed. This leads to an extensive experimental infrastructure, which acts as a basis for the statistical analysis.

Principal Component Analysis

The data obtained during the systematic production and characterisation of the OSCs is evaluated by principal component analysis. The multivariate statistical method is used in this thesis to investigate the influence of the pro-

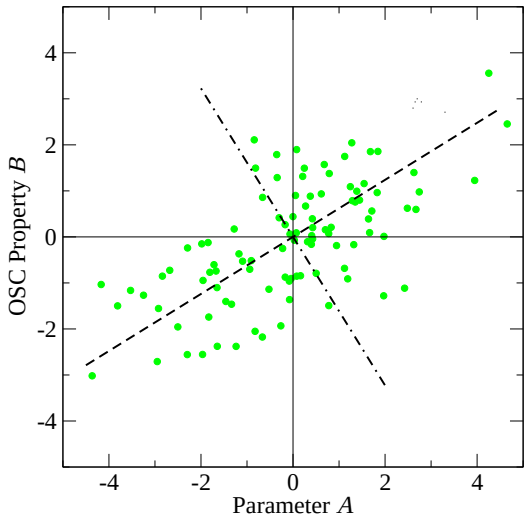

Figure 1.4: *A 2D scatter plot showing correlated data. The correlations are easily identified visually. However, it is difficult to quantify how the information in the data is distributed, or to perform this analysis in many dimensions. In this simple example, representing the data with the dashed line alone would retain nearly 85% of the information in the data.*

duction parameters on OSC performance and subsequently find the causes for the large variations seen in the OSC properties, despite the similar production conditions. This is done by analysing the correlations between the many OSC production parameters and OSC properties (see figure 1.4). The goal of the analysis is to identify those production parameters in the complicated OSC system which have a significant influence on OSC properties. Subsequently the physical origin of such correlations can be investigated in order to gain a better understanding of the physics involved.
Knowledge about the correlations found is compared with results of electrical simulations of the OSC, which form part of the theoretical work in our group. Finally, a statistical prediction model is developed on the basis of the PCA and a new method to optimise the production process is proposed.

Content of the thesis

First, in chapter 2, the principles of photovoltaic energy conversion are presented in terms of inorganic semiconductor physics by considering a simple electronic two-level system. Before describing the presented bulk heterojunction solar cells, the differences between inorganic semiconductors and organic semiconductors are highlighted. This brief diversion is necessary to be able

to present the physics of organic solar cells with their specific features. Two approaches for modelling organic solar cells are presented.

Chapter 3 then introduces the investigated OSCs and focuses on their production process. Each production step is described and the important parameters are presented. A detailed understanding of each step is necessary in order to structure and standardise the recorded production parameters for a comparable production process.

The characterisation methods used and the automation of these experiments to allow a high and reliable throughput form the topic of chapter 4. The principles of the standard characterisation methods are presented and measurement uncertainties discussed. A reliable OSC characterisation system with a high throughput is paramount for the efficient handling of many parameter variations during OSC production at the characterisation stage. This requires automation of the main experiments, the components and performance of which are presented.

The data analysis methods, which were used, and the computational tools developed in order to efficiently handle the large amount of data obtained during production and characterisation, are the focus of chapter 5. The methods used to analyse measurement data and the principal component analysis (PCA) used to determine the interdependence between the production process and the measured OSC properties are presented. The concept of an electronic laboratory notebook (ELN) is introduced and the process of the structured and standardised data acquisition, handling and processing is described.

Chapters 3 to 5 describe the basis for reliable acquisition of measurement data and thus sound data analysis, which is presented in chapter 6. A large run of experiments with the smallest number of varying parameters allowed by the production process was conducted. The main effects seen in the measured data are described. Using PCA, the interdependence between production parameters and measurement results is analysed and the results are discussed. Finally, a statistical model based on the principal component analysis is proposed to optimise the production process.

Chapter 2

Fundamentals

The important concepts for the physics of organic solar cells (OSC) will be presented here. A simple and general electronic model for a solar cell is used to describe the basic processes for the conversion of the energy of light into electrical work. Then the discussion moves to the special properties of organic semiconductors and solar cells made of these materials. The main steps of the solar energy conversion in OSCs are described and the current state of research is presented.

2.1 Solar Cell Model System

The key issue of all currently investigated solar cells is the optimal use of semiconductor material. The special feature of semiconductors – both from inorganic and organic materials – are two quasi-continua of charge carrier transport levels, which are separated by an energy exceeding by far k_BT at moderate temperatures T (k_BT at room temperatures $\approx 0.26\mathrm{m}e\mathrm{V}$). The energetically lower quasi-continuum is nearly completely filled with electrons, whereas the upper one is nearly empty. They are called quasi-continua, because the energetic distance between the discrete levels within a quasi-continuum is much smaller than k_BT. The region between the quasi-continua is called forbidden region or energy gap E_G, because it has no available electronic levels. The simple electronic model system of a semiconductor with two levels is shown in figure 2.1. In inorganic semiconductors the lower level is called the valence band and consists of occupied "binding" levels. These electronic levels are delocalised over the whole semiconductor in the ideal case due to perfect crystallinity. In organic semiconductors the basic entities are molecules and the delocalisation of the levels, which is responsible

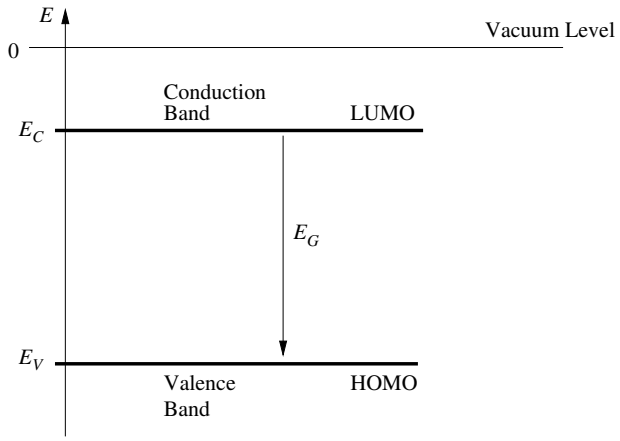

Figure 2.1: *A simple two-level model system as an example for the description of the basic processes in a solar cell. In the case of organic semiconductors, the valence band (energy at edge E_V) corresponds to the Highest Occupied Molecular Orbital (HOMO) and the conduction band (energy at edge E_C) Lowest Unoccupied Molecular Orbital (LUMO). The two levels are separated by a gap of width E_G without any available electronic states.*

for the semiconductor behaviour, is much less pronounced due to the weak Van-der-Waals binding. Here the bands are formed by the occupied binding orbitals of the single molecules, the so-called molecular orbitals (MO). The HOMO (Highest Occupied Molecular Orbital) in molecular semiconductors corresponds to the edge of the valence band in inorganic semiconductors. However, for simplicity, the whole quasi-continuum of occupied binding levels is often called HOMO. The energetically higher lying quasi-continuum is nearly completely empty and is called conduction band. This corresponds to the LUMO (Lowest Unoccupied Molecular Orbital) in the molecular picture. Although the physics derived for inorganic semiconductors can only be applied to a certain extent to organic semiconductors, the basic solar cell principles can be described with the help of the model two-level system shown above following Würfel [6] and Sze [7].

2.1.1 Thermal Equilibrium in a Semiconductor

In thermal equilibrium in the dark, the probability of electron occupation $f_F(E)$ of one-electron states with energy E is described by the Fermi-Dirac

distribution:

$$f_F(E) = \frac{1}{\exp\left(\frac{E-E_F}{k_B T}\right) + 1}, \tag{2.1}$$

where T denotes the temperature of the black body radiation. A state with energy at the Fermi energy E_F hence has an occupation probability of 1/2 as evident from equation 2.1. The occupation probability of electronic states a few $k_B T$ below E_F is nearly unity at moderate temperatures, whereas a few $k_B T$ above E_F it is nearly zero. In order to calculate the number n of electrons per unit volume in the energy interval $[\mathcal{E},\ \mathcal{E} + d\mathcal{E}]$, the states' occupation probability $f_F(E)$ has to be multiplied by the density of states $D_e(E)$ in this energy interval. Hence the density of electrons between $\mathcal{E}$ and $\mathcal{E} + d\mathcal{E}$ is then given by:

$$dn(\mathcal{E}) = D_e(\mathcal{E}) f_F(\mathcal{E}) d\mathcal{E}. \tag{2.2}$$

Intrinsic (undoped) semiconductors used for solar energy conversion feature a Fermi energy which lies within the gap many $k_B T$ away from the conduction and valence band edge. As the occupation probability is nearly zero a few $k_B T$ above E_F, the Fermi distribution $f_F(E)$ in equation 2.2 can be approximated for $E_C - E_F > 3/2 k_B T$ by the Boltzmann distribution

$$f_B(E) = \exp\left(-\frac{E - E_F}{k_B T}\right). \tag{2.3}$$

Therefore the electron density in the conduction band is given by

$$n = \int_{E_C}^{\infty} D_e(E) f_B(E) dE \approx N_C \exp\left(-\frac{E_C - E_F}{k_B T}\right). \tag{2.4}$$

E_C is the energy of the conduction band edge and N_C, called the effective density of states of the conduction band, contains the constant factors of integration. This simplification of equation 2.2 is valid as long as n is small compared to N_C.

The occupation probability for energies E lying a few $k_B T$ below E_F is according to equation 2.1 nearly unity. Rather than describing single electrons in the valence band, unoccupied one-electron states of the valence band can be described as missing electrons or holes. Thus they have the same density of states as the electrons. This way the number of particles which need to

be described, is reduced by several orders of magnitude and some symmetry in the description is introduced. The density of holes in the valence band is therefore, analogous to calculating the electron density in the conduction band, given by

$$p = \int_{-\infty}^{E_V} D_e(E)(1 - f_F(E))dE \approx N_V \exp\left(-\frac{E_F - E_V}{k_B T}\right), \tag{2.5}$$

where E_V is the energy of the valence band edge and N_V is the effective density of states of the valence band.
An important relation can be obtained by combining equations 2.4 and 2.5 to

$$n_i^2 = np = N_C N_V \exp\left(-\frac{E_G}{k_B T}\right), \tag{2.6}$$

where n_i being the intrinsic charge carrier density, which is a constant property of the material, and $E_G = E_C - E_V$. The product np is independent of the position of the Fermi level and hence cannot be altered by doping the semiconductor. For an intrinsic semiconductor all electrons in the conduction band originate from the valence band and hence $p = n$. Using this equality and equations 2.4 and 2.5, the position of the Fermi energy E_F relative to valence and conduction band can be calculated as follows:

$$E_F = \frac{1}{2}(E_V + E_C) + \frac{1}{2}k_B T \ln \frac{N_V}{N_C}. \tag{2.7}$$

At low temperature or at $N_V \approx N_C$ the Fermi level of a intrinsic semiconductor is in the middle of the gap.

2.1.2 Semiconductor under Illumination

Illuminating the described model system with photons of energy higher than E_G creates additional charge carriers in the system. The system is then not in equilibrium with the ambient, but with the light source. If the photons have an energy $\hbar\omega > E_G$, electrons in the valence band can absorb photons and be excited to the conduction band. This leaves a hole in the valence band and the number of both electrons and holes grows by the same amount, as determined by the charge carrier generation rate $\mathcal{G}$. The relaxation between both bands is relatively slow due to the large energy difference and happens in the ideal case only through radiative recombination of electrons and holes. However,

within the bands the thermal relaxation is rapid, resulting in two different Fermi distributions, one for electrons in the conduction band, another for holes in the valence band. The corresponding charge carrier densities can be derived analogous to equation 2.4 and 2.5, leading to

$$n = N_C \exp\left(-\frac{E_C - E_{F,C}}{k_B T}\right), \tag{2.8a}$$

$$p = N_V \exp\left(-\frac{E_{F,V} - E_V}{k_B T}\right), \tag{2.8b}$$

where $E_{F,C}$ is called electron quasi-Fermi level (n-QFL) and $E_{F,V}$ hole quasi-Fermi Level (p-QFL) respectively. The product np now exceeds n_i^2 (equation 2.6). The average energy, which can be extracted from an electron-hole pair is equal to the difference of the Fermi energies of valence and conduction band, $E_{F,V}$ and $E_{F,C}$ respectively

$$E_{F,C} - E_{F,V} = E_G + \underbrace{k_B T \ln \frac{np}{N_C N_V}}_{<0}. \tag{2.9}$$

With increasing illumination, hence with increasing number of charge carriers, the splitting of the QFL increases. However neither occupation probability can reach 1/2 in a semiconductor with only one gap. The splitting of the Fermi energies remains always smaller than E_G, because the excitation competes with two effects: spontaneous emission and stimulated emission. Both are getting more likely with increasing charge carrier densities. In the two-level model system all three effects, i.e. absorption, spontaneous and stimulated emission, are all connected via the Einstein coefficients.
The simplest case of spontaneous decay processes is the radiative recombination of electrons and holes, leading to photoluminescence (PL). Without external influence, an electron decays directly from the conduction band to the valence band and recombines with a hole emitting a photon of energy $\hbar\omega = E_G$. The recombination rate $\mathcal{R}$ per unit volume is given by

$$\mathcal{R} = r(np - n_i^2), \tag{2.10}$$

with radiative recombination constant r. In equation 2.10 the number of intrinsic charge carriers is subtracted, because only excess charge carriers (with respect to the equilibrium case) lead to recombination.

The second effect is the stimulated emission. It describes the transfer of an electron from the conduction band to the valence band due to the stimulation of an atom by an incoming photon. When the excited state is perturbed by the incoming photon, a second photon with the same wavefunction as the stimulating photon can be emitted and the formerly excited state then returns into its ground state. As before, this process is getting more likely with increasing occupation of the conduction band and increasing photon density with energies close to E_G.

2.1.3 Charge Carrier Extraction at the Contacts

So far the model semiconductor has been considered without contacts and the charges could not leave the system. Under illumination extra charges are generated in the semiconductor and the energy of the absorbed light is stored as chemical potential energy in the system. Suitable contacts are required to extract these charges for converting the chemical potential energy into electrical energy. Ideal contacts, i.e. contacts at which no charges and no energy are lost during charge carrier extraction, have to satisfy following requirements:

1. The contacts have to be semipermeable, i.e. only permeable for the respective type of charge carriers. This guarantees that no current is lost at the contacts.

2. The Fermi levels of the contacts have to match the QFL of their respective charge carriers. This way no chemical potential energy is lost during charge carrier extraction.

The second condition is however only valid if transport problems on the way to the electrodes can be neglected, i.e. if no energy is lost on the way to the contacts.

Contacts: The Ideal Case

The case of ideal contacts is shown in figure 2.2. Both contacts have semipermeable membranes and hence allow only the selective passage of the respective charge carriers. The workfunctions Φ_m, i.e. the Fermi levels of the contacting metal, match the QFLs of the allowed charge carrier at the membranes. Their difference, $\Phi_{m1} - \Phi_{m2}$, defines the built-in potential V_{bi}.

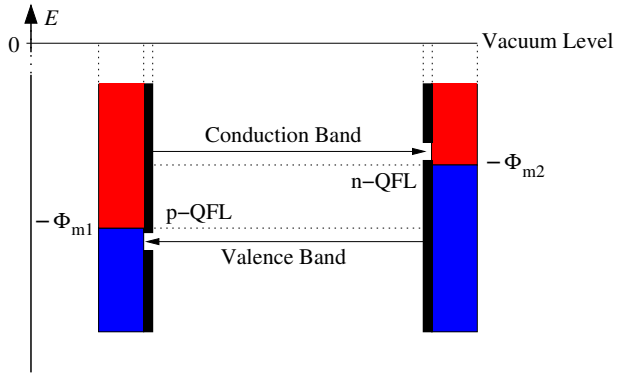

Figure 2.2: *Ideal contacts at which no energy and charge carriers are lost during the conversion of chemical potential energy to electrical energy. Each contact is only permeable to its respective type of charge carriers and the workfunctions of the contacts match the QFL of the corresponding charge carrier under illumination. The built-in potential* V_{bi} *is given by the difference of the metal workfunctions* $\Phi_{m1} - \Phi_{m2}$.

For the stationary case, the continuity equation for electrons and holes can be used to calculate the extractable current. The extent of the QFL splitting depends on the generation rate $\mathcal{G}$, on the extracted charge carrier current density $\mathbf{j}$[1] and the recombination rate $\mathcal{R}$. For the stationary case the continuity equation becomes:

$$0 = \frac{\partial n}{\partial t} = \frac{\partial p}{\partial t} = \mathcal{G} - \mathcal{R} - \nabla \cdot \mathbf{j} \tag{2.11}$$

Using equations 2.9 and 2.10 in equation 2.11 leads to an expression for the extractable current in the ideal case:

$$\nabla \cdot \mathbf{j} = \mathcal{G} - r n_i^2 \left(\exp\left(\frac{E_{F,C} - E_{F,V}}{k_B T} \right) - 1 \right). \tag{2.12}$$

Equation 2.12 describes a fundamental relation in photovoltaics, which is shown in figure 2.3: the extracted energy per electron-hole pair has an exponential relation to the extracted current. The figure also shows that at a given generation rate $\mathcal{G}$ there is a value of the QFL splitting at which the extractable power $(E_{F,C} - E_{F,V})\nabla \cdot \mathbf{j}$ reaches its maximum. The splitting of the QFLs is influenced by $\mathcal{G}$ and by the bias voltage applied to the contacts. This exponential behaviour is reflected in the current-voltage characteristic of a real solar cell, i.e. the current response of a solar cell during a voltage

[1] Throughout this work, small bold font for variables denote vectors, whereas large bold font, e.g. $\mathbf{M}$, denotes matrices.

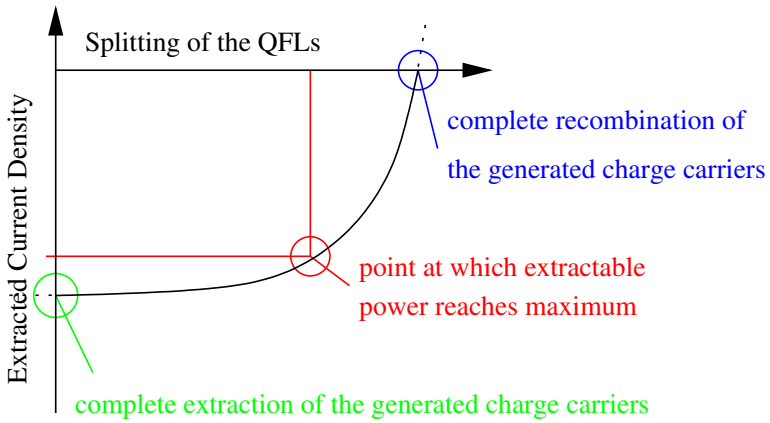

Figure 2.3: *The extractable current as function of QFL-splitting in an illuminated semiconductor. The graph depicts a fundamental relation in photovoltaics: the extracted energy per electron-hole pair has an exponential relation to the extracted current.*

sweep (see section 4.1.1). To highlight the correspondence and to explain the basic features of the current-voltage characteristic, a typical example is shown in figure 2.4.

Equation 2.12 also shows that in the ideal case $\mathbf{j}$ increases linearly with the generation rate at short circuit, i.e. when $E_{F,C} - E_{F,V} = 0$ and all charges are extracted. At open circuit, i.e. when $\mathbf{j} = 0$ and all generated charge carriers recombine, the splitting of the QFL increases logarithmically with $\mathcal{G}$ (see equation 2.9).

Figure 2.4 is used to qualitatively describe the behaviour of non-ideal contacts in the following sections. The two extreme cases, i.e. either contact workfunctions at the QFLs or semipermeable membranes, but same contact workfunctions, will be qualitatively discussed in the following sections. In real OSCs a superposition of these two cases can be observed.

Electric Field driven Solar Cell

If a semiconductor is contacted with electrodes with different workfunctions, this difference leads to a built-in potential V_{bi}, which is given by the difference of the metal work functions $\Phi_{m1} - \Phi_{m2}$. In the example used to illustrate this case (figure 2.5), the Fermi levels of the contact materials match the corresponding QFL, but the contacts lack the selective permeability. For simplification, the vacuum level is not drawn explicitly, but the energy scale

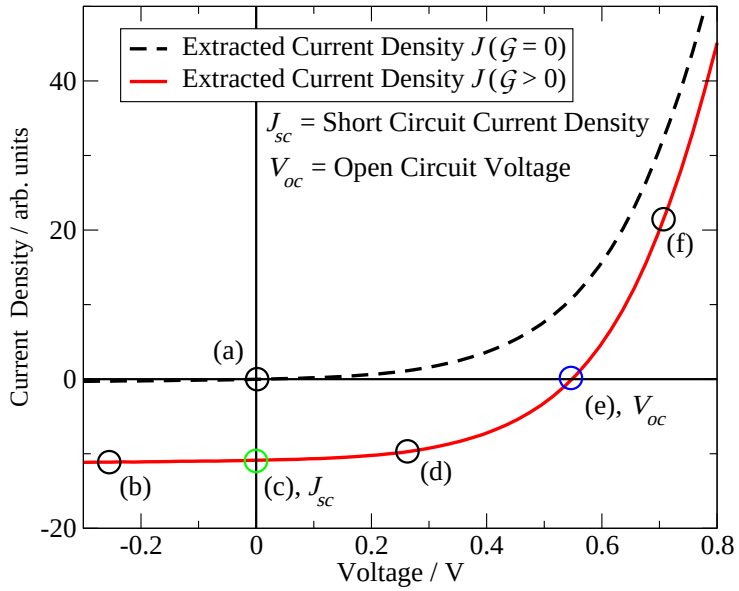

Figure 2.4: *A typical current-voltage characteristic of a real solar cell in the dark ($\mathcal{G} = 0$) and under illumination ($\mathcal{G} > 0$). It resembles the fundamental relation of equation 2.12, which is visualised in figure 2.3. At the intersection with current or voltage axis, the extractable power is zero. Between them in the fourth quadrant, there is a point at which the extractable power $|VJ|$ reaches its maximum. The points on the IV-curve which are labelled from (a) to (f) will be used to qualitatively describe the behaviour of non-ideal contacts.*

is the same as in figure 2.2.

Fig. 2.5 (a): Without any illumination and bias, the chemical potentials align. Electrons from the low workfunction contact and holes from the high workfunction contact are injected into the semiconductor until the created built-in potential V_{bi} opposes further current flow and equilibrium is reached.

Fig. 2.5 (b): Illumination of the semiconductor leads to a splitting of the QFLs. Because injection of additional charges into the solar cell is energetically unfavourable, only the photogenerated charge carriers are extracted from the device.

Fig. 2.5 (c): At short circuit conditions ($V = 0$V), the difference between the potentials of the two contacts is zero, but a gradient in the chemical potential energy drives the charges to their respective contacts.

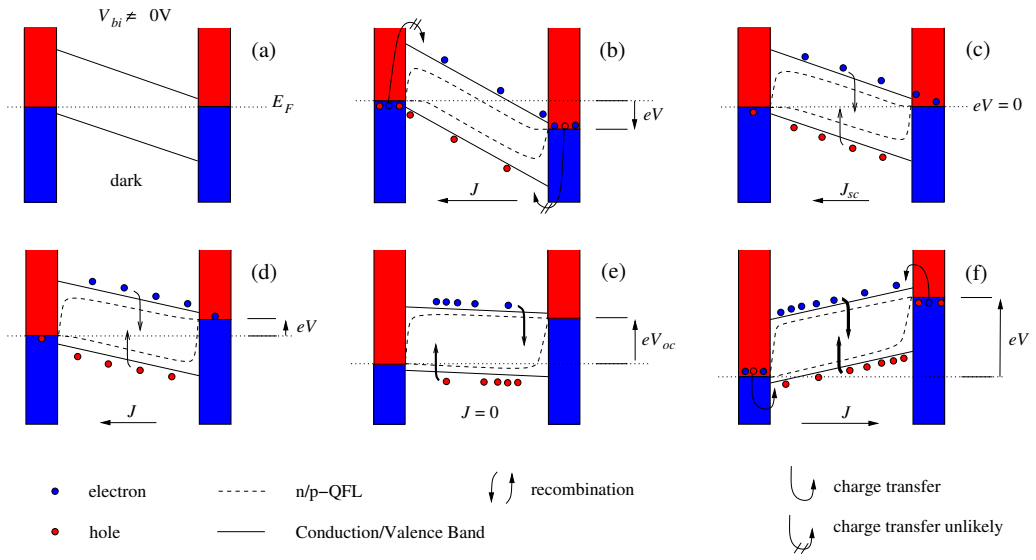

Figure 2.5: *The energy diagrams of a solar cell with asymmetric contacts at the corresponding charge carrier transport levels of the semiconductor. Different bias conditions are shown and the letters refer to the marked positions on the current-voltage characteristic in figure 2.4: (a) after contact formation in the dark with contacts in short circuit, (b) illuminated and reverse bias, (c) illuminated and contacts in short circuit, (d) illuminated and with external load, (e) illuminated and at open circuit, (f) illuminated and forward bias (adapted from [8]).*

Fig. 2.5 (d): At small forward bias, i.e. when an external load is attached, the potential difference reduces the electric field inside the solar cell. Both recombination increases and some charges are lost at the wrong contact due to the non-existent semipermeable membranes.

Fig. 2.5 (e): Under open circuit conditions, no current can be extracted from the solar cell, because all charges recombine inside. This is however not necessarily at the bias voltage at which there is no internal electrical field in the solar cell, but can be reached for values below the difference in workfunction of the contacts.

Fig. 2.5 (f): If the forward bias is further increased, the contacts start to inject additional charge carriers. They either recombine in the bulk or at the opposite electrode.

Solar Cell with semipermeable Membranes

The opposite extreme case is given, if the contacts are semipermeable, but have the same workfunction, which does not match either QFL in the semiconductor. The resulting built-in field V_{bi} is zero. Assuming symmetric Fermi levels of the contacting material located in the middle of the gap, the effects can be illustrated with figure 2.6, which shows the band diagram of a semiconductor at different bias conditions. Again for simplicity the vacuum level is not shown (see figure 2.2).

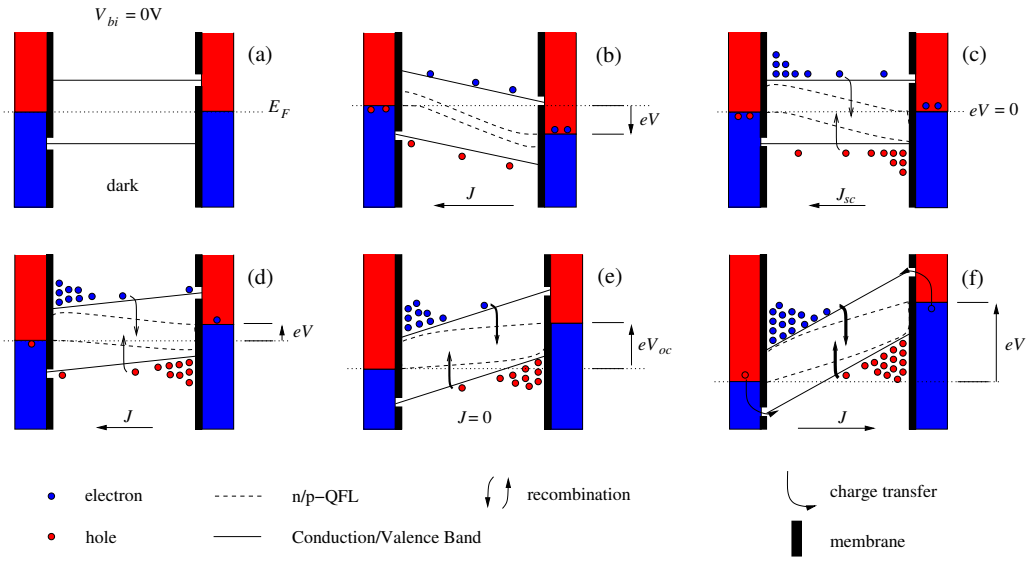

Figure 2.6: *The energy diagrams of a solar cell with semipermeable membranes and symmetric contacts under different bias conditions. The letters refer to the marked positions on the current-voltage characteristic in figure 2.4: (a) after contact formation in the dark without bias, (b) illuminated and reverse bias, (c) illuminated and contacts in short circuit, (d) illuminated and with external load, (e) illuminated and at open circuit, (f) illuminated and forward bias (adapted from [8]).*

Fig. 2.6 (a): Without any illumination and bias, the Fermi level is constant throughout the semiconductor and equals the work functions of the contacts. The resulting built-in potential $V_{bi} = 0$. The system is in thermal equilibrium with the ambient at temperature T.

Fig. 2.6 (b): Illumination of the semiconductor leads to a splitting of the QFLs due to the photogenerated charge carriers. Applying a reverse

bias under illumination leads to a quick extraction of nearly all photogenerated charge carriers and recombination can largely be neglected.

Fig. 2.6 (c): At short circuit conditions, the internal electrical field is zero, but the concentration gradient, which builds up due to accumulation of charges at their non-permeable contact, drives the charge carrier to their respective contact. As the charge carrier concentration in the device rises, recombination increases and not all charges are extracted.

Fig. 2.6 (d): At small forward bias, i.e. when a small external load is attached, the electrical field opposes the diffusion. The diffusion gradient of the QFLs however still drives the charge carriers to their respective electrode, but recombination rises further.

Fig. 2.6 (e): Under open circuit conditions, no current can be extracted from the solar cell, because all charge carriers recombine in the bulk. The open circuit voltage equals the difference between the two QFLs at the contacts.

Fig. 2.6 (f): If the forward bias is further increased, the contacts start to inject charge carriers, which accumulate at the opposite electrode. The charges cannot recombine at the surface of the membranes, but only in the bulk.

2.2 Organic Semiconductors

Before describing the particular processes of the solar energy conversion in OSCs, it is necessary to highlight the differences between organic, i.e. carbon-based, and inorganic semiconductors, e.g. silicon.
The conducting and semiconducting properties of polymers were discovered when poly-acetylene (PA, see figure 2.7, left), a simple polymer, was accidentally doped with iodine concentrations, which were three orders of magnitude larger than intended [2]. It turned out that with high doping levels, PA changed from being an insulator to being a good conductor, an effect, which had not been observed in polymers before. This conducting and semiconducting behaviour was subsequently found in other polymers as well and it was possible to create new materials with these properties. The common

structural feature of all these materials is the alternation between single and double bonds between C-atoms.

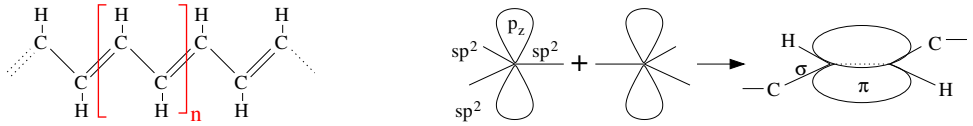

Figure 2.7: *Chemical structure of trans-poly-acetylene (PA, left) and the formation of the delocalised π bonds along the polymer chain (right) from the* p_z *orbitals when adding polymer repetition units. These π bonds are the origin for the (semi-)conducting properties of organic materials.*

PA is often used for describing how the semiconducting properties in a polymer can arise due to its simple chemical structure, consisting of weakly coupled CH units forming a quasi-1D lattice [9, 10]. A single carbon atom has its orbitals 1s and 2s filled and two electrons in p-orbitals, totalling six electrons, of which the four electrons in the 2s, $2p_x$, $2p_y$ orbitals are the valence electrons. In PA three of the four valence electrons are in three new sp^2 orbitals. Two of the σ-type bonds connect along the 1-D polymer backbone and the third forms a bond with the hydrogen side group. Only one electron, which does not join the hybridisation process, remains in the p_z orbital, which is perpendicular to the plane defined by the σ bonds. The p_z orbitals from neighbouring carbon atoms overlap and form a delocalised π bond. In the energy band model, this would be equivalent to the σ-bonds forming low-lying, completely filled bands, while the π bond leads to an only partially filled band from which the important electronic properties arise. If all bond lengths were equal, a unit cell would consist of one CH monomer and PA would be a conductor, because the π bond would only be half occupied in the simple picture. However, the Peierls instability leads to a dimerisation of the periodic 1-dimensional structure of the polymer [11]. This means that the bonds between neighbouring carbon atoms alternate between a longer single and shorter double bonds ($\Delta \approx 0.08$ Å). The consequence is that the π band splits energetically into two bands, π and π^*, because the unit cell now consists of two CH monomers. One band is completely occupied (HOMO or valence band) and the other completely unoccupied (LUMO or conduction band) respectively, resulting in a 1-D intrinsic semiconductor.

2.2.1 Excitations

Due to the low dielectric constant (ϵ_r ≈3-4) compared to most inorganic semiconductors (>10) and the small overlap of the molecular orbitals, organic semiconductors are characterised by strongly bound excited states. Excitons, as the excited states are best described as, thus have Coulombic binding energies ranging from about 100meV to 1eV and are localised on a few polymer repetition units or a molecule [12]. The exciton is electrical neutral and thus to first order unaffected by external electric fields and thus moves by diffusion. For inorganic semiconductors typical binding energies of photogenerated electron-hole pairs are typically far below k_BT (ca. 26meV at room temperatures) such that free charge carriers are generated upon photoexcitation due to thermal dissociation. Figure 2.8 illustrates this fundamental difference. The categorisation into conventional semiconductors, i.e. most inorganic, and excitonic semiconductors, which includes organic semiconductors, has been done by the ratio of the width r_C of the Coulombic potential well at k_BT and the Bohr radius of the relevant charge carrier r_B [13]:

$$\gamma = \left(\frac{r_C}{r_B}\right) \approx \left(\frac{e^2}{4\pi\epsilon_0 k_B r_0 m_e}\right)\left(\frac{m_{eff}}{\epsilon_r^2 T}\right), \tag{2.13}$$

where e is the electronic charge, ϵ_0 the permittivity of free space, r_0 the first Bohr radius of an electron of the hydrogen atom, m_e the mass of the electron and m_{eff} the effective electron mass in the semiconductor. If $\gamma > 1$ an excitonic behaviour is observed.

An important consequence of the locally bound exciton is the strong interaction with the lattice. The promotion of an electron from valence state to conduction state and the confinement of the resulting anti-bonding wavefunction to a small number of carbon atoms leads to a large rearrangement of the valence electrons. As result, the local bond lengths change, which subsequently affects both optical and electronic properties.

2.2.2 Charge Carriers and Charge Carrier Transport

The free charge carriers in organic materials are also localised to within a few polymer repetition units or a molecular unit and strongly couple to the lattice, which locally changes both optical and electronic properties of the material. These charges, i.e. electrons and holes in the π^* and π orbitals

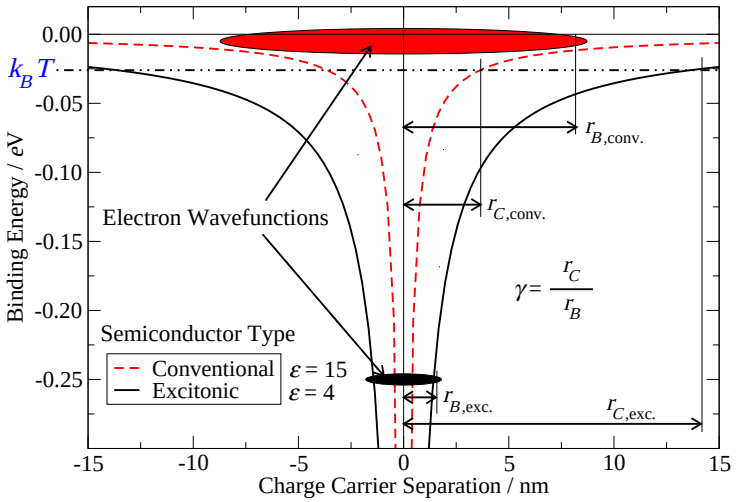

Figure 2.8: *A schematic plot of the fundamental difference between organic and inorganic semiconductors (redrawn from [13]). The calculations assume the positive charge of the photogenerated electron-hole pair at 0nm. It shows that in conventional, i.e. most inorganic semiconductors, free charge carriers are generated upon photoexcitation, because the electron wavefunction extends further than r_B, i.e. the radius of the Coulomb potential at k_BT. However, in excitonic semiconductors, e.g. organic semiconductors, the photogenerated electron-hole pair is electrostatically bound. The two fundamental differences are the dielectric constant ϵ_r and the Bohr radius of the relevant charge carriers. When $\gamma = r_C/r_B > 1$, the wave function of the electron is spatially restricted and "fit" deep into the potential well, i.e. is less delocalised..*

respectively, can move along the delocalised π bands of the 1-D polymer backbone. However, due to defects caused by twisting and bending of the polymer backbone the delocalisation of both π and π^* orbitals is in reality limited to about 10-20 polymer repetition units, the so-called conjugation length. The transport over these defects, which is can be considered to be equivalent to the transport between different molecules, is much slower than band transport and is best described as thermally assisted hopping process. This hopping of charge carriers between localised sites is the dominant charge carrier transport mechanism in disordered organic materials at ambient temperatures. Whereas the mobility for band transport decreases with increasing temperature, actually the charge transport in organic materials improves due to activated hopping. A higher charge carrier mobility in semiconducting polymers would be achieved by aligning and ordering the polymer, but is limited by the high gain of entropy for the unordered structure.

An important consequence of this behaviour is that band diagrams, which

are often used for representing semiconducting polymers, can only be a crude approximation of the available energies. They do not imply that there is band transport nor that the energy levels remain the same in presence of charge carriers.

The experimental investigation of the charge carrier transport is difficult. Both electrical and optical properties of the material can be highly anisotropic through the 1-D nature of the electronic system and the measured mobilities strongly depend on both the morphology of the material, i.e. the arrangement of the molecules, and the method used [14].

There are currently two models describing the hopping transport between two localised orbitals, i.e. over a defect on the polymer backbone, between different molecules: the Miller-Abrahams model [15] and the diabatic model based on the electron transfer theory of Marcus [16].

In the Miller-Abrahams model the transfer rate ω_{ij} from hopping site i to j with energy E_i and E_j respectively are given by:

$$\omega_{ij} = \omega_0 |V_{ij}|^2 \begin{cases} \exp(\frac{-(E_j - E_i)}{k_B T}) & \text{if} \quad E_j > E_i \\ 1 & \text{otherwise} \end{cases} \tag{2.14}$$

If sites i and j have the same energy, the transfer rate is simply given by the product of proportion ω_0 and the square of the overlap integral of the electronic wavefunctions $|V_{ij}|^2$. If the final state is higher in energy than the starting state, the transfer rate is reduced by the Boltzmann factor. Since organic molecules are only bound by Van-der-Waals forces, the distance dependence of the overlap integral can be approximated by

$$|V_{ij}|^2 \propto \exp(-2\zeta |R_{ij}|) \tag{2.15}$$

where R_{ij} is the distance between both electron orbital centres of site i and j and ζ is proportional to the inverse of the localisation radius of the orbitals. The diabatic model is a result of first order perturbation theory [16]. The hopping rate from site i to j is given by:

$$\omega_{ij} = |V_{ij}|^2 \sqrt{\frac{\pi}{\hbar k_B T E_\lambda}} \exp\left(\frac{-(E_i - E_j - E_\lambda)^2}{4 k_B T E_\lambda}\right). \tag{2.16}$$

The reorganisation energy, E_λ, is a parameter of the material, which is determined by the vibrational modes of the molecules in the mixed phase. Contrary to the Miller-Abrahams model hopping events between states with

lower energy and states of higher energy can be thermally activated and get faster with increasing temperature.

Despite their differences, both models satisfy the requirements for a detailed balance, i.e. there are no sinks or sources in the charge carrier flow in both models. Monte-Carlo simulations for systems with Gauss-distributed spatial and energetic disorder have shown that the mobility μ increases significantly for high electric fields for both models, while being constant for small (in this context) electric fields (up to ca. 0.3MV/cm) [17, 18]. The typical electric fields in OSC are in the order of 0.1 MV/cm.

Organic Semiconductors for OSCs

The structures of three common organic semiconductors used for organic solar cells are shown in figure 2.9: poly(2-methoxy-5-(3,7-dimethyloctyloxy)-1,4-phenylene vinylene) (MDMO-PPV), regioregular poly(3-hexylthiophene) (RR-P3HT) and the fullerene derivative 1-(3-methoxycarbonyl)-propyl-1-1-phenyl-(6,6)C_{61} (PCBM). The first two are semiconducting polymers, like PA. The last one belongs to the group of semiconducting molecules. The structure of the materials is more complex than the one of PA, but they share the same structural feature of alternating single and double carbon bonds. The mechanism of charge transport is similar and dominated by hopping.

"Regioregular" means that the alkyl side chains of the P3HT are aligned in a periodic structure as opposed to the "regiorandom" case. PPV and Polythiophene are the actual conjugated polymer backbones, and the additions label the side chains. The primary use of the side chains is to make the materials soluble in organic solvents. Without side chains the polymer would hardly or not at all be soluble and therefore very difficult to process from solution. Additionally, the side chains can change the electro-optical properties of the materials and thus be used to tune the materials. Finally, the morphology in the solid is crucially influenced by the regularity of the side chains [19]. The fullerene derivative PCBM has so far shown the best OSC results in combination with polymers [20]. Again the functional side group is necessary to make the material soluble.

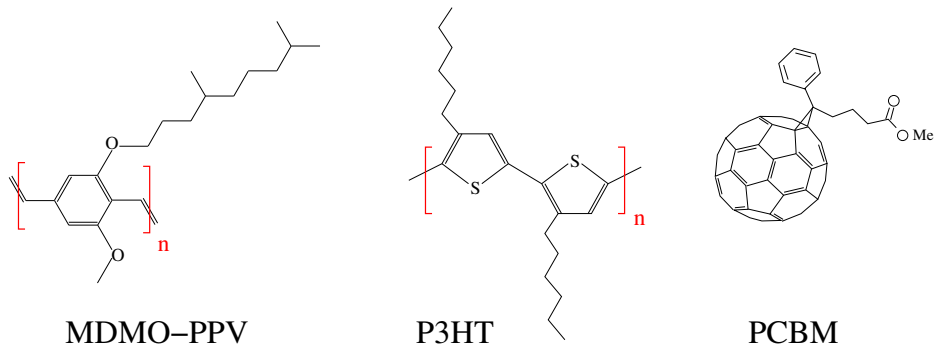

Figure 2.9: *The chemical structure of three common organic semiconductors used in organic solar cells. A combination of MDMO-PPV and PCBM for several years has been the standard research material. Today, most of research is carried out with P3HT and PCBM, because of the higher achieved power conversion efficiencies and an increased environmental stability.*

Table 2.1: *Summary of the main differences between organic and inorganic semiconductors. The table shows the values of materials used for photovoltaics. Crystalline silicon is chosen as example for the inorganic semiconductor, because it dominates the market for inorganic solar cells. The values for the organic semiconductor are typical for materials used for organic photovoltaics.*

	crystalline silicon	organic
Basic Entities	atoms	molecules
Bulk Structure	crystalline	amorphous
Dielectric Constants	11.9	$\approx 3-4$
$\gamma = r_C/r_B$	<1	>1
Excitation Binding Energies at 300K	$< k_BT \approx 0.26$meV	>100meV
Optical Gap	$1.1e$V	$\approx 2e$V
Lattice coupling of excitations/charge carriers	weak	strong
Dominant transport mechanism	band transport	hopping
Charge carrier mobility μ	100-1000cm^2/Vs	«0.1cm^2/Vs
T-dependence of mobility	$T\uparrow \Rightarrow \mu\downarrow$	$T\uparrow \Rightarrow \mu\uparrow$
Absorption Coefficient at $2e$V	≈ 2500/cm	≈ 16000/cm

2.3 The Bulk Heterojunction Solar Cell

The simple two-level electronic model system presented in section 2.1 allows the conversion of light energy into chemical potential energy. With suitable contacts this energy can be converted into electrical energy and is available to external consumers.

A bulk heterojunction solar cell has characteristics from the two-level model system (see section 2.1) the corresponding fundamentals will be presented

in the following sections. Its core feature is the donor-acceptor system, an intimate blend of an organic semiconducting electron donor material and a corresponding electron acceptor material. Then the analogy to the two-level model system from the previous sections is established. Charge carrier transport, interfaces between organic semiconductors and contacts, as well as recombination processes are still under intensive investigation and the current state of the art is presented as far as necessary for this work.

2.3.1 Principles of the Donor-Acceptor System

Excitons in pure polymer layers decay within less than $1\mu s$ with emission of a photon (photoluminescence, PL) and due to the strong exciton binding energies a spontaneous separation into free charge carriers is highly unlikely at room temperatures. In the case of solar cells this recombination is undesired and avoided by introducing a second material with a different electron affinity. Consequently a heterojunction between the materials is formed. If the energy gained by the electron in moving to the second material, i.e. the electron acceptor, exceeds the Coulombic binding energy of the exciton, charge separation will occur, leaving a hole on the donor material as shown in figure 2.10.

In the kind of OSCs treated in this work a semiconducting polymer is used as electron donor and the fullerene derivative PCBM as electron acceptor. In the case of MDMO-PPV the transfer of the excited electron to the PCBM takes place in less than 45fs [21], and for P3HT still faster than some picoseconds, leading to a conversion of nearly 100% of the excitons into free charge carriers. The achieved charge separation is meta-stable, i.e. the back reaction is much slower with life times in the milliseconds [13]. Hence both materials are often treated as one effective material with the HOMO of the donor and the LUMO of the acceptors as lower and upper level. Therefore we are in some respect dealing with a two-level system, the basic principles of which have been described in section 2.1.

There is an analogous process for generation of excitons on the PCBM. Here the electron of the exciton remains on the PCBM whereas the hole is transferred to the π-level of the polymer, which is equivalent to the transfer of an electron from the polymer HOMO to the PCBM HOMO. However, due to the higher band gap of PCBM, this process can be neglected in the solar

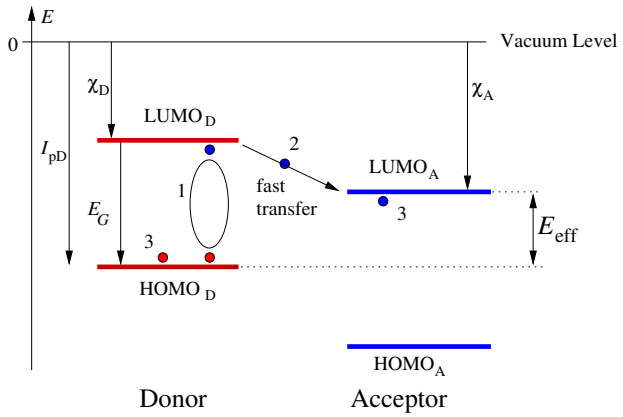

Figure 2.10: *The energy levels of a donor-acceptor system. The differences in electron affinity χ and ionisation potential I_p between the two materials are the key for an efficient charge separation in the donor-acceptor system. When in close proximity, a strongly bound exciton on the donor material (1) can dissociate into free charge carriers by transferring the electron to the acceptor material (2), if the difference in the electron affinity χ of donor and acceptor. i.e. the difference between the two LUMOs is large enough. The dissociation of an excitation on the acceptor depends on the difference in the ionisation potentials I_p. For the materials used in OSCs, the charge transfer is very fast, e.g. <45fs for a combination of MDMO-PPV and PCBM as donor and acceptor material respectively [21]. The charge separated state (3) is meta stable with the back reaction being in the order of milliseconds. However, a substantial part of the exciton's energy is lost during dissociation and the effective electrical gap E_{eff} is much smaller than the optical gap E_G (ΔE typically >0.5eV).*

spectrum.

The fundamental limitation of the donor-acceptor system is obvious from figure 2.10: a substantial amount of energy, typically more than 0.5eV, is lost during the dissociation of the exciton, i.e. the transfer of the electron from the donor to the acceptor. Due to the fast transfer the maximum attainable splitting of the electron and hole QFLs is limited by the HOMO of the donor and the LUMO of the acceptor. This implies that the effective electrical gap E_{eff} of the combined materials is much smaller (about 1.2-1.7eV for the combination of P3HT and PCBM as electron donor and electron acceptor respectively) than the optical gap E_G of either P3HT or PCBM.

The dissociation at the interface leads to a large concentration gradient of charge carriers, which drives them away from the donor-acceptor interface and generates the photovoltage. The limit of the maximum attainable V_{oc}

is thus given by E_{eff} rather than by the difference in workfunctions of the contacts [13]. The E_{eff} can be changed by using an acceptor or donor with different LUMO or HOMO respectively. Subsequently changes in V_{oc} are observed [20].
Using different donor-acceptor materials raises the question of how big the energy difference of the levels involved in the transfer has to be in order to extract the maximum power [22]. This question has not been answered so far, because the details of the charge transfer are not completely understood yet and will strongly depend on the involved materials.

2.3.2 The Bulk Heterojunction

The first OSCs were realised as bi-layer devices of donor and acceptor. They reached a power conversion efficiencies of around 1% [23]. Excitons are generated throughout the device, however, they typically diffuse only about 10nm (MDMO-PPV, [24]) before decaying. Hence only excitons created within this distance of the planar interface between donor and acceptor material split effectively into free charge carriers. This considerable limitation was solved by blending donor and acceptor material which – by virtue of the mesoscopic morphology – can create a large interfacial area between donor and acceptor on length scales comparable to the exciton diffusion length [25]. The resulting interpenetrating donor-acceptor network is called a bulk heterojunction, because the heterojunction is distributed throughout the photovoltaic active volume. It is an ongoing research challenge to realise the optimal morphology in which the phase separation is small enough to have efficient charge carrier separation while still to ensure that there are continuous pathways, i.e. percolation paths, to the corresponding contact.
The OSC structure shown in figure 2.11 is currently the most widely investigated structure and will be used as model system for describing the key features of organic bulk heterojunction solar cells.
The OSC is built on an indium-tin-oxide (ITO) coated glass substrate. The ITO electrode is transparent in the visible range. To facilitate hole extraction from the absorber layer, the substrate is additionally coated with the transparent organic conductor poly(3,4-ethylenedioxythiophene) (PEDOT) highly doped by the organic acid poly(styrene-sulfonate) (PSS) [26]. PEDOT:PSS[2]

[2]The semicolon, i.e. ":" denotes mixtures of two materials.

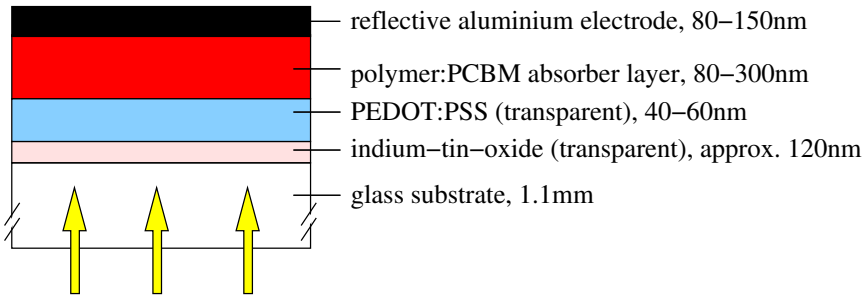

Figure 2.11: *The typical layer structure of a polymer-PCBM OSC. A glass coated with indium-tin-oxide (ITO) serves as substrate. A thin PEDOT:PSS layer on top of the ITO, acts as anode for the polymer:PCBM layer, which will be called absorber layer throughout this work. The cathode is realised through an evaporated aluminium layer. Both PEDOT:PSS and absorber layer are spin-coated from solution. The illumination is through the substrate.*

serves as the hole contact and its chemical structure is shown in figure 2.16.

The photovoltaic active absorber layer, consisting of a polymer:PCBM blend is applied from solution. Finally, the electron contact of the absorber layer is realised by evaporating an 80-150nm thick, highly reflecting aluminium (Al) electrode onto the absorber. Sometimes a 0.6nm thick lithiumfluoride (LiF) layer is being evaporated between absorber layer and aluminium cathode, because it is claimed that this improves the OSC performance [12, p. 217]. The whole OSC production process is described in detail in chapter 3.

The absorption of light takes primarily place in the absorber layer. Various semiconducting polymers have been used, of which the more common ones are PPV-derivatives and P3HT, being introduced in figure 2.9. However, with the currently used organic materials the overlap between their absorption and the solar spectrum is rather weak, which is illustrated in figure 2.12.

The optical constants for the absorber blend were taken from Hoppe et al. [27]. The AM1.5g solar spectrum as specified by the IEC-norm 903-3 equals the insolation at 48° latitude at a clear day with an integrated intensity of $1000\mathrm{W/m^2}$. The peaks in the absorption spectra of both absorbers at about 300nm can be attributed to the PCBM and the peak at around 500nm to the respective polymer. The absorption spectrum of the absorbing layer is as first approximation the superposition of the absorption spectrum of the components. This can be explained by the weak interaction between the molecules in their ground stated (Van-der-Waals forces). Figure 2.12 clearly

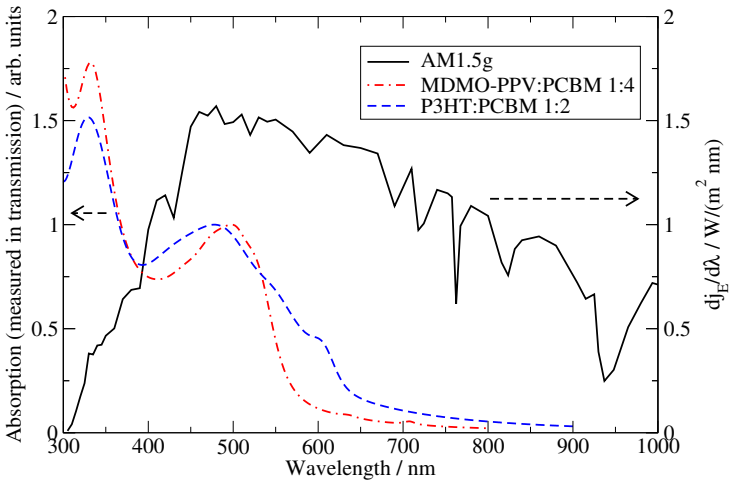

Figure 2.12: *The absorption spectrum for OSCs with a MDMO-PPV:PCBM (1:4 by weight) and P3HT:PCBM (1:2 by weight) as absorber layer as measured in transmission (data taken from [27]). For comparison, the AM1.5g spectrum is shown on the right axis. Due to an additional absorption shoulder in the red spectral region P3HT can harvest more of the sun light than MDMO-PPV.*

shows that the absorption of the photovoltaic active materials covers only a small part of the solar spectrum. MDMO-PPV, the polymer being previously at the focus of research, has been replaced by P3HT in the last two years, because the latter absorbs further into the red of the solar spectrum. The characteristic shoulder at 600nm in the P3HT absorption spectrum is caused by an improved ordering of the P3HT chains [28].

After the absorption of light free charge carriers are generated with a high probability due to the fine mixture of donor and acceptor. With the transfer of the electron to the lower lying acceptor level of the PCBM, the exciton on the donor polymer dissociates. This is a very efficient process such that already small amounts of PCBM lead to a nearly complete quenching of photoluminescence (PL), as can be seen in figure 2.13. However, a much larger amount of PCBM is necessary in order to extract the separated charges from the absorber layer.

2.3.3 Charge Carrier Transport

The way the polymer and the PCBM molecules arrange in the bulk heterojunction, i.e. the morphology of the active layer, has a decisive effect on the

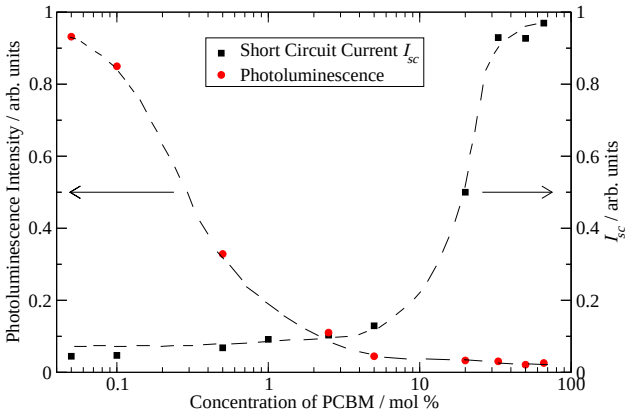

Figure 2.13: *Photoluminescence (PL) and short circuit current I_{sc} are shown as function of the molar PCBM concentration in a polymer matrix of MDMO-PPV (redrawn after [12, p. 166]). Already at a PCBM concentration of 1mol%, the PL is significantly quenched. However, PCBM concentrations of more than 17mol% are necessary to observe the onset of I_{sc}, which saturates for more than 30mol%PCBM.*

charge carrier transport and thus on the OSC performance. The two components are not mixable (but soluble in a common solvent) and the phase separation has to be similar size as the exciton diffusion length (about 10nm) for efficient exciton dissociation. The low charge carrier mobilities also limit the maximum device thickness.

When mixing MDMO-PPV and PCBM, nearly all excitons already dissociate at 1mol% PCBM concentration, as can be inferred from the extinction of the polymer's photoluminescence. However, as figure 2.13 shows, a much higher PCBM concentration (about 20mol%) is necessary for sufficient charge transport to the electrode. For MDMO-PPV it has been shown that the maximum efficiency is reached for PCBM concentrations of up to 80mol%, depending on the thickness of the absorber. Efficiencies of around 3% are reported in literature. However, it is apparently not the electron mobility, which requires such a high PCBM concentration, but the hole mobility in MDMO-PPV, which benefits from the high PCBM concentration [29]. This leads to two limitations of the MDMO-PPV:PCBM OSC: PCBM is hardly absorbing the solar spectrum and the morphology is not thermodynamically stable, i.e. the PCBM has the tendency to form clusters, which can exceed the exciton diffusion length [30].

P3HT:PCBM based OSCs require much less PCBM and an η approach-

ing 5% has been reported for concentrations between 1:0.6-0.8 polymer to PCBM [31]. P3HT can be made to crystallise in the absorber layer, improving the hole mobilities by nearly three order of magnitude, reaching values close to the ones obtained for pristine spin-coated films (about 10^{-8}Vs/cm^2). Still μ_h is at least one order of magnitude lower than the electron mobility in the bulk [14]. Modification of the morphology on the nanometre scale is achieved by a heat treatment of the OSC after production, often with temperatures up to 150°C. During the heat treatment, the structure of the morphology, which has been frozen when the solvent evaporated during spin-coating, can relax to a energetically more favourable configuration. P3HT with a high regioregularity can form nano- or even micro-crystalline domains in the absorber layer, which lead to the observed increase μ_h. Much research is currently focussed on optimising the morphology and a thermal post-treatment step has become a standard process for P3HT:PCBM based OSCs.

An additional issue which has to be considered when describing the transport in a bulk heterojunction are the percolation paths, i.e. whether there is a continuous path of the same material to the respective electrode. Once the exciton has dissociated the charge carriers – the hole on the polymer and the electron on the PCBM – have to find a way towards their respective electrode. Depending on the phase separation, i.e. the degree of mixing of polymer and PCBM, there are e.g. regions of the polymer which have direct contact to no electrode or only the cathode. However, the phase separation itself is in the most cases not directly accessible. Its dimensions require atomic force microscopy (AFM) and it is often not possible to infer from the AFM surface the morphology in the bulk.

2.3.4 Charge Carrier Extraction at the Contacts

As described in section 2.1.3, ideal contacts need to satisfy the following two requirements: (1) they have to be semipermeable only to the respective charge carriers and (2) have to contact the corresponding transport levels. Then the chemical potential energy in the semiconductor can be converted without loss into electrical energy in the external circuit. However, real contacts in solar cells do generally not meet both requirements and the solar cell performance therefore depends significantly on the choice of electrodes.

When the contact between a metal and a semiconductor is formed, charge carriers are transferred across the interface until the Fermi level of the metal and semiconductor align at the interface and throughout the combined system. The simple picture in figure 2.14 shows a Schottky contact formation, i.e. between a semiconductor, here p-type, and a metal. In this example, electrons flow from the metal into the semiconductor charging it negatively. The redistribution of charges due to equilibration of the Fermi levels creates a potential difference leading to a bending of the bands inside the semiconductor, which eventually stops the transfer of further charges through the interface once the Fermi levels are equal. The energy barrier for injecting

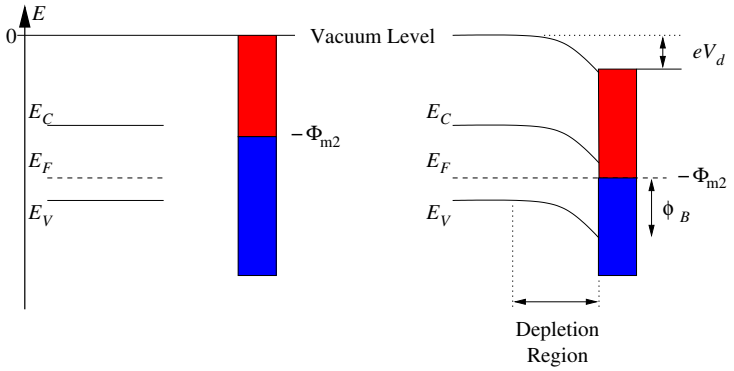

Figure 2.14: *The energy diagram of a p-type semiconductor and a metal prior to contact formation (left) and after contact formation (right). Upon contact formation, charges are transferred across the interface until the Fermi levels of on both sides of the contact are equal. The electric field caused by the transferred charges leads to a bending of the electronic bands inside the semiconductor, the region of which is called depletion region. The vacuum level is displaced by eV_d and a barrier ϕ_B forms at the interface.*

holes into the metal in this simple picture is then given as

$$\phi_B = E_V + \Phi_{m2} \tag{2.17}$$

The region of band bending is called the depletion region. For organic semiconductors the depletion region can extend, depending on the material, through the whole absorber layer [32].

This simple picture neglects several important issues and there is much research going on with regard to the properties of metal-organic interfaces. A detailed description of the physical processes involved at the interfaces between metals and organic semiconductors is beyond the scope of this work.

A very important factor is the incommensurability of the crystal structures (crystalline vs. amorphous) of the interfacing materials. Further factors influencing the interface formation are, e.g. the wave function hybridisation, charge transfer and chemical reactions. The interested reader is referred to the reviews in references [33, 34]. Contact models for contacts between inorganic semiconductors and metals have to be used carefully and be viewed in the light of the fundamental differences between organic and inorganic semiconductors (see table 2.1). In the following sections, only the main issues are summarised. Furthermore, it is described how the performance of OSCs depends on the choice of electrode materials.
The formation of the interfaces depends on:

- the energy levels, crystal structure, surface morphology, molecular structure and alignment at interface,
- the sequence in which the materials are deposited (organic-metal or metal-organic),
- the method of deposition of the materials and its parameters (evaporation or coating from solution),
- the workfunction of the two materials and possible difference in vacuum levels.

The contacted bulk heterojunction solar cell has three planar interfaces between different materials (figure 2.11), leading to the energy diagram shown in figure 2.15. The properties of these interfaces will be discussed in the following.

The Polymeric Anode

The most commonly used anode is the organic conductor PEDOT:PSS, supported by the metal oxide ITO, leading to two interfaces for the charge carrier: ITO|PEDOT:PSS[3] and PEDOT:PSS|Absorber.
ITO is used as transparent electrode in many applications, e.g. flat panel displays, where good electrical conductivity as well as high optical transparency in the visible region and processability are paramount. ITO alone could serve as anode in OSCs or OLEDs, but it has been shown that an

[3]The vertical dash, i.e. "|", denotes the planar interface between two materials

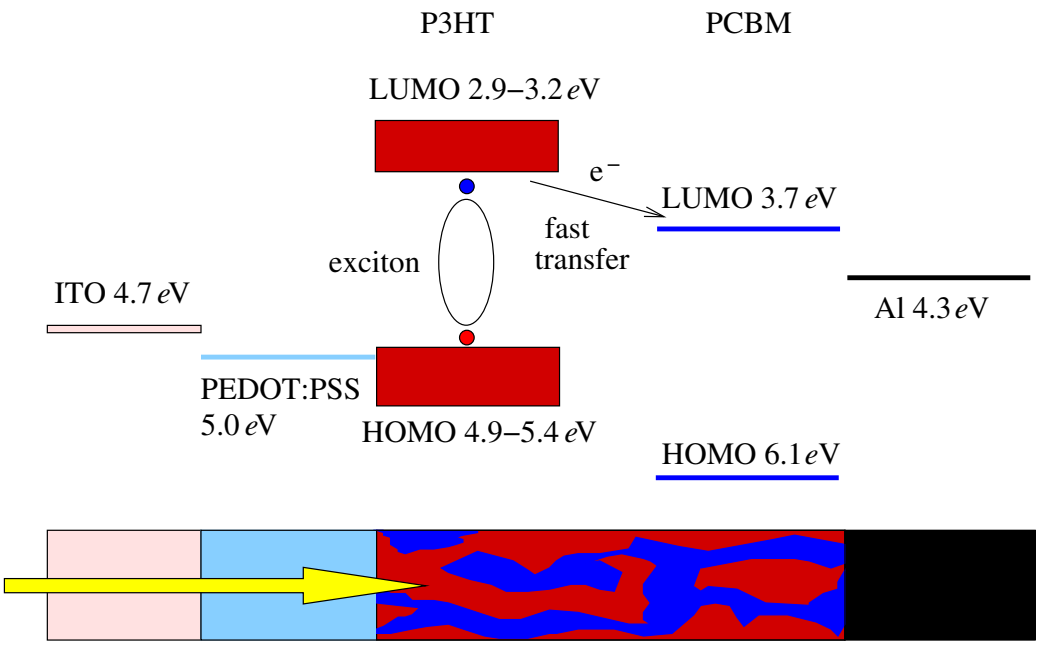

Figure 2.15: *The complete energy scheme for P3HT:PCBM OSCs. The energy levels of P3HT can only be given as approximate values, because they vary and depend on the method used to measure them. The energy levels for PCBM are better determined, but there is still a controversial discussion about the values. The energy levels of P3HT and PCBM are drawn side-by-side for simplification, although they are intimately mixed as the idealised sketch beneath the energy diagram illustrates. Semipermeable membranes in OSCs are sometimes visualised as structural features where e.g. only P3HT has physical contact to the PEDOT:PSS layer.*

additional layer of PEDOT:PSS improves the device performance considerably [26]. Its chemical structure is shown in figure 2.16. Studies using UV photoemission spectroscopy (UPS) have shown that the vacuum levels of a semiconducting polymer spin-coated onto a PEDOT:PSS layer and of the PEDOT:PSS itself align and the barrier for hole injection is determined by the workfunction of PEDOT:PSS instead of ITO [35]. PEDOT:PSS typically has a higher work function than ITO, matching more closely the HOMO (VB) of the semiconducting polymers, hence reducing the barrier for hole transport over the interface. Additionally, the PEDOT:PSS helps to reduce the variations from ITO, the topological as well as chemical properties of which can differ even between batches of the same manufacturer.

PEDOT itself is an insoluble polymer, but it has several good properties in its oxidised state like high conductivity, good transparency and stability [36].

However, simple processability, e.g. from solution, is of high importance for many applications. The low solubility can be circumvented by either polymerising and doping EDOT, the monomer, in situ or by stabilising it with poly(styrene sulfonic acid) (PSS), a soluble poly-electrolyte, while polymerising it in a solvent. In mixture, the PSS-acid donates a proton from its HO_3S-group to a sulfur atom of PEDOT. This leads to a positive doping of PEDOT, while the PSS guarantees charge neutrality, leading to the oxidised state of PEDOT with its advantageous properties.
There are different kinds of PEDOT:PSS commercially available and their conductivity, work function and chemical properties can be further modified to suit the particular application [37]. Especially a heat treatment after spin-coating increases the conductivity of the PEDOT:PSS layer up to two orders of magnitude by changing the morphology of the film. Other methods, e.g. including further additives, are currently being researched [36, 38].

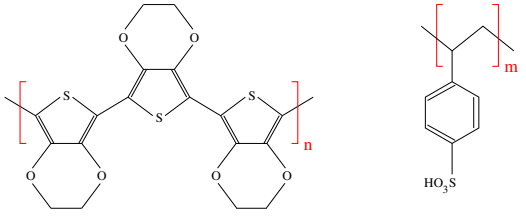

PEDOT PSS

Figure 2.16: *The chemical structure of poly(3,4-ethylenedioxythiophe) (PEDOT) and poly(styrene-sulfonate) (PSS). In mixture, PSS oxidises PEDOT, making it a highly conducting polymer. It is used in organic electronics as anode, because it facilitates hole transport across the anode interface.*

The electrical contact between ITO, PEDOT:PSS and HOMO level of P3HT is ohmic [14]. Changing the work function of PEDOT:PSS by chemically altering it has a direct influence on the V_{oc} of an OSC. The V_{oc} scales linearly with a slope of 0.8 with the workfunction of the PEDOT:PSS layer until the workfunction exceeds the HOMO level of the polymer. Then the V_{oc} suddenly drops, as there are then no available states for hole injection from the polymer into the PEDOT:PPS layer [37].

The Metal Cathode

The cathode is typically realised by vacuum deposition of a low workfunction metal through evaporation on the organic absorber layer. A thin layer of alu-

minium is the most common cathode, but other materials have been tested, e.g. Ca|Ag. Still, the interface formation between the absorber layer and the evaporated metal cathode has up to now not been accurately described.

For inorganic semiconductors, the contact formation to metals is well researched. However, the contact between organic semiconductors and metals has on the one hand strong bonds in the metal and weak van-der-Waals bonds in the organic semiconductor. Additionally, their structures are incommensurate. In the metal there are very many charge carriers and the transport is band-like. Organic semiconductor have very few charge carriers and a transport mechanism which is dominated by thermally assisted hopping. These differences make direct transfer of contact models from the inorganic picture to contact between metals and organic materials not possible. The details of the ongoing debate on how the interface properties form are however beyond the scope of this work.

The dependence of V_{oc} on the metal workfunction has been investigated by Brabec et al. for the MDMO-PPV:PCBM combination [20], who also determined for comparison the influence of the acceptor strength of the electron acceptor (fullerene). Whereas the V_{oc} exhibited only a weak dependence on the change in workfunction, is was directly proportional to the acceptor strength of the fullerene, suggesting that the difference in energy levels (HOMO donor to LUMO acceptor) is more relevant to V_{oc} than the metal workfunctions.

Mihailetchi at al. [39] showed for another PPV-derivative that depending on the used metal for the cathode, an ohmic or non-ohmic contact is realised at the interface to the organic semiconductor, and calculated the associated barriers and voltage drops. They claim that in the case of non-ohmic contacts the V_{oc} is only determined by the workfunction difference of the contacting metal as expected from the metal-insulator-metal picture [7]. In the ohmic case, however, the V_{oc} is governed by the difference in HOMO and LUMO level of donor and acceptor respectively in agreement with the findings of Brabec et al.. Here, the workfunctions of the cathode is pinned close to the LUMO of the acceptor and band bending leads to a voltage drop of typically 0.2V across the interface. The term ”pinning” is used in OSCs in a different context than for inorganic semiconductors.

2.3.5 Loss Mechanisms

Just like the charge transfer at the interfaces between organic and inorganic materials is an active field of research, so are charge recombination processes both in the bulk of the absorber and at the interfaces. The assessment of the optical losses is important in quantifying the number of absorbed photons in the photovoltaic active absorber layer. With a charge separation of the exciton faster than picoseconds in the bulk heterojunction, the direct radiative recombination of the exciton is unlikely as evident from the quenching of the photoluminescence [21]. Thus, it can be assumed that every photogenerated exciton dissociates. However, the free charge carriers still can recombine before being extracted at the contacts and the current understanding of the mechanisms is presented here.

Interface Recombination

Due to the different structure of metal (crystalline) and absorber (amorphous) and the continuous distribution of electronic states in the metal, the presence of states in the energy gap of the semiconductor at the interface is very likely. These states facilitate non-radiative charge recombination and losses can be high, as known from silicon solar cells. There the contact area is reduced as much as possible in order to avoid interface recombination losses or a barrier for the opposite charge carrier is created by a local field. However, no quantitative studies on the effect of interface recombination in organic semiconductors have been published to the best of my knowledge.

Bulk Recombination

The large interface area between donor and acceptor in the bulk heterojunction is necessary for a very efficient separation of photogenerated excitons. However, the large interface area and the intimate mixing also suggest the possibility of high recombination in the bulk, because donor and acceptor are spatially not well separated.
Studies with transient absorption spectroscopy on MDMO-PPV:PCBM layers have shown two different decay regimes [40, 41] of the photogenerated hole on MDMO-PPV, which are both associated with the recombination of hole on the polymer and an electron on the PCBM. They detected a fast regime with decay times $<$20ns, which depended strongly on the intensity of

the excitation pulse, and a slow regime with decay times between 300ns and 10ms, which quickly saturates with excitation density. The long-lived holes are thought to be trapped in localised states above the transport edge of the polymer HOMO. At pulse intensities comparable to solar irradiation, the slow regime was found to be dominating. It decays with a power law and the process is thermally activated. At high intensities, these localised trap levels get saturated and further polarons are in states where transport is easier. It is interesting to note that the decay between 300ns and 1ms is primarily associated with decay in bulk of the polymer and is independent of the PCBM concentration apart from time scales >1ms. Their conclusion is that at solar intensities, if mobility of untrapped holes is sufficiently high ($>10^{-3}\mathrm{cm}^2/\mathrm{Vs}$), charge recombination is sufficiently slow and does not influence the short circuit current.
If the mobility is lower or other recombination mechanisms come into play, the dependence of the photocurrent on the incident light intensity is not linear any more. Thus intensity dependent measurements can be used to assess recombination mechanisms in solar cells. In the ideal case, the photogenerated current should scale linearly with the incident light intensity P_{ill}. However, in the real case, this behaviour often deviates from the linear relation. Assuming a power law relation between photogenerated current I the relation can be written as

$$I(P_{ill}) \propto P_{ill}^{\alpha}, \tag{2.18}$$

where α is the scaling coefficient, i.e. the slope of I versus P_{ill} in a loglog plot. The scaling coefficient can give information on the dominant recombination mechanism. If the recombination is bimolecular, i.e. depends on the densities of free holes and electrons, $\alpha \approx 0.5$. For monomolecular, e.g. trap assisted recombination processes, α is expected to be 1.

Optical Losses

Optical losses in the OSC set an upper limit on the number of charges, which can be generated under illumination. Reflections at the interfaces and absorption of photons in layers, which are not photovoltaic active, reduce the number of photons available for absorption in the absorber layer (see figure 2.11). The main reflections occur at the air-glass interface and at the metal electrode. The latter reflection leads to the creation of an optical

interference pattern, because the thickness of the layer structures is in the same order at the wavelength of the incident light. Thus interference effects have a crucial effect on the absorption and any optical treatment has to be carried out coherently. The interesting region for the current materials (P3HT:PCBM) is between 300nm and 800nm. Optical simulations have shown that below 350nm most of the light is absorbed in the glass [42]. However, the AM1.5g photon flux is very small in this interval. Up to 550nm most photons are absorbed in the photovoltaic layer. At higher wavelengths, the absorption of the photovoltaic active materials decreases (see figure 2.12) and more photons are absorbed in PEDOT:PSS layer and the cathode.

2.4 OSC Modelling

Several attempts in modelling the current-voltage behaviour of OSCs have been made. There are two main approaches: microscopic models starting from transport, continuity and Poisson equations and equivalent circuit models built on basic electrical units like resistors and diodes. Both approaches will briefly be presented here.

2.4.1 Microscopic Models

The microscopic models proposed for OSCs are all based on the metal-insulator-metal picture [43, 44, 45, 46]. The interpenetrating network of donor and acceptor in the absorber layer is here replaced by one virtual semiconductor, which combines properties of both materials. Table 2.2 briefly summarises its typical properties. One justification for this approach is that the dissociation of the photogenerated excitons is a femtosecond reaction and the free charge carriers end up on different materials [25]. This virtual semiconductor is contacted with cathode and anode at the respective energy. For this system, the standard equations for describing the transport through a semiconductor are solved self consistently. Usually only the direction normal to the absorber layer, i.e. only one spatial dimension, is considered, because

Table 2.2: *In the microscopic models of OSCs the absorber layer consisting of a blend of donor and acceptor is replaced by one single virtual semiconductor, which inherits the properties from either donor or acceptor.*

	Virtual Semiconductor
Valence Band	HOMO of polymer
Conduction Band	LUMO of PCBM
Optical Gap	Gap of Polymer
Electrical Gap	PCBM LUMO - polymer HOMO
Fermi Level	intrinsic, i.e. mid-gap
Hole Mobility	polymer hole mobility μ_p
Electron Mobility	PCBM electron mobility μ_n
Contacts	ohmic

of the planar structure of the OSC. In this case the equations are:

$$J_n(x) = e\mu_n n(E_{ext} + E(x)) + k_B T \mu_n \frac{dn(x)}{dx} \tag{2.19}$$

$$J_p(x) = e\mu_p p(E_{ext} + E(x)) - k_B T \mu_p \frac{dp(x)}{dx} \tag{2.20}$$

$$0 = \frac{1}{e}\frac{dJ_n(x)}{dx} + \mathcal{G}(x) - \mathcal{R}(x) \tag{2.21}$$

$$0 = -\frac{1}{e}\frac{dJ_p(x)}{dx} + \mathcal{G}(x) - \mathcal{R}(x) \tag{2.22}$$

$$0 = e(p(x) - n(x)) + \epsilon_r \epsilon_o \frac{d(E_{ext} + E(x))}{dx} \tag{2.23}$$

The first two equations (2.19 and 2.20) describe the current density of electrons and holes with respect to drift and diffusion contributions assuming diffusion coefficients obeying the Einstein relation. μ_n and μ_p are mobilities for electrons and holes in the virtual semiconductor respectively. E_{ext} is the externally applied electric field through the OSC and $E(x)$ the electric field in the OSC which is caused by the rearrangement of the charge carriers. Equations 2.21 and 2.22 are the continuity equations for electrons and holes respectively. $\mathcal{G}(x)$ is the location dependent charge carrier generation rate. $\mathcal{R}(x)$ captures various recombination processes, ϵ_r is the effective dielectric constant for the material and ϵ_0 denotes the permittivity of free space. Finally, equation 2.23 is the Poisson equation. For a unique solution to equations 2.19-2.23 the carrier densities and the potential at the contacts need to be specified as boundary conditions, which is usually done by assuming Boltzmann statistics for the charge carriers there.

Assumptions on generation rate $\mathcal{G}$ and recombination rate $\mathcal{R}$ differ from

model to model. The shape of the generation rate $\mathcal{G}(x)$ in the thin absorber region deviates substantially from the exponential decay, which is however often assumed for light absorption. For a more realistic generation profile, optical interference effects in the thin film system need to be taken into account, because the wavelength of the irradiated light is of the same order of magnitude as the thin film system.
In addition to the current-voltage curves the characteristics of the energy level inside the virtual semiconductor and the charge carrier densities can be calculated with the help of the continuum model. However, many of the parameters necessary for the microscopic models are difficult to obtain experimentally. Furthermore, the parameters often cannot be considered constant, because they depend e.g. on the preparation conditions of the device. As consequence, similar IV-characteristics can be reproduced using different parameter sets, the values of which still might be reasonable for the investigated materials.

2.4.2 Equivalent Circuit Models

Equivalent circuit models are extensively used to parameterise the electrical characteristics of inorganic solar cells [47]. These models are discussed for OSCs as well. The simplest equivalent circuit for solar cells is shown in figure 2.17.

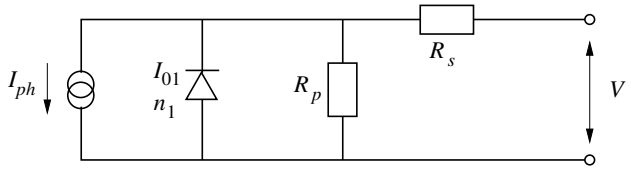

Figure 2.17: *A simple equivalent circuit model for solar cells. It consists, from left to right, of a current source for the photogenerated current I_{ph}, a diode with its characteristic dark saturation current I_{01} and ideality factor n_1, a bulk resistance R_p and a serial resistance R_s.*

The circuit consists of a current source for the photogenerated current I_{ph}, a diode, which is described by the dark saturation current I_{01} and the diode ideality factor n_1, and the serial and parallel resistance R_s and R_p respectively. The corresponding current equation is given by

$$I - I_{01}\left(exp\left(\frac{e(V - IR_s)}{n_1 k_B T}\right) - 1\right) - \frac{V - IR_s}{R_p} + I_{ph} = 0, \qquad (2.24)$$

where k_B is the Boltzmann constant, T the temperature of the device, V the externally applied bias voltage.

R_p takes the leakage current through the solar cell into account. R_s has contributions from the bulk and the interface, which can be distinguished by carefully varying the absorber layer thickness [48]. In the ideal case, $R_s = 0$, $R_p = \infty$ and equation 2.24 can easily be solved. In this simple picture, the illuminated IV-curve equals the dark IV-curve just being shifted by the photogenerated current. If $R_s \neq 0$, the equation has to be solved numerically. Using a set of sensible parameters $\{I_{01}, n_1, T, R_s, R_p, I_{ph}\}$ leads to typical IV-characteristics.

Equivalent circuit models have been applied to OSCs and attempts have been made to extend the simple model above in order to account for the deviations seen in OSCs. The extension of the simple model is said to be necessary to account for the bias dependence of the photocurrent I_{ph}, the illumination dependent dark saturation current I_{01} and the illumination dependent parallel resistance R_p.

Schilinsky et al. proposed a modification to the simple diode model to take the bias dependence of the photocurrent and the illumination dependence of R_p in a P3HT:PCBM bulk heterojunction solar cell into account [49]. With the assumption that the photogenerated charges are only driven by the electric field, the photocurrent changes sign when the external field compensates the built-in field. Their modification is similar to what is used in models for amorphous silicon [50, 51]. The illumination dependence of R_p is in their model explained by separating R_p into $R_p(dark)$, the parallel resistance in the dark, and $R_p(ill)$, an intensity dependent term. $R_p(ill)$ is often called photo-shunt, because of its intensity dependence. Its physical origin and meaning is not clear yet.

Yoo et al. try to included the seen deviation from the single diode model by adding a second, intensity dependent diode parallel to the first one [52]. They also added a light intensity dependent second R_p, which is analogous to the model proposed by Schilinsky. With the help of this model, they successfully determined the intensity dependence of the model parameters, but do not discuss the physical origin and meaning of these parameters. In addition to produce adequate fits, this is currently the main problem of the equivalent circuit models, i.e. establishing a link between the fit parameters and a physical explanation.

Chapter 3

OSC Production

This chapter introduces the organic solar cells (OSCs) used in this work and describes their production process at a laboratory scale. Each production step is presented with its main parameters, which are recorded for the data analysis. As far as there are standard procedures, these will be summarised. The description is detailed, because the analysis of the interdependence between OSC production and OSC properties obtained during characterisation are at the focus of chapter 6.

3.1 Standard OSC Layer Structure

The many different types of organic solar cells described in literature result from the large variety of available organic semiconductors and production technologies. They range from the evaporation of organic layers from very pure oligomers onto suitable substrates [53, 54] to coating of substrates with organic semiconductors from solution [25, 55, 56]. The OSCs investigated here are of the latter type and this section introduces what will be the standard OSC used in this work.

The layer structure of the standard OSC is shown in figure 3.1. It has already been used as example when describing the OSC fundamentals in chapter 2. Its main features are quickly summarised here again, specifying the materials used in this work.

The OSC is built on an indium-tin-oxide (ITO)-coated glass substrate. The ITO supports the conductivity of a thin, transparent layer of poly(3,4-ethylenedioxythiophene) (PEDOT), which is doped with poly(styrene-sulfonate) (PSS) and spin-coated on top of the ITO. The PEDOT:PSS layer has proven to facilitate the contact to the absorber layer and the hole transport across this

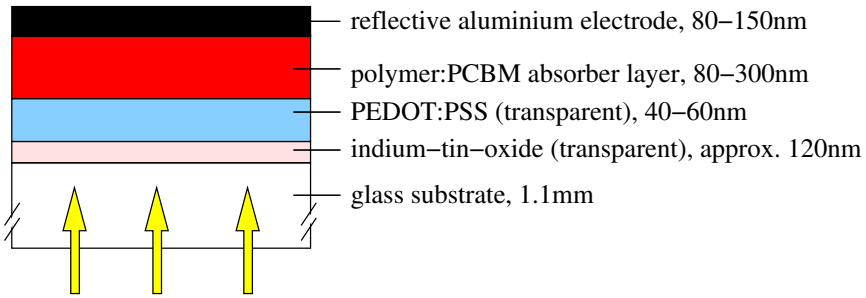

Figure 3.1: *The layer structure of the standard OSC used in this work. It is based on an ITO-coated glass substrate, on which the other layers are subsequently added during the production process. The polymer:PCBM absorber layer is the photovoltaic active region. The illumination is through the glass substrate and transparent ITO/PEDOT:PSS anode, i.e. here from below.*

interface [26]. The photovoltaic active absorber layer consists of a blend of an electron donating polymer and the electron accepting fullerene derivative, which is applied by spin-coating as well. The materials used here are the polymer P3HT (poly(3-hexylthiophene)) and the electron acceptor PCBM (1-(3-methoxycarbonyl)-propyl-1-1-phenyl-(6,6)C_{61}). Typical ratios of P3HT:PCBM are between 1:0.5 and 1:2 by weight. The thickness of the absorber layer is with 100-300nm sufficient for efficient light absorption in their absorbing regime due to the high absorption coefficients of the used materials. The cathode is realised through an evaporated aluminium electrode. The illumination of the OSC is from the substrate side through the ITO and PEDOT:PSS layer.

3.2 OSC Production Process

The production process investigated in this work can be described as sequence of different process groups, which consist generally of several process steps. An overview is shown in figure 3.2. The process groups are shown in boxes and the name of the outcome of each group is shown in hexagons. The measurements (yellow ellipse) are shown for completeness and their corresponding details are described in chapter 4. An illustrative way of representing the production process of the standard OSC is shown on the left in figure 3.2, where the formation of the layer structure of the substrates after each process group is depicted. One important point of the production process is that for spin-coating steps, the substrates can only be handled sequentially, whereas

Table 3.1: *The general parameters recorded for every production step in addition to the process specific parameters. They are all mandatory, apart from the comment, which can be used to note details otherwise difficult to record.*

Parameter	Symbol	Standard
Substrate		e.g. S 123
Timestamp		YYYY-MM-DD HH:MM
Location		process dependent
Researcher		login name
(optional: Comment)		

all other allow the processing of more than one substrate at a time (batch). This is depicted on the right in figure 3.2 and leads to different time intervals between steps for the substrates within one batch when moving from a sequential to a batch process step.

A detailed structuring and understanding of the OSC production process is necessary to allow its standardisation and adequate mapping to an electronic protocol (see section 5.2.2). This includes the definition of a well defined set of production parameters, which needs to be recorded for every OSC made in order to allow comparative OSC production and subsequent testing.

Using these process groups the production process is described in more detail in the following sections, beginning with the two separate preparation processes for substrates and for solutions. At the end of the description of each process group, a table lists all parameters recorded for the data analysis, their corresponding symbols used later as abbreviations, and standard values, if there are any. The parameters in table 3.1 are mandatory for each step and not explicitly repeated while describing the steps in the following sections.

3.2.1 Substrate Preparation and Cleaning

The starting material for the standard OSCs is bought as large ITO-coated float glass plates (40×35cm^2, Merck). The ITO has a sheet resistance of 20Ω/□ and is structured by laser ablation to obtain a pattern defining the anode area and the necessary interconnects of the OSCs on each substrate. For our substrates, this will lead to six or ten OSCs per substrate after evaporation of the cathode, the overlap of which with the ITO defines the photovoltaic active area (see section 4.2.1). After structuring of the ITO, these

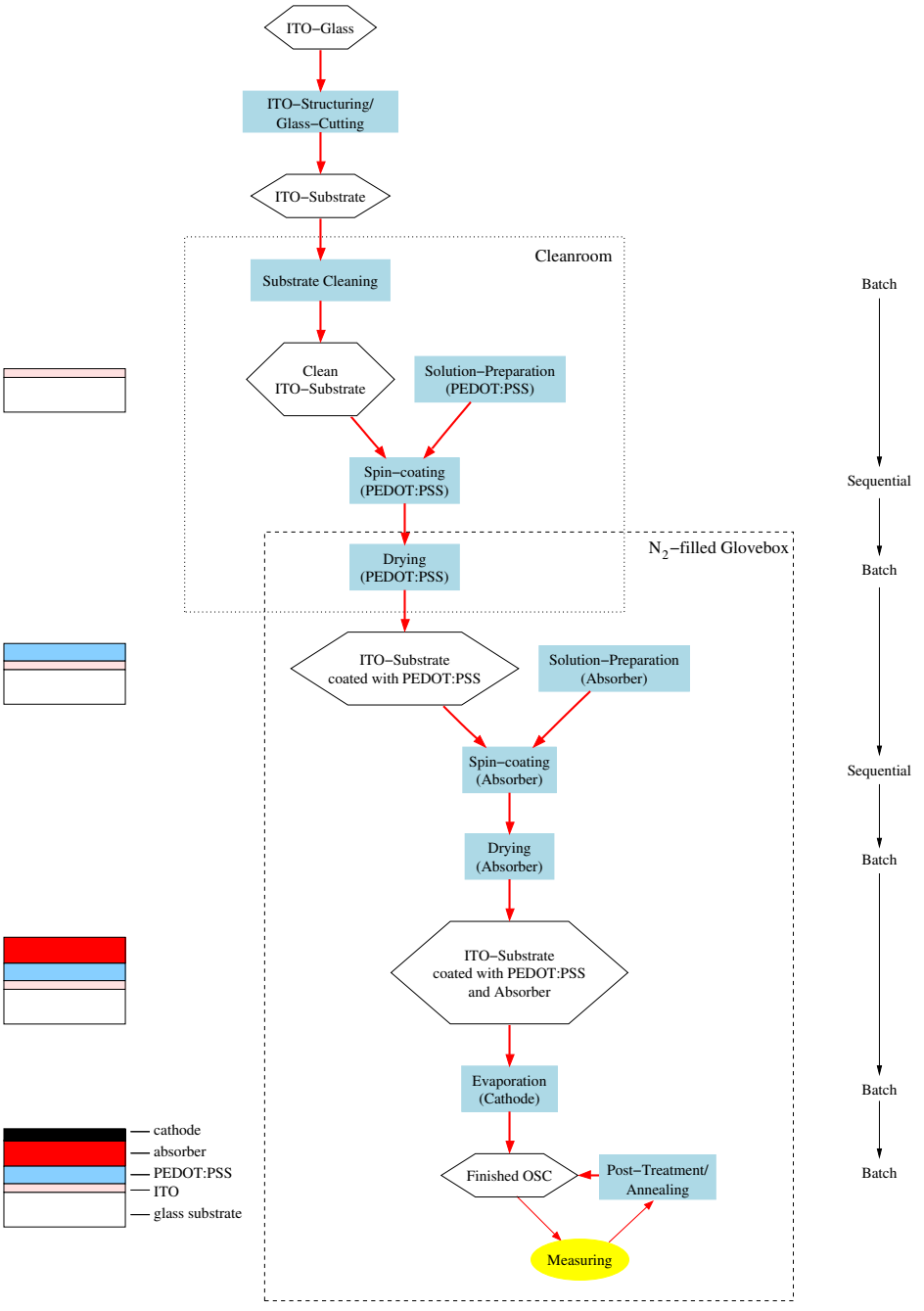

Figure 3.2: *The schematic step by step formation of the layer structure (left), the simplified production process of the standard OSC (middle), and the way the processes are carried out (right). The process is shown as sequence of process groups (blue boxes) and the substrate's state at its different stages (hexagons). The main measurements (yellow ellipse) are shown here for completeness and they are described in detail in section 4.1. Substrate cleaning and PEDOT:PSS spin-coating is done under cleanroom conditions and all subsequent steps are carried out in gloveboxes filled with inert gas. The processes can either be carrier out for one (sequential) or more than one (batch) substrates at once.*

plates are cut to so-called ITO-substrates of $25\times25\text{mm}^2$ and subsequently each substrate is engraved with an unique identifier (ID). This ID is used to continuously track the substrates during production and characterisation.

The cut and engraved substrates are then thoroughly cleaned, starting by manually wiping them using glass detergent in order to remove dust from structuring, cutting and storing. This treatment is followed by two acetone and two isopropanol treatments and a final bath in deionised (DI) water (all 600s), all with sonification. If necessary the substrates are stored in a separate beaker filled with DI water until the production continues after cleaning. The wet cleaning is usually carried out in batches of 24 substrates. When needed, the substrates are taken out of the DI water and immediately blow dried with nitrogen. Subsequently their ITO-side is exposed to ozone in a UV-photoreactor (1200s) to remove any organic residue. Additionally it has been shown that the UV-ozone treatment modifies the surface's wetting properties, reduces the surface roughness and increases the work function of ITO [57]. The clean ITO-substrate is then ready for the next process step. Clean substrates, or in general, clean surfaces, are essential for OSCs, because the layers of an OSC are much thinner ($< 300\text{nm}$) than an average dust particle (several μm diameter). Any contamination would have a negative effect on the OSC by introducing unwanted inhomogeneities in the thin layers. Hence the last two cleaning steps, i.e. the cleaning in DI-water and the UV-ozone treatment, are carried out directly before the next process group, in the case of the standard OSCs the spin-coating with PEDOT:PSS. The parameters recorded during substrate cleaning are shown in table 3.2.

3.2.2 Solution Preparation

The second main preparation step is the preparation of the solutions to be used for spin-coating. Two different kinds of solutions are the basis for the organic layers of an OSC: the PEDOT:PSS solution[1] for the polymeric anode and a solution, consisting of a mixture of polymer and PCBM, for the photovoltaic active blend layer.

[1]Technically, PEDOT:PSS is a colloidal suspension, but the term solution will be used as in coating solution.

Table 3.2: *The parameters recorded during substrate cleaning for each of the i cleaning steps. The cleaning procedure usually starts with manually wiping the ITO-substrates using glass detergent, followed by a series of ultrasonic baths in solvents. The last bath is in DI-water, before the substrates are quickly blow dried and exposed to an UV-ozone treatment.*

Parameter	Symbol	Standard
Method		manual wiping, then wet cleaning
Detergent (wiping)		standard glass detergent
Solvents (wet cleaning)		2x acetone, 2x isopropanol, 1x DI water
Duration of i^{th} bath	$t_{bath}(i)$	600s
Temperature of i^{th} bath	$T_{bath}(i)$	Room Temperature (RT)
Use of sonification		yes
Duration of UV-Ozone treatment	t_{UV}	600s

PEDOT:PSS

PEDOT:PSS is bought from H.C. Starck and is available in several different formulations. PEDOT:PSS is used as organic anode on top of the ITO facilitating the hole extraction out of the device [26]. The formulations differ in their suspending solvent, in the size of the dispersed droplets and their degree of PEDOT's doping with PSS.
For the standard OSCs, PEDOT:PSS formulation AI 4083 is used as received and only filtered through a 0.45μm filter prior to spin-coating.

Absorber Solution

The ingredients, i.e. solution material and solvent, for the absorber solutions are bought separately and stored in dark in the glovebox, where the preparation takes place as well. The absorber solution is made by mixing an electron donating polymer and the electron acceptor PCBM in the desired amounts into an organic solvent. The choice of solvent and the concentrations of donor and acceptor have a large influence on the absorber properties and hence on the OSC properties [30, 58]. For this work, the standard polymer is P3HT 4002E (Rieke Metals), the standard electron acceptor material is PCBM (Solenne BV), dissolved and mixed together in o-dichlorobenzene. The three most common ways of preparing absorber solutions are shown in figure 3.3. To keep track of the way a solution is prepared and used, each vial containing a solution receives an unique ID and the solution preparation

process is recorded in a similar way to the process steps of the substrate. The standard procedure (1) begins with adding the amounts of PCBM, polymer and solvent, which are desired for the final solution, into a vial. Subsequently the absorber solution is filtered and continuously stirred on a magnetic stirrer. If necessary the solution is heated while stirring to facilitate dissolving of its ingredients. An absorber solution is characterised by the parameters given in table 3.3 and by its absorption spectrum, which is recorded for every solution.

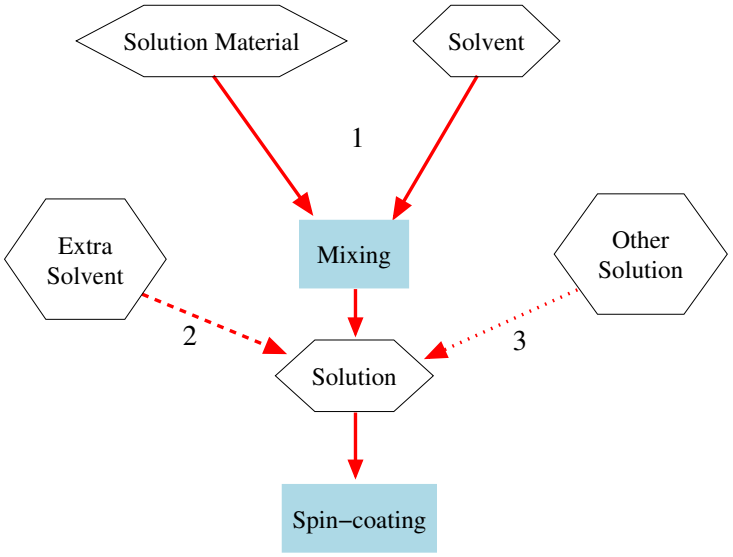

Figure 3.3: *Process overview of the absorber solution preparation. For the standard process (1), the solution materials and solvents are combined into one solution, which is continuously mixed until being used in the spin-coating process. Two alternatives are preparing one highly concentrated "master" solution at a fixed polymer:PCBM ratio (1) and diluting it with extra solvent (2) or making two separate "master" solutions (1) with one component only and mixing them in the desired ratios and extra solvent (2,3). Solvents and solutions can additionally be filtered at any stage.*

Whereas the absorber solution in the standard process is already prepared in the concentrations and ratios desired for spin-coating, the other two approaches offer more flexibility: a highly concentrated "master" solution with a fixed ratio of polymer:PCBM is made (1) and can be later diluted to the desired concentration by adding extra solvent (2), making the preparation of series of concentrations simple. The third approach is to mix separate highly concentrated solutions of polymer and PCBM (1). These "master" solutions, together with extra solvent (2), then can be easily combined (3) to give new

Table 3.3: *The parameters characterising an absorber solution. An absorber solution usually consists of two components: an electron donor and an electron acceptor. The standard materials are P3HT (4002E, Rieke Metals) and PCBM (Solenne BV) respectively.*

Parameter	Symbol	Standard
Mixing method		Magnetic Stirrer
Mixing temperature	T_{mix}	ambient
Electron donor		P3HT (4002E, Rieke Metals)
Electron acceptor		PCBM (Solenne BV)
Concentration of donor	c_D	10-30mg per ml
Concentration of acceptor	c_A	10-30mg per ml
Solvent		o-dichlorobenzene (DCB)
Solution filter		0.45μm PTFE Membrane

solutions at the desired concentration and ratios. The latter method is the most flexible, yet requires the most preparation steps. These three ways are not mutually exclusive, but simply offer different degrees of flexibility.
Filtering the solution after preparation is a necessary step to reduce the impurities contained in the solution, which would otherwise create inhomogeneities in the absorber film during spin-coating (see section 3.2.3). However, when a solution is filtered, a certain amount of the polymer and the PCBM are retained in the filter. Thus the concentration of the solution after filtering will have changed slightly, making the comparison between absorber solutions, which were filtered separately, difficult.

3.2.3 Spin-coating and Drying of the organic Layers

Spin-coating is a common method of application of thin films to substrates. The concept is shown in figure 3.4 (left). The substrate is held fixed on a vacuum chuck, the solution dispensed on the substrate and the substrate then spun at high speeds. During spinning a thin wet film forms on the substrate. The solvent evaporates both during and after spin-coating [59]. Although only one substrate can be coated at once, this method is simple and for laboratory purpose sufficient. However, the sequential processing introduces different time intervals the substrates have to wait before and after spin-coating due to the change from and to a batch process respectively. The main drawbacks of this method are the high loss of solution (>90%) and the limitations to substrate size. However, for investigating the physics of

the devices, it is more than sufficient. With the prospects of a roll-to-roll production, there are many other film coating techniques which are scalable and currently investigated for OSC, but not used in this work [60].

Directly after spin-coating, the thin spin-coated layer formed on the substrate still contains residual solvent, which needs to be removed prior to further processing. The layers are hence dried in vacuum and/or at elevated temperature. Furthermore, the way the substrates are dried can have an effect on the properties of the layer [38, 61]. The parameters recorded during spin-coating and drying are listed in tables 3.4 and 3.5.

Two identical spin-coaters (Model 4000 from Electronic Micro Systems) are available. One is installed in a cleanroom, the second spin-coater is installed in a glovebox with a dry N_2 atmosphere. The spin-coaters are programmable and each spin-coating stage is defined by its parameters for ramp, spin speed and spin duration.

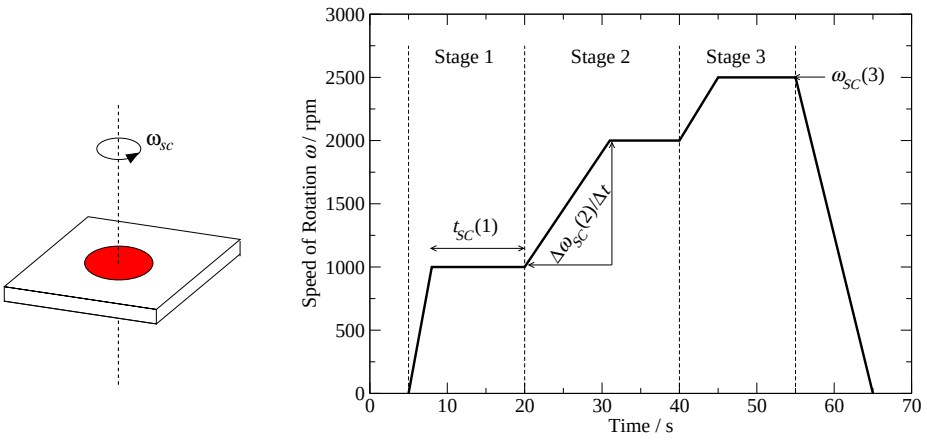

Figure 3.4: *The concept of spin-coating is shown on the left. A droplet of solution (shown in red) is spread on the substrate, which is subsequently spun at high speed. An exemplar speed profile of a spin-coating program with three stages is shown on the right. Each spin-coating stage is characterised by a set of three parameters, of which here only one per stage is indicated.*

PEDOT:PSS Spin-coating and Drying

After the UV-ozone treatment, i.e. the final step of substrate cleaning, PEDOT:PSS AI 4083 is spin-coated onto the substrate in cleanroom conditions. This PEDOT:PSS formulation requires filtering (0.45μm) and is spin-coated

Table 3.4: *The parameters characterising the spin-coating. The ambient temperature and the volume dispensed on the substrate during spin-coating are recorded as well as the spin-coating program number, which maps to the spin-coating speed profile.*

Parameter	Symbol	AI 4083	Absorber
Temperature	T_{SC}	ambient	ambient
Solution Volume	V_{sol}	$>100\mu$l	70μl
Atmosphere		cleanroom air	dry N_2
Ramp of stage i	$\frac{\Delta\omega_{SC}(i)}{\Delta t}$	10000rpm/s	100rpm/s
Speed of stage i	$\omega_{SC}(i)$	3000rpm	500-2000rpm
Dwell of stage i	$t_{SC}(i)$	60s	60-210s

Table 3.5: *The parameters recorded for drying of the spin-coated layers. There are two drying stages for the PEDOT:PSS layer: a 600s drying at 200°C and the subsequent transfer of the still hot substrates into the vacuum of a glovebox airlock. The absorber layer is dried inside the glovebox in a vacuum chamber.*

Parameter	Symbol	AI 4083	Absorber
Temperature	T_d	200°C (oven), 200°C→ambient (airlock)	ambient
Pressure	p_d	1bar (oven), ≈ 0.1bar (airlock)	≈ 0.1bar
Duration	t_d	600s (oven), ≈ 1h (airlock)	several h

at 3000rpm for 60s. The result is a PEDOT:PSS layer of about 50nm thickness as measured with an atomic force microscope.
After spin-coating the PEDOT:PSS AI 4083 film is dried at 200°C for 600s in an oven in the cleanroom, as recommended in the PEDOT formulation guide [62]. This heating removes any residual H_2O and improves the properties of the layer considerably, e.g. the conductivity increases by an order of magnitude due to increased crystallinity [36]. Subsequently, the still hot substrates are transferred into the vacuum lock of the glovebox, where they are allowed to cool down under vacuum.

Absorber Solution Spin-coating and Drying

The spin-coating process for the absorber solution is carried out inside the glovebox. The absorber solution is typically filtered during its preparation, so filtering it directly prior to spin-coating is usually not necessary.
After spin-coating, the ITO-substrates with PEDOT:PSS and absorber layer is dried in a vacuum chamber inside the glovebox.

3.2.4 Evaporation of the Cathode

The cathode is realised by evaporating aluminium through a shadow mask onto the substrates. The active area of the OSC is defined by the overlap of the shadow mask pattern and the structured ITO electrode.
The evaporation chamber (BOC-Edwards) is equipped with two tungsten boats for thermal evaporation and one device for electron beam evaporation, permitting the evaporation of a large variety of metals and dielectrica. Depending on the shadow mask, up to nine substrates can be loaded at once into the evaporation chamber. The chamber is then evacuated. The shadow mask is attached to a motor inside the evaporation chamber, enabling a continuous rotation of the mask during evaporation for a homogeneous layer. When a sufficient vacuum is reached ($< 5 \cdot 10^{-6}$mbar), the evaporation is started. The current through the tungsten boats or from the filament of the e-beam source is manually controlled during the evaporation process. This leads to variations between different batches and repeating exactly the same evaporation conditions is not possible. The layer thickness is monitored by an oscillating crystal. The standard cathode consists of about 100nm aluminium, which is thermally evaporated. The parameters are shown in table 3.6.
The thin lithiumfluoride (LiF) layer between absorber and Al-cathode, which is often seen in literature, is omitted, because it has been reported that the LiF-Al interface degrades at the temperatures (>140°C) the substrates are exposed to during post-treatment [14].

3.2.5 OSC Post-Treatment/Annealing

For OSCs made from P3HT:PCBM based absorber solutions, a post-treatment (PT, also called annealing) of the OSC after evaporation is a critical step for its performance. Especially for solutions with fast evaporating solvents, e.g. chlorobenzene, exposing the OSC to a thermal treatment and/or a prolonged voltage bias can, within certain limits, improve the OSC efficiency considerably. Two major effects are observed. First, small defects in the absorber layer, which cause shunts and worsen the diode characteristics, are literally burned out during PT. Second, the short circuit current density J_{sc} can substantially be increased due to a combination of increased absorption, a better mobility of the charge carriers and an improvement of the contacts. The open circuit voltage V_{oc} and the fill factor FF benefit as well, but usually

Table 3.6: *The parameters recorded during the evaporation. The process starts with the evacuation of the evaporation chamber. When reaching a certain vacuum, typically below* $5 \cdot 10^{-6}$mbar*, the layers are subsequently evaporated through a shadow mask onto the substrates.*

Parameter	Symbol	Standard
Shadow Mask		
Timestamp for layer i		YYYY-MM-DD HH:MM
Evaporation source for layer i	$evap_{src}(i)$	thermal
Material for layer i		Al
Base pressure for layer i	$p_{base}(i)$	$< 5 \cdot 10^{-6}$mbar
Rotation of mask for layer i		on
Evaporation pressure of layer i	$p_{evap}(i)$	
Current for layer i	$I_{evap}(i)$	
Thickness of layer i	$d_{evap}(i)$	Al $\approx$ 100nm
Time for evaporating layer i	$t_{evap}(i)$	
Evaporation Rate for first 5nm of layer i	$\frac{\Delta d_{5nm}}{\Delta t}(i)$	< 0.1nm s^{-1}
Total time of vacuum	t_{evac}	several h

to a lesser extent. The changes occurring in the OSC during the annealing are still under investigation with changes in the interface and changes in the absorber layer being at the focus of research. The exact parameters of the post-treatment have to be tailored for every material combination and exceeding the optimal parameters can quickly destroy the OSC. For slowly evaporating solvents, e.g. tetrahydronaphthalene, the improvements due to annealing are small, because the absorber layer dries much slower, leaving enough time for the formation of a better morphology.

To illustrate the effect of post-treatment, figure 3.5 shows the IV-curve of a P3HT:PCBM (c_D:c_A, 1:0.7) OSC made from an o-dichlorobenzene based absorber solution. In the non-annealed case, it does not even exhibit a good rectifying behaviour. Its performance can be improved drastically by heating it to 150°C for 300s. The power conversion efficiency η rises substantially due to an increase in J_{sc} (+38%), FF (+22%) and V_{oc} (+21%) upon post-treatment.

In this work, the post-treatment is performed on a temperature controlled hotplate (IKA GmbH & CO. KG) inside the glovebox and the corresponding parameters shown in table 3.7, where simultaneously a bias voltage can be applied as well. PT can be repeated with characterisation in between.

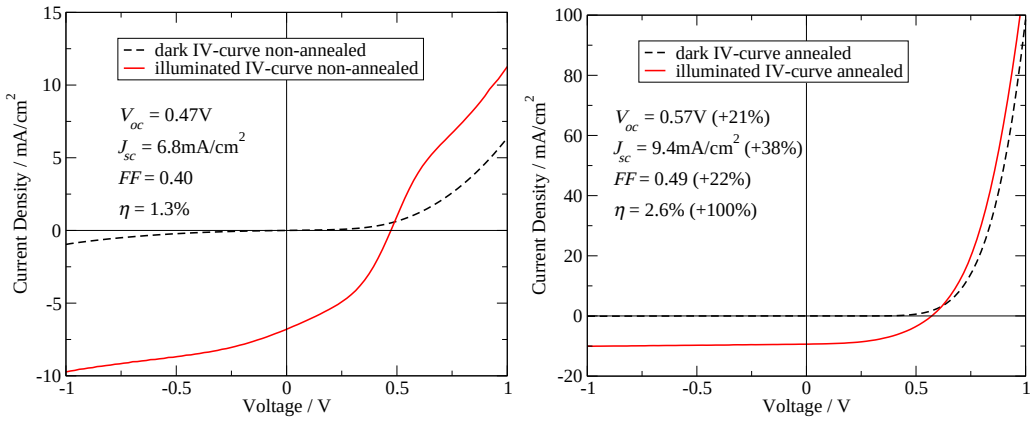

Figure 3.5: *The effect of the post-treatment on the IV-characteristics of a P3HT:PCBM OSC made from o-dichlorobenzene (S 408 p7). On the left the dark and illuminated IV-curves before the post-treatment are shown. A drastic increase in performance is reached after a post-treatment step of t_{pt}=300s at T_{pt}=150°C, as can be seen on the right (note the change in scale of the y-axis). The power conversion efficiency η doubled after the post-treatment and at the current rose nearly one order of magnitude at +1V forward bias.*

Table 3.7: *The parameters recorded during the post-treatment of the finished OSC. The parameters are not optimised yet, but already lead to a significant improvement of the P3HT:PCBM organic solar cell.*

Parameter	Symbol	Standard
Temperature of post-treatment step	T_{pt}	80-150°C
Time of post-treatment step	t_{pt}	300-900s
Voltage bias	V_{pt}	0V

3.2.6 Packaging

Packaging is generally not necessary for the OSCs made and characterised in this work, but it briefly is mentioned here, because it completes the production process. The main measurements are all carried out in an inert gas atmosphere. If a substrate is taken out of the glovebox and its OSCs should remain operational they need to be protected against the oxygen and water vapour in the air. For laboratory purposes, the simplest packaging is done by using epoxy to glue a second glass directly onto the cathode on the substrate.

3.3 Summary

- The OSC production process was structured and analysed for the parameters necessary to describe a standardised production process on a laboratory scale. Despite the simple production, more than 40 production parameters were found, which are now routinely recorded for every substrate.

- The production process consists of a sequence of process steps, of which most can be carried out for several substrates at once, e.g. the substrate cleaning, and a few only for one substrate at a time, e.g. the PEDOT:PSS spin-coating. One batch typically consists of eight substrates.

- Most of the production parameters can be controlled very well, e.g. the spin-coating speed for the PEDOT:PSS or the absorber layer. These parameters can be made identical for any desired number of substrates.

- The time intervals before and after spin-coating differ always for the substrates within one batch due the sequential nature of the process. However, they had not been considered at all before during the analysis of the measured data.

- A few parameters cannot be fully controlled with the present equipment. E.g. two evaporation processes cannot be made identical due to the manual control of the evaporation process.

Chapter 4

Measurement Methods and Automation

In this chapter the measurement methods and their automation are described. The measurement concepts and their basic setups are shown and sources of measurement errors are discussed in the first part of this chapter. The second part focuses on the automation of these methods, which is paramount for a reliable and fast characterisation of the organic solar cells (OSCs).

4.1 Measurement Methods

Three main measurement methods for OSCs are presented in this section. They are current-voltage measurements, spectral response measurements and absorption measurements, all of which are performed inside gloveboxes in a nitrogen atmosphere. These methods are supplemented by atomic force microscopy (AFM) and impedance measurements.

4.1.1 Current-Voltage Measurement

The current-voltage measurement, short IV-measurement, is the standard measurement for characterising solar cells. A linear voltage sweep, in our case usually between $\pm$1V, is applied to the OSC and the resulting current I in the circuit is measured. In order to allow comparison between different solar cells the current is usually scaled to J, the current density being an intensive property. The measurement is carried out both without and with illumination. In the dark, the IV-curve shows a diodic behaviour; under illumination, extra charge carriers are generated in the solar cell and the

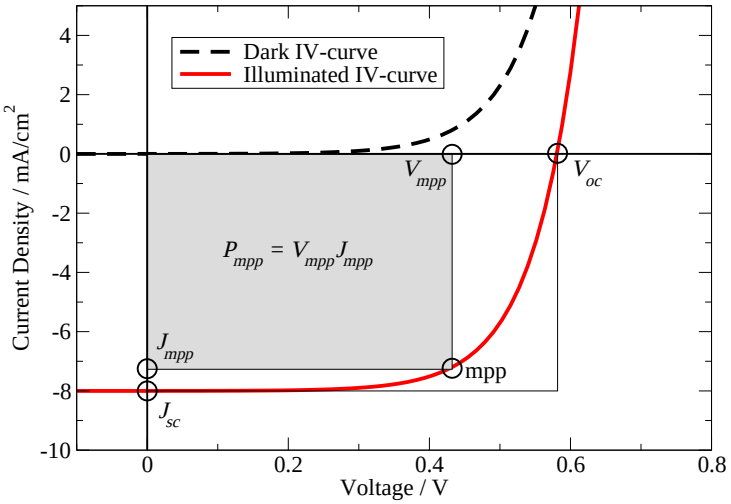

Figure 4.1: *Typical dark (black) and illuminated (red) IV-curves of a solar cell with a focus on the forth quadrant. The important parameters are indicated: the open circuit voltage V_{oc}, the short circuit current density J_{sc}, the voltage V_{mpp} and the current density J_{mpp} at the maximum power point (mpp). The fill factor FF is the ratio of the area of the filled square, i.e. the maximum extractable power $P_{mpp} = V_{mpp}J_{mpp}$, to that of the empty square ($V_{oc}J_{sc}$). From these parameters and the incoming illumination intensity P_{ill} the power conversion efficiency η is calculated as given in equation 4.2.*

dark IV-curve is shifted in the negative direction. Exemplar IV-curves for both cases are shown in figure 4.1.

Under illumination, the key figures of a solar cell can be determined directly from the IV-curve. The open circuit voltage V_{oc} and short circuit current density J_{sc}[1] are the intersections of the illuminated IV-curve with the V-axis and J-axis respectively. In the fourth quadrant the electric power $P_{el} = VJ$ is negative and this power can be extracted from the solar cell. The maximum power P_{mpp} generated by the solar cell is at the maximum power point (mpp), the point on the curve where the absolute value $|P_{el}|$ reaches its maximum in the fourth quadrant. The corresponding voltage and current density is denoted as V_{mpp} and J_{mpp} respectively. The ratio between the real maximum power P_{mpp} and product of $V_{oc}J_{sc}$ is called fill factor FF.

$$FF = \frac{V_{mpp}\ J_{mpp}}{V_{oc}\ J_{sc}} \tag{4.1}$$

Finally, the power conversion efficiency η is the ratio between P_{mpp} and the

[1]Strictly speaking, J_{sc} is negative, but following convention its absolute value will be quoted throughout this thesis.

intensity of the incident light P_{ill}.

$$\eta = \frac{P_{mpp}}{P_{ill}} = FF\frac{V_{oc}\ J_{sc}}{P_{ill}} \tag{4.2}$$

This fraction of the incident light intensity is converted into electrical power and is available to external loads.

The basic measurement setup is shown in figure 4.2. A Keithley 2400 Source-Meter, controlled by a LabView program, is used for generating the voltage sweep and measuring the resulting current through the OSC. The OSC is connected in a four wire configuration to avoid parasitic serial resistance of the cables and the interconnects on the substrate. When measured in dark, the OSCs are covered to ensure absolute darkness. For illuminated IV-curves, two different light sources are available. They are employed in two different setups, which will be briefly described below.

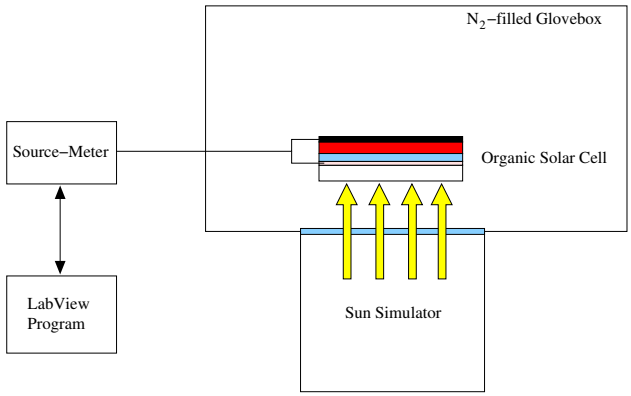

Figure 4.2: *The basic IV-measurement configuration is depicted. A LabView controlled Keithley 2400 Source-Meter is used to record the IV-curve of the OSC in a four wire configuration. There are two light sources available in different setups for measuring IV-curves. In the one shown, the illumination of the OSC is provided by a sun simulator. Its light is transmitted into the glovebox through a borosilicate window. The second setup, which is used for IV-measurements, is mainly used for the spectral response measurement (section 4.1.2) and thus shown in figure 4.5.*

Sun Simulator

The sun simulator (SolarCelltest 575 from K. H. Steuernagel Lichttechnik GmbH) generates a spectrum close to the standard AM1.5g solar spectrum with a homogeneous illumination on an area of about $10\times10\text{cm}^2$. The simulated sun light is coupled into the glovebox from below through a borosilicate glass window. Before recording the IV-curve on the sun simulator, the

illumination intensity is measured with a calibrated solar cell (LOTSDSC5, Fraunhofer ISE Callab) and corrected for the spectral mismatch (see section 4.1.2) such that the OSC generates the J_{sc} which it would have when exposed to an intensity of 1000W/m^2 with the spectrum of the sun. While on the sun simulator, all OSCs are cooled by a fan. The temperature for the OSCs has been measured with a thermocouple and stabilised below 35° C after five minutes. IV-measurements were then started after the substrate temperatures had equilibrated. Although this is not according to the standard reporting conditions (SRC[2]), it allows reliable and comparable testing.

Xenon Lamp

In the second setup the illumination is provided by a 1000W Xenon-lamp with a stabilised power supply (both by company Müller GmbH). This setup has a dual use. It can be used for IV-curves at different illumination intensities and the spectral response, which will be described in section 4.1.2, can be measured there. The light of the Xe-lamp is coupled into the glovebox through an optical quartz glass fibre cable (custom made by Schölly Fiberoptic GmbH), with a high transmission into the UV range. The light beam is homogenised before being focused onto one OSC at a time. The area of the light spot is approximately 1×1cm^2, which is still larger than the used photovoltaic active area. Variations in the illumination intensity are achieved by inserting neutral density filters into the light beam in front of the measured solar cell, allowing intensities between about 2 and 0.001 suns. Lower intensities are in principle possible, but then the setup requires a better shielding against stray light. The lamp intensity is measured in parallel with a monitor diode to compensate for any lamp drift. The intensity at the OSC is then calculated using the transmission of the filter and both the intensity and spectrum of the lamp. This setup is described in more detail in the section on spectral response measurements (see figure 4.5), because most components are only necessary there. For IV-measurements all components of the setup are set such that the white light of the Xe-lamp is transmitted directly and not being modulated.

[2]The standard reporting conditions state an illumination of 1000W/m^2 with the standard spectrum AM1.5g and the solar cell at 25°C.

Measurement Uncertainties

The main uncertainties in the IV-curve and its derived parameters arise from measuring the illumination intensity and from assessing the photovoltaic active area. The measurement accuracy of the Keithley source-meter is not limiting the accuracy of the IV-measurement.

The main problem in assessing the illumination intensity an OSC "sees" is due to the fact that the spectra of the used lamps differ from the standard reference spectrum AM1.5g for which efficiencies should be reported. Measuring and adjusting the intensity of the lamp is done with calibrated silicon solar cells. However, both the reference cell and the measured OSC have a different spectral response (see section 4.1.2). Without any further correction this difference leads to a wrong calculation of the light intensity seen by the OSC. If the spectral response of both the reference solar cell and the measured solar cell are known, this source of error can be corrected by introducing a mismatch or spectral correction factor [63]. Calculating the spectral response and the mismatch factor is described in section 4.1.2.

The homogeneity of the illuminated area is the second critical issue with regard to the illumination intensity. For the setup with the Xe-lamp, the homogeneity has been measured to be better than 4% across the photovoltaic active area of the used OSCs. Since the light spot of the Xe-lamp is always focussed the same way on an OSC, there are no differences in illumination between different OSCs. On the sun simulator, the variations in illumination intensity have been measured with a calibrated reference silicon solar cell (LOTSDSC5) and amount at 1 sun to less than 5% on the $\approx 10 \times 10\text{cm}^2$ area used for measurements. Here, the variations have a bigger influence on the measurements, because the intensity can vary from OSC to OSC, depending on where on the sun simulator it is being measured. This source of uncertainty will be corrected in future by mapping out the spatial inhomogeneities and considering them during the calculations of J and η.

The last major source of uncertainty is given by measuring the photovoltaic active area of the OSC. The active area is given by the overlap between anode and cathode as shown in figure 4.3. The active area is underestimated when cross-talk, e.g. ITO shorts between different OSCs, leads to an extra contribution in current or overestimated, if the pattern of top and bottom electrode does not match. The active area of the OSCs in this work is in the

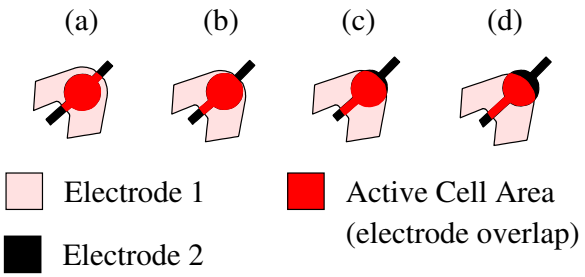

Figure 4.3: *Definition of the photovoltaic active area of an OSC. Generally, in plane conduction can be neglected and thus the active area of an OSC is defined as overlap between the two electrodes as shown in (a) (see also sections 3.2.4 and 4.2.1). Depending on the tolerances of the pattern, a certain misalignment is allowed without changing the active area as shown in (b). In the examples shown in (c) and (d) the misalignment is beyond the tolerances and the area loss amounts to* $\approx -9\%$ *and* $\approx -25\%$ *respectively.*

order of a few mm^2 and uncertainties in the area can cause errors in the area of 10% or more. Both cases, however, can be reduced by a careful inspection of substrates.

4.1.2 Spectral Response Measurement

For the spectral response (SR) measurement the solar cell is illuminated with monochromatic light and its short circuit current density response at each wavelength during a sweep of wavelengths λ is recorded. The spectral response is then defined as

$$SR(\lambda) = \frac{J_{sc}(\lambda)}{P_{ill}(\lambda)}, \tag{4.3}$$

where P_{ill} is the incident illumination power of the photons at a given wavelength λ. In reality the $J_{sc}(\lambda)$ is recorded for wavelength intervals $[\lambda, \lambda + \mathrm{d}\lambda]$, where in our case $\mathrm{d}\lambda = 5\mathrm{nm}$. Using the number of incoming photons N_{ph} to normalise $SR(\lambda)$ the external quantum efficiency EQE can be calculated as

$$EQE(J_{sc}, \lambda) = \frac{J_{sc}(\lambda)}{e \cdot N_{ph}(\lambda)}, \tag{4.4}$$

where e is the elementary charge. Thus the EQE is the ratio of electrons measured in external circuit to the number of photons incident on the solar cell. Sometimes the EQE is referred to as incident photon to converted electron efficiency (IPCE), but the term EQE will be used throughout this thesis. An exemplar EQE measurement of an OSC is shown in figure 4.4.

If the optical losses in a solar cell are known, the internal quantum efficiency (IQE) can be calculated as

$$IQE(J_{sc}, \lambda) = \frac{EQE(J_{sc}, \lambda)}{A_{act}(\lambda)} \tag{4.5}$$

where $A_{act}(\lambda)$ is the light absorption in the active layer. The IQE only considers photons, which are absorbed in the active layer. It is therefore the ratio of electrons in the external circuit to the number of photons absorbed in the active layer. IQE and EQE give insight into both the charge carrier generation and transport processes in a solar cell.
Using equation 4.3 and the standardised AM1.5g solar spectrum it is possible to calculate the J_{sc}^{SR} with respect to the standard AM1.5g spectrum as

$$J_{sc}^{SR} = \int_{\lambda=0}^{\lambda=\infty} SR(\lambda) \cdot E_{AM1.5g}(\lambda) d\lambda, \tag{4.6}$$

where $E_{AM1.5g}$ denotes the AM1.5g spectrum given in $\frac{W}{m^2 nm}$. The J_{sc}^{SR} obtained by equation 4.6 has to match the results for J_{sc} from an IV-measurement at 1000W/m^2 and AM1.5g spectrum (see section 4.1.1).

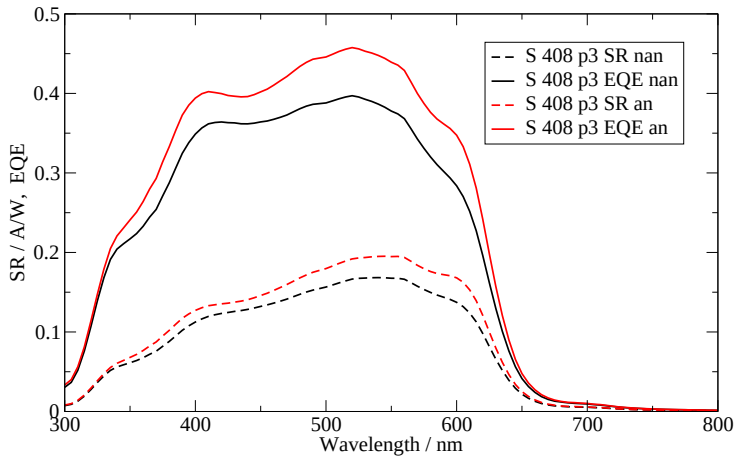

Figure 4.4: *A characteristic SR and EQE curve of a P3HT:PCBM OSC for both the non-annealed (nan) and annealed (an, $T_{pt} = 150°C$, $t_{pt} = 300s$) case. During annealing the short circuit current of the OSC improved and both curves are shifted up. Additionally, some features, e.g. the shoulder at 600nm is getting more pronounced, indicating a reordering of the P3HT chains during annealing [64].*

The SR measurement setup, of which parts are also used for the intensity dependent IV-measurements, is shown in figure 4.5. Before the light

of the 1000W Xenon-lamp enters a grating monochromator (ARC Spectral-pro 150), it is passed through a filter wheel to cut off higher diffraction orders in the monochromator. In the monochromator the light is spectrally decomposed (FWHM≈ 5nm) and then fed into the UV-transmitting optical fibre cable. The spectral range extends from 300nm in the UV to about 1200nm in the infrared. 10% of the fibres are diverted to a monitor diode measuring any drift of the illumination intensity while measuring the SR of a solar cell. The remaining bundle of fibres enters the glovebox. These fibres end at an optical bench where the emanating light beam is modulated by a light chopper wheel rotating at about 310Hz and then passes through the optical system as shown in figure 4.5. The components generate a light spot ($1\times1\text{cm}^2$), which is larger than the photovoltaic active area of the used OSCs. The illumination is homogeneous within 4% on the photovoltaic active area. The short circuit current response of the solar cell to the chopped monochromatic light is then measured with a lock-in amplifier (model 5210, Signal Recovery) using the chopper output as reference signal to discriminate the SR signal from the steady state background illumination. The illumination intensity of the lamp at each wavelength $P_{ill}(\lambda)$ (1-7mW/cm^2 per 5nm) is recorded as reference measurement with a calibrated silicon solar cell (Hamamatsu, Fraunhofer ISE Callab) of known SR prior to measuring OSCs. Combining the reference measurement with the current of the monitor diode, the SR, EQE and J_{sc}^{SR} of the measured OSC is calculated. The setup is controlled by a LabView program and is described in more detail in [65].

Spectral Mismatch Factor

The spectral response of the J_{sc} is very important for the accurate determination of the photovoltaic power conversion efficiency η. The spectrum E_s of even the best sun simulator does not equal the reference AM1.5g spectrum $E_{AM1.5g}$, which is the standard solar spectrum used for comparisons between different solar cells. This spectral mismatch and the difference in the spectral responses between the calibrated reference solar cell SR_{ref} and the solar cell to be tested SR_{test} need to be taken into account when measuring the illumination intensity. This is especially true for OSCs, which have a spectral response differing significantly from the inorganic solar cells used for calibration of the equipment [66]; there are currently no available reference OSCs. A spectral mismatch factor M, by which these differences are taken

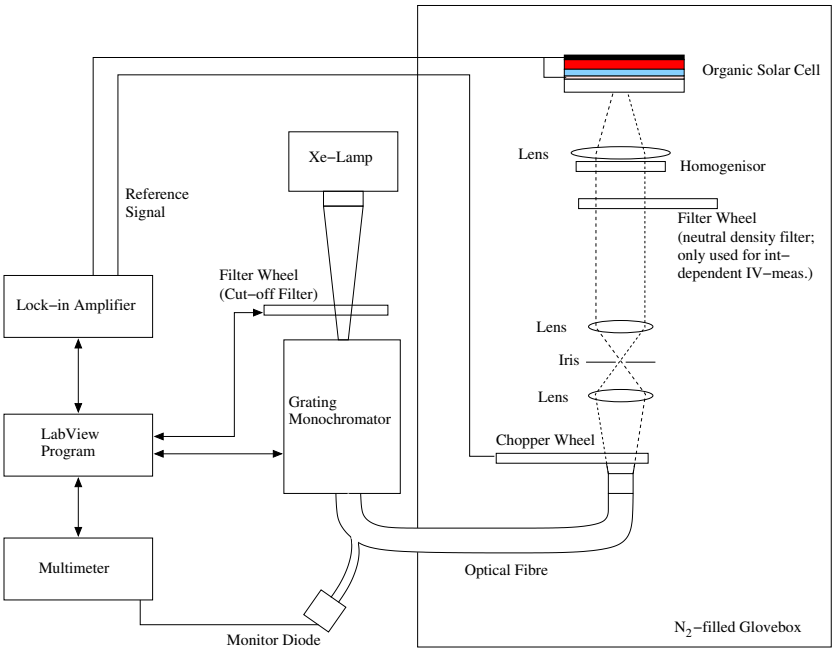

Figure 4.5: *The basic measurement setup for measuring the SR. The light of a Xe-lamp is spectrally decomposed in a grating monochromator and fed into the glovebox through an optical fibre. The light is modulated by a chopper wheel and passed through a set of optical elements to achieve a homogeneous illumination on the whole solar cell area. A monitor diode measures in parallel the intensity of the Xe-lamp. The $J_{sc}(\lambda)$ is measured via a voltage drop ΔV across a resistor by a lock-in amplifier receiving the chopper signal as reference. The whole setup is controlled by a LabView program.*

into account, is defined as

$$M = \frac{\int_0^\infty E_{AM1.5g}(\lambda) SR_{ref}(\lambda) d\lambda \int_0^\infty E_s(\lambda) SR_{test}(\lambda) d\lambda}{\int_0^\infty E_s(\lambda) SR_{ref}(\lambda) d\lambda \int_0^\infty E_{AM1.5g}(\lambda) SR_{test}(\lambda) d\lambda}, \tag{4.7}$$

where E_s (in $\frac{W}{m^2 nm}$) has to be known and the SR of reference cell and test cell can be measured as described above. M is then used to adjust the intensity of the solar simulator such that the short circuit current I_{sc} of the reference cell is I_0/M, where I_0 is its calibration value at SRC. The used reference cell is a calibrated silicon solar cell (LOTSDSC5), which is equipped with a colour filter to modify its spectral response such that is closer to SR of organic solar cells. M is in this case 1.09 on the sun simulator and always included when stating IV-data.

4.1.3 Absorption Measurement

In the absorption measurement the reflection of the light by the OSC is monitored. For the used OSCs it can be carried out in normal reflection geometry. The highly reflective back electrode acts as mirror to the white incident light shone normal onto the OSC. The reflected signal R_{sample} is then spectrally decomposed in a spectrometer. In order to calculate the reflectivity R, this spectrum is compared to two reference spectra, which have been recorded before. The dark reference spectrum R_{dark} is taken without any sample (thus no reflected signal) to compensate for the background signal of the fibres due to internal reflections in the setup. The white reference spectrum R_{white} is measured with a glass substrate having only a reflecting electrode. The absorption A then can be calculated via the reflectivity R as

$$A = 1 - R = \frac{R_{sample} - R_{dark}}{R_{white} - R_{dark}}. \tag{4.8}$$

Optical interference effects play an important role for all optical OSC investigations, because the thickness of the active layer in an OSC is of the same order of magnitude as the wavelength of the sun or probing light. Small changes in the layer thickness can have a significant effect on the absorption due to interference phenomena. Thus all optical treatment has to be carried out coherently. In addition to assessing the absorption of an OSC, this measurement is used in conjunction with optical simulations of the layer system to deduce e.g. estimates for the thickness of the absorber layer.

An Avantes AvaSpec-2048 spectrometer is used in our setup, which is shown schematically in figure 4.6. It has a CCD with 2048 pixels, leading to a measurable range of wavelengths from about 280nm to 1000nm (resolution $\approx$ 0.6nm). The light source consists of two lamps: a deuterium lamp (range 200-400nm) and a halogen lamp (range 400-2000nm). The two lamps and the spectrometer are each connected to an optical fibre cable, which is again led into the glovebox. Inside the glovebox, the two cables unite in a Y-connection into one cable, ending in an adjustable lens in front of the measurement sample. The light, which is coming from the lamps, is reflected at the aluminium interface of the sample and collected by the fibre going to the spectrometer. The spectrometer is controlled by a LabView Program.

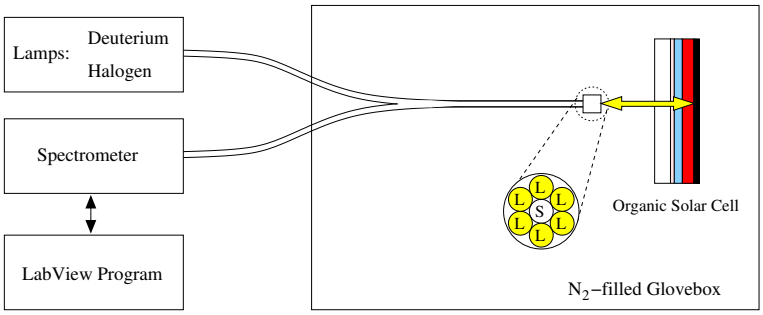

Figure 4.6: *The basic measurement setup for measuring the absorption. The light is carried through an optical fibre into a glovebox and shone perpendicular onto the OSC, where it is reflected at the highly reflecting Al-cathode of the OSC. The reflected signal is coupled into a second optical fibre leading directly to the spectrometer. The close up of the end of the optical fibre cable shows the six single fibres (L) coming from the lamps and the one fibre (S) going to the spectrometer.*

Measurement Uncertainties

In the particular setup being used for the absorption measurements (see section 4.2.3 and figure 4.12), the end of the optical fibre pointing to the substrate is approximately 5cm from the OSC. Thus small deviations from the normal incident angle, e.g. caused by a slightly tilted substrate, change the reflected signal and introduce uncertainties in the calculated absorption. Through a careful checking of the effect of a substrate's position in front of the fibre, it was possible to identify a systematic behaviour, which is taken into account when calculating the absorption. Repeated cross-checking confirmed the validity of this approach. The resulting error was calculated to be 5% for the absolute value of A.

4.1.4 Auxiliary Measurements

The above described measurements constitute the main part of the characterisation used in this work. They are supplemented by further measurements, which will be briefly described here with references for further reading. The surface morphology and the film thickness are measured with an Atomic Force Microscopy (AFM, Digital Instruments Nanoscope) [67]. The optical constants for the used materials are obtained by ellipsometry (J.A. Woollam MA-2000U) [65, 68]. They are necessary for the optical simulation of the absorption of the OSC. With the help of impedance measurements, charge

carrier transport phenomena can be investigated and electronic bottlenecks in the OSC can be analysed (Zahner IM6) [32].

4.2 Measurement Automation

To realise a consistent data acquisition for a large set of experimental data, all common measurement methods have been combined in one multi-purpose automated measurement setup. This combination allows a reliable OSC characterisation by the experiments described in the previous sections with the necessary high throughput. This is paramount for the efficient handling of the many parameter variations during the OSC production at the characterisation stage. Furthermore it enables an efficient material screening and the analysis of the influence of the the production parameter on the OSC. The measurement setup consists of four main components which will be described in the following sections:

- Versatile Substrate Framework
- Multiple Substrate Mount and Multiplexer Unit
- XY-Table with integrated optical Bench
- LabView Program

The technical drawings of the multiple mount and the construction and first assembly of the XY-table were part of a technicians work supervised during this thesis [69].

4.2.1 Versatile Substrate Framework

With the intention to improve OSC characterisation, the previous substrates (see figure 4.7) had two main shortcomings: they only had four OSCs of $\approx 0.7\text{mm}^2$ on a $15\times15\text{mm}^2$ substrate, too few for basic statistics per substrate, and the contacting method allowed only this layout on the substrate. Further points with room for improvement were that they were connectable only by a two-wire configuration and had large variations in the photovoltaic active area of each OSC. These variations originated in the ITO structuring process and made the manual determination of the active area of each OSC necessary. Thus new OSC substrates were developed by the group to overcome these

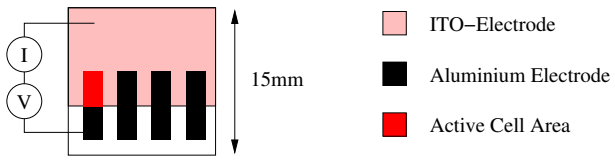

Figure 4.7: *The schematic structure of the previously used substrate. Four OSCs of approximately 7.5mm^2, given by the overlap of ITO and aluminium electrode, were realised on a 15×15mm^2 substrate.*

drawbacks and to facilitate the characterisation process. The common feature of all new substrates is that they have the same contact pad pattern at the periphery of their 25×25mm^2 substrate area (see figure 4.8). This pattern of 22 small contact pads constitutes the versatile substrate framework, which acts as standard template for various substrate layouts, i.e. the way the available area is used. With the contact pads always at the same position and still a large free area available, this framework fulfils both requirements of creating a standard for the substrates and providing large flexibility for substrate layouts at the same time.

The available area of this framework is now large enough allowing many different substrate layouts, though still small enough for good substrate handling and efficient material usage. Any substrate layout which builds on this framework can be used in the same experimental setup where all pads are contacted at the same time. Hence only the external circuitry has to be changed accordingly.

The two substrate layouts, which are most commonly used for OSCs in our laboratory, are shown in figure 4.8. Every OSC on a substrate has a distinct number and can be addressed individually in a four-wire measurement. The used nomenclature to address a particular OSC is "S 419 p9" for substrate S 419, OSC 9. The "p" is for pixel, as an OSC is often referred to as well. The photovoltaic active area is given by the overlap between bottom and top electrode.

The so-called 25×25_10 layout is used throughout this work for the OSCs, which have been described in section 3.1. It has ten OSCs per substrate with a photovoltaic active area of 5.3mm^2 each. An example of such a substrate is shown in picture 4.9 (left). The so-called 25×25_6 layout has only six OSCs per substrate, but allows for more flexibility in electrode materials. The active area of the OSCs is 8.1mm^2. The tiny feet of the photovoltaic active area

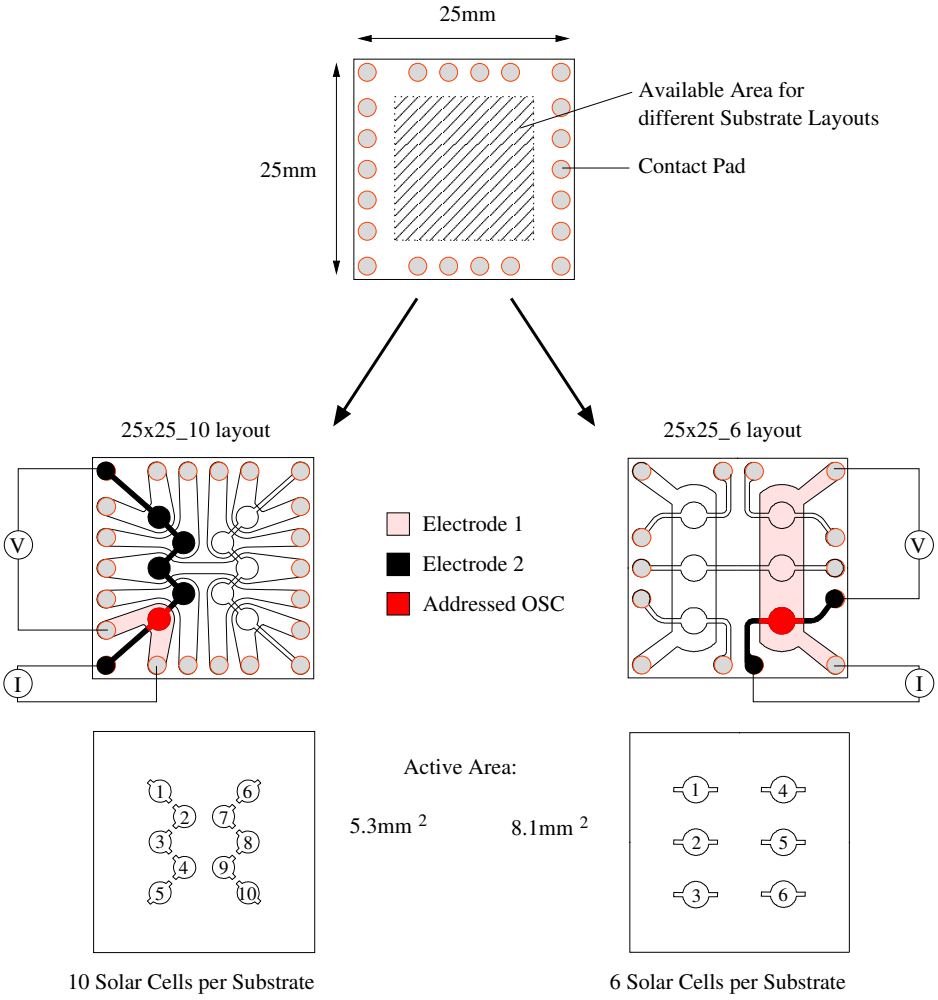

Figure 4.8: *The substrate framework of the 22 contact pads at the periphery of a 25×25mm² substrate is shown at the top. The standard 25×25_10 layout with 10 OSCs (left) and 25×25_6 layout with six OSCs (right) are both based on this framework. Each OSC can be individually addressed and measured in four-wire configuration. The used nomenclature for referring to a particular OSC is "S 419 p9" for substrate S 419, OSC 9 alias pixel 9. The second layout only uses 18 of the 22 available contact pads, but allows for more flexibility in electrode materials. The overlap between the two electrodes is shown and defines the active area of a OSC.*

amount to about 9% and 12% for the 25×25_10 and the 25×25_6 layout respectively. These feet provide certain built-in tolerances for the misalignment of bottom and top electrode (see figure 4.3). In-plane conduction can be neglected for the currently used materials.

Other layouts based on this substrate framework have been developed, e.g. for organic field effect transistors (OFETs), and just require a different wiring

to the measurement equipment for characterisation [70].

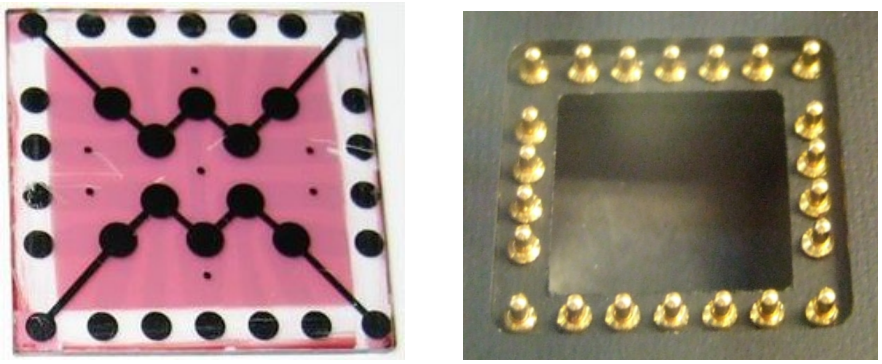

Figure 4.9: *A picture of the 10 OSCs on a substrate with 25×25_10 layout (left) and the corresponding test probe structure of one mount field (right). The Al-interconnects and the contact pads are clearly visible on the substrate, as is the absorber layer (red). The transparent ITO-structure shows only as very faint pattern. All contact pads of the substrate are contacted simultaneously by contact probes, from where each contact is wired to the external multiplexer unit for switching them to the measuring equipment.*

4.2.2 Multiple Substrate Mount and Multiplexer Unit

The second issue to address in order to improve the OSC characterisation were the actual measurements themselves. Already with the old substrates, the main bottleneck in the experimental cycle was the characterisation of the OSCs. The equipment allowed only working with one substrate at a time and every OSC had to be contacted manually and be switched, one after the other, to the measuring equipment. This meant frequent manual interaction, e.g. every minute for the IV-measurement. With the new, but necessary change in substrates this bottleneck would have been aggravated due to the increased number of OSCs per substrate.
To address this problem, a multiple mount was designed and made, which can hold and at the same time contact all contact pads of the above described substrate framework on up to nine substrates. Its dimensions were chosen such that all substrates in the mount lie within the approximately $10\times10\text{cm}^2$, the area in which the illumination from the sun simulator remains nearly homogeneous. Further properties of the multiple mount are as follows:

- The multiple mount is as thin as possible to allow large incident angles of light.

- Illumination of the substrates in the mount is possible from either side with nearly the same aperture.
- The photovoltaic active layer of the mounted substrates is in the symmetry plane of the mount.
- The mount is compact, robust and simple to handle despite working in the glovebox.
- The mount can either be used stand alone or be mounted on an XY-table.

The mount's frame is made out of black anodised aluminium. The receptacle, which holds the substrates, is milled out of glass-fibre re-enforced plastic (GRP), because each of the 198 test probes (Fa. Ingun, see figure 4.9) has a spring force of 1N and bending of the receptacle needed to be as low as possible (e.g. for absorption measurements). Each of the probes on the receptacle is individually connected to the mount's connector (ITT Cannon). For loading/unloading of substrates, the mount can easily be disassembled into two parts (see figure 4.10).
From the connector each contact is lead as single micro coax cables (Filotex) through a vacuum-proof seal to a multiplexer unit (Keithley 2750 DMM) outside the glovebox. The cables are twice protected by UV-proof spiral wraps. Failsafe measures, like spare cables, were already included while assembling and integrating the cables into the glovebox. By switching the corresponding relays in the multiplexer unit, each OSC on a substrate is individually addressable. The wiring was checked with both a test substrate equipped with different resistors and a 25×25_10 substrate, on which OLEDs were built.
Illumination is possible from either side of the mount, thus it can be used for alternative OSC concepts as well [71]. The photovoltaic active layer lies in the symmetry plane of the mount, hence the distance to the light source remains the same for both cases of illumination.
The multiplexer unit itself is only used for switching the 198 connections coming from the multiple mount to eight coax cables, which then are connected to other electronic equipment required for the particular experiment. Depending on the specific wiring of these outputs, IV, SR and OFET measurements can be carried out, but are not limited to those however. Both

switching of the relays and controlling the measurement equipment is done by the central LabView program.
Finally, the mount is designed such that it can be used standalone for measuring OSCs on the sun simulator, where all mounted substrates can be illuminated at the same time, or be mounted on its corresponding XY-table, where OSCs selectively can be illuminated by moving them into the light beam.

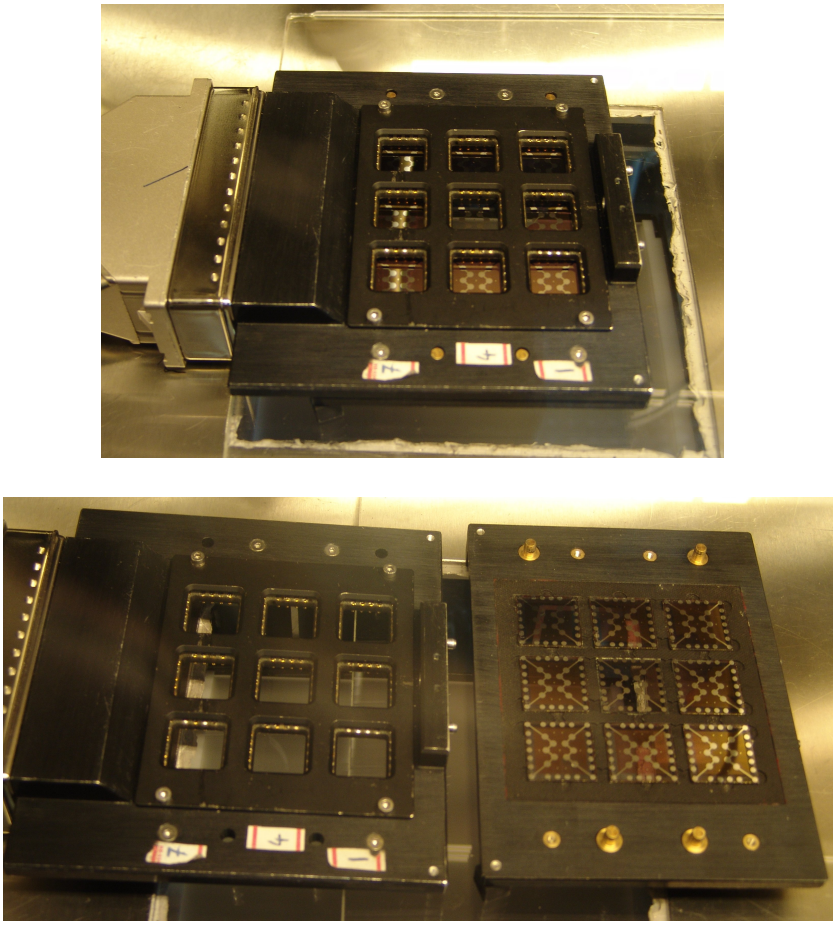

Figure 4.10: *The fully loaded mount with nine substrates ready to be measured is shown on the top. The image at the bottom shows the opened mount which allows an easy loading/unloading of the substrates onto/from the receptacle on the right.*

4.2.3 XY-Table with integrated optical Bench

The versatility of the automated measurement setup is further enhanced by the option of attaching the multiple mount onto the sled of a computer controlled XY-table. The XY-table had been built such that it easily fitted the

existing optical bench, which had already been used for SR measurements. The sled can move the multiple mount such that each point on the mount can be positioned accurately in the spot of the light beams coming from the optical bench and guide pins on the sled ensure that the multiple mount is always normal to the incident light. The components on the optical bench are currently configured such that SR, IV-curves (incl. light intensity dependent) and absorption measurements can be carried out on every OSC in the mount. The sled of the XY-table has a traverse path of about $150\times150\text{mm}^2$ and covers enough area such that the setup can be extended by further experiments. The whole construction was kept as compact as possible for the use inside a glovebox. A picture of the XY-table, optical bench and multiple mount is shown in figure 4.11. A close-up of the sled is shown in figure 4.12. The frame of the XY-table is made out of standard aluminium profiles and the sled moves with four double bearing units on rails (all ITEM) for each x-axis and y-axis. Two stepper motors (Mineba) are connected via Oldham couplings to miniature ballscrew assemblies (Bosch Rexroth) and drive the sled. The motors are controlled by the central LabView program addressing a stepper driver module (310 Trinamic). The double bearing units on the two rails of the Y-axis are synced by a cam belt. The mount can be fixed on the sled in either the standard or the inverted way such that proper illumination is provided as desired. Additionally, having not one central y-axis, but two rails at the frame, leaves the central part of the XY-table accessible from both sides for further extensions. Great care was devoted to the positioning accuracy and the repeatability of the sled's moves to less than 100μm. The table has two high precision reference switches (Euchner), used to determining the table's reference position before every measurement. The exact position of the mount in front of the light beam was determined using a reference diode covered with a mask of small aperture.

4.2.4 LabView Program

The multiple mount, the multiplexer unit, the XY-table and all other measurement components are controlled and tied together by an advanced LabView program. The concept was developed during the course of this thesis and the programming was carried out by Martin Meier.

The LabView program has a very modular design such that it can easily

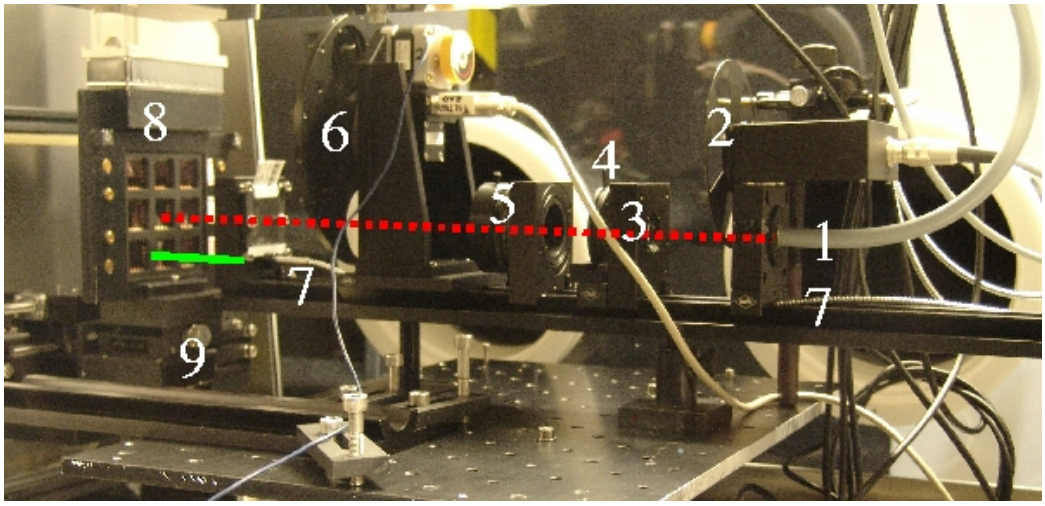

Figure 4.11: *A side view of the setup with XY-Table, multiple mount and integrated optical table. The components are as follows: quartz glass fibre coming from the monochromator (1), chopper wheel (2), condenser lens (3), iris (4), collimating lens (5), filter wheel equipped with neutral density filters (6), optical fibre for absorption measurements (7), the multiple mount (8) and the sled of the XY-table (9). The optical axes for SR/intensity dependent IV-measurements and absorption measurements are shown in red (dashed) and green respectively.*

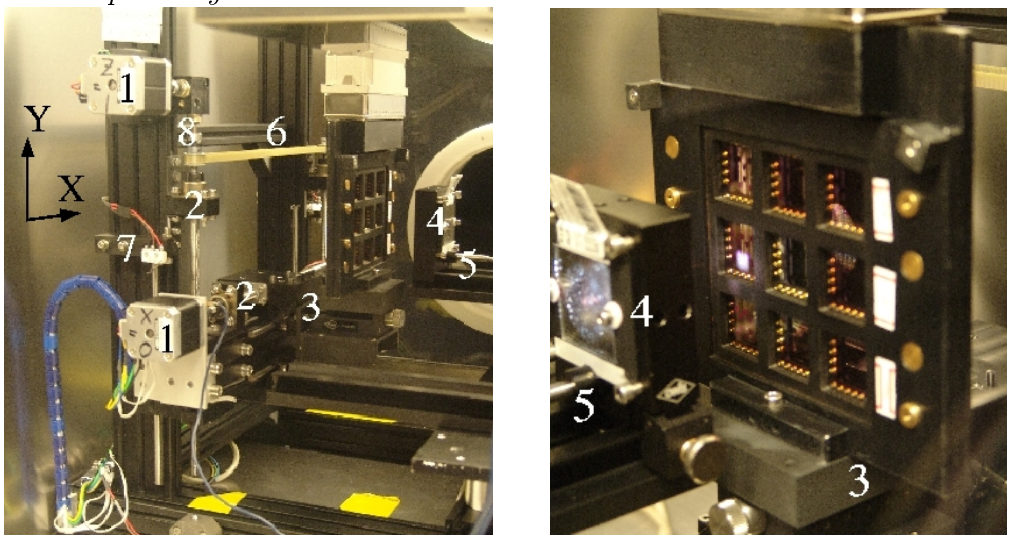

Figure 4.12: *A close up picture of the XY-table. The sled can accurately position the attached multiple mount with respect to the optical bench (left). The white light spot from the Xe-lamp is shown on an OSC being measured (right). The parts in detail are: stepper motors (1), ball bearing units (2), movable sled (3), homogeniser (4), glass fibre for absorption measurements (5), cam belt for synchronising the vertical ball screw assemblies (6), emergency stop switch (7), oldham coupling (8).*

be extended by new measurement methods, substrate layouts, mounts and other elements. The two main components are a graphical user interface (GUI) for the creation of a measurement program file and the actual program execution, which then sequentially carries out the measurements according to that file. The program execution uses the different program modules, e.g. switching the relays of the multiplexer, and carries out the requested type of measurement. A directed graph of the procedure is shown in figure 4.13.

The creation of a measurement program file is carried out through the GUI. Information on the configuration of the mount (standard/inverse), the substrate loading and their type is all entered there. It also offers the selection of the measurement module, which contains the specific routines for the particular measurement method and if necessary the choice for specific measurement option, e.g. the number of measurement points or the range of the voltage sweep of the IV-curve. Each OSC can be individually selected for particular measurements.

This program file is subsequently loaded by the program part responsible for sequentially executing the measurements listed in the file. Keeping the measurement program creation and its execution separate allows the simple and quick re-loadings of the same mount loading file, which is often done. Depending on the characterisation method, modules for the switching of relays, moving the sled or turning the filter wheel with the neutral density filters are used. During a measurement the results are shown graphical. The measurement results are stored and sorted by their measurement method and by date, assigning a unique, but structured name for each saved file. All saved files contain both information about the measurement and the raw measurement data. More detail about the structure of the output file is given in chapter 5.2.3.

4.2.5 Performance of the automated Setup

The automation of the measurement setup is an essential assistance in carrying out OSC characterisation. The time for each single measurement, i.e. one IV-curve on one OSC, did not improve much, but there are far fewer human interactions necessary. Before the automation was installed, manual interactions were frequently required. The contacts had to be switched by hand from one OSC on a substrate to the next and after the measurements

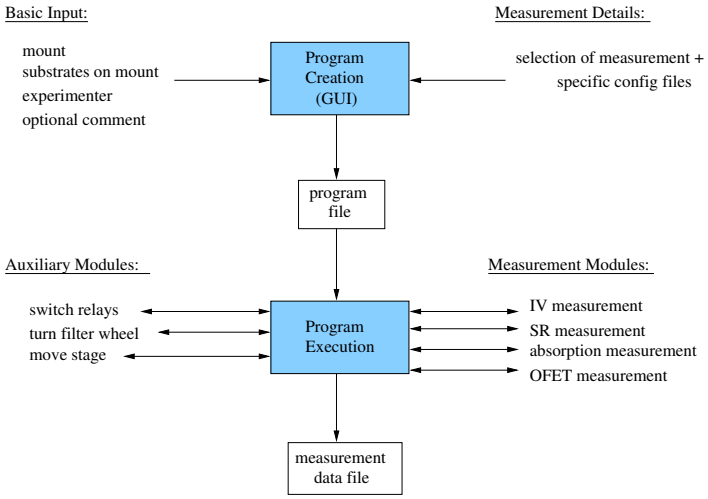

Figure 4.13: *The simplified structure of the LabView program, which controls and ties together all measurement equipment of the automated setup. A graphical user interface (GUI) handles the creation of a program file which is subsequently executed step by step. Depending on the particular measurement various modules can be addressed during program execution.*

on one substrate were completed, a new substrate had to be loaded into the test setup.

With the help of the multiple mount, the XY-table and the LabView program, the procedure of OSC characterisation has improved significantly. Table 4.1 compares the number of manual interactions and the break between them before and after the automation of the measurements for the standard measurement procedures.

Table 4.1: *A comparison of the number and the frequency of manual interactions before and after the automation of the measurement setup for the standard measurement procedure of nine substrates with 10 OSCs each. All 90 cells are usually measured with dark, illuminated and intensity dependent IV-measurements. SR-measurements are usually carried out only on two OSCs per substrate, which are selected to represent the average OSC per substrate. Preparation and starting the automated setup takes about 5-10min.*

	No. of Interactions	Break between Interactions
IV (dark or at 1 sun) before	90	1min
IV (dark or at 1 sun) after	1	approx. 90min
SR before	18	approx. 35min
SR after	1	approx. 10h
IV (intensity dependent) before	no. of filters×90	1min
IV (intensity dependent) after	1	no. of filters× ≈90min

For SR-measurements, every 35min the contacts had to be switched manually to the next OSC and the measurement program had to be restarted, but for the IV-measurement, the manual interactions were every minute prior to the automation.
It now takes about 5 to 10 minutes to load the multiple mount and create a new measurement program. Once that is done, no further manual interaction is necessary until the measurement program has finished. For a fully loaded multiple mount with 10 OSCs per substrate, i.e. 90 OSCs, the IV-measurement takes about 90min per illumination intensity, whereas the SR-measurement of two OSCs per substrate takes about 10h. Measuring the SR for every OSC on all nine substrate is possible as well (≈52h), but the extra information gained does not justify the time required during the standard characterisation cycle. The OSCs for SR measurements are generally selected such that the represent average OSC on that substrate. For intensity dependent measurements, each OSC is measured several times with a different neutral density filter, and the length of time for a complete measurement depends on the numbers of filters used. Typically five different filters are used and for the lowest intensities, the measurement is carried out twice with different ranges of the voltage sweep to get a better resolution. Hence the measurement runs for about 10h. Both SR and intensity dependent IV-measurements are well suited for running over night.
Figure 4.14 shows the development in the number of IV and SR measurements along a time line starting with the first version of the LabView program. The different components came into use one after the other and the setup has grown continuously more elaborated. The capabilities of the setup were extended by the absorption measurement in January 2006, which could directly be integrated into the automated setup. This proves the simplicity of extending the capabilities of the measurement setup. Measuring the absorption of a fully loaded multiple mount with 10 OSCs per substrate takes about 15min.
The series of exemplar measurements in figure 4.15 shows the range of measurements which can currently be conducted with the automated setup. With the help of this setup, the characterisation of the OSCs is no bottleneck anymore.

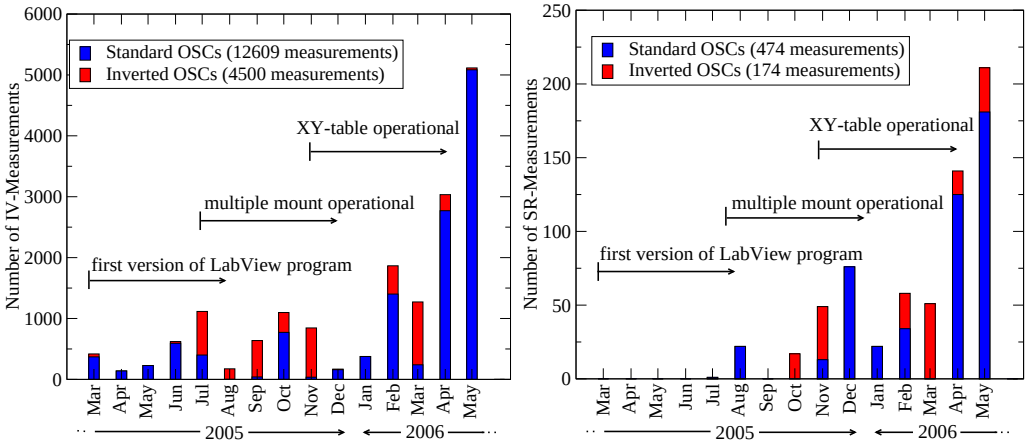

Figure 4.14: *The development of the number of IV (left) and SR (right) measurements since the first versions of the LabView program was running. The multiple mount was finished in July 2005 and has been used extensively for IV and SR measurements since then. The full integration of the mount and the XY-table took place in November 2005. IV-curves were measured on 259 and 193 unique substrates of the standard OSCs (10 OSCs per substrate), which are used in this thesis, and the "inverted" OSCs (6 OSCs per substrate), which is an alternative OSC concept being researched in our laboratory, respectively [71]. For the SR measurement the numbers are 116 and 72 respectively.*

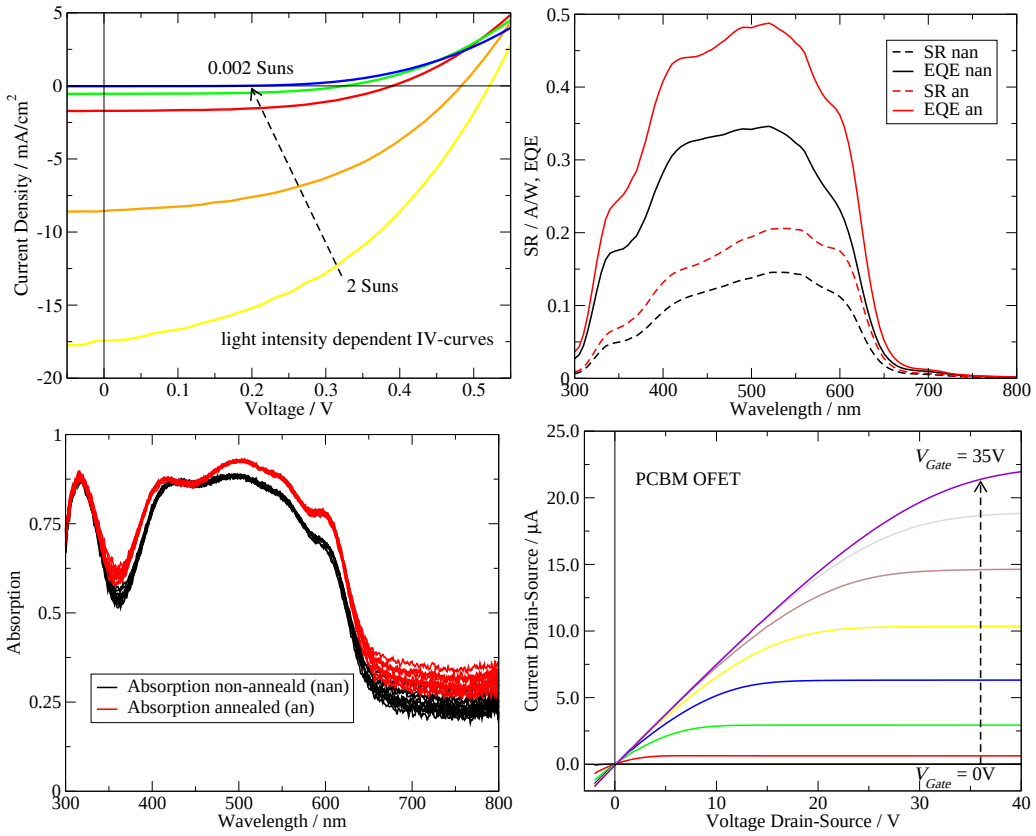

Figure 4.15: *A brief overview of measurements, which can currently be obtained with the automated setup. The top left figure shows IV-curves taken at different illumination intensities. The SR-measurement in the top right graph is shown for an OSC in the non-annealed (nan) and the annealed (an, $T_{pt} = 150°C$, $t_{pt} = 300s$) state to highlight the improvements during annealing. The graph on the bottom left shows the absorption measurement for all OSCs on the same substrate, again for the non-annealed and the annealed state. Finally, the graph on the bottom right shows the results of an OFET measurement on a PCBM only device in order to determine the electron mobility μ_e [70].*

4.3 Summary

- The standard OSC characterisation methods used are the current-voltage characteristics (dark/illuminated/intensity dependent), spectral response measurements and absorption measurements.
- To achieve a reliable and efficient characterisation process, the standard measurements were all integrated into an automated measurement setup, which consists of a versatile substrate framework, a multiple mount, an XY-table and a LabView program.
- Due to a versatile and flexible substrate framework, different substrate layouts, e.g. substrates with different number and types of OSCs or even with OFETs, have all the same standardised contact structure for test probes and can be measured in the same experimental setup.
- The multiple mount can hold and contact up to 90 OSCs on nine substrates simultaneously. Via a multiplexer unit, each OSC can individually be electrically addressed and measured. The multiple mount can be used directly on the sun simulator or on the XY-table.
- The XY-table can accurately ($<$0.1mm) position each OSC in the multiple mount in front of an optical bench, which is equipped with two optical axes. One axis is used for spectral response measurements and light intensity dependent current-voltage characteristics, the other for absorption measurements.
- The central LabView program controls all measurement equipment which is involved in the automated setup and handles the standardised storage of the measured data.
- The assistance of the automated setup has greatly simplified the characterisation process and freed manpower for other tasks, e.g. the production of OSCs.

Chapter 5

Data Analysis Methods and Environment

In this chapter the methods for the data analysis and the fundamental data handling and organisation is described. First, the theory of the methods used for condensing measurement results into useful parameters and for analysing the data is presented. Then the computational environment, in which the data analysis is carried out, is specified. At its centre is an electronic laboratory notebook (ELN), which contains all production parameters, measurement data and deduced parameters for every organic solar cell (OSC). This data then has to be prepared to be of use for the data analysis and the necessary steps of data preparation are described. The chapter closes with a brief overview of the computational tools used and the precautions taken to ensure data and code integrity.

5.1 Data Analysis Methods

The methods used to extract information from measurements and the OSC preparation process are presented in this chapter. Spline functions are used for approximating noisy measured data or the Levenberg-Marquardt Algorithm (LMA) for fitting models to such data. With the help of the presented methods, parameters are extracted from the measured data. These parameters, together with the production parameters, form the data which is subsequently analysed using the principal component analysis (PCA) in the search for patterns and trends with physical origin.

5.1.1 Fitting of Functions to Data

Most measurements in this work yield two-dimensional curves, which are described by a set of data $\{y_i\}$ taken at discrete points $\{x_i\}$ $(i = 1, \ldots, N)$. Whereas the values $\{x_i\}$ of the controlling variable are usually assumed to be exact, the data $\{y_i\}$ is generally subject to certain errors, i.e.

$$y_i = f(x_i) + \epsilon_i, \tag{5.1}$$

where ϵ_i is the error in the measurement, which may originate for example from a normal distribution with standard deviation σ_i. In order to extract parameters from the data, e.g. the intersection of the curve with axes or features like derivatives, often values in between x_i and x_{i+1} or the curve derivatives at some x are of interest for the analysis. Hence it would be useful to find a function f, which adequately approximates the data continuously while taking the measurement errors into account. Fitting with a polynomial would be one possibility if there is no prior knowledge about the function to fit. However, using a polynomial, which is globally defined for data with many data points, might quickly become unfeasible due to the high polynomial order required for approximation.

A common and efficient method is to describe such data by a function f, which is composed of piecewise defined low order polynomials that are smoothly connected. The resulting function is called a spline. Splines are often used for representing curves, because of their simple construction and easy handling even in more than two dimensions.

Splines are of degree k, if they are composed of polynomials of degree k. Cubic splines, i.e. $k = 3$, are the most common type and they are used in this work to extract OSC properties from measurement data if no model function is known (see section 5.3.2). Their basics are briefly described here following references [72, 73].

A spline f has to satisfy two main conditions:

1. it has to be as smooth as possible while

2. still approximating the data adequately.

Suppose that set $\{x_i\}$ is ordered such that $x_1 < x_2 < ... < x_N$. A measure

for the smoothness of the function f is given by

$$J(f) = \int_{x_1}^{x_N} [f''(x)]^2 \, dx, \tag{5.2}$$

the integrated square of the second derivative of f, which is an approximation for the total curvature of the function. To approximate the data adequately, f is determined in such a way that $J(f)$ of equation 5.2 is a minimum under the constraint

$$D(\{y_i\}, f) \equiv \sum_{i=1}^{N} \left(\frac{y_i - f(x_i)}{\sigma_i} \right)^2 = S, \tag{5.3}$$

where S is the smoothing condition and σ_i is used to weigh the difference between measured and fitted data points. When setting $S = N$, i.e. to the number of data points, $D(\{y_i\}, f)$ takes care of the second spline condition that the fitted function retains consistency with the measurement points and the difference between measured and fitted data at each measurement point is in the order of magnitude of the measurement errors. Minimisation of equation 5.2 under the constraint of equation 5.3 is achieved by introducing a Lagrange parameter λ,

$$\tilde{S}(f, \lambda) = \int_{x_1}^{x_N} [f''(x)]^2 dx + \lambda \left(\sum_{i=1}^{N} \left(\frac{y_i - f(x_i)}{\sigma_i} \right)^2 - N \right), \tag{5.4}$$

and minimising the resulting functional. For a given λ, a function $f_\lambda(x)$ is obtained. λ has to be chosen such that f_λ satisfies equation 5.3. The minimisation yields following conditions for f:

$$f^{(4)} = 0 \text{ for } x_i < x < x_{i+1}, \quad i = 1, \ldots, N \tag{5.5}$$

$$f^{(m)}(x_i)_- - f^{(m)}(x_i)_+ = \begin{cases} 0 & \text{for } m = 0, 1; \quad i = 2, \ldots, N-1 \\ 0 & \text{for } m = 2; \quad i = 1, \ldots, N \\ 2\lambda \frac{f(x_i) - y_i}{\sigma_i} & \text{for } m = 3; \quad i = 1, \ldots, N \end{cases} \tag{5.6}$$

where $f^{(m)}$ denotes the m^{th} derivative of f and $f^{(m)}(x_i)_\pm = \lim_{h \downarrow 0} f^{(m)}(x_i \pm h)$. Condition 5.5 requires that in $[x_i, x_{i+1})$

$$\begin{gathered} f = a_i + b_i(x - x_i) + c_i(x - x_i)^2 + d_i(x - x_i)^3; \\ x_i \leq x \leq x_{i+1}, i = 1, \ldots, N \end{gathered} \tag{5.7}$$

with parameters $\{a_i, b_i, c_i, d_i\}$ to be determined. The conditions in equation 5.6 demand that f is twice continuously differentiable at all x_i, but the third derivative is discontinuous an amount to be determined. Thus $f(x)$ is composed of cubic polynomials, which are continuously differentiable up to f''. The parameters $\{a_i, b_i, c_i, d_i\}$ can be determined from 5.6 and many fast computational algorithms are available for that purpose.
Splines can be used both for interpolation and smoothing data in two or more dimensions. The smoothing condition S for curves weighted by σ_i is usually chosen in the range of $N \pm \sqrt{2N}$. Interpolating splines constitute a subset of the more general smoothing splines. Here $S = 0$ and the resulting spline goes through every original data point y_i, independent of their weighting.

5.1.2 Fitting of Models to Data

If one can assume that there is a globally defined model function $f = f(x, \mathbf{p})$, which adequately describes the measurement data $\{x_i, y_i, \sigma_i\}$ $(i = 1, \ldots, N)$ (see equation 5.1) with some adjustable fit parameters $\mathbf{p}^T = (p_1, \ldots, p_m)$[1], $(m < N)$, these parameters have to be chosen such that the fit of the model to the data is as good as possible while taking the measurement errors σ_i into account. Fitting the model function to the data allows further to test the model assumptions. If the model structure adequately describes the measurement data, then the curve can be parameterised and the data necessary to reproduce the curve can be reduced to the fit parameters. For an adequate physical model, the parameters can be attributed to certain physical properties of the investigated system and used to explain its behaviour.
Fitting of models to data is usually done by least square curve fitting. The challenge consists in finding the parameters $\mathbf{p}$, for which $S(\mathbf{p})$, the sum of the squares of some residuals r_i $(i = 1, \ldots, N)$, is minimised. The residuals r_i in the most common case are defined as the vertical difference between the model function f at x_i and the actual measurement data y_i weighted with σ_i,

$$S(\mathbf{p}) = \sum_{i=1}^{N} r_i(\mathbf{p})^2 = \sum_{i=1}^{N} \left(\frac{y_i - f(x_i, \mathbf{p})}{\sigma_i} \right)^2 . \tag{5.8}$$

Three common numerical algorithms specialised for this kind of least squares problem, which arises from curve fitting, are the method of gradient descent,

[1] $\mathbf{p}^T$ denotes the transpose of the column vector $\mathbf{p}$.

the Gauss-Newton Algorithm (GNA) and the Levenberg-Marquardt Algorithm (LMA) [74]. Starting from an initial guess for the parameters $\mathbf{p}_0$, an algorithm's reliability and speed of convergence towards a solution crucially depends on how the parameters are updated from one to the next iteration. In this work, the LMA is used. Its procedure and advantages over the method of gradient descent and the GNA will be briefly explained [75, 76, 77]. The algorithm is presented here in terms of $S(\mathbf{p})$ as a sum of some general residuals $r_i(\mathbf{p})$ because, depending on the function to fit, often other definitions of the residuals than those shown in equation 5.8 are more appropriate. For ease of notation, the $r_i(\mathbf{p})$ are written as residual vector $\mathbf{r}(\mathbf{p})$ and

$$S(\mathbf{p}) = \mathbf{r}(\mathbf{p})^T \mathbf{r}(\mathbf{p}). \tag{5.9}$$

Whereas the method of gradient descent only uses gradient information at a parameter point $\mathbf{p}_0$ for calculating the next step $\triangle\mathbf{p} = \mathbf{p} - \mathbf{p}_0$ towards a possible minimum, both GNA and LMA improve this by additionally using curvature information of S at $\mathbf{p}_0$ obtained from the second derivative of S. The GNA's approach is to Taylor expand the gradient $\nabla S(\mathbf{p})$ at $\mathbf{p}_0$, resulting in

$$\nabla S(\mathbf{p}) = \nabla S(\mathbf{p}_0) + (\mathbf{p} - \mathbf{p}_0)^T \mathbf{H}(\mathbf{p}_0) + \mathcal{O}(3), \tag{5.10}$$

where $\mathbf{H}(\mathbf{p}_0) = \nabla^2 S(\mathbf{p}_0)$ is the Hessian matrix of S at $\mathbf{p}_0$. Assuming that S has quadratic behaviour around $\mathbf{p}_0$, terms of order $(\mathbf{p} - \mathbf{p}_0)^3$ and higher are neglected. Solving equation 5.10 for $\nabla S(\mathbf{p}) = 0$ leads to

$$\mathbf{H}(\mathbf{p}_0)(\mathbf{p} - \mathbf{p}_0) = -\nabla S(\mathbf{p}_0), \tag{5.11}$$

which is the parameter update rule for the GNA.
If the Hessian matrix $\mathbf{H}$ and its inverse $\mathbf{H}^{-1}$ can be found, then equation 5.11 can be solved for $\mathbf{p}$. With $S(\mathbf{p})$ being a sum of residuals, the gradient vector and the Hessian matrix of S at $\mathbf{p}$ are then defined as follows:

$$\nabla S(\mathbf{p}) = 2\sum_{i=1}^{n} r_i(\mathbf{p}) \nabla r_i(\mathbf{p}) = 2\mathbf{J}(\mathbf{p})^T \mathbf{r}(\mathbf{p}), \tag{5.12}$$

$$\mathbf{H}(\mathbf{p}) = \nabla^2 S(\mathbf{p}) = 2\mathbf{J}(\mathbf{p})^T \mathbf{J}(\mathbf{p}) + 2\sum_{i=1}^{n} r_i(\mathbf{p}) \nabla^2 r_i(\mathbf{p}), \tag{5.13}$$

where $\mathbf{J}(\mathbf{p})$ is the Jacobian matrix of $\mathbf{r}$ at $\mathbf{p}$ with elements $J_{ij} = \partial r_j / \partial p_i$.

Solving equation 5.11 essentially reduces to a set of linear equations, if $\mathbf{r}(\mathbf{p})$ is linear in the parameters $\mathbf{p}$, but for non-linear cases the Hessian matrix itself is often difficult or impossible to compute.
However, for the least square problem, one can often approximate the Hessian matrix using the Jacobian with the following reasoning: if it is possible to approximate the elements r_i by linear functions ($\nabla^2 r_i(\mathbf{p})$ is small) or the elements r_i are small, the Hessian simply becomes $2\mathbf{J}(\mathbf{p})^T\mathbf{J}(\mathbf{p})$, just like in the linear case. The Jacobian matrix and its inverse are usually much easier to calculate than the Hessian matrix. Both GNA and LMA use this feature of the least square problem.
Using the approximation of 5.13 in equation 5.11 leads to

$$\mathbf{J}(\mathbf{p})^T\mathbf{J}(\mathbf{p})(\mathbf{p}-\mathbf{p}_0) = -\mathbf{J}(\mathbf{p})^T\mathbf{r}(\mathbf{p}_0) \tag{5.14}$$

This parameter update rule is used by the GNA and leads to quick conversion. However, the rate of conversion is sensitive to the initial guess $\mathbf{p}_0$. The key feature in which the LMA improves compared to the GNA, is to add a damping factor ξ to equation 5.14 such that

$$(\mathbf{J}(\mathbf{p})^T\mathbf{J}(\mathbf{p}) + \xi\mathbf{I})(\mathbf{p}-\mathbf{p}_0) = -\mathbf{J}(\mathbf{p})^T\mathbf{r}(\mathbf{p}_0), \tag{5.15}$$

where $\mathbf{I}$ is the identity matrix. The size of the non-negative damping factor ξ is adjusted at each iteration, depending on the changes in S, and aids the convergence of the algorithm. A smaller ξ is used, if the reduction of S is rapid, resembling more the behaviour of the GNA. ξ is increased if an iteration step gives insufficient reduction in the residual, thus damping the influence of the curvature and tending towards the method of gradient descent. Basically, the LMA interpolates between GNA and the method of gradient descent. The convergence of the LMA is more robust than that of the GNA, but might be a bit slower for well-behaved functions and good starting guesses for $\mathbf{p}_0$.
The iteration stops when the improvements in minimising S by changing $\mathbf{p}_0$ to $\mathbf{p} = \mathbf{p}_0 + \triangle\mathbf{p}$ are below a certain defined threshold or – as safeguard mechanism – if a given number of iterations is reached.

5.1.3 Datamining

The collection of parameters from the OSC preparation (chapter 3.2), the automation of the main characterisation methods (section 4.2) and the OSC

properties deduced from measured data with the help of splines (section 5.1.1) or least-square fitting (section 5.1.2) lead to a very large amount of data. This data is both too large to be searched manually for patterns and already for small data sets exhibit a very complex interdependence. Yet one would like to answer the following two main questions:

- If the preparation parameters are kept the same, how large are the effects of statistical variations on the measured data?
- If some preparation parameters are intentionally varied, is the effect seen in the measured data (if there is any) due to the intentional variations or due to statistical effects?

The process of searching answers and discovering patterns in data, generally with the help of computers and database software, is called datamining. The selection of the statistical method for datamining is critical for being able to find patterns, which help to explain the correlation between OSC preparation parameters and trends in measured data. These patterns are sometimes called structural patterns, because they show a structure, which helps to understand properties of the data. The goal is with their help to identify latent, i.e. hidden factors, in the data which are determining the data's properties. As the dependencies between several variables have to be examined, there is a vital need for multivariate methods, because analysing the effect of only one variable in the presence of other variables only reveals partial information. This is of particular importance for the complex OSC system. The data has to be analysed for the effect of intentional as well as unintentional variations of preparation parameters on the experimental results.
The principal component analysis (PCA) is one of the best known multivariate methods. It has shown to be a suitable method for the analysis of the data and was chosen also considering the development of a statistical model (section 6.3). With its help, it is possible to determine variables, which have the largest influence on the properties of the data, find out the correlations between the variables and thus detect pattern in the data.

Principal Component Analysis

One suitable method to analyse the correlations and interdependencies between not two, but between more variables is the principal component anal-

ysis (PCA) [72, 78, 79]. This method is also known as Karhunen-Loève transform and is probably the oldest and best known multivariate method. The term "variable" does not denote a variable in the classical sense, but a realisation function. The variables in this case are given by the parameters from the recorded production process and the measured properties of the OSCs. The realisation of such a variable describes the mapping of an OSC parameter to a scalar value. The realisations of several variables for one OSC yield a data set, e.g. the values of all parameters the OSC has been made with.

The PCA is a multivariate statistical method for numerically examining the correlations in a set of data. The PCA uses the fact that the variance of the data is a measure of its information content. The focus is on analysing the influence of many interdependent variables, and not only one isolated variable, in order to find the dominating correlations between production parameters and OSC characteristics. The theory of the PCA will be described in the following paragraphs, starting with the introduction of multivariate terminology and closing with a small example.

Manufacturing and characterisation of an OSC leads to a data set, which can be described as an $p \times 1$ observation vector

$$\mathbf{y} = \begin{pmatrix} y_1 \\ y_2 \\ \vdots \\ y_p \end{pmatrix}, \tag{5.16}$$

where the y_i represent the realisation of the preparation parameters (e.g. concentration of the absorber solution, spin-coating speed, etc.) and scalar OSC properties (e.g. open circuit voltage V_{oc}, etc.) of the OSC the observation vector belongs to. Since the y_i are all belonging to the same object, they tend to be correlated. Having a set of n observation vectors $\mathbf{y}_1, \mathbf{y}_2, \ldots, \mathbf{y}_n$ of n OSCs, the observation vectors can be transposed and combined into a $n \times p$ data matrix $\mathbf{Y}$:

$$\mathbf{Y} = \begin{pmatrix} \mathbf{y}_1^T \\ \mathbf{y}_2^T \\ \vdots \\ \mathbf{y}_i^T \\ \vdots \\ \mathbf{y}_n^T \end{pmatrix} = \begin{pmatrix} y_{11} & y_{12} & \cdots & y_{1j} & \cdots & y_{1p} \\ y_{21} & y_{22} & \cdots & y_{2j} & \cdots & y_{2p} \\ \vdots & \vdots & & \vdots & & \vdots \\ y_{i1} & y_{i2} & \cdots & y_{ij} & \cdots & y_{ip} \\ \vdots & \vdots & & \vdots & & \vdots \\ y_{n1} & y_{n2} & \cdots & y_{nj} & \cdots & y_{np} \end{pmatrix} \begin{matrix} \text{OSC } 1 \\ \text{OSC } 2 \\ \vdots \\ \text{OSC } i \\ \vdots \\ \text{OSC } n \end{matrix} . \tag{5.17}$$

The first subscript represents a particular OSC, whereas the second subscript corresponds to a particular variable. Thus one row contains the observed values of all variables for the same OSC, whereas a column lists the values of one variable for all OSCs. An alternative way of writing $\mathbf{Y}$ is using the columns:

$$\mathbf{Y} = (\mathbf{y}_{(1)}, \mathbf{y}_{(2)}, \ldots, \mathbf{y}_{(p)}), \tag{5.18}$$

where e.g. $\mathbf{y}_{(2)}$ is the $n \times 1$ vector containing the observations of the second variable on all n OSCs. This notation is useful when considering the realisation of one variable for all OSCs, e.g. for the calculation of mean or standard deviation of a variable.

Plotting the data matrix results in a scatter plot with n data points in a Cartesian coordinate system spanned by the p axes of the variables. The approach of the PCA is to find a new set of axes for the data such that the first new axis in the scatter plot is lying in such a way that the variance of the data set (a measure of information content) is maximised along this axis. The second axis is chosen to capture the second highest variance while being orthogonal to the first axis and so forth. All new axes are a linear combination of the axes given by the original variables. The transformation of the axis can be obtained as follows:

Let one data set be described by a $n \times p$-dimensional data matrix $\mathbf{Y}$ as defined in 5.17. The $p \times p$ - dimensional covariance matrix $\mathbf{S}$ has elements

$$s_{jk} = \frac{1}{n-1} \sum_{i=1}^{n} (y_{ij} - \bar{y}_{(j)})(y_{ik} - \bar{y}_{(k)}) = \mathrm{Cov}(\mathbf{y}_{(j)}, \mathbf{y}_{(k)}), \tag{5.19}$$

where $\bar{y}_{(j)}$ denotes the average value of $\mathbf{y}_{(j)}$, i.e. average of the j^{th} variable. A diagonal element s_{jj} of $\mathbf{S}$ equals the variance of the j^{th} variable.

$\mathbf{S}$ is symmetric and positive definite. Hence it is possible to diagonalise it through an orthogonal transformation such that

$$\mathbf{\Lambda} = \mathbf{\Gamma}^T \mathbf{S} \mathbf{\Gamma}, \tag{5.20}$$

with $\mathbf{\Lambda}$ being diagonal and having the positive eigenvalues λ_α ($\alpha = 1, \ldots, p$) of $\mathbf{S}$ chosen in decreasing order as diagonal entries. Since $\mathbf{S}$ is positive definite, its eigenvalues are non-negative. The matrix $\mathbf{\Gamma}$ for the transformation has the corresponding normalised eigenvectors $\hat{\mathbf{e}}_\alpha$ as columns. The eigenvectors are called principal component vectors (PCV), because they span the new

coordinate system. The new data matrix $\mathbf{Z}$ is composed of p variables $\mathbf{z}_{(\alpha)}$ and defined as

$$\mathbf{Z} = \mathbf{Y}\mathbf{\Gamma}. \tag{5.21}$$

This equals an orthogonal transformation of the original data matrix $\mathbf{Y}$ by the eigenvectors of the corresponding covariance matrix $\mathbf{S}$. The $\mathbf{z}_{(\alpha)}$ are called principal components (PCs) of $\mathbf{Z}$, i.e. the variables describing the data in the transformed coordinate system. The covariance matrix of $\mathbf{Z}$ is diagonal and the diagonal entries $\mathrm{Cov}(\mathbf{z}_{(\alpha)}, \mathbf{z}_{(\alpha)}) = \mathrm{Var}(\mathbf{z}_{(\alpha)})$ are given by λ_α. Hence the new variables $\mathbf{z}_{(\alpha)}$ are uncorrelated. Given that the variance measures the information content and the principal components $\mathbf{z}_{(\alpha)}$ are sorted by descending λ_α often the first few principal components can adequately describe the variations in the data, because they account for most of the variance. Thus a reduction of variables to describe the data is often possible while retaining most of the information content. However, the core interest in this work is finding interdependencies in the data.

The eigenvectors $\hat{\mathbf{e}}_\alpha$ contain the principal component coefficients. Their elements $\hat{\mathbf{e}}_{(\alpha)i}$ can be considered as the contribution of $\mathbf{y}_{(i)}$ to the principal component $\mathbf{z}_\alpha$.

The principal components obtained via $\mathbf{S}$ are not scale invariant and consequently changing the units of a variable e.g. from seconds to hours will change both eigenvectors and eigenvalues of $\mathbf{S}$. Hence for the analysis it is preferable to have the variables in the data set to be commensurate, i.e. similar in measurement scale and variance. If the variables are not commensurate, $\mathbf{S}$ is replaced by the correlation matrix $\mathbf{R}$ for which the variables $\mathbf{y}_{(i)}$ are additionally normalised by their standard deviation $\sigma_{\mathbf{y}_{(i)}}$

$$\mathbf{y}_{(i)} \rightarrow \tilde{\mathbf{y}}_{(i)} = \frac{\mathbf{y}_{(i)} - \bar{\mathbf{y}}_{(i)}}{\sigma_{\mathbf{y}_{(i)}}}, \tag{5.22}$$

before calculating the principal components as described above. However, when the principal components of $\mathbf{R}$ are expressed in terms of the original variables they will no longer be orthogonal.

One important feature of the PCA, which has to be considered when interpreting the results, is that the PCA does not differentiate between production parameters and OSC properties, i.e. governing and dependent variables. It treats all variables equally and shows only their correlation. Consequently great care is necessary when interpreting the principal components. Still

	A	B
OSC 1	2.67	0.60
OSC 2	2.48	0.62
⋮	⋮	⋮
OSC 99	1.32	-0.17
OSC 100	0.70	0.16

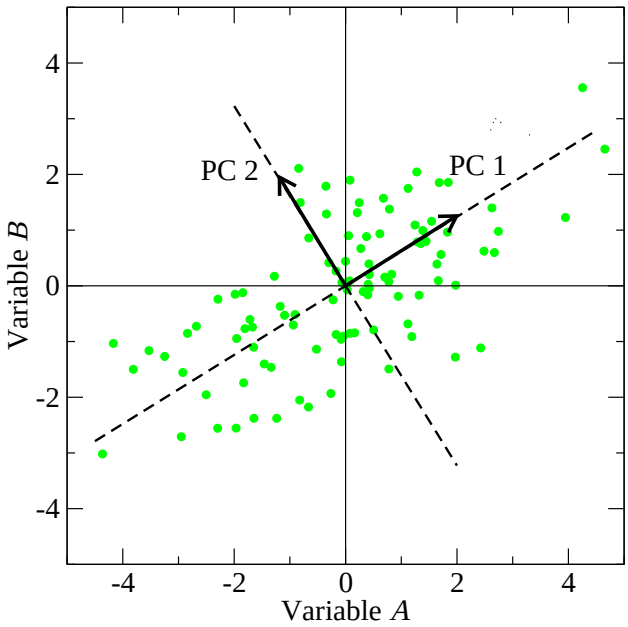

Figure 5.1: *The plot shows the realisations of the two variables A and B for 100 solar cells. The variables A and B are can be e.g. one production parameter and one measured OSC property respectively. The plot shows that the two are clearly correlated. The principal component vectors (PCV) are the unit vectors $\hat{\mathbf{e}}_{PC1}$ and $\hat{\mathbf{e}}_{PC2}$ and their directions are shown on top of the data. They are a linear combination of the original coordinate basis vectors. The principal components (PCs) are the new variables and give the coordinates of the OSC data with respect to the PCVs.*

from the PCA it is possible to identify parameters in the production process of organic solar cells, which have a significant influence on the device properties and performance.

The main principles of the PCA will be explained with a small example comprising 100 solar cells described by two arbitrary variables, A and B, which for example can be one preparation parameter and a measured OSC property. The data is shown after subtracting the mean from A and B as scatter plot in figure 5.1.

The covariance matrix $\mathbf{S}$ and the principal components are determined as described above. The details of the resulting principal components are shown in table 5.1 and the directions of the two PCVs are drawn on top of the original data in figure 5.1.

In this example, representing the data with only the first PC, i.e. only one dimension, would retain more than 80% of the variance in the data set.

	PC 1	PC 2
A	0.850	-0.527
B	0.527	0.850

	Eigenvalue	% of Variance	Cumulated %
PC 1	4.05	82.3	82.3
PC 2	0.75	17.7	100.0

Table 5.1: *The results of a PCA on the OSC data shown in figure 5.1. The table on the left shows as row and column header the original variables and the new variables, i.e. principal components (PCs), respectively. The matrix in the table is the matrix* $\mathbf{\Gamma}$*, which describes the transformation between the original variables and the PCs. The columns of* $\mathbf{\Gamma}$ *correspond to the normalised eigenvectors of the covariance matrix* $\mathbf{S}$ *of the OSC data. These vectors are called principal component vectors (PCVs) and form the new basis for the OSC data. If* $\hat{\mathbf{e}}_A$ *and* $\hat{\mathbf{e}}_B$ *are the original basis vectors, then the first unit vector of the new basis is given by* $\hat{\mathbf{e}}_{PC1} = 0.850\hat{\mathbf{e}}_A + 0.527\hat{\mathbf{e}}_B$*. This means that variable A is contributing 0.85 and variable B 0.527 to PC 1. The corresponding eigenvalues* λ_α *of the PCVs are shown in the table on the right. The table on the right shows that when expressing the OSC data with the principal components PC 1 already accounts for more than 82% of the variance in the data set.*

5.2 Data Management

The various sources and the large amount of data challenge the data management. Without an adequate and efficient data management right from the first step of the OSC assembling any data analysis at a later stage is hardly possible. In this section, the necessary requirements and the developed data structure, in which the data analysis is carried out, are presented. It describes where the data is coming from, how it is stored, accessed and exchanged for the data analysis. At the centre of the data management is an electronic laboratory notebook (ELN), which has been developed as part of this work. It unites all production parameters, measured data and deduced OSC properties, and thus provides a structured and simple access to all recorded data. The object orientated programming language Python is used for handling the data. Where necessary, Python is supplemented by other software tools for specific tasks (see section 5.4).

5.2.1 Background

An adequate series of documented OSC preparation and validation records is the prerequisite to permit a sound statistical and physical analysis. There is a large number of degrees of freedom during the OSC production which needs to be recorded (section 3.2) and vast amounts of measurement data is

obtained through the automation of the main OSC characterisation methods (chapter 4). As the effects of parameter variations on the properties of an OSC are usually not attributable to one particular variation, the complete history of an OSC has to be considered when interpreting the results of the characterisation. Furthermore, the data has to be managed in a way, which allows easy and reliable handling.
So far, the details of preparation steps had been recorded in each group member's paper-based laboratory book. The entries were written in individual styles and a general access to this information was difficult. Similarly, measured data was generated in different experimental setups with different conventions of storing the data, in many cases even without information on what the raw data represented in a data file. However, an easy and reliable access to both kinds of information is a key component for a systematic analysis. For this reason, a central repository was created, where all data, from production processes up to the deduced OSC properties, is stored in detail in a structured and standardised way. This central data repository is called electronic laboratory notebook (ELN). It constitutes the data base on which the data analysis is built.

5.2.2 Data Acquisition and Data Flow

The data for the analysis is coming from two main sources:

- Parameters from the OSC production process
- Data from the OSC characterisation

Additionally there is auxiliary data with e.g. important material constants or device settings, which complement OSC preparation parameters and measurement data. Various types of data have to be managed and despite their different sources, all data is gathered and integrated into one central structure, the ELN.

Manufacturing Data

During the OSC production process, the recording of the various different process steps and their parameters (see section 3.2) is necessary. Starting with paper-based route cards to standardise the OSC preparation parameters, the whole recording of the production was moved directly to an elec-

tronic protocol. The production data now is entered via a webinterface into a relational database (MySQL with Ruby on Rails, [80, 81]) which maps the complete production process for both substrates and solutions. Both the webinterface and the underlying database have been designed such that they can easily be adapted to new parameters or process steps. Two screenshots are shown in figure 5.2. When entering a process step in the webinterface, a set of mandatory fields always has to be filled. Basic syntax checks validate the type of entry to increase the data quality. Pull-down menus are available for many parameters, ensuring a consistent and standardised way of entering information into the database. The production data can be entered and accessed real-time by more people at the same time from any networked computer in the group.

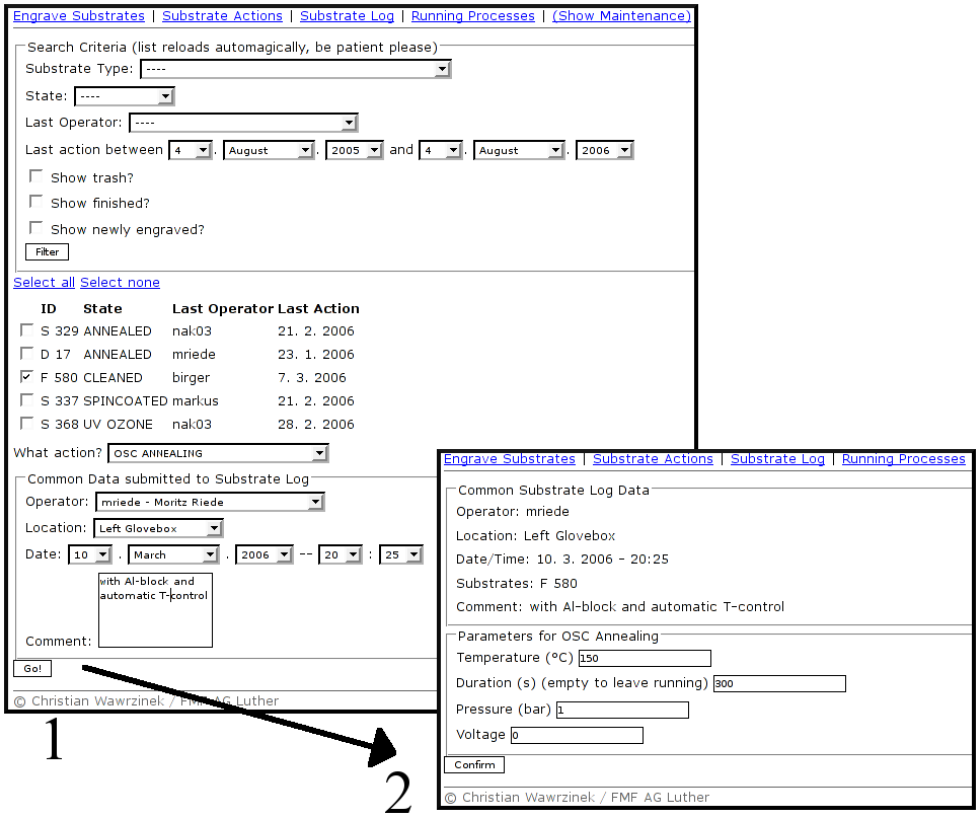

Figure 5.2: *Two screenshots from the webinterface, which is used to record all production details of the OSCs. The substrates for the next process step (here only F 580) is selected for an OSC-annealing step (1). Depending on the selected process, its process details can be entered the next page appearing after pressing "Go!" (2). The production data and auxiliary information can be entered and accessed from any networked computer in the group.*

The MySQL-database also handles all auxiliary information necessary during production. This includes details e.g. on the materials available for the absorber solutions and for evaporation, as well as the settings of the equipment, e.g. speed profiles of the spin-coating programs. All this can also be accessed and maintained through the same webinterface.
The measurement data from the characterisation is not included in the MySQL-database. When handling experimental data of various kinds, a relational database has several shortcomings, e.g. information on the measured data has to be stored separately from the raw data and the queries for retrieving data can become very complex. However, for recording the production parameters through an user-friendly webinterface, the MySQL-database with Ruby on Rails was the quickest realisable and most pragmatic solution for moving from a paper based to an electronic protocol. The relational database now replaces paper based notes in the laboratory for the standard processes making instead all information available in electronic form, accessible from any computer in the group.
Because the measured data would be separate from the production data, the MySQL-database therefore is only an intermediate step on the way to combining all necessary data. The subsequent data transfer from the MySQL-database to the ELN is done via the extended markup language (XML, [82]). XML is a platform independent general purpose markup language, which makes XML very flexible and powerful for data exchange between different systems.

Measurement Data

The second major source of data is the measurement data. Prior to the automation of the main characterisation methods (section 4.2), measured data had been stored differently for every measurement method. The output files then generally only contained raw data without extra information, making the attribution of a data file to a particular measurement and OSC often difficult.
The standard measurements are now all controlled by one central LabView program described in section 4.2.4, which stores the measured data in a standardised way independent of the actual measurement method. However, the used LabView version (7.0) so far lacks sufficient support for writing its output files directly as XML files [82], which would have been the best way to

facilitate the data transfer to the ELB. Hence an alternative but yet flexible way of storing the data was developed. The output files that LabView writes consist now each of two parts. The first part contains detailed information about how the measured data was obtained, i.e. measurement method, all device settings, date, time, what raw data to expect, etc.. This data is called "meta-data", because it is describing other data (the raw data, in our case). The second part of the file then contains the actual measured data in raw form. This file structure allows the necessary flexibility for including new measurements while ensuring that each measurement file contains all relevant details and is self-describing.
The LabView program employs features like mandatory fields, pull-down menus, and basic syntax checking to ensure the standardisation and quality of the meta-data entered when a measurement program file is created (see section 4.2.4).

```
[GLOBAL]                              -1.0001E+0 -391.1394E-6
SUBSTRAT_TYP=S-25x25_10               -979.8641E-3 -388.3007E-6
SUBSTRAT_NAME=S00488                  -959.6226E-3 -386.0499E-6
PIXEL=6                               -939.3851E-3 -384.0616E-6
DATUM=07.06.2006                      -919.2286E-3 -381.6252E-6
UHRZEIT=22:19:28                      -899.0260E-3 -380.5942E-6
OPERATOR=MRIEDE                       -878.8596E-3 -376.0848E-6
HALTER=9fach                          -858.6711E-3 -373.6755E-6
BELEUCHTUNG=1.0000E+3                 -838.5005E-3 -371.4882E-6
MESSMODUL=IV                          -818.3069E-3 -369.1783E-6
LAMPE=SunSim                          -798.1007E-3 -366.4062E-6
REFZELLE=LOTSDSC5                     -777.8957E-3 -364.4078E-6
    ⋮                                       ⋮           ⋮
[SPALTENBESCHRIFTUNG]
SPALTE1=Spannung[V]
SPALTE2=Strom[A]
```

Figure 5.3: *Excerpts from the files that the LabView program controlling the automated characterisation setup writes. The raw measured data (right) alone does not make much sense, because it contains no information on what is contained in the columns. Thus the raw data is complemented with meta-data (left), i.e. data describing the raw-data. Those two parts are joined into one output file, which is then self-explanatory.*

With the standardised structure of the output file from LabView, the data from the different experiments is now self-explanatory. This makes the transfer of the data into the ELN straight-forward.

Measured data obtained by measurement methods, which are not integrated in the automated setup, are only used to complement the data from the standard experiments of the automated setup. Because the data files are not handled by the central LabView program, their data format depends on the measurement equipment, usually plain text files without much meta-data (e.g. data from impedance measurements) or even proprietary binary file formats (e.g. AFM images). There are too many non-standardised data structures and this data either is manually being imported into the ELN or administrated separately.

5.2.3 Electronic Laboratory Notebook

The data collected from the production process and from the main characterisation methods are merged into one central repository in order to have one place from where all data is accessible.

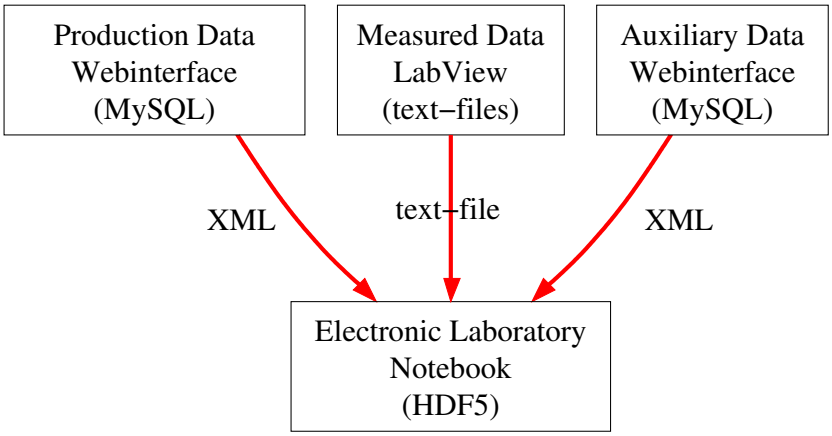

Figure 5.4: *A directed graph showing the sources, storage methods and the transfer of data. The two major data sources for the analysis are the production process and the OSC characterisation. This data is completed by auxiliary data containing details on used materials and equipment. All data is united in one central repository, called electronic laboratory book (ELN). The arrows show the transfer of the data with the corresponding data exchange format. The measured data is transferred as is.*

Uniting and structuring all data from the various sources in one central repository requires a flexible file format. There are several file formats available tailored for storing complex scientific data of which the Hierarchical Data Format (HDF5) offered the best framework for this work [83]. HDF5 is a binary, self-describing and portable file format with a well-documented soft-

ware interface to all major programming languages including Python. It can deal with almost any type and any size of data suitable for digital storage and provides the largest flexibility for handling the complex data coming from OSC production and characterisation. The data in the file can be organised in a hierarchical structure, allowing for a clear and organised way of storing and accessing the data.

This data-centric approach for the electronic laboratory notebook was chosen, because changes in processes and associated data can be easily implemented. The result is an electronic laboratory notebook in form of one HDF5-file, which not only has information on the process details, but also contains the actual experimental data and the subsequent analysis performed on the measurement data. The main structure of the central HDF5 file is shown in figure 5.5. Within the ELN, there is a continuous track of each OSC and all modifications are traceable.

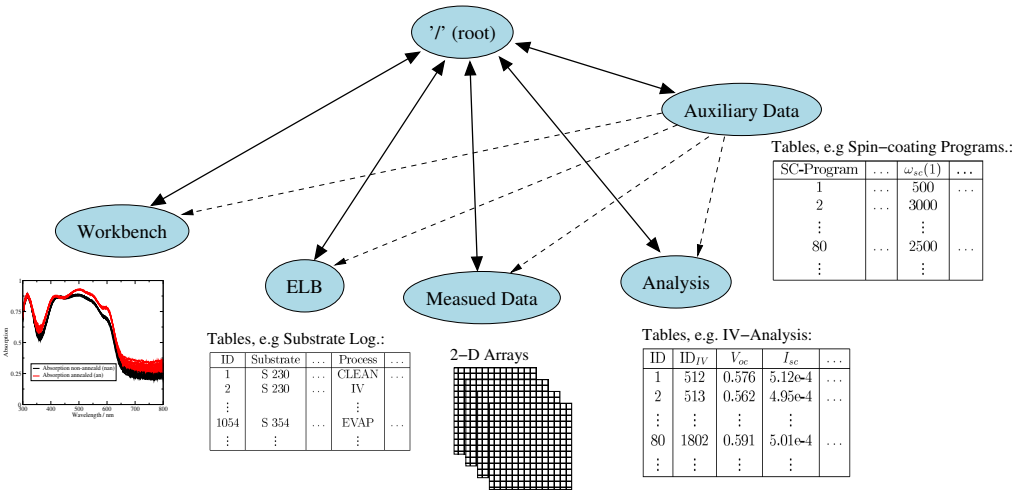

Figure 5.5: *The primary structure of the data in the central HDF5-file The data is organised in a structure comparable to a directory structure on the harddisk of a computer. It has one central root node from where five groups branch. The workbench is for testing purposes to leave the actual data unaffected. The ELB is the electronic log base, the group where the electronic protocols of all substrates are stored. The measured data is stored in self-describing arrays in the data group. The analysis group contains tables with the parameters extracted from the measured data. Finally, the auxiliary data provides information e.g. on the speed profiles for the different spin-coater programs. All groups are linked via the root group.*

The HDF5 data definition allows a structuring of its content in a hierarchical way, similar to a directory structure on a computer, starting from one root

node. The ELN contains five primary groups, which are used to organise the data. The measured data group contains all raw data in form of arrays, which are stored along with their metadata, such that each array is self-describing. The electronic log base (ELB) contains the complete history of all OSCs, from the first production step to the most recent measurement or analysis step. The analysis group contains all simple analysis results like the extracted OSC properties from each IV measurement. The auxiliary group contains the extra data necessary for describing the OSC history, e.g. the mapping of spin-coating program to a defined spin-coating speed profile. Finally, the workbench group is used for testing and working with the data. The HDF5 framework allows to specify read/write permission to groups and only when importing new data, write access to the ELB and measured data group is granted. The analysis group is only writable when performing data analysis and any work done under the workbench group leaves all other groups untouched, ensuring that accidental modification of neither measured data nor the electronic protocols can occur.
The ELN has been structured in a way, which allows the efficient searching and retrieval of data. The most common queries, e.g. the retrieval of the history of a certain set of OSCs, have been automated. However, the queries are not limited to these requests and special queries can easily be created. The retrieved data is further processed and prepared for the analysis. The data flow from acquisition to analysis is shown schematically in figure 5.6.

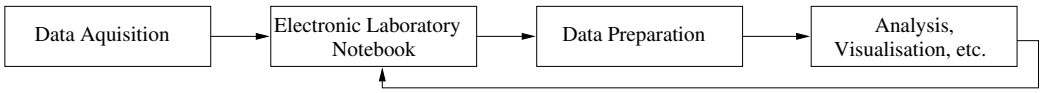

Figure 5.6: *The stages the data takes from its acquisition to analysis. All data is united in the electronic laboratory notebook, from where it can be retrieved for the analysis. Data integrity and validity is ensured by systematic data cleaning (see section 5.3.1) and useful parameters have to be deduced from the measured data prior to the data analysis (see section 5.3.2).*

5.3 Data Preparation

The data acquired during OSC production and characterisation has to be treated before it is of use for analysis and interpretation. Its validity and quality as to be assured and the measurement results have to be condensed

into a format useful for the further analysis. These steps are described in the following sections.

5.3.1 Data Cleaning

Checking the quality of the data and the associated correction and pruning is usually called data cleaning. The data in this work consists of two main components: the production parameters and the measurement results. Whereas for the production parameters human errors, i.e. wrong entries in the ELN, need to be corrected, the measured data has additionally to be checked for artefacts from the measurements. Data cleaning is an essential cornerstone for a reliable data analysis and this section is intended to describe how the data cleaning is carried out in order to obtain a consistent and reliable base of data for the analysis.

Manufacturing Data

The webinterface, through which the details of production for each substrate are entered, already provides important measures for assuring data consistency, completeness and quality. The use of mandatory fields and syntax checking ensures that e.g. if a temperature is required, it has to entered numerically. Similarly, pull-down menus limit the options to sensible choices for certain parameters, e.g. offering only valid spin-coating programs. However, these mechanisms cannot safeguard against all mistakes and these errors need to be found and corrected before the data is used for the analysis. If a parameter in question is found, e.g. unreasonable long or negative time intervals between production steps, one must resolve the issue with the person who entered the data. If in doubt, the parameter is either set to a value indicating "unknown" or the whole corresponding data set for the substrate is exempt from the analysis requiring the parameter.

Measured Data

To ensure the quality of the OSCs, all are already visually inspected for damages and defects in the photovoltaic active region during production. Often a particular behaviour in the measured data is not caused by variations in the production process, but by such defects. This measurement data, together with measurement data, which is obviously flawed due other reasons, has to

be treated separately in order to obtain a useful set of data for the analysis. To describe and quantify the cases, in which an OSC is not considered for the analysis, they have been categorised as follows:

- OSCs with only partial coverage of absorber layer
- Defects due to bubbles during spin-coating of the absorber layer
- Scratches in the absorber layer and Al-cathode caused by handling
- Particles in the absorber layer from dust or agglomerates
- Contact Problems
- Unspecified

Figure 5.7 shows the effect of these defects on the illuminated IV-curves and absorption measurement as well as corresponding pictures. The degree to which they affect the measurements varies and generally depends on the extent of the defect. The primary causes of the above mentioned defects are briefly discussed here.
The PEDOT:PSS layer is very homogeneous and covers the whole substrate area. Hence, if the area of an OSC is only partially covered during the subsequent spin-coating with the absorber layer, the aluminium cathode has direct contact to the PEDOT:PSS layer. The extent of the S-shaped IV-curve depends on the overlap area of the PEDOT:PSS|aluminium contact. The PEDOT:PSS|aluminium is creating a Schottky-like contact, while the area covered with absorber layer (if any) still generates photocurrent (see figure 5.7 A). An only partially covered OSC also affects the absorption measurement. In the region without absorber layer most of the light is reflected, leading to a different spectrum due to a missing layer (see figure 5.7 B).
Whereas bubbles have never been observed in the PEDOT:PSS layer, bubbles in the absorber layer can occasionally be created during the spin-coating of the absorber solution. While spinning the substrate, the bubble distorts the otherwise smooth film and can lead to a very inhomogeneous absorber layer. This inhomogeneity in thickness often affects more than one OSC per substrate, because of the comparably large size of bubbles. Bubbles cause S-shaped IV-curves as shown in figure 5.7 A and appear in the absorption

spectrum, where they equal in their signature those of partially covered OSCs (figure 5.7 B).

Scratches in the organic layers can arise during handling the substrates while moving them from one process step to the next. Due to the small size, a scratch usually does not appear in the absorption spectrum, but can deteriorate the IV-curve substantially with multifaceted behaviour. A scratch through absorber and PEDOT:PSS layer prior to the aluminium evaporation will contribute a short circuit between ITO and Al electrodes as seen in figure 5.7 A. A scratch after Al-deposition can exhibit a wide range of characteristics. It can e.g. cause an ohmic behaviour if ITO and aluminium establish a good contact or an instable behaviour of the IV-curve, if an existing small scale short circuit is burned out during the voltage sweep. Furthermore, scratches after cathode evaporation can destroy an aluminium interconnect and effectively render the OSCs on the same bus (see figure 4.8) useless.

Despite spin-coating the PEDOT:PSS layer under cleanroom conditions and filtering the solutions used for the absorber layer during preparation, particles on the substrate surface or from the solutions occasionally are seen in the layers. The effect of these particles on the measurement results depends on their size and quantity. Small particles in low quantities (1-2 per OSC) do not seem to affect the IV properties. More or larger particles however can cause anything from a Schottky-like contact to ohmic behaviour by introducing changes in the absorber layer (see figure 5.7 C). Due to their small size with respect to sampled area for absorption, these particles are generally not seen in absorption spectrum unless they cause large distortions with variations in layer thickness (see figure 5.7 D 4).

The OSCs are contacted in a four point measurement configuration. However, if the contact probes do not have a good contact to the aluminium or ITO interconnects, the IV measurement data is getting distorted. This manifests itself in spikes in the IV-curve, as seen in figure 5.7 C.

Finally, if an IV measurement is obviously flawed, e.g. showing a Schottky-like behaviour, but no damage to the OSC can be found (even when looking at the photovoltaic active area with a microscope), it is categorised as ”unspecified” for excluding it from the analysis.

Once the measurement data set is cleaned, it can be analysed and parameters can be extracted.

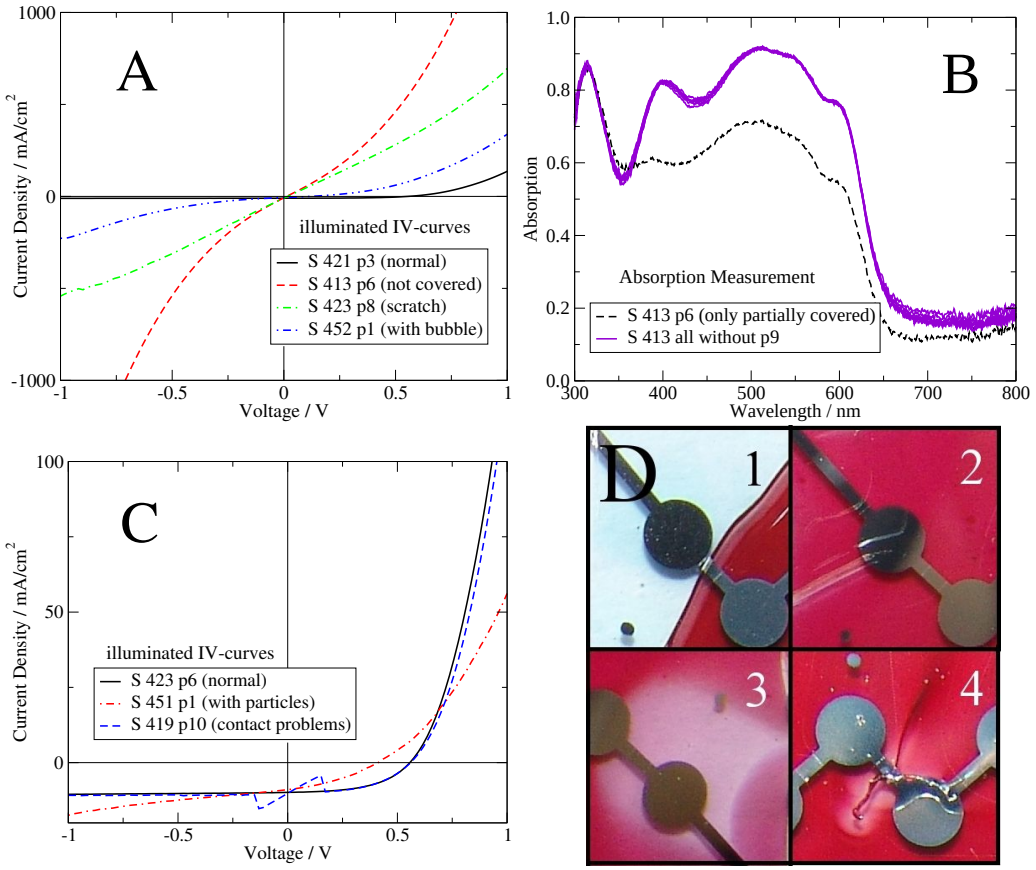

Figure 5.7: *The categorisation of measurement data upon pruning prior to the data analysis. (A) shows the effects on IV-curves when the OSC is not completely covered with the absorber layer, a bubble during spin-coating causes strong inhomogeneities in the absorber layer or a scratch creates a short circuit. Signatures in the absorption spectrum of a bubble and a partially covered OSC are similar and the example of a non-covered OSC is shown in (B). (C) shows an S-shaped IV-curve causes by several particles in the photovoltaic active region and contacting problems. In (D) pictures of the four cases illustrated above are shown: no coverage with absorber (1), scratches in the cathode (2), inhomogeneities caused by a bubble during spin-coating (3) and a large particle (4).*

5.3.2 Extraction of OSC Properties from Measured Data

Most measurements used in this work yield two-dimensional curves. The information contained in these curves has to be extracted by condensing the measured data into a set of meaningful scalar OSC properties. Some properties can be directly read from a measured curve, others have to be determined by fitting functions or suitable models to the curve. The following sections describe how the data of the main measurements was treated and

which properties were obtained for the data analysis. The feature aggregation is carried out with automated Python scripts.

Current-Voltage Measurements

The current voltage measurement is the main measurement on solar cells (section 4.1.1). It is primarily used to determine the power conversion efficiency η through determining V_{oc}, J_{sc} and FF at a given illumination intensity P_{ill}. But the IV-curve contains much more information, which can be extracted. Figure 5.8 shows schematically the OSC properties used for the data analysis.

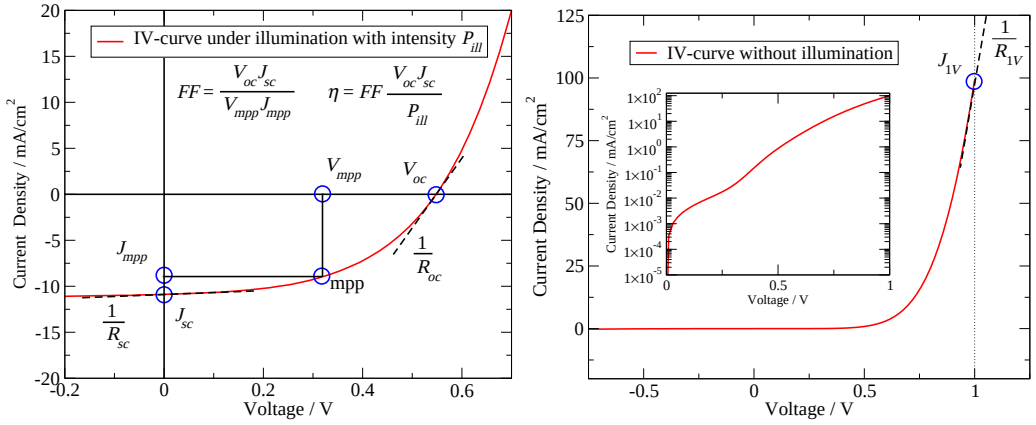

Figure 5.8: *The measurement properties, which can be directly read from IV-curves. In addition to V_{oc}, J_{sc}, FF and η for an illuminated IV-curve, following properties can be extracted from the data as shown on the left: R_{sc}, the reciprocal slope at short circuit; R_{oc}, the reciprocal slope at open circuit; V_{mpp} and J_{mpp}, the voltage and current density respectively at the maximum power point (mpp); On the right, I_{1V} and R_{1V} are the current density and the reciprocal slope at $+1V$ forward bias respectively and can be obtained from both dark (shown) and illuminated IV-curve. The log-plot inset on the graph on the right shows a two-diodic-like behaviour.*

In literature, often the same names for the properties are defined differently, thus a brief description of the selected ones is given. They are all obtained via smoothing spline unless noted otherwise.

The OSC properties V_{oc}, J_{sc} and FF are extracted to calculate η. Together they constitute the standard solar cell properties.

V_{mpp} and J_{mpp} is the voltage and the current density respectively at the coordinates of the maximum power point (mpp), i.e. the optimal working

point for a solar cell. Its value is obtained during the same procedure as V_{oc}, J_{sc} and FF.

In addition to these properties, there are further properties, which are of interest when analysing the behaviour of organic solar cells. R_{sc} is the reciprocal slope at short circuit, i.e. $\frac{\partial V}{\partial J}\big|_{V=0\mathrm{V}}$. It might be related to the series resistance R_s. In amorphous silicon solar cells, R_{sc} is sometimes used to determine further properties of the solar cell, e.g. the built-in potential V_{bi} [50]. R_{oc}, the reciprocal slope at open circuit, i.e. $\frac{\partial V}{\partial J}\big|_{V=V_{oc}}$. It might be related to the parallel resistance R_p.

R_{1V} is the reciprocal slope at 1V forward bias, i.e. $\frac{\partial V}{\partial J}\big|_{V=1\mathrm{V}}$. It should be a measure of how good the interfaces can inject charges into the bulk of the OSC. R_{1V} is obtained via linear regression, because splines can under certain circumstances start to oscillate at the boundaries. In literature R_{1V} is sometimes called R_s, which however can really only be obtained by fitting a suitable model to the curve. Finally, J_{1V}, the current at 1V forward bias may be a measure of R_s.

The log-plot of a dark IV-curve as shown as inset in figure 5.8 on the right-hand side is currently investigated. Fitting numerically a two-diode model does not yield an adequate fit. The log-plots of different OSCs show a distinct different behaviour and the origins are subject to ongoing research.

Further properties can be deduced from the IV-curve by fitting a model function to the data. The simple diode equation 5.23 (repeated from section 2.4.2) is fitted with the Levenberg-Marquardt Algorithm (LMA, section 5.1.2) to the data. For good OSCs, good fits can be achieved with this model function (see figure 5.9 left). However, it is not possible with this model to reproduce, e.g. the kink of the IV-curve in the fourth quadrant (see figure 5.9 right), which is often observed.

$$I - I_{01}\left(exp\left(\frac{e(V - IR_s)}{n_1 k_B T}\right) - 1\right) - \frac{V - IR_s}{R_p} + I_{ph} = 0, \tag{5.23}$$

where I_{01} is the dark saturation current, n_1 the diode ideality factor, I_{ph} the photogenerated current and R_s and R_p the serial and parallel resistances. The equivalent circuit model was shown in section 2.4.2.

Absorption Measurements

The results from the absorption measurements (section 4.1.3) are used for both assessing the quality of the spin-coated layers and calculating the ab-

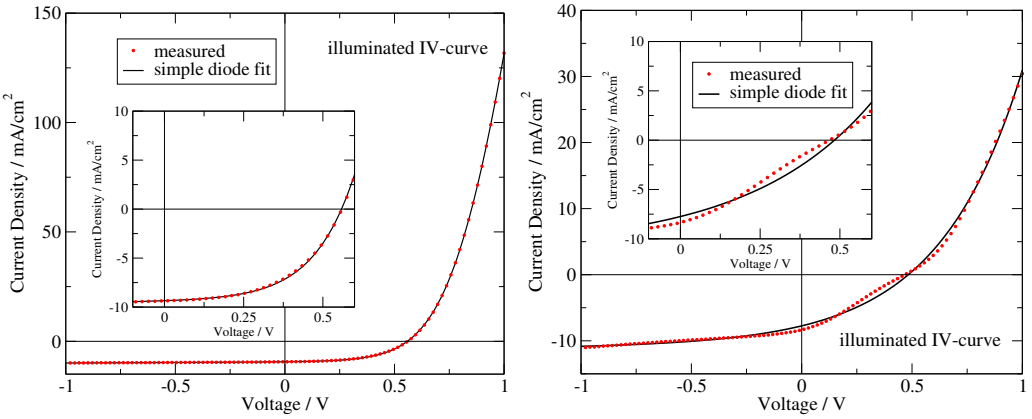

Figure 5.9: *Measured data for which a good fit (left) can be obtained by fitting the simple diode model (equation 5.23). The fit parameters for the left IV-curve are as follows:* $I_{01} = 76\mu A/cm^2$, n_1=4.4, $I_{ph} = 9.4mA/cm^2$, R_s=0.9Ωcm^2 *and* R_p=2kΩcm^2. *However, IV-curves often exhibit a kink in the fourth quadrant where the simple diode model does not adequately describe the data (right).*

sorber layer thickness, an important parameter for OSCs. The organic layers in an OSC have thicknesses which are of the same order of magnitude as the wavelength of the incoming light. The interference pattern, which forms due to the reflection of the incoming light at the aluminium cathode, reacts very sensitive to the thickness of the layers and any optical calculations have to be carried out coherently.

Optical simulations revealed a linear correlation between the position of the first minimum in the absorption spectrum and the thickness of the absorber layer, assuming that the thickness of the other layers remains constant [65]. Figure 5.10 shows both simulated and the measured absorption spectra of OSCs of different absorber layer thickness. By comparing local minima in the absorption spectra with results from optical absorption simulations of the OSC layer system, the absorber layer thickness can be calculated.

This method has several important advantages over measuring the film thickness with AFM or Decktak. It is much quicker, can be easily done for every OSC on a substrate and is non destructive, because the substrates are neither taken out of the glovebox nor mechanically damaged for measuring the film thickness. Furthermore, deducing the layer thickness from AFM measurements is very dependent on the smoothness of the film. Especially for thicker absorber layers (>150nm), the surface roughness with peak to valley

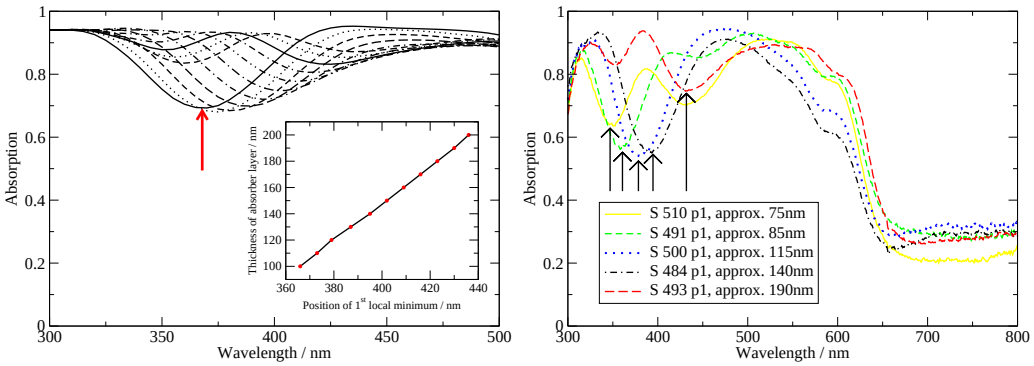

Figure 5.10: *Simulated absorption features of OSCs with different absorber layer thickness. The inset shows the absorber layer thickness as function of the position of the indicated local minimum. Additional minima have been considered for films thicker than 160nm. On the right measured absorption of OSCs with different spin-coating speeds (500 to 2000rpm) and the same absorber solution (no. 270) are shown. The position of the first local minimum used is indicated and the deduced estimates for the absorber layer thickness shown.*

distances of up to 100nm are often observed and make an exact measurement of the layer thickness difficult. The light spot from the absorption measurement on the other hand has an approximate diameter of 0.8mm in the plane of an OSC. This is much less than the active area of an OSC, but it averages the layer thickness over a much larger area than an AFM.

However, calculating the absorber thickness from the local extrema in the absorption spectrum has a few caveats. The optical properties have to be determined well for all material used and starting at an absorber thickness of about 160nm, more than one minimum occurs in the region between 320-540nm in the absorption spectrum. Then a unique relation between position of minima and absorber thickness is not given any more. Prior knowledge about the approximate film thickness from spin-coating speed and absorber concentration is then required [59]. Preliminary measurements have been within 10% of the thickness measured with AFM, but still have to be verified for a larger set of measurements.

The extrema from the measured absorption spectra are extracted using smoothing splines. The inverse of the curvature was taken as measure for the error in the wavelength at which the extremum occurred. The most prominent extremum is a local minimum between 330nm and 400nm, but there are

typically more extrema, which can be used for calculating and confirming the absorber layer thickness. The first four prominent extrema are usually extracted.

Spectral Response Measurements

The EQE and SR curves obtained from the spectral response measurement can currently only be used qualitatively. For the last few months, during which the experiments were carried out, it was not possible to reconcile the results of the J_{sc}^{SR} calculated from the SR (section 4.1.2) and the J_{sc} from the IV-measurements (section 4.1.1). There is an offset with the J_{sc}^{SR} being about 30% lower than J_{sc}. Despite careful checking of the setup and the calculations, the source for the systematic deviations has not been found yet. The search continues and the reference cells used to measure the spectrum of the Xe-lamp are at the time of writing being recalibrated at the Fraunhofer ISE Callab.
The EQE contains information on both absorption properties and charge carrier transport. Although only the shape of the EQE and SR curves are available for the analysis, the data can be used to make qualitative deductions and relative comparisons:

- Comparison of the shapes of EQE and absorption spectra,
- Extent of the shoulder at 600nm,
- Relative height of peaks at 400nm and 550nm,
- Relative changes of the shape due to annealing.

Considering these points can aid the interpretation of IV-curves and absorption measurements.
If the systematic error is found and resolved, the following additional properties are of interest for the analysis:

- IQE, calculated from EQE and the absorption measurements,
- Comparison of IQE and EQE.

The data of all conducted SR measurements has been recorded in such way that once the current issues are resolved, it should be in principle possible to correct the data and to carry out quantitative studies with the SR data as well.

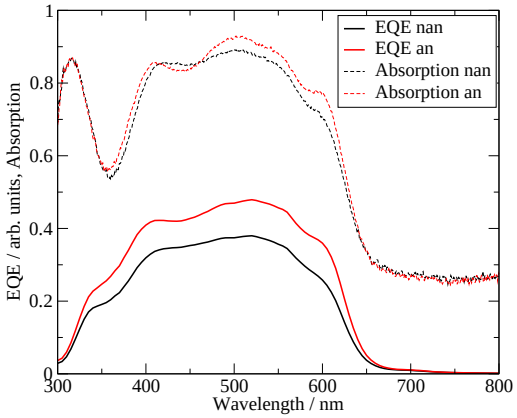

Figure 5.11: *The EQE and the corresponding absorption spectrum of OSC S 421 p1 (P3HT:PCBM, 1:0.7 in DCB). The characteristics are shown for both the non-annealed (nan) and the annealed (an, T_{pt}=150°C, t_{pt}=300s) case. This plot illustrates the changes due to annealing and allows a comparison of the shapes of absorption and EQE. Upon annealing the characteristic absorption shoulder of P3HT at 600nm is getting more pronounced. The absorption spectrum changes little in comparison to the EQE, which shows a significant increase between 320 and 630nm.*

5.4 Computational Tools and Practise

This final section on the computational environment will give a very brief overview of the computational tools used and of the computational practise adhered to throughout this work. The data handling is primarily done with the script language Python, the capabilities of which are extended with a series of modules.

Python

Python (ver 2.4.2) was chosen for data handling, because it is a powerful and easy to learn scripting language. Python is available free of charge and one of its strength is that it is made for extension with external modules. These modules provide interfaces to all used components and offer very good support for numerical computing and for analysing data [84]. The modules used in this work are all available free charge and briefly summarised here.

- Pytables is a Python interface to the HDF5 library [85]. It provides an easy way for accessing and manipulating data and tables inside a HDF5 file.

- SciPy is a large collection of Python libraries and provides the fundamental packages for scientific computing with Python [86]. This package includes modules for graphics, optimisation, interpolation and many other purposes.

- GracePlot [87] is a Python interface to Grace [88], the versatile plotting program being used for the graphs in this work.

- The package mpfit is a small yet flexible module for fitting functions to data based on the Levenberg-Marquardt Algorithm (section 5.1.2) [89, 90]. It allows detailed model and parameter descriptions.

Matlab

The principal component analysis (section 5.1.3) is carried out within the statistics package of Matlab, a high level computing language. Matlab is designed for rapid code development and visualisation and in many areas it is a de-facto standard environment for scientific computing. However, it is non-free and Python offers more flexibility for all other required tasks.

Computational Practise

In order to manage the complex project, the computational practise followed will be quickly summarised. A large part of the reliability of a computational projects depends on the standards adhered during programming.
The modular structure of Python allows for a high reuse of the code written. The goal followed is the DRY-approach, which stands for "don't repeat yourself". This way, changes in program structure or parts of the code have to be carried out only at one place and do not require adjustments at several parts of a program.
Python offers a good code verification and testing environment. All code is checked within the unit test framework, before being used on the actual data [91]. This way it is ensured that the script is doing what it is supposed to do. Any errors can thus be detected before the code is used at a critical stage in the ELN.
The electronic files of the whole project are managed by Subversion, an open source revision control system [92]. This applies to the Python source code, the ELN and the remaining parts of this thesis. The history of every file

is documented and each file can be restored in a previous revision. While modifying the HDF5 file, the script revision is recorded and modifications can be traced back to the program, which carried out the changes.

5.5 Summary

- In order to manage the large base of data, both with respect to quality and size, the tools for an efficient data management were developed.
- An electronic laboratory notebook (ELN) unites data, which is coming from two main sources: (1) from the production process, which is logged through an user-friendly webinterface, and (2) from the automated OSC characterisation, the data of which is made available in a standardised format.
- The data in the ELN is hierarchically structured to allow an efficient access. Data integrity is ensured by using the unit testing framework, specifying read/write permissions to parts of the ELN and tracking any change and associated scripts.
- The most common queries of the ELN have been automated, yet special queries can be easily implemented.
- OSC properties are extracted from the measured data using cubic splines and by fitting model functions to the measured data using the Levenberg-Marquardt Algorithm.
- Principal component analysis (PCA) has been chosen as multivariate method to search for correlations between the production data and OSC properties.
- Prior to analysis, the data is carefully checked and if necessary pruned. The OSC preparation protocols are checked for missing or unreasonable parameters. The measurement data is cleaned of OSCs, the observed measurement characteristics of which can be explained by obvious defects in the OSC.

Chapter 6

Experiments and Analysis

In this chapter the influence of the production process on the performance of organic solar cells is investigated. First of all a large run of experiments with a limited set of variations of the production parameters is described. The resulting variations in OSC properties are examined both with respect to the variations between the OSCs on one substrate and their variations between different substrates. The range of observed OSC characteristics are described with the example of three representative substrates covering the range of obtained power conversion efficiencies η. In order to determine the causes of the observed spread in OSC properties, the data of the experiments is searched for correlation between production parameters and measurement results by means of principal component analysis (PCA). The correlations are analysed for their physical origin and a model for optimising the production process is proposed.

6.1 Influence of the Production Process

During the production of the OSCs more than 40 parameters are recorded for each substrate (section 3.2). The parameters were divided into three groups: (1) parameters, which can be controlled well, e.g. the spin-coating speed used for coating the substrates, and can be made identical for each substrate; (2) the time intervals before and after a spin-coating step intrinsically vary from substrate to substrate within one batch due to its sequential nature (see figure 6.1); (3) there are parameters, which vary due to the human factor in the production process, e.g. the manual control of the evaporation process, or due to outside influences, e.g. the temperature during spin-coating.
The variations of the parameters in groups (2) and (3) will be called "unin-

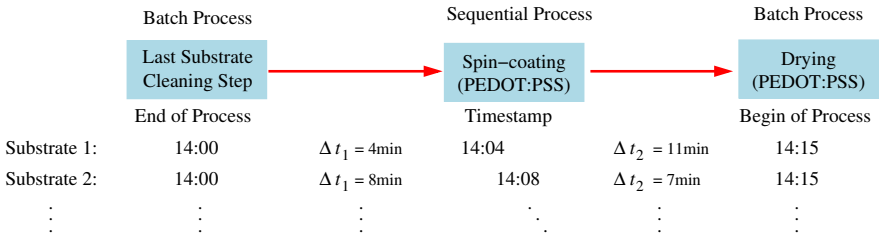

Figure 6.1: *The difference in time intervals caused by the sequential nature of the spin-coating process. The example of the PEDOT:PSS spin-coating illustrates the difference in time intervals which arises from the sequence of batch processes and the spin-coating, i.e. a sequential process, where only one substrate at a time can be processed. A batch usually consists of eight substrates. The time intervals are obtained from the difference in the timestamps of the consecutive process steps in the electronic laboratory notebook (ELN).*

tentional" parameter variations in this chapter with the following reasoning: they all vary and their variations are not or only very difficult to control. The work is conducted with other researchers in the laboratory leading to certain variations in the production process, e.g. when the evaporation chamber is only available at a certain time. These variations due to the human factor in the production and outside influences like the temperature during spin-coating introduce scatter in the production parameters. Thus there is a minimal set of parameters, which "unintentionally" varies between every OSC made in our laboratory. "Unintentionally" does not imply that these variations are not useful. Quite the contrary, because this scatter leads to variations in the OSC properties, which will be used in section 6.2 to analyse the influence of the involved production parameters.

Summarising, there exists a smallest set of parameters, which unintentionally varies between every made OSC. Prior to any intentional variation of parameters in the production process, it essential to investigate the variations, which can be caused by this minimal set of such unintentional parameter variations. Without this knowledge it is at a later stage difficult to assess, whether the variations observed in OSC properties are caused by the unintentional variations or due to the intentional variation of additional parameters. The question is: How much do the OSC properties vary due to the unintentional variations? Thus during this run of experiments, all parameters, which could be kept the same, were intentionally kept fixed, and a standardised production pattern was followed.

Table 6.1: *A brief summary of the main parameters held fixed during this series of OSC production. The detailed production process is described in chapter 3.2.*

Parameter	Value
Substrate Cleaning Procedure	standard
UV-Ozone Treatment	t_{UV}=1200s
PEDOT:PSS Spin-coating	filtered AI 4083, $\omega_{SC}(1)$=3000rpm, $t_{SC}(1)$=60s
PEDOT:PSS Drying (oven)	T_d=200°C, t_d=600s
Absorber Solution no. 263	P3HT:PCBM, c_D=15ml/ml, c_A=10.5mg/ml, DCB
Absorber Spin-coating	solution no. 263, $\omega_{SC}(1)$=1500rpm, $t_{SC}(1)$=90s
Evaporation Materials	aluminium only
OSC Post-Treatment	T_{pt}=150°C, t_{pt}=300s

6.1.1 OSC-Production and Characterisation

In a series of five batches, 36 substrates with 10 OSCs each were made and characterised. The standard production procedure is described in section 3.2. All production parameters, which can be controlled well, were kept constant for all batches and thus table 6.1 only briefly summarises them. The following paragraphs give specific details on the production and the characterisation process where necessary.

The absorber solution (no. 263) was made by diluting the stock solution number 262 (P3HT:PCBM, c_D=30mg/ml, c_A=21mg/ml, $c_D : c_A = 1 : 0.7$, DCB) with o-dichlorobenzene (DCB) to a P3HT concentration of 15mg/ml and by subsequently filtering it through a 0.45μm filter (PTFE membrane). From there on it was continuously stirred on a magnetic stirrer at ambient temperatures.

After vacuum deposition of the aluminium cathode and prior to the OSC post-treatment, all OSCs were characterised by IV-measurements without and with illumination on the sun simulator (1000W/m^2 AM1.5g-equivalent). Subsequently absorption measurements on all OSCs and the spectral response (SR) measurements on two OSCs on each substrate were carried out. The OSCs for the SR measurement were selected on basis of their performance in the illuminated IV-measurement to represent average OSCs per substrate. The same measurement cycle was repeated after the OSC post-treatment ($T_{pt} = 150$°C, $t_{pt} = 300$s) with the same OSCs selected for the SR as before in order to allow comparison. Unfortunately the set of SR data is not complete for some of the batches due to technical problems with the

setup. Hence it is only used to supplement the conclusions.
Of the more than 40 recorded production parameters, it was found that 15 parameters varied during the production. These variations are called unintentional variations due to reasons described in 6.1 and all had not been investigated systematically before. The following list explains all 15 production parameters, with the variables and the short names used in the tables with the PCA results (section 6.2). For ease of notation, the time intervals before and after the spin-coating processes are labelled Δt_1 to Δt_4. For the same reason, the layer index i for the evaporation is dropped, because there is only the aluminium cathode layer:

- Δt_1=Δt[UV→PEDOT-SC]: The time interval between the UV-Ozone treatment and the spin-coating (SC) of PEDOT:PSS in the cleanroom.
- Δt_2=Δt[PEDOT-SC→Oven]: The time interval between PEDOT:PSS spin-coating and putting the substrates into an oven for PEDOT:PSS drying.
- OP=Order of PEDOT-SC: In the attempt to keep the time interval between the UV-Ozone treatment and the PEDOT-SC short, the batch of eight substrates was split into 2×4 substrates for cleaning and PEDOT-SC. Each group was prepared consecutively with a delay of approximately 20min (see figure 6.2).
- $t_d(P)$=Duration of PEDOT Drying: The duration of transferring the substrates with the fresh PEDOT:PSS layer into the glovebox. During this time the substrates are kept under vacuum in the airlock of a glovebox.
- Δt_3=Δt[Airlock→Absorber-SC]: The time interval between taking the substrates out of the airlock into the glovebox and spin-coating the absorber layer.
- T_{SC}=Temperature during Absorber-SC: The temperature inside the glovebox during spin-coating the absorber layer.
- t_{sol}=Age of Absorber-Solution: The time since the preparation of the absorber solution no. 263.

- Δt_4=Δt[Absorber-SC→Vacuum]: The time interval between spin-coating the absorber layer and putting the substrates into vacuum for drying.
- $t_d(abs)$=Duration of Absorber Drying: The duration of drying the absorber layer under vacuum prior to the evaporation step.
- t_{evac}=Duration of Evaporation Vacuum: The period the substrates spent in the high vacuum ($<10^{-5}$mbar) of the evaporation chamber before the Al-cathode is deposited.
- p_{base}=Evaporation Base Pressure: The base pressure in the evaporation chamber for the deposition of the aluminium cathode.
- p_{evap}=Evaporation Pressure: The average pressure during the deposition of the Al-cathode.
- $\frac{\Delta d_{5nm}}{\Delta t}$=Aluminium Rate <5nm: The evaporation rate of the first 5nm aluminium on the absorber layer, i.e. when the hot metal atoms get in direct contact with the absorber layer.
- d_{evap}=Al-Layer Thickness: The final layer thickness of the Al-cathode.
- t_{evap}=Duration of Evaporation: The time the deposition of the Al-layer took.

These variations constitute the least number of parameters varying during OSC production and their range of variations is shown in table 6.2. Due to a temporary limitation of being able to evaporate only four substrates at a time, the first two batches were split into two sequential evaporation processes. The second evaporation process of batch 2 (4 substrates) was excluded from the analysis, because its production differed from the above described procedure in more than the selected parameters, leaving batch 2 with only four substrates. For the same reason, the complete batch 4 (8 substrates) had to be exempt from the analysis. Thus five batches lead to a total number of 36 substrates.
The parameter OP, i.e. the order of spin-coating of PEDOT:PSS, was included in the analysis, because a univariate visualisation of the power conversion efficiency η versus the duration of PEDOT:PSS drying ($t_d(P)$) revealed the only clear correlation in the whole data, which was obvious when looking

Table 6.2: *The range of variations of the production parameters. The mean values and the standard deviation σ, as well as the minimum and maximum value of the varying production parameters are given. Δ is the difference between the minimum and the maximum values. The order of PEDOT:PSS spin-coating (PEDOT-SC) is either 1 for the first or 2 for the second of the 2×4 substrates for PEDOT-SC.*

	Units	Mean	σ	Min	Max	Δ
Δt_1=Δt[UV→PEDOT-SC]	min	6.5	4.3	1	18	17
Δt_2=Δt[PEDOT-SC→Oven]	min	5.7	2.9	1	13	12
OP=Order of PEDOT-SC				1	2	
$t_d(P)$=Duration of PEDOT Drying	min	101.9	36.9	46	162	116
Δt_3=Δt[Airlock→Absorber-SC]	min	40.1	56.4	6	203	197
T_{SC}=Temp. during Absorber-SC	°C	25.4	0.8	24.3	26.6	2.3
t_{sol}=Age of Absorber-Solution	days	10.6	8.3	0.1	22.0	21.9
Δt_4=Δt[Absorber-SC→Vacuum]	min	15.2	8.8	2	40	38
$t_d(abs)$=Duration of Absorber Drying	h	27.9	4.2	23.8	38.7	14.9
t_{evac}=Duration of Evaporation Vacuum	h	18.3	1.8	14.9	20.3	5.4
p_{base}=Evaporation Base Pressure	10^{-6}mbar	1.8	0.3	1.5	2.4	0.9
p_{evap}=Evaporation Pressure	10^{-6}mbar	8.9	1.8	7.0	13.0	6.0
$\frac{\Delta d_{5nm}}{\Delta t}$=Aluminium Rate < 5nm	nm/s	0.12	0.11	0.04	0.40	0.36
d_{evap}=Al-Layer Thickness	nm	99.5	9.3	80	114	34
t_{evap}=Duration of Evaporation	s	639	210	330	915	585

only at two variables. Due to the known critical time step between UV-Ozone treatment and PEDOT:PSS spin-coating, each batch (8 substrates) was split into 2×4 substrates, in order to keep the time interval between UV-Ozone treatment and PEDOT:PSS spin-coating (Δt_1) low. Hence four substrates at a time were exposed to UV-Ozone, then spin-coated with PEDOT:PSS and dried in the oven before being transferred (still being hot) into the airlock of the glovebox. The airlock was subsequently evacuated. The second four substrates then were added to the same airlock about 20 minutes later, after going through the same process steps. All eight substrates were taken out of the airlock at the same time inside the glovebox. It turned out that the order made a difference to the OSC performance, thus the inclusion of this production detail as production parameter. As can be seen in figure 6.2, the four substrates of a batch which went first into the airlock (OP=1), tend to have a lower efficiency than the second four (OP=2). The difference between the efficiencies is caused by changes in the FF (figure 6.2, right-hand side). Due to the staggered process these differences could have been introduced at three places: during the UV-Ozone treatment, during the PEDOT:PSS dry-

ing in an oven and while opening the airlock for the second four substrates of a batch. The first two can be ruled out due to following reasons: (1) the UV-Ozone device needs no special preparation and is only used for the substrate conditioning. Any impurities would affect both the first and the set of second four substrates. (2) The temperature of the oven was checked with a thermometer and even if there were variations in temperature, the PEDOT:PSS behaviour is constant around 200°C, i.e. the used temperature for drying, and would have started to deteriorate only above 250°C [36]. The only reason left is the brief opening of the airlock to add the second four, still hot substrates. At this stage, the first four substrates have already cooled down considerably. The most likely reason is that the hygroscopic PSS accumulates water at its surface, deteriorating the interface. This however does not change the workfunction of the PEDOT:PSS layer, because the open circuit voltage V_{oc} was hardly affected at all by OP. What has been negatively affected appears to be charge transfer probability at the interface, probably due to a barrier. OP shows a clear tendency with the FF within one batch, but the majority of the variations are due to causes which will be investigated later in this chapter.

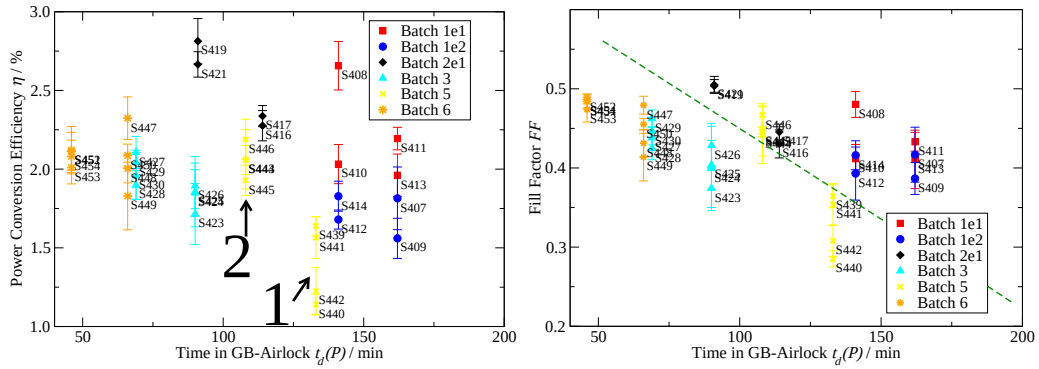

Figure 6.2: *The power conversion efficiency η (left) and the fill factor FF (right) versus the time the substrates spent in the airlock on their transfer into the glovebox (46-162min). The absolute time spent in the airlock appears to have less effect on η than the order in which the substrates were put into the airlock, as indicated using batch 5 as example. "1" denotes the first four substrates, which subsequently spent more time in airlock than the second four ("2"). The variations in η between the first and second four substrates of a batch are due to significant changes in FF. The dashed line in the right hand graph is a guide for the eye. The short circuit current density J_{sc} is affected little and the open circuit voltage V_{oc} hardly (not shown).*

Any influence during the production process, which is difficult to quantify or to incorporate into the data analysis was carefully considered and reduced as much as possible. Each manual step was assigned to a specific experienced experimenter such that the manual steps remained as consistent as possible. All substrates were taken from the same ITO-glass batch and structured in the same batch. During data cleaning all production parameters in questions were resolved and no data of any substrate had to be excluded due to unknown or obviously wrong entries. The data cleaning procedure is described in section 5.3.1.

Summary

- 360 OSCs on 36 substrates were made in five batches (4×8 and 1×4 substrates). It has been found that the smallest set of variations during production consists of 15 parameters out of the more than 40 recorded ones and are subject to unintentional variations.

- For 14 of the 15 considered production parameters the unintentional variations cannot be avoided due to the nature of the production process or the human factor. The set of parameters consists e.g. of the time intervals between production steps involving spin-coating, which vary due the combination of batch and sequential processing, the temperature during spin-coating of the absorber and the parameters of the manually controlled evaporation of the aluminium cathode.

- The splitting of one batch (8 substrates) into 2×4 substrates for the spin-coating of the PEDOT:PSS layer, additionally made an extra parameter (OP) for their order necessary, because it affected the OSC properties. The first four substrates had a reduced FF, which is most likely due to their exposure to ambient conditions after they had cooled down. This parameter can and will be avoided in future by using a second airlock for transferring the substrates into the glovebox after spin-coating of the PEDOT:PSS layer.

- Variations in OP cannot explain all variations in η, because even when removing the substrates, which are negatively affected by OP, the range of variations in the power conversion η would only reduce from 1.1%↔2.8% to 1.7%↔2.8%.

Table 6.3: *Summary of the data pruned prior to analysis of the annealed OSCs. The numbers of excluded OSCs (74 out of 360) are shown grouped with their respective batch ("B"). Batch 1 and 2 were split into 2 evaporation processes ("e"). The OSCs were excluded, because their abnormal characteristics can be explained by obvious defects like scratches rather than variations in the production process. For only five OSCs, the type of defect could not be determined. In cases, when a combination of exclusion categories is observed, e.g. a non covered OSC due to a bubble, the OSC is only counted once. The complete overview with details on every substrate can be found in the appendix on pages 188 and 189.*

	B1e1	B1e2	B2e1	B3	B5	B6
Not covered	1	2	1	-	-	2
Bubbles	1	2	-	-	-	2
Scratches	5	2	-	5	2	1
Particles	1	1	3	4	3	6
Contact Problems	1	3	4	5	10	2
Unknown	-	-	-	2	2	1
Remaining/maximum OSCs	31/40	30/40	32/40	64/80	63/80	66/80

6.1.2 Measurement Results

Before analysing the measurement results, the data was cleaned as described in section 5.3.1. A total of 74 of the 36×10 OSCs, i.e. 21%, had to be excluded from the analysis and the summary is shown in table 6.3. One substrate of batch 5 (S 445) lost five OSCs due a contact problem affecting the interconnection of one complete Al-cathode (see section 4.2.1) explaining the high number of contact problems in this batch. A more detailed table, describing each substrate with its working/excluded OSCs and averages from its working OSCs can be found in the appendix on pages 188 and 189.

Despite keeping the majority of the parameters fixed during production, the IV measurement results averaged per substrate for the annealed OSCs show a high spread. The average power conversion efficiency η for each substrate versus the open circuit voltage V_{oc}, short circuit current density J_{sc} and the fill factor FF is shown in figures 6.3 and 6.4 with their respective standard deviations[1]. The substrates from each production batch appear to form clusters, but even within one seemingly similar batch the differences are considerable. The largest variations are observed in FF (0.29±0.01 to 0.50±0.01).

[1]Due to defects, not all substrates have the same number of working OSCs, the values of which were used for the calculation of averages and standard deviations.

Batches 1e1 and 1e2 were split at the evaporation process and form two different clusters in the scatter plots. However, at this point it is not possible to attribute the difference solely to the evaporation process, because 1e1 and 1e2 differed in absorber drying times ($t_d(abs)$) as well. Furthermore, from the scatter plots it is evident that there have to be more parameters with an influence on the shown OSC IV properties, than the parameters of the evaporation process. Even substrates, which were evaporated in the same evaporation process, exhibit a significant spread. The dependence of production parameters and OSC properties will be discussed in section 6.2 using a principal component analysis.

The histogram in figure 6.4 is based on the efficiencies of all 286 OSCs used in the analysis. The average η using all 286 OSCs is 2.0±0.4%. The long tail in the histogram indicates that apparently no fundamental upper limit of η has been reached and there is much room for improvement. The range of the obtained results is summarised in table 6.4. The physical aspects of the differences, both between substrates and between the OSCs on one substrate, will be discussed in the following sections.

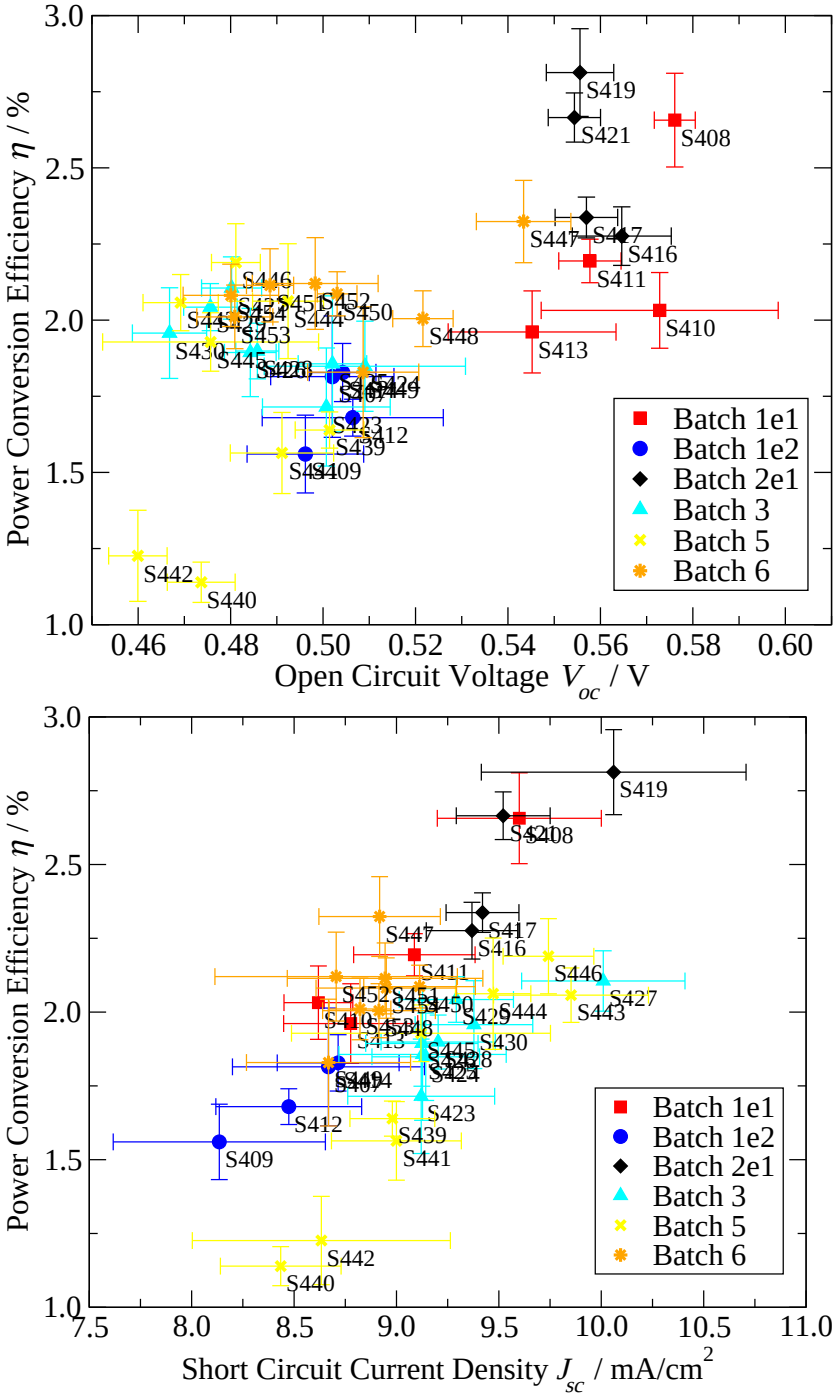

Figure 6.3: *Two scatter plots showing the average values (symbols) and the standard deviations (error bars) of the power conversion efficiency η versus the open circuit voltage V_{oc} and the short circuit current density J_{sc} respectively for each of the 36 substrates after post-treatment. Batch 1 had to be split into two evaporation processes (e1, e2) and the data has been cleaned as described in 5.3.1. The batches appear to form clusters, but the overall spread is significant, despite only considering parameters, which had not been investigated systematically before.*

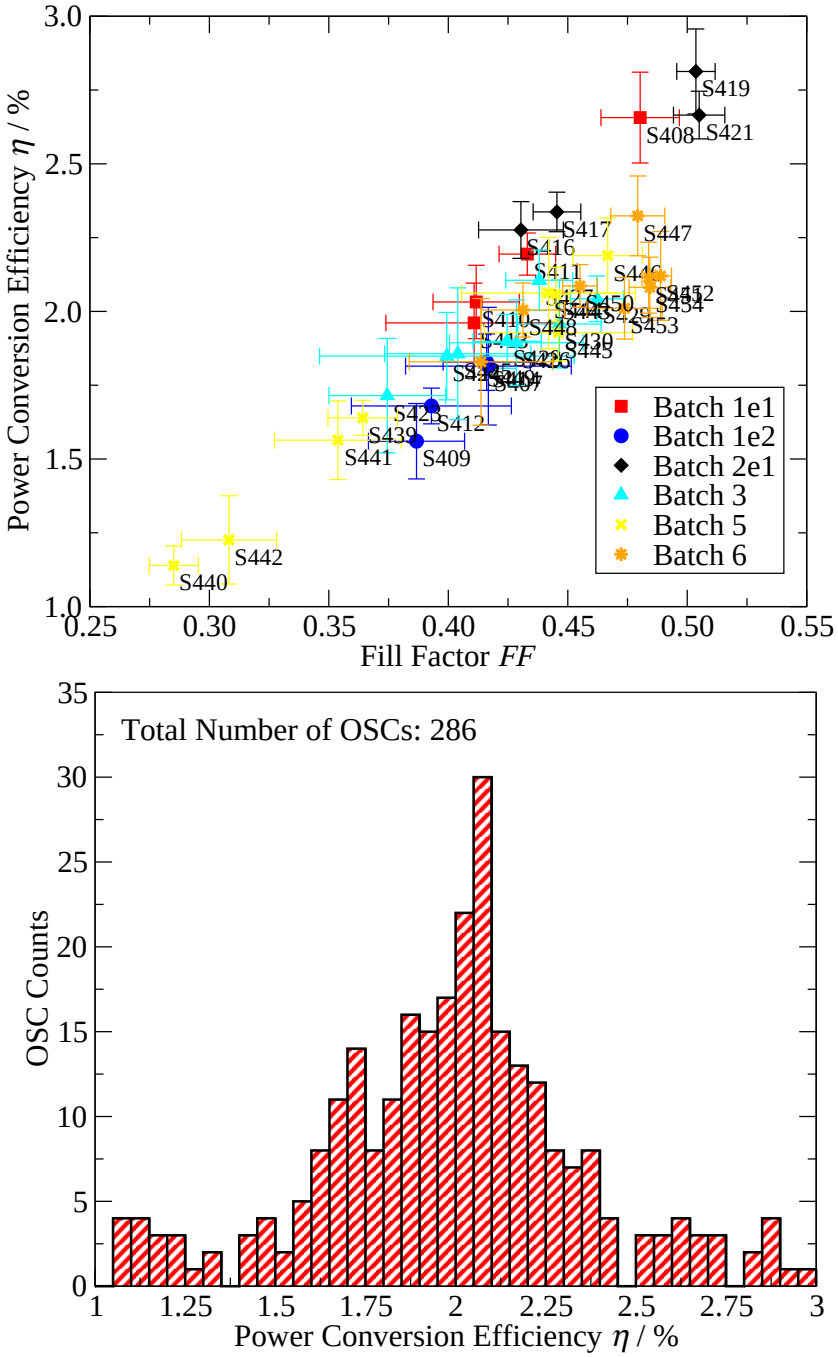

Figure 6.4: *One scatter plot showing the average values (symbols) and the standard deviations (error bars) of the power conversion efficiency η versus the fill factor FF for each of the 36 substrates after post-treatment. Batch 1 had to be split into two evaporation processes (e1, e2) and the data has been cleaned as described in 5.3.1. The FF exhibits the highest variations of the main OSC properties. Also, the linear relation between FF and η is apparent. The histogram shows the distribution of efficiencies from the same data for every working OSC.*

Table 6.4: *The range of the OSC properties obtained for the 36 substrates. Shown are the values for the open circuit voltage V_{oc}, the short circuit current density J_{sc}, the fill factor FF and the position of the first minimum in the absorption spectrum averaged of over all substrates, as well as the best and worst substrate with its values. Δ is the absolute difference between the two extremes.*

	Average	Min	Max	Δ
V_{oc} / V	0.51±0.03	0.46±0.01 (S 442)	0.58±0.00 (S 408)	0.12
J_{sc} / mA/cm^2	9.1±0.44	8.1±0.5 (S 409)	10.1±0.7 (S 419)	1.9
FF	0.43±0.05	0.29±0.01 (S 440)	0.50±0.01 (S 421)	0.21
η / %	2.0±0.3	1.1±0.1 (S 440)	2.8±0.1 (S 419)	1.7
1^{st} Abs Min / nm	357±2	353±1 (S 449)	363±1 (S 419)	10

Table 6.5: *An overview of the standard deviations σ of the open circuit voltage V_{oc}, short circuit current density J_{sc}, fill factor FF and power conversion efficiency η of the 36 substrates in terms of percent of the average value. Shown is the number of substrates, the σ of which is less than 1%, 2%, etc.. The table shows that σ for V_{oc} is always less than 5% of the mean, whereas for the other OSC properties σ is larger.*

σ in % of mean	V_{oc}	J_{sc}	FF	η
≤1%	3	0	2	0
≤2%	24	4	6	0
≤3%	31	10	11	1
≤4%	33	26	19	7
≤5%	36	29	23	14
≤7.5%	36	36	29	25
≤10%	36	36	35	31
≤14%	36	36	36	36

6.1.3 Discussion of the experimental Results

Origin of the Variations per Substrate

Variations of the OSC characteristics on one substrate set the lower limit of the achievable variations, because these OSCs have seen exactly the same production steps including the same time intervals. The OSCs on the same substrate are rather reproducible, especially the position of the first absorption minimum (σ<1.5nm for 89% of the substrates) and V_{oc} as table 6.5 shows. The variations in V_{oc}, J_{sc} and FF subsequently lead to the variations in η.

The small relative variations in V_{oc} within a substrate show that the contact

properties do not change much per substrate. Thus the interfaces on either side of the absorber layer, i.e. PEDOT:PSS anode and aluminium cathode, can be considered rather uniform on the same substrate. Differences in the PEDOT:PSS workfunction across the substrates would immediately be reflected in the V_{oc}, whereas changes in the workfunction of Al at the interface can not be ruled out, because V_{oc} is only very weakly dependent on the metal workfunction [20]. Different contact barriers for charge injection and extraction would only be seen in V_{oc} in the extreme cases.

Variations in J_{sc} substrate-wise are slightly larger (see table 6.5). The short circuit current density J_{sc} reacts very sensitively and in a non-linear way to variations in the thickness of the absorber layer due to the optical interference pattern formed by reflections off the aluminium cathode [65]. The average standard deviation σ for the position of the first absorber minimum, a measure for the thickness of the absorber layer, per substrate is 1.0nm (σ_{min}=0.3nm, σ_{max}= 2.2nm). However, a clear relation between absorption minimum and J_{sc} within substrates is not observed. Other factors like morphological differences or particles in the photovoltaic active area might play a more important role, but are difficult to quantify and give rise to several uncertainties. The current density was computed under the assumption that the photovoltaic active areas of all OSCs is 5.3mm^2 and that area is given by the overlap between the ITO bottom electrode and the Al top electrode. It is however possible that during production the pattern of the two electrodes does not match as shown in figure 4.8 on page 72. This can happen because the ITO is structured on plates containing 36 substrates, which have to be cut manually into 25×25mm^2 pieces. Cutting the glass at an angle or not along the right line shifts the ITO pattern with respect to the evaporated aluminium pattern. The 25×25_10 layout (see figure 4.8) can only correct for a certain amount of offset. However, this could only explain some of the variations, because typically all OSCs on a substrate would be affected by a reduction of the photovoltaic active area if the pattern of top and bottom electrode does not align.

The FF exhibits the highest variations per substrate. By comparing the variations in J_{sc} with those of FF no correlation is seen and the variations in FF appear to be of different origin than the variations in J_{sc}. However, even though V_{oc} varies much less per substrates, the variations between FF and V_{oc} weakly correlate. This suggests that some variations have the same

origin, e.g. interface properties. The FF furthermore reacts very sensitively to changes in mobility, which is related to the morphology in the device.

Variations between Substrates

As the scatter plots in figures 6.3 and 6.4 show, there are on the one hand good OSCs with an η approaching 3%. On the other hand there are poorly performing OSCs, for which the fill factor FF is due to a kink in the fourth quadrant below 0.3 and the resulting efficiencies reach only around 1%. Three representative IV-curves covering the spread in η are shown in figure 6.5 with the corresponding values given in table 6.6. Using these three examples, particular effects causing the variations in η are explained in the following sections.

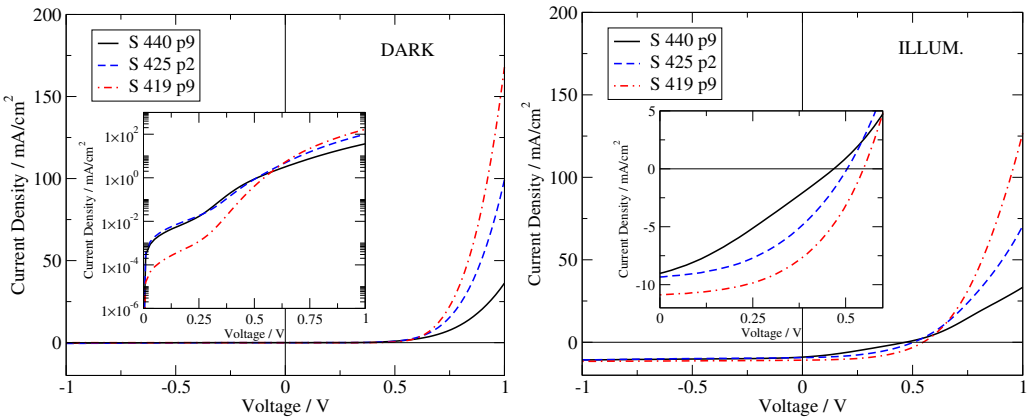

Figure 6.5: *Three representative IV-curves (annealed) from data covering the efficiency range between 1% and 3%. The left-hand side figure shows dark measurements. The inset here presents the positive voltages in a logarithmic scale. A two-diodic-like behaviour is clearly visible. Measuring the illuminated IV-curves of the same OSCs lead to the right-hand side figure. Here the fourth quadrant is shown enlarged as inset. The most notable difference is the FF, which is less than 0.3 for OSC S 440 p9 and reaches 0.50 for OSC S 419 p9. The corresponding OSC properties are shown in table 6.6.*

The variations in the shown OSC properties are substantial. Although the organic layers (PEDOT:PSS and absorber) on the substrates were always spin-coated with the same spin-coating speed, the absorption spectra differ between substrates as shown in figure 6.6, indicating a different layer thickness. The shift of about 10nm of the first absorption minimum would be equivalent to a difference of about 15nm in the absorber layer thickness. The

Table 6.6: *The main characteristics of the OSCs, the IV-curves of which are shown in figure 6.5. Three representative OSCs were chosen to cover the range of power conversion efficiency η from about 1% to 3%. The physical origin of the observed features will be discussed in turn in section 6.1.3.*

	V_{oc} / V	J_{sc} / mA/cm^2	FF	η / %	Pos of 1st Abs-Min / nm
S 440 p9	0.47	9.0	0.30	1.3	357
S 425 p2	0.50	9.3	0.44	2.1	353
S 419 p9	0.55	10.9	0.50	3.0	363

cause of these differences is not clear yet. Neither a correlation with the temperature during spin-coating (T_{SC}) nor with the age of the solution (t_{sol}), e.g. through a change in viscosity with age, was observed. Different wetting properties of the surface onto which an organic layer is spin-coated cannot be excluded as possible cause. This has to be confirmed with a separate batch, which needs to be characterised with absorption, transmission and AFM measurements. This, however, was not possible during the course of this work. The external quantum efficiencies in figure 6.6 are not representative for η, but indicate, which part of the absorption spectrum contributes to J_{sc}.

Low Efficiency: The OSCs on substrate S440 (batch 5) exhibit the lowest FF and the lowest efficiencies of the made substrates in the experimental series (see table 6.7). The most prominent feature of these OSCs is the pronounced kink of the IV-curves in the fourth quadrant, a considerable deviation from the ideal exponential shape, and a very low current at +1V forward bias. The kink leads to a significant reduction of FF and also affects V_{oc} and J_{sc} negatively thus severely degrading the power conversion efficiency η. Such a small FF can be observed for space charge limited current, to which organic semiconductors are prone due to their low charge carrier mobility. Space charge limited current is observed, when the low mobility leads to a built up of charge carriers, which is not neutralised by the equal number of opposite charge carriers. This accumulated charge reduces the externally applied electric field, i.e. one of the driving forces of the charge carriers, thus slowing down the current flow. In bulk heterojunction organic solar cells the photovoltaic active region consists of an intimate mixture of P3HT and PCBM. In this blend, the hole mobility μ_h is typically at least an order of

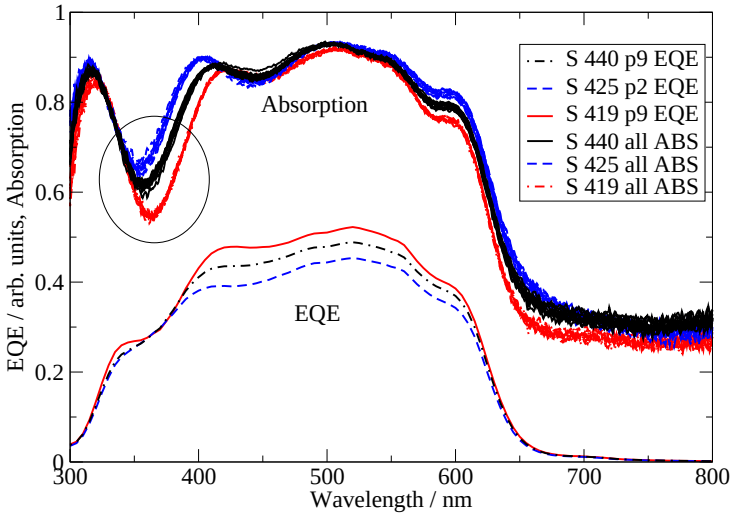

Figure 6.6: *The external quantum efficiency (EQE) for the same OSCs as shown in figure 6.5 and the absorption spectra (ABS) of all OSCs on the corresponding substrates. The OSCs per substrate have nearly the identical absorption spectrum, but the difference between the three substrates, especially the difference in the position of the first absorption minimum around 350nm (circled) indicates different film thicknesses, despite the same spin-coating speed for the absorber layer. The shape of the EQE shows similar features, but is currently not representative of the power conversion efficiency η due to problems with the measurement method (see section 4.1.2).*

magnitude lower than the electron mobility μ_e. It has recently been shown that space charge photocurrent can already occur at 1 sun illumination, if the mobilities of holes and electrons differ by two orders of magnitude or more. In the space charge limit the FF is not able to exceed 0.43 [14, 93]. Thus in order to analyse the physical origin of the small fill factor, the curves were analysed for space charge limited photocurrent. The photocurrent density J_{ph} is defined as

$$J_{ph} = J_{dark} - J_{ill}, \tag{6.1}$$

where J_{dark} and J_{ill} are the current densities in the dark and under illumination respectively. In the ideal case, the mean charge carrier drift length $w = \mu\tau E$ exceeds the device thickness L and all photogenerated charge carriers are extracted and J_{ph} saturates at $e\mathcal{G}L$ assuming homogeneous charge carrier generation. μ is the charge carrier mobility, τ their lifetime, E the electric field and $\mathcal{G}$ the optical generation rate of electron-hole pairs. However, if w of either charge carrier is smaller than L, a space charge will form

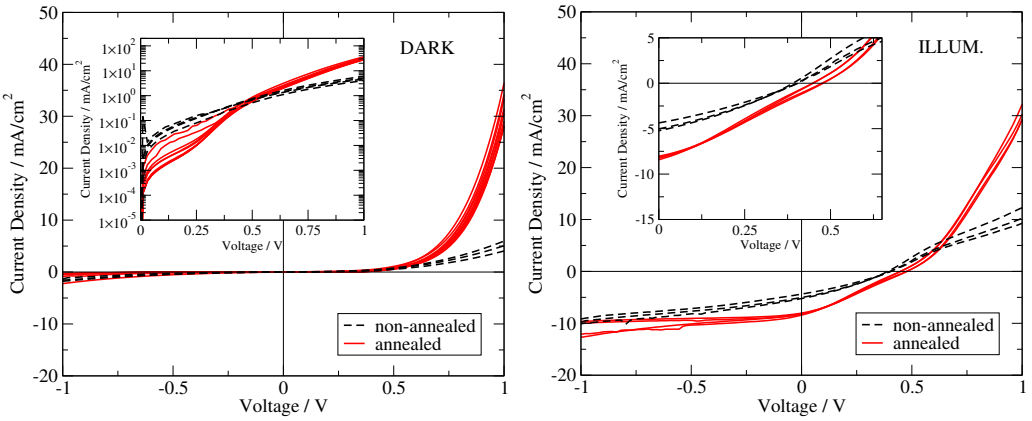

Figure 6.7: *Dark and illuminated IV curve of the working OSCs on substrate S 440. The detrimental feature is the kink in the IV-curve between 0 and 0.6V, which drastically reduces the power conversion efficiency η.*

and the increased recombination will have a significant effect on J_{ph}. In OSC the hole mobility μ_h is typically at least one order of magnitude lower than the electron mobility μ_e and if w_h is smaller than L, holes will to a larger extent accumulate in the device, making the applied E non-uniform. In steady state most of the voltage drop V will occur over a region L_1 at the anode at which the hole accumulate, where L_1 is given by the mean drift length of the hole w_h. In that case, almost all photogenerated current is generated within L_1 and

$$J_{ph} = e\mathcal{G}L_1 = e\mathcal{G}(\mu_h\tau_h)^{1/2}V^{1/2}. \tag{6.2}$$

The accumulated holes will not be neutralised at the anode by an equal amount of electrons, thus leading to space charge. If the photogenerated current equals or exceeds the space charge limited current

$$J_{scl} = \frac{9}{8}\epsilon_0\epsilon_r\mu_h\frac{V^2}{L_1^3}, \tag{6.3}$$

then the photogenerated current is space charge limited [93]. In equation 6.3 $\epsilon_0\epsilon_r$ denotes the dielectric permittivity. If $J_{ph} = J_{scl}$, then the maximal photocurrent density is

$$J_{ph} \propto \mathcal{G}^{3/4}V^{1/2}. \tag{6.4}$$

Equations 6.2 and 6.4 both predict a square root dependence of I_{ph} on V, but a different dependence on the generation rate $\mathcal{G}$. Defining V_0 as the

compensation voltage where the dark and the illuminated IV-curves intersect, i.e. where $J_{ph} = 0$, the dependence of the photocurrent J_{ph} on the effective voltage $V - V_0$ can be visualised (figure 6.8). Although no intensity dependent IV-curves of non-annealed OSCs were recorded, figure 6.8 shows that the $1/2$ power dependence on the bias voltage (indicated by dotted line) is not given. This implies that neither the mean hole drift length w_h is smaller than L (which would lead to equation 6.2) nor the measured photocurrent exhibits the signatures of a space charge limited photocurrent, which should have been observed between the indicated positions of J_{sc} and V_{oc}. As expected, the $3/4$ power dependence on $\mathcal{G}$ has subsequently not been observed for J_{ph} at V=0V in this sample (figure 6.8, right-hand side). Instead, a slightly sublinear dependency between intensity and J_{sc} is seen. However, as J_{sc} is only little affected by recombination, it is not possible to deduce the dominant charge carrier recombination mechanism [40, 41].

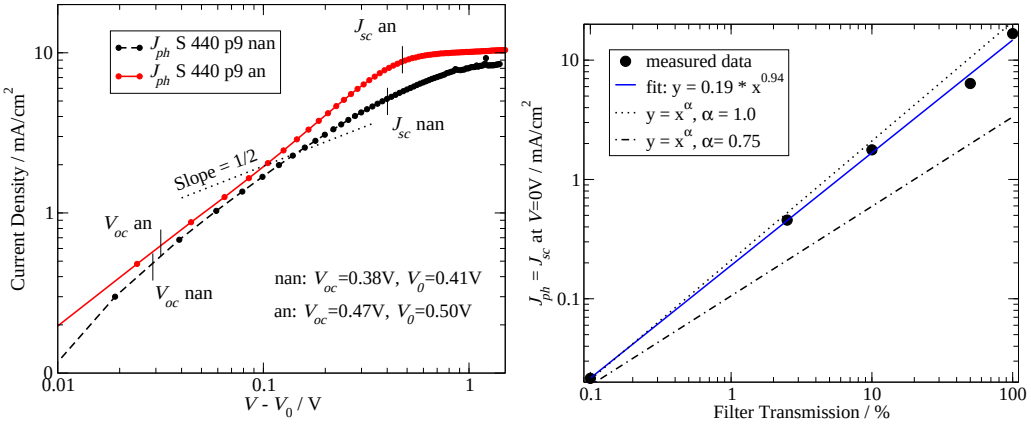

Figure 6.8: *A loglog-plot of the photocurrent J_{ph} versus the effective voltage V-V_0 for the non-annealed (nan) and annealed (an) case (left figure). V_0 is the voltage at which dark and illuminated IV-curves intersect. Furthermore the intensity dependence of J_{sc} for the annealed case is plotted in the right figure. There is not indication of space charge limited photocurrent characteristics (slope $1/2$ between V_{oc} and J_{sc}), neither in the non-annealed case nor indication in the annealed case. The intensity dependence of J_{sc} of the annealed sample is slightly sublinear with an exponent $\alpha = 0.94$.*

Thus, even for the worst OSC considered the mean hole drift length w_h is large enough with respect to L, i.e. the thickness of the absorber layer and the photocurrent not limited by space charge. Hence, the kink in the fourth quadrant is of another origin.

Table 6.7: *The main OSC properties of substrate S 440. The table shows the non-annealed and annealed averages for the number of working OSCs on the substrate. Δ gives the percentage change with respect to the non-annealed values.*

	S 440 non-annealed	S 440 annealed	Δ / %
No of working cells	6	8	
V_{oc} / V	0.38±0.02	0.47±0.01	+24
J_{sc} / mA/cm^2	4.8±0.3	8.4±0.3	+75
FF	0.31±0.02	0.29±0.01	-6
η / %	0.6±0.1	1.1±0.1	+83

In reference [14] the authors do not state the solvent of the absorber solution. However, from the increase in photocurrent and absorption they observe, the solvent was most likely a fast evaporating, i.e. low boiling point, solvent, leading to disadvantageous morphology in the non-annealed state. Their measured hole mobility was below 10^{-7}cm^2(Vs)$^{-1}$, whereas the electron mobility was three orders of magnitude higher. The absorber solution 263, with which substrate S 440 was prepared, however uses DCB as solvent, which has a high boiling point (180°C). Thus the morphology in the non-annealed case is already more advantageous and the hole mobility μ_h is already sufficiently high as not to lead to space charge limited photocurrent.

The slope of J_{ph} between the indicated J_{sc} and V_{oc} is nearly 1 in the annealed case, indicating that in this region J_{ph} is approximately proportional to V. In reverse bias, all photogenerated charge carriers are extracted and J_{ph} as well as J saturates, excluding a shunt resistance a possible cause. At forward bias J_{ph} has a linear relationship with $V - V_0$ until the electrode start to inject charges. Substrate S 440 belongs to the four substrates of batch 5, which were spin-coated with PEDOT:PSS first, i.e. OP=1. Figure 6.2 clearly shows a correlation between OP and the FF. Substrates with OP=1 were exposed to ambient conditions after they have cooled down from the PEDOT:PSS drying temperature, which apparently has a detrimental effect on the FF. This suggests that the PEDOT:PSS interface might have degraded. Subsequent impedance spectroscopy measurements additionally indicate an barrier at the Al-interface which affects charge extraction [94]. Simulations have indeed shown that the kink in the IV-curve can be reproduced by lowering the transfer probability of electrons into the cathode. Whereas at J_{sc} the built-in potential is still large enough to drive the electrons across the Al interface,

increasing the bias in forward direction reduces the electric field in the device. Subsequently, the charges are less likely to cross the barrier and an increasing number of charge carriers remains in the device in steady state. They start to recombine at a bias voltage, where the contacts do not inject yet, leading to a significant reduction in J, i.e. a deviation from the good diodic behaviour. The current density J follows a near linear trend both before the electrodes start to inject and after the electrode inject (above approx. 0.6V). This is a strong indication of a low transfer rate from electrons into the absorber layer.

Medium Efficiency: Substrate S 425 (batch 3) is an average substrate with a power conversion efficiency η of 1.9±0.2%. The other properties can be found in table 6.8.

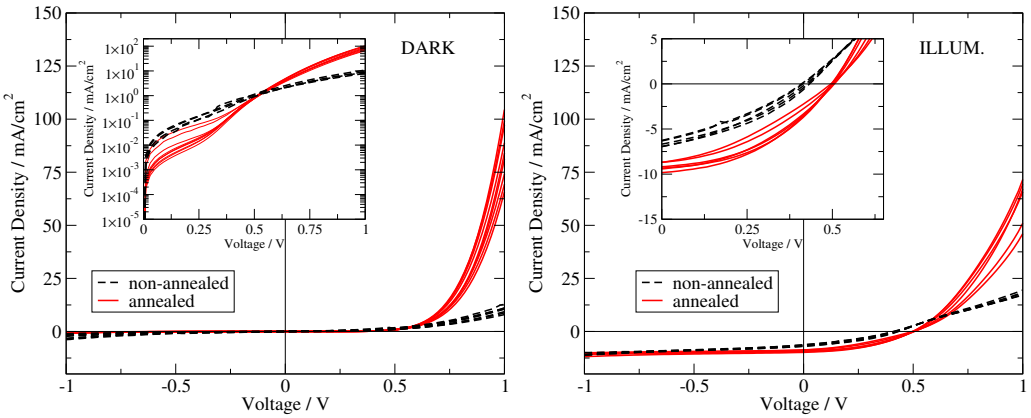

Figure 6.9: *Dark (left) and illuminated (right) IV-curves of the working OSCs on substrate S 425. The insets show a log-plot of the current in dark and a close-up of the photovoltaic region under illumination. In the non-annealed case, the charge injection from the electrodes is poor, leading to a turning point at* $V \approx 0.6\,V$.

The fill factor FF is significantly higher than in the previous substrate (S 440) and there is no kink in the fourth quadrant. However, two features both substrates share is that in the non-annealed case the devices do not block in reverse bias and at forward bias in the non-annealed case a turning point is visible at around 0.6V under illumination.
The turning point and the low current in forward bias in the non-annealed case might indicate that the aluminium of the cathode has a too high work-function, which is then closer to the P3HT HOMO than to the PCBM LUMO.

Table 6.8: *The main OSC properties of substrate S 425. The table shows the non-annealed and annealed averages for the number of working OSCs on the substrate. Δ gives the percentage change with respect to the non-annealed values.*

	S 425 non-annealed	S 425 annealed	Δ / %
No of working cells	8	9	
V_{oc} / V	0.42±0.02	0.50±0.01	+19
J_{sc} / mA/cm^2	6.6±0.5	9.1±0.4	+38
FF	0.33±0.03	0.40±0.03	+21
η / %	0.9±0.2	1.9±0.2	+111

Thus charge injection is severely inhibited in forward bias, but current extraction from the device is only little affected. The turning point around 0.6V disappears during annealing and the current density increased by nearly an order of magnitude at 1V forward bias. The barrier, which inhibited charge injection in the non-annealed case, is apparently reduced significantly and consequently, the electrodes can supply more current at the same bias voltage.

The opening of the diode in reverse bias might be due to small defects in the absorber layer, which enable charge carriers to pass through. This also implies that parts of the electrode are failing, because charges are injected. If the workfunction of the aluminium in the non-annealed case is too high, the current could originate from hole injection from the Al-cathode via one-electron states in the band gap caused by these effects.

The physical origin of the turning point at about 0.6V and the opening of the diode in reverse bias is subject to current discussions and investigated by electrical device simulations.

High Efficiency: The OSCs on substrate S 419 (batch 2e1) already show in the non-annealed state a good diodic behaviour with no apparent opening of the diode in reverse bias as shown in figure 6.10 (left). The OSC properties for the non-annealed and annealed case are given in table 6.9.

Something, which has been observed throughout batch 2e1, but for no other batch, is the decrease of the V_{ov} upon annealing. For substrate S 419, the V_{oc} dropped from 0.65V to 0.56V, i.e. nearly 100mV. In darkness, the interfaces start to inject earlier in the annealed than in the non-annealed case when going to forward bias. This is also visible for the illuminated case. The

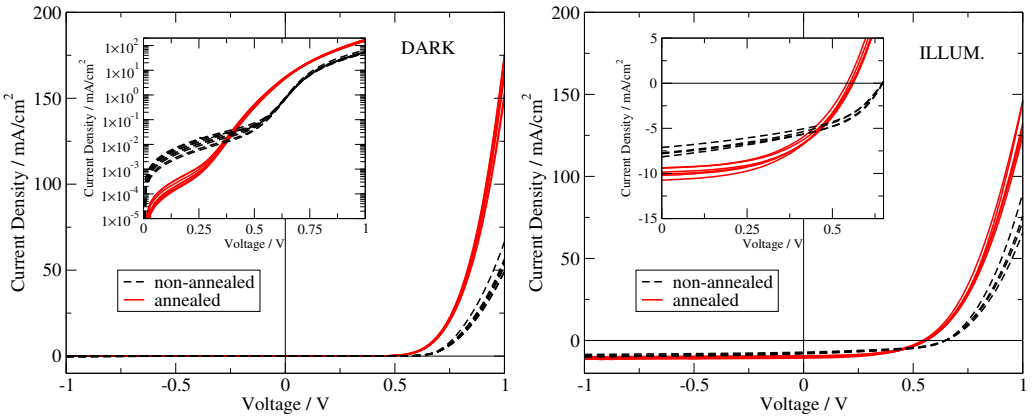

Figure 6.10: *Dark (left) and illuminated (right) IV-curves of the working OSCs on substrate S 419. The insets show a log-plot of the current in darkness and a close-up of the photovoltaic region under illumination respectively. The OSCs of S 419 already in the non-annealed state exhibits a good rectifying behaviour. Upon annealing the electrodes start to inject charges at a lower bias than in the non-annealed state and V_{oc} is reduced under illumination. However, the improvements in J_{sc} and FF outweigh this effect and as a consequence the average efficiency rises from 2.3 to 2.8%.*

Table 6.9: *The main OSC properties of substrate S 419. The table shows the non-annealed and annealed averages for the number of working OSCs on the substrate. Δ gives the percentage change with respect to the non-annealed values. The negative change in V_{oc} upon annealing is only observed in this batch.*

	S 419 non-annealed	S 419 annealed	Δ / %
No of working cells	5	6	
V_{oc} / V	0.65±0.00	0.56±0.01	-14
J_{sc} / mA/cm^2	7.8±0.4	10.1±0.7	+29
FF	0.46±0.02	0.50±0.01	+9
η / %	2.3±0.1	2.8±0.1	+22

physical origin of this behaviour of the decreasing V_{ov} upon annealing can be explained as follows. It is well known that the electron and hole mobilities in the absorber can improve by up to several orders of magnitude during annealing [14]. The OSCs of substrate S 419 already showed in the non-annealed case a good diodic behaviour, i.e. they had good interfaces and no shunts which would have a detrimental effect on the curves. However, with the low mobility of the charge carriers, under steady state conditions there are more charge carriers in the device than in the annealed case. The

increased charge carrier density leads to an increased splitting of the QFL (see equation 2.9) and thus a higher V_{oc} is possible in the non-annealed case. After annealing, the mobility of the charge carriers is increased and they do not remain as long in the device as before, thus reducing the charge carrier density and the splitting of the QFL. V_{oc} is reduced, but the overall efficiency still increases, due to an improvement in J_{sc} and FF.
It is yet not understood why the substrates from this batch had this behaviour. Their absorber layer dried very long in the vacuum and in the evaporation chamber, but these time intervals for batch 6 were longer. Only the duration of evaporation is the shortest (315s) for batch 2e1. Still, the duration of evaporation for batch 1e1 was only 15s longer and did not show a drop in V_{oc} upon annealing. In literature both behaviours can be found, e.g. for dropping V_{oc} upon annealing see reference [95] and for an increasing V_{oc} see reference [96], but neither comment on the change in V_{oc}.
OSCs, which do not exhibit a good diodic behaviour in the non-annealed case, do not show this effect, because shunts have an adverse effect on the V_{oc} which dominates. During post-treatment, these shunts are burnt out and the V_{oc} rises, i.e. this improvement outweighs the decrease in V_{oc} due to an increased charge carrier mobility.

6.1.4 Conclusions

- Despite the variations of the least number of production parameters possible, it was found that the spread in the OSC properties is much larger than the expected. For a reproducible production process variations in the power conversion efficiency η of $\pm 10\%$ around the mean, i.e. here $(2.0 \pm 0.2)\%$, would be reasonable, but a spread of nearly $\pm 50\%$ around the mean was obtained ($1.1\% \leq \eta \leq 2.8\%$). The largest variations are seen in the fill factor FF, which varies between 0.29 and 0.50. The variations in V_{oc} and J_{sc} were 0.46-0.58V and 8.1-10.1mA/cm^2 respectively.

- FF is the key parameter governing the power conversion efficiency η in the experiments. Improving the FF from the obtained values to 0.6, which is often reported in literature, will lead to an $\eta > 3.5\%$.

- The production parameters, which unintentionally varied in this set of experiments, are hardly mentioned in literature, but introduced a

significant spread in the measured OSC properties. This puts the results published in literature into a new light, if only the results of a few OSCs without shown significance are presented, and stresses that a high number of experiments has to be conducted to verify the effects observed in OSCs.

- V_{oc} appears to be the most reproducible property of the OSCs on the same substrate.

- The variations in J_{sc} per substrate are likely due to a combination of morphological effects and particles in the absorber layer, although variations resulting from errors in the active area cannot be excluded.

- The FF of the OSCs on the same substrate varies most. It is affected by both the transfer rates at the contacts and the charge carrier transport through the blend of P3HT and PCBM, which is highly dependent on the morphology, i.e. the way P3HT and PCBM arrange during drying and annealing of the absorber. This is consistent with the fact that the morphology might change within a substrate.

- The lowest observed FF cannot be explained by space charge limited current which is often observed in organic semiconductors. Rather, limitations from the interfaces are thought to cause the found characteristics, with contributions from both aluminium and PEDOT:PSS interface. Subsequent impedance spectroscopy measurements seem to confirm this assumption.

- J_{sc} scales slightly sublinear with light intensity even for the worst OSCs. Thus recombination only plays a minor role at short circuit conditions and no conclusions can be drawn on the dominant recombination mechanism.

- V_{oc} increases upon annealing on average by 70mV. Then the behaviour of non-annealed IV-curves is dominated by shunts, which are reduced during annealing. If the non-annealed IV-curves show a good diodic behaviour V_{oc} can fall up to nearly 100mV due to the increase of the mobility and the subsequently reduced splitting of the QFLs in the device. In both cases V_{oc} ends up in the same region for the annealed devices.

6.2 Principal Component Analysis

The main observed phenomena in the measured OSCs and their underlying physics presented in section 6.1 can qualitatively be explained, but it is difficult to identify a dependency between specific production steps and the OSC properties. All substrates differ in not only one production parameter at a time, but several. In order to analyse the correlations between the production parameters and the OSC properties, the principal component analysis (PCA, see section 5.1.3) is used. The aim is to find out where the observed variations in the OSC properties come from in the production process, and to systematically determine the correlation between the OSC properties and the production parameters.

During production, the majority of the production parameters could be kept constant and only a limited set was subject to unintentional variations (see section 6.1.1). As the data is not commensurate, i.e. differs in scale and variances, the correlation matrix $\mathbf{R}$ (see section 5.1.3) is used for all PCAs in this section and only the measurement data from annealed OSCs is used. Through a diagonalisation of $\mathbf{R}$ one obtains the corresponding eigenvectors $\hat{\mathbf{e}}_\alpha$ and eigenvalues λ_α. The eigenvectors are called principal component vectors (PCV) and form the basis of the new coordinate system, into which the original data is transformed. The new variables describing the data are called principal components (PCs) and are linear combinations of the original variables. The PCs are sorted by descending eigenvalue λ_α, which is a measure of the information content of a PC.

When interpreting the results of a PCA, the high dimensionality of the space must be kept in mind. Considering the largest contributions of a PCV in order to explain a trend can only be considered to be a 0^{th} order approximation. To move parallel to one PC, all components have to be considered simultaneously according to their weight.

Assuming that all important production parameters were included in the analysis, it should be possible to trace the origin of the variations in OSC properties back to the unintentional variations of a particular production process (see section 6.1). Understanding these effects will eventually allow an adjustment of those production parameters, such that they have a positive effect on OSC performance. Furthermore, if additional intentional variations of production parameters are introduced, it should be possible to separate

observed effects into originating from unintentional variations and intentional variations.

6.2.1 Correlation between Production Parameters

When interpreting the results of a PCA including production parameters and measurement result, correlations between the production parameters alone have to be taken into account. Thus, as a first step a PCA was performed on the 15 production parameters only. If the production parameters were all independent variables, the principal components would be nearly the original variables. However, despite trying to avoid correlations between production parameters by carefully planning and adjusting the parameters for compensation, the PCA reveals several correlations, as seen from table 6.10. It shows the first 6 of the total 15 PCVs the PCs of which contain more than 89% of the variance in the data set. The table shows as row and column header the original variables and the new variables, i.e. principal components (PCs), respectively. The matrix in the table is the matrix $\mathbf{\Gamma}$, which describes the transformation between the original variables and the PCs. The columns of $\mathbf{\Gamma}$ correspond to the normalised eigenvectors of the correlation matrix $\mathbf{R}$ of the OSC data, i.e. they are the PCVs. Looking at the PCV of a PC, the contribution of an original variable to the PC can be seen.

If two parameters in one PC exhibit the same sign, their corresponding production parameters are correlated. When one of the two was changed in one direction for a substrate the other parameter was changed into the same direction. This leads to a correlation which is picked up by the PCA during the analysis. Consider for example PC 1, here the age of the absorber solution (t_{sol}) with a contribution of 0.43 and the temperature during absorber spin-coating (T_{SC}, 0.34) correlate positively because the set of experiments was conducted during spring, when the temperatures in the laboratory showed the same tendency as did the outside temperatures. Effectively, the age of the absorber solutions gives some kind of time direction in the data. This is also visible in its correlation with the base pressure of evaporation (p_{base}, 0.38). Parts of the evaporation chamber had been maintained before the series of experiments started and during the experiments the base pressure degraded slightly with time. With the experience gained during this set of experiments and a subsequent longer series of experiments, such correlations

Table 6.10: *The results of the PCA of the production parameters. The table shows that the first 6 of 15 principal components (PC) contain already more than 89% of the total variance of the data. The row and column header show the original variables and the new variables, i.e. principal components (PCs), respectively. Despite trying to avoid correlations between production parameters, the PCA reveals several undesired correlations, indicated by the high contribution of several original variables to the same PCV. These correlations have to be considered as background correlations when interpreting the results of PCAs including measurement results. The discussed values are in bold. The full table can be found in the appendix on pages 190 and 191.*

	PC 1	PC 2	PC 3	PC 4	PC 5	PC 6	···
Δt_1=Δt[UV→PEDOT-SC]	-0.19	0.15	0.54	-0.09	0.06	0.07	
Δt_2=Δt[PEDOT-SC→Oven]	-0.11	0.06	-0.49	0.32	0.22	-0.10	
OP=Order of PEDOT-SC	0.05	-0.11	0.10	-0.43	-0.11	0.48	
$t_d(P)$=Duration of PEDOT Drying	-0.39	0.16	0.09	0.16	0.05	-0.34	
Δt_3=Δt[Airlock→Absorber-SC]	0.01	-0.25	-0.26	-0.57	0.09	-0.12	
T_{SC}=Temp. during Absorber-SC	**0.34**	-0.13	0.14	-0.12	0.16	-0.50	
t_{sol}=Age of Absorber-Solution	**0.43**	-0.01	0.12	0.14	0.26	0.03	
Δt_4=Δt[Absorber-SC→Vacuum]	0.00	0.00	0.51	0.07	-0.22	-0.12	···
$t_d(abs)$=Duration Absorber Drying	-0.06	0.59	-0.02	-0.15	0.14	0.02	
t_{evac}=Duration Evaporation Vacuum	0.41	-0.15	0.02	0.25	-0.22	0.04	
p_{base}=Evaporation Base Pressure	**0.38**	0.10	0.02	0.22	0.23	0.37	
p_{evap}=Evaporation Pressure	0.07	0.25	-0.10	0.23	-0.60	0.04	
$\frac{\Delta d_{5nm}}{\Delta t}$=Aluminium Rate < 5nm	-0.34	-0.13	0.03	0.20	0.30	0.45	
d_{evap}=Al-Layer Thickness	0.13	0.43	-0.25	-0.27	-0.26	0.09	
t_{evap}=Duration of Evaporation	0.21	0.45	0.10	-0.11	0.38	-0.06	
Eigenvalue λ_α	4.38	2.56	2.12	1.75	1.55	1.12	
Variance / %	29.2	17.1	14.2	11.7	10.3	7.5	···
Cum. Variance / %	29.2	46.3	60.4	72.1	82.4	89.9	

eventually can and should be made to average out.

The results of this PCA will be taken into account as background correlations when interpreting the results from the PCA with both production parameters and measurement results.

6.2.2 Correlation between OSC Properties

During the characterisation, measured data is obtained for both electrical and optical properties of an OSC, from which the OSC properties are derived. All OSCs on one substrate have been subjected to exactly the same production parameters, not even the time intervals between steps varied among them. Although the variations in the properties of the OSCs on one substrate are

small (see section 6.1.3), the experimental series showed that the assumption of all OSCs on one substrate being the same does not hold.
For example, one subtle difference, which had not been considered before, is the radial distance of the OSC on a substrate from the centre of the substrate (see figure 4.8). This is motivated by the nature of the spin-coating process, during which the film of absorber solution dries from the centre on outwards, possibly having an effect on both the optical and electrical properties of an OSC. Transmission measurements with polarised light have shown a different angle dependence of the transmission at the centre and at the periphery of a substrate [65]. The effect on the corresponding electronic properties has yet to be shown. The question is, what is due to statistical variations per substrate and what can be explained by e.g. the difference in radial position of the OSCs?
Thus, a PCA taking only the measured properties of OSCs into account was carried out and should reveal such correlations, if any. This analysis applies the observations from all 286 OSCs, trying to find explanations for the spread per substrate. Table 6.11 shows the first ten of 16 principal component vectors. The meaning of the OSC properties, which were included in the PCA are described in section 5.3.2. The power conversion efficiency is not included in the analysis, because it is a linear combination of V_{oc}, J_{sc} and FF. Fitting the simple diode model to the IV-characteristics (see section 5.3.2) generally did not yield sensible parameters for the OSCs with a FF below 0.4. Since all OSCs were included in the PCA, the model parameters are omitted.

PC 1

The first principal component (46.7% of the variance) is dominated by the electrical properties of the OSCs as shown with bold in the PC 1 column of table 6.11. Neither the radial distance to the substrate centre nor the position of the extrema in the absorption spectrum have a significant contribution. However, the correlation between the electronic properties is generally as expected. The higher the current density at 1V forward bias (J_{1V}) the lower the resistance there R_{1V}, which holds both for the dark and the illuminated case. V_{mpp} and J_{mpp} contribute in the same direction, which is expected from the positive correlation with FF. The higher R_{sc}, the lower R_{oc} is also expected for the same reason. It is interesting to note that from the set of the

Table 6.11: *This table shows along the columns the first 10 of a total of 16 principal component vectors obtained from the correlation matrix* $\mathbf{R}$ *between the OSC properties only. The analysis included both electrical and optical properties. The meaning of the variables is described in section 5.3.2. The full table can be found on pages 192 and 193.*

	PC 1	PC 2	PC 3	PC 4	PC 5	PC 6	PC 7	PC 8	PC 9	PC 10	⋯
Radial Distance	-0.04	0.06	**0.35**	-0.43	0.72	-0.27	0.27	-0.02	0.09	-0.05	
V_{oc}	0.18	**-0.32**	**0.40**	-0.29	-0.15	0.10	-0.38	-0.02	-0.06	-0.39	
J_{sc}	0.19	**0.24**	**0.39**	0.39	-0.12	-0.46	-0.17	0.15	0.16	-0.12	
FF	**0.35**	0.06	-0.17	0.02	0.05	0.10	0.18	-0.22	0.05	0.02	
J_{1V} dark	**0.29**	0.09	-0.30	0.05	0.18	0.17	0.15	0.58	-0.13	-0.43	
R_{1V} dark	**-0.33**	0.00	0.23	0.06	-0.10	0.21	-0.02	0.14	0.46	0.15	
J_{1V} ill	**0.33**	-0.07	0.06	-0.02	0.05	0.18	0.00	0.54	0.24	0.34	
R_{1V} ill	**-0.32**	0.14	-0.04	0.13	-0.10	0.12	0.32	-0.06	0.23	-0.65	⋯
V_{mpp}	**0.33**	-0.16	0.13	-0.16	-0.07	0.13	-0.19	-0.15	-0.09	-0.23	
J_{mpp}	**0.31**	0.17	0.17	0.25	-0.05	-0.24	0.09	-0.05	0.25	-0.10	
R_{sc}	**0.30**	-0.13	0.09	-0.11	-0.13	0.34	0.35	-0.27	0.46	0.05	
R_{oc}	**-0.33**	-0.13	0.17	-0.14	-0.05	0.14	-0.10	0.37	0.14	-0.07	
Absorption 1^{st} Min	0.02	**0.42**	0.22	-0.37	-0.42	0.01	0.22	0.14	-0.29	0.10	
Absorption 1^{st} Max	0.03	**0.54**	0.13	-0.21	-0.13	0.19	0.04	-0.04	-0.07	0.02	
Absorption 2^{nd} Min	0.04	**0.30**	**-0.46**	-0.42	-0.02	-0.21	-0.47	-0.04	0.47	-0.08	
Absorption 2^{nd} Max	0.01	**-0.39**	-0.17	-0.28	-0.41	-0.54	0.39	0.16	0.07	-0.01	
Eigenvalue λ_α	7.47	2.94	1.46	1.23	0.95	0.56	0.48	0.33	0.25	0.13	
Variance / %	46.7	18.4	9.1	7.7	5.9	3.5	3.0	2.1	1.6	0.8	⋯
Cum. Variance / %	46.7	65.0	74.1	81.8	87.7	91.3	94.3	96.3	97.9	98.8	

main OSC parameters V_{oc}, J_{sc} and FF, only FF has a considerable influence on PC 1, whereas both V_{oc} and J_{sc} contribute less. This is not surprising, because V_{oc} and J_{sc} are not governed to the extent by, e.g. interface barriers, as is FF.

PC 2

The largest contributions to PC 2 (18.4% of the variance) come from the extrema of the absorption spectrum. V_{oc} and J_{sc}, which had the least influence of the electronic parameters on PC 1, are the electronic parameters with the largest influence on PC 2. Again the radial distance of the OSCs to the substrate centre has only negligible influence. The extrema of the absorption show an interesting behaviour. Whereas the first three extrema being observed at small wavelengths exhibit the same trend, the forth extremum (second maximum) shows the opposite trend. The first minimum is associated with the film thickness of the absorber layer, as shown by optical simulations [65]. However, the shift of the other extrema has not yet been analysed systematically. If indeed these extrema show the same trend in the optical simulations, more than the first absorption minimum could be used for determining the layer thickness, increasing the quality of the thickness estimations. Assuming that the first absorption minimum is a measure of the absorber layer thickness, the correlations with V_{oc} and J_{sc} indicate that the thicker the OSCs, the lower the V_{oc}, but the higher J_{sc}. The absorber thickness was in the range of 80nm, a region, where optical simulations show that a further increase of J_{sc} is possible up to 90nm due to increased light harvesting. This agrees with the discussed PCA. The V_{oc} however decreases with increasing absorber layer thickness in the range obtained. A reduction of V_{oc} with increasing thickness of the absorber layer is sometimes reported in literature, but has not seen in the OSCs made by our group so far.

PC 3

PC 3 (9.1% of the variance) has four contributions with an absolute value of more than 0.3: the radial distance of the OSC to the substrate centre (0.35), V_{oc} (0.40), J_{sc} (0.39) and the second absorption minimum (-0.46). PC 3 is the first PC on which the radial distance has a significant contribution. It suggests that an increase of the distance to the centre of the substrate correlates with an increase of the two electronic parameters (V_{oc} and J_{sc})

and a decrease in the position of the second absorption minimum. The fact that only one of the absorption extrema contributes significantly to PC 3 is surprising. The position of the second minimum varies between 435 and 459nm. However, the maximum observed difference in polarised transmission is in between 500 and 600nm [65]. Thus rather a dependence with the second absorption maximum, which lies in this region, would be expected, if the observed difference in polarised transmission has an effect on the electrical properties. This has to be further investigated with absorption, polarised transmission and IV measurements on a new set of substrates.

Other Observations

PC 5 (5.9% of the variance) has three dominant contributions larger than 0.4: the radial distance (0.72), the position of the first (-0.42) and second absorption maximum (-0.41). At first sight, this trend seems contradicted by the corresponding values on PC 4. However, in 0^{th} order approximation the three mentioned parameters dominate PC 5, whereas there are other parameters on PC 4 which need to be taken into account as well, e.g. an lowering of the position of the 2^{nd} absorption minimum. The analysis takes place in a 16-dimensional space and all significant contributions have to be taken into account. Otherwise, the chosen direction based on only a few dominant contributions to a PCV deviates too much from the actual PCV. Furthermore it is likely that the PCs from PC 4 and onwards cover the noise in the data, rather than real pattern by virtue of their small eigenvalue.

Conclusions

- The FF correlates strongly with the electrical properties (all with absolute contributions above 0.29) on the first principal component (46.7% of the variance). However, there are two notable exceptions: the V_{oc} and the J_{sc}. This is as expected, because V_{oc} and J_{sc} are less affected by interface barriers, which have a stronger influence on the other electrical properties.

- V_{oc} and J_{sc} correlate more with the optical properties, which are found on the second PC, containing nearly 20% of the data variance. Since the optical properties can be used as measure of the absorber film thickness, V_{oc} and J_{sc} appear to depend on the device thickness, rather

than the interface barrier, which affects FF. The effect of different absorber layer thickness has to be investigated further, but as first approximation it can be said that J_{sc} raises and V_{oc} falls with increasing absorber layer thickness. This behaviour is claimed by some groups, but has not been observed in our group before.

- The radial distance has its first significant contribution to PC 3 (only 9.1% of the variance). The first two PCs have little contribution of the radial distance of the OSCs on a substrate, indicating that more than 65% of the variance in the data can be explained by statistical variations.

- Considering PC 3, the higher the radial distance, the higher V_{oc} and J_{sc}, but at the same time the second absorption minimum shifts to shorter wavelength. The origin of this behaviour has not been found yet. The shift of only the second absorption minimum might indicate a changed absorption at 450nm, which in turn can affect V_{oc} and J_{sc}. This has to be investigated with optical simulations of the absorption spectrum.

6.2.3 Correlations between Production Parameters and η

Although only few parameters were varied during the production of the OSCs, as shown in section 6.1.2, the obtained OSC properties have a considerable spread, e.g. FF varies between 0.29 and 0.50. The main phenomena and their underlying physics in the measured OSCs were previously discussed, but the production parameters causing the spread, have yet to be identified. In order to assess the influence of the production parameters on the OSC performance, a PCA was carried out with the above described set of 15 production parameters and the key solar cell property, namely the power conversion efficiency η. All OSCs on a substrate saw the same process parameters and therefore the analysis was done substrate-wise using the average η per substrate. This furthermore gives every substrate the same weight in the analysis, despite some substrates having different number of working OSCs (due to defects described in section 5.3.1).
All production parameters, which were introduced in section 6.1.1, were included into the analysis. The PCA is a linear method and in order to locally

approximate complex non-linear system it needs as many parameters as are thought to be influential. If any of the chosen parameters does not have a significant influence on η, they will appear in the PCA with little contribution to the first principal component vectors (PCVs).
The first 10 of 16 PCVs are shown in table 6.12. The table also lists the eigenvalue λ_α, the percentage of variance and the cumulated values for each principal component near the end of the table. The last line in the table shows the absolute value of the product of the contribution of the variable η to the PC and the eigenvalue of the PC, i.e. $|\eta\ \lambda_\alpha|$. The first six PCs contain together already nearly 90% of the variance of the data. Including the PCs up to PC 10 can account for nearly 100% of the variance.
From a simple system one would expect that most properties are governed by fewer PCs. However, this is not the case and at least seven of the 16 PCs are necessary to capture more than 90% of the variance. There appears to be no clear cut tendency and detective work and physical intuition is necessary to make sensible inferences from the data.

PC 1

The first principal component contains most of the variance in the data (27.4%), but only a very weak contribution from η (-0.01). Comparing this PCV to the first principal component vector of the PCA on the production parameters (table 6.10) shows that both are nearly equal. This and the fact that η contributes little to PC 1, indicates that PC 1 contains only the correlations between production parameters which do only little correlate with the variable η. Therefore using only the eigenvalue λ_α is not an adequate measure for assigning the relevance of a PC for the interdependence between production parameters and η.
One approach for assigning a measure of relevance would be to consider the absolute value of the product of a PC contribution to η and the PC eigenvalue λ_α, i.e. $|\eta\ \lambda_\alpha|$. Ranking according to this weighted λ_α would allow an ordering of the PCs with respect to their influence on η. The order of the three most relevant PCs for η is then PC 2, PC 4 and PC 3 in descending order. These PCs show both a large λ_α anf significant contributions from the variable η. PC 1 follows according to this ranking only on position 9.
The high correlation between the production parameters again stresses the need to consider the background correlations, i.e. the results of the PCA

Table 6.12: *This table shows the first 10 of a total of 16 principal component vectors obtained from the correlation matrix* $\mathbf{R}$ *between production steps and the average power conversion efficiency* η *per substrate. They are ordered by their eigenvalue, but in order to assess their relevance for* η*, the absolute product of the PC eigenvalue* λ_α *and the contribution of the variable* η *is shown in the last row. This measure is used to assign a relative importance to each PC for its effect on* η*. The values discussed in the text are highlighted in bold. The complete table can be found in the appendix on pages 194 and 195.*

	PC 1	PC 2	PC 3	PC 4	PC 5	PC 6	PC 7	PC 8	PC 9	PC 10	⋯
Δt_1=Δt[UV→PEDOT-SC]	-0.19	0.24	**-0.43**	-0.19	0.15	0.16	0.03	-0.40	-0.34	0.16	
Δt_2=Δt[PEDOT-SC→Oven]	-0.11	0.00	**0.42**	0.20	-0.44	-0.02	0.24	0.41	-0.30	0.12	
OP=Order of PEDOT-SC	0.05	-0.16	-0.07	-0.03	0.50	0.38	0.53	0.33	-0.08	-0.37	
$t_d(P)$=Duration of PEDOT Drying	-0.38	0.20	-0.06	-0.05	-0.17	-0.21	0.38	-0.11	0.01	0.19	
Δt_3=Δt[Airlock→Absorber-SC]	0.01	-0.20	0.07	**0.53**	0.39	-0.08	-0.06	-0.08	-0.50	0.38	
T_{SC}=Temp. during Absorber-SC	0.34	0.00	**-0.25**	**0.26**	-0.01	-0.29	0.41	-0.07	0.14	0.18	
t_{sol}=Age of Absorber-Solution	0.43	0.05	-0.15	0.05	-0.21	0.17	0.04	-0.02	-0.01	0.08	
Δt_4=Δt[Absorber-SC→Vacuum]	0.00	0.09	**-0.43**	**-0.32**	0.07	-0.19	-0.21	0.70	-0.16	0.30	
$t_d(abs)$=Duration Absorber Drying	-0.06	**0.53**	0.21	-0.01	0.14	0.17	0.05	0.07	0.19	0.10	⋯
t_{evac}=Duration Evaporation Vacuum	0.41	-0.19	-0.01	-0.23	-0.14	-0.11	0.01	-0.10	-0.18	-0.07	
p_{base}=Evaporation Base Pressure	0.38	0.07	0.03	-0.09	-0.23	0.41	-0.11	-0.05	-0.25	0.08	
p_{evap}=Evaporation Pressure	0.07	0.06	0.31	**-0.53**	0.07	-0.25	0.32	-0.16	-0.40	-0.03	
$\frac{\Delta d_{5nm}}{\Delta t}$=Aluminium Rate $<$ 5nm	-0.34	-0.12	-0.07	0.01	-0.25	0.49	-0.05	-0.02	-0.22	0.01	
d_{evap}=Al-Layer Thickness	0.13	0.28	0.41	-0.07	0.36	-0.05	-0.35	0.02	-0.06	0.02	
t_{evap}=Duration of Evaporation	0.21	**0.48**	0.00	0.14	-0.01	0.23	0.22	0.05	0.08	0.24	
η	**-0.01**	**-0.42**	**0.21**	**-0.32**	0.14	0.24	0.11	-0.05	0.37	0.66	
Eigenvalue λ_α	4.4	2.9	2.2	1.8	1.7	1.3	0.7	0.6	0.2	0.1	
Variance / %	27.4	17.9	13.8	11.5	10.8	8.1	4.5	3.5	1.5	0.8	⋯
Cum. Variance / %	27.4	45.3	59.1	70.5	81.4	89.5	94.0	97.5	99.1	99.9	
$\lvert\eta\lambda_\alpha\rvert$	0.05	1.20	0.47	0.59	0.23	0.31	0.08	0.03	0.09	0.08	⋯
Relative Order	9	1	3	2	5	4	8	10	6	7	

with only production parameters (table 6.10), when interpreting the results of this PCA.

PC 2

$$t_d(abs) \uparrow \ \wedge t_{evap} \uparrow \ \wedge \eta \downarrow$$

The three highest contributions to PC 2 (17.9% of the variance) are the duration of absorber drying ($t_d(abs)$, 0.53), the time it took to evaporate the Al cathode (t_{evap}, 0.48) and the power conversion efficiency η (-0.42). As 0^{th} order approximation, i.e. when only considering the dominant contributions, this suggests in that increasing both parameters, results in a decrease of η. Notable changes compared to the background correlations (table 6.10) are seen in the temperature during absorber spin-coating (T_{SC}, -0.13→0.00), the evaporation pressure (p_{evap}, 0.25→0.06) and the Al-layer thickness of the cathode (d_{evap}, 0.43→0.28).

The duration of the absorber drying in vacuum ($t_d(abs)$) and η appear to correlate negatively. However, it has to be kept in mind that this contribution was slightly higher in the PCA with production parameters only (0.59), making it most likely an artefact from the production process. The negative correlation is counter-intuitive, because one would assume that after a longer drying time of the absorber, less solvent molecules are left. The solvent used, o-dichlorobenzene (DCB), has a high boiling point of 180.5°C and it is expected that despite the very thin spin-coated layer (≈ 80nm), the film contains residual solvent. The absorber layer of all substrates were dried in a vacuum lock for more than 23h at a pressure <0.1bar and subsequently put into the high vacuum (<10^{-5}mbar) of the evaporation chamber for more than 14h. Measuring the change in weight of a substrate due to the evaporation of the solvent is below the detection limit of the available equipment (<0.01mg). There is no unanimous opinion on the importance of this parameter between the research groups working on OSCs. Whereas Li et al. carefully state that a longer drying might be beneficial due to the removal of residual solvent, other research groups built good OSCs from the same materials despite of drying less than 3h [97]. Most research publications on OSC do not state the time of drying.

The second largest contribution to PC 2 is from the duration of the cathode evaporation (t_{evap}). During the evaporation process, the absorber layer is

exposed to the aluminium atoms evaporating from a resistively heated tungsten boat. The other parameters associated with the evaporation process have much less influence on PC 2. Even the deposition rate of the first 5nm aluminium ($\frac{\Delta d_{5nm}}{\Delta t}$), i.e. the rate at which the first hot Al-atoms are deposited onto the absorber layer, has little influence, although this is the only time when the atoms directly impact on the absorber layer. After 5-10nm the Al-layer is closed and furthermore begins to act as mirror to the IR-radiation from the evaporation source. Still, it is known from experience that substrates, which had been exposed to a long evaporation step, tend to have a lower η, making thermal effects the most likely cause. The evaporation chamber is not equipped with a thermometer, but estimations for the heat transfer can be made. Under the assumption that the evaporation source can be approximated as black body (emissivity=1), an order of magnitude estimation of the total energy radiated per unit surface area in unit time j_E can be obtained via the Stefan-Boltzmann-law

$$j_E = \sigma_{\mathrm{sb}} T^4, \tag{6.5}$$

where σ_{sb} is the Stefan-Boltzmann constant and T the temperature of the black body. At the evaporation base pressure of approximately 10^{-5}mbar, the boiling point of aluminium is about 1100K. The area of the glowing tungsten boat is circa 1cm^2, thus the radiated power into the half-sphere amounts to roughly 10W. The perpendicular distance between radiating surface and substrates is approximately 20cm, so that the received irradiance per cm^2 is about 25mW, i.e. small. Most of this power is even reflected by the substrate as soon as Al-layer is closed. The second cause for an increase in temperature of the substrate is the latent heat during condensation of the Al (10.9 kJ/g) and the subsequent crystallisation (397 J/g). Assuming a 100nm thick Al layer, a rough estimate of the latent heat amounts to an energy of about 0.3J per cm^2, which is distributed during the 5 to 15min of evaporation. This contribution is indeed very small as well. Why the long evaporation has a negative influence is not clear at the moment. The PCA and general experience from the laboratory exhibit the same tendency, i.e. a longer evaporation step is reducing η. To completely rule out thermal effects an installation of a thermocouple inside the evaporation chamber is planned, but could not be carried out within the time of this thesis.

It is interesting to note that the temperature during absorber spin-coating

(T_{SC}) has no influence on PC 2 when the PCA includes η, but contributed 0.12 to PC 2 of the background correlations. Also the contribution of the pressure during cathode evaporation (p_{evap}) drops from 0.25 to 0.06 and the contribution of the thickness of the absorber layer (d_{evap}) is substantially reduced. Although physical explanations can be found, one has to be careful when deducing a causal dependence from the PCA by considering the changes with respect to the background correlations, because all 16 dimensions, i.e. variables have to be considered.

PC 3

$$\Delta t_1 \downarrow \ \wedge \Delta t_2 \uparrow \ \wedge \Delta t_4 \downarrow \ \wedge \eta \uparrow$$

Considering $|\eta\ \lambda_\alpha|$ PC 3 is on position 3 of relative importance (13.8% of the variance). The three highest contributions on PC 3 are the time interval between UV-Ozone treatment of the substrates and spin-coating of the PEDOT:PSS layer (Δt_1, -0.43), the time interval to the subsequent drying of the PEDOT:PSS layer in the oven (Δt_2, 0.42) and the time interval between spin-coating of the absorber layer and its drying in vacuum (Δt_4, -0.43). η has a contribution of 0.21. However, all three production parameters were higher in the background correlations and their contribution was only slightly reduced when including η in the analysis. Thus no firm deductions can be made, because these correlations appear to be artefacts from the production process. The fourth highest contribution, the thickness of the aluminium layer (d_{evap}), however exhibited a strong increase in is absolute value (-0.25→0.41).
An important fact on PC 3 is the change in sign of the dominating correlations with respect to the background correlations. Furthermore a large increase of the contributions of the duration of absorber drying ($t_d(abs)$, -0.02→0.21) and the evaporation pressure (p_{evap}, -0.10→0.31) as compared to the background correlations. The correlation of the evaporation pressure with η has the same trend as to PC 4. The duration of absorber drying suggests a longer time is beneficial for η, apparently contradicting its contribution on PC 2. However, it has to be kept in mind that the PCVs of PC 2 and PC 3 are perpendicular and thus pointing into different directions. If the proposed methodology of interpretation, i.e. taking into account the changes with respect to the background correlations, proves to be valid, then the influence of the absorber drying to PC 3 would be considered stronger

on η than its contribution to PC 4, because in the latter case it only decreased slightly from a value which had been already high in the background correlations.

PC 4

$$\Delta t_3 \uparrow \ \wedge \Delta t_4 \downarrow \ \wedge p_{evap} \uparrow \ \wedge \eta \downarrow$$

PC 4 (11.5% of the variance) has the second largest value of $|\eta\ \lambda_\alpha|$ (0.59). The influential variables for PC 4 are the time interval between finishing the drying of the PEDOT:PSS layer and spin-coating of the absorber layer (Δt_3, 0.53), the evaporation pressure (p_{evap}, -0.53), the time between absorber spin-coating and absorber drying (Δt_4, -0.32) and η (-0.32). One distinct change with respect to the background correlation (table 6.10) is again that the PC has changed sign for the most prominent contributions, with some exceptions however: the time interval between UV-Ozone treatment and PEDOT:PSS spin-coating (Δt_1) and the subsequent time interval between PEDOT:PSS spin-coating and its annealing in the oven at elevated temperatures (Δt_2). The contributions to PC 4 collapsed for the order of PEDOT-SC (OP, -0.43→0.03) and the aluminium evaporation rate <5nm ($\frac{\Delta d_{5nm}}{\Delta t}$, 0.20→0.01).
The time interval between finishing the drying of the PEDOT:PSS layer and the spin-coating of the absorber layer (Δt_3) has a high contribution on PC 4, albeit its absolute value is lower than for the background correlations (0.57→0.53). Thus no sensible deduction can be made, because it appears to be an artefact from the production process.
The contribution of the evaporation pressure (p_{evap}, -0.53) to PC 4 has the same sign as the contribution from η, i.e. the higher the pressure during evaporation, the better η. Its absolute contribution to PC 4 more than doubled with respect to the background correlations. Generally, the higher the evaporation pressure, the quicker the evaporation. This is in line with what has been observed on PC 2 for the duration of evaporation (t_{evap}) and this trend is known from experience. The two parameters, evaporation pressure and evaporation duration, appear with a significant contribution to two different PCs, both essentially stressing that a quick evaporation process is beneficial for η. However, it is interesting to note that the aluminium evaporation rate <5nm ($\frac{\Delta d_{5nm}}{\Delta t}$), i.e. the rate in which the first Al-atoms condense on the absorber surface, has little influence up to PC 5.

The third significant influence is observed for the time interval between spin-coating of the absorber layer and drying of the substrates in vacuum (Δt_4, -0.32). The longer the delay, the higher the efficiency. The substrates are spin-coated for 90s at 1500rpm. This is longer than it takes for the wet layer to dry as indicated by a prominent colour change from yellowish to dark violet. However, for o-dichlorobenzene (DCB) the absorber layer still contains some residual solvent, when taking the substrate off the spin-coater. By putting the substrates into vacuum early, the residual solvent is more rapidly removed, inhibiting further rearrangement of polymer chains and PCBM molecules. This freezes the morphology in a non-relaxed way. Only during OSC post-treatment, i.e. at elevated temperatures, the structure can relax, but not to the extent as it could during the initial drying. Exactly this has been demonstrated by Li et al. [61]. They spin-coated the absorber layer from DCB, but stopped before the layer changed its colour. Subsequently, they varied the speed of solvent evaporation, e.g. by keeping a substrate in a saturated solvent atmosphere or rapidly removing the solvent by heating the substrate on a hot plate. The best OSCs were produced on the substrates on which the absorber layer was allowed to dry most slowly. However, new experiments did not reproduce the reported behaviour, because all OSCs exhibited a very rough absorber surface, which was most likely the cause for the low efficiencies.

Other Observations

The temperature during spin-coating of the absorber layer (T_{SC}) shows on both PC 3 and PC 4 a significant increase of its contribution when compared to the background correlations. On PC 3 it changed from 0.14 to -0.25 and on PC 4 from -0.12 to 0.26. The correlations with η suggest in both cases that the colder the temperature T_{SC}, the higher η. A lower temperature leads to a slower evaporation of the solvent, thus to a more advantageous morphology. This is again in line what has been proposed by Li et al. [61]. The influence of the time interval between UV-Ozone treatment and PEDOT:PSS spin-coating (Δt_1) and η, mentioned at the beginning of section 6.1, might show on PC 2. There the contribution of the parameter has increased from 0.15 to 0.24, suggesting that a shorter time interval leads to a higher efficiency. However, this interpretation only includes one variable and the other variables need to be considered as well.

As the order of PEDOT:PSS spin-coating was included in the analysis, this effect should have been picked up by the PCA. Indeed, it can be found for PC 5, where the absolute contribution increased from 0.11 to 0.50 with respect to the background correlation, i.e. showing a significant increase in contribution upon including η in the analysis. This suggests, as also seen in figure 6.2, that the second four substrates being spin-coated with PEDOT:PSS have a higher efficiency. However, here again the changes have to be seen the light of the other parameters as well, and for a 0^{th} order approximation at least Δt_2, Δt_3 and d_{evap} need to be considered.
The highest contribution of η to any PC is observed on PC 10 (0.66). However, in the light of the small λ_α (0.1), it is most likely due to artificial correlations with the production parameters and statistical scatter.
The following parameters did not have a significant contribution to the PCVs, which were relevant for η as discussed above: the duration of PEDOT Drying ($t_d(P)$) first appears in PC 7 (4.5% of variance) with a contribution larger than 0.3. A plot of this parameter with respect to η has been shown in figure 6.2 on the left side. However, already making the deduction from this plot that $t_d(P)$ has no influence, would have been to early. It shows some scatter and $t_d(P)$ has to be interpreted in the context of all other production parameters. The age of the absorber solution (t_{sol}) has a significant contribution to PC 1 (0.43), which however only contains correlations between production parameters. Thus both parameters have only little effect on the power conversion efficiency η within the ranges of values used for the presented PCA (table 6.2). Their effect will still be monitored in future experiments, but the present data suggests that little effort in optimising these two parameters in necessary due to their negligible influence.

Conclusions

- With 15 production parameters and only 1 OSC property (here η), the correlations between the production parameters dominate the first principal component (PC 1) of the PCA. Generally, all correlations from the production parameters have to be taken into account as background correlations when interpreting the PCA results. It was subsequently found that the eigenvalue λ_α of a principal component alone is not an adequate measure for describing a PC's importance for η. Therefore the proposed order is based on the product of the contribution of η and

λ_α to a PC, i.e. $|\eta\ \lambda_\alpha|$.

- The contributions to PC 2, which was found to be the PC with the highest relevance for η, suggest that if the drying time of the absorber layer and the duration of the cathode evaporation increase, then η is decreasing. There is no unanimous opinion about the drying time in literature and a comparison with the background correlations suggests that it is an artefact from the production process. The effect of a long evaporation process however, has before been observed to have an impact on the OSC performance and the PCA confirms this. One possible origin is thought to be the thermal stress during evaporation, although a first estimate of the heat transfer has turned out to be very low ($<$30mW/cm^2). However, in order to rule out thermal stress as cause for a decreasing η it is planned to install a thermocouple inside the evaporation chamber.

- PC 3 is the third most relevant to η. However, the three most dominant contributions (Δt_1, Δt_2, Δt_4) appear to be artefacts from the production process. Thus no firm conclusions can be drawn from PC 3.

- The second most relevant PC to η is PC 4. It suggests that a higher evaporation pressure (p_{evap}) and a longer time between absorber spin-coating and drying of the absorber (Δt_4) are beneficial to η. As a higher evaporation pressure typically implies a shorter evaporation duration, PC 4 implies the same as PC 2. The second effect, i.e. the effect of Δt_4, has been observed by another research group [61]. New experiments could however not reproduce the results.

- Two parameters did not have any significant contribution to the first seven PCs, which are considered most relevant to η: the duration of PEDOT Drying ($t_d(P)$) and the age of absorber-solution (t_{sol}). Both have in the presented data little influence on η and can receive less attention in future experiments.

6.3 Development of a Statistical Model

Based on the principal component analysis (PCA) conducted on this set of data, a model was developed for the optimisation of the production parame-

ters. The PCA in section 6.2.3 has shown that there are correlations between production parameters and OSC properties. The information about these correlations will be used in the model to estimate OSC properties only based on the production parameters. If the validation of the model is successful, the model can be used to optimise the production parameters in order to obtain improved OSC properties.

This new approach presented here uses the fact that the first few principal components capture most of the variance of the data, whereas the variance contained in the last few principal components is close to 0. The corollaries of this are used to develop the model.

The derivation of the model is here presented for a general set of $p-1$ production parameters $y_1, \ldots, y_{p-1}$ and 1 OSC property y_p. Thus for each OSC there exists an observation vector, which is given by

$$\mathbf{y} = \begin{pmatrix} y_1 \\ y_2 \\ \vdots \\ y_{p-1} \\ y_p \end{pmatrix}, \tag{6.6}$$

where $y_1, \ldots, y_p$ represent the recorded values of the p variables. n such observation vectors, i.e. the data from n OSCs, form the $n \times p$ data matrix $\mathbf{Y}$, on which a PCA is performed (see section 5.1.3). The result of the PCA is a set of p principal component vectors (PCV), which form an alternative basis for describing the original data with the distinct feature: the PCVs are ordered such that the first coordinate in the transformed coordinate system, i.e. the first principal component (PC), contains most of the variance of the data. The variance of each PC is measured by the eigenvalue of the corresponding PCV. The other PCs follow ordered with decreasing eigenvalues. Thus when expressing the observation vector $\mathbf{y}$ in terms of the principal components, the coordinates along PC 1 show the highest variations, whereas its coordinates along the last PC should show nearly no variations at all.

The observation vector $\mathbf{y}$ can be transformed into the coordinate system of the PCVs. The transformed observation vector $\mathbf{z}$ has then components

$$\begin{aligned} z_1 &= \hat{\mathbf{a}}_1^T\ \mathbf{y} \\ z_2 &= \hat{\mathbf{a}}_2^T\ \mathbf{y} \\ &\vdots \\ z_p &= \hat{\mathbf{a}}_p^T\ \mathbf{y} \end{aligned}, \tag{6.7}$$

where the $\hat{\mathbf{a}}_i$'s are the p eigenvectors of the $p \times p$ correlation matrix $\mathbf{R}$ of the data (see section 5.1.3). As the principal components are ordered by their eigenvalue λ_α, the last principal component $z_p = \hat{\mathbf{a}_p}^T \mathbf{y}$ has the smallest eigenvalue, which represents the direction of minimum variance, because the variance along z_p, i.e. $s^2_{z_p}$, equals λ_p. Hence, one obtains a near linear relationship among the variables that is approximately constant over the data set. Having an eigenvalue close to zero implies that the corresponding PCVs are orthogonal to the hyperplane containing the variations of the data. Now given the $p-1$ production parameters, it is possible to approximate the expected measurement result by solving the linear equation

$$z_p = \hat{\mathbf{a}_p}^T \mathbf{y} = \sum_{i=1}^{p-1} a_{p_i} y_i + a_{p_p} y_p \approx 0. \tag{6.8}$$

This principle is now applied on the principal components of the correlation matrix $\mathbf{R}$ of all considered 15 production parameters and three main solar cell properties (V_{oc}, J_{sc}, FF). It is the same data as has been used before (section 6.2), but with η replaced by V_{oc}, J_{sc} and FF. The corresponding observation vector is hence given by

$$\mathbf{y} = \begin{pmatrix} \Delta t_1 \\ \Delta t_2 \\ OP \\ t_d(P) \\ \vdots \\ t_{evap} \\ V_{oc} \\ J_{sc} \\ FF \end{pmatrix} =: \begin{pmatrix} p_1 \\ p_2 \\ p_3 \\ p_4 \\ \vdots \\ p_{15} \\ V_{oc} \\ J_{sc} \\ FF \end{pmatrix}. \tag{6.9}$$

This PCA leads to 18 principal components. Table 6.13 shows the last four PCVs of this PCA. These four corresponding PCs contain together less than 1% of the variance.

For the development of the model, the PCs with the lowest eigenvalues should be chosen. The lower an eigenvalue of a PC, i.e. the lower the variance along that PC, the better is the approximation of equation 6.8. However, there is a limit. If the chosen PC has nearly zero contribution ($<10^{-8}$) of the values the model should predict, a large numerical error would be introduced.

For the chosen data and its PCA the last PC has little or no contribution ($<10^{-15}$) of either V_{oc}, J_{sc} or FF and using this PC would introduce large errors into the model. Thus the principal components 15, 16, 17 were chosen for the development of the statistical model. They all contribute nearly zero ($<10^{-3}\%$) to the variance of the data. This model could have been developed only using η, leading to only one linear equation (equation 6.8). However, η is obtained at constant light intensity P_{ill} used for measuring and thus only a function of V_{oc}, J_{sc} and FF, which correspond to different aspects of an OSC. Employing these three parameters should improve the quality of the model, because they can reflect effects of production parameters, which might not show up in their combination, but considered alone, have a distinct trend.
Using three PCs and the three measurement results for the model structure leads to a linear system of three equations with three unknowns. For ease of notation let the principal component vectors 15, 16 and 17 be denoted by 18×1 vectors $\mathbf{a}$, $\mathbf{b}$ and $\mathbf{c}$. The observation vector $\mathbf{y}$ of an OSC has 18 dimensions as well: 15 production parameters and the three solar cell properties V_{oc}, J_{sc}, FF (see equation 6.9). For the PCA and hence also for the model structure all variables were normalised to have zero mean and unit standard deviation, because they were of different size and variances. The normalised observation vector is $\tilde{\mathbf{y}}^T = (\tilde{p}_1, \tilde{p}_2, \ldots, \tilde{p}_{15}, \tilde{V}_{oc}, \tilde{J}_{sc}, \tilde{FF})$, where

$$\tilde{x} = \frac{(x - \bar{x})}{\sigma_x} \tag{6.10}$$

with $\bar{x}$ being the mean and σ_x the standard deviation of a variable x. $\tilde{\mathbf{y}}$ can thus be rewritten as

$$\tilde{\mathbf{y}} = \begin{pmatrix} \tilde{\mathbf{p}} \\ \hline \tilde{V}_{oc} \\ \tilde{J}_{sc} \\ \tilde{FF} \end{pmatrix}, \tag{6.11}$$

with $\tilde{\mathbf{p}}^T = (\tilde{p}_1, \ldots, \tilde{p}_{15})$. The linear equations 6.8 from the three PCs and the observation vector then can be expressed as

$$\begin{pmatrix} a_{16} & a_{17} & a_{18} \\ b_{16} & b_{17} & b_{18} \\ c_{16} & c_{17} & c_{18} \end{pmatrix} \begin{pmatrix} \tilde{V}_{oc} \\ \tilde{J}_{sc} \\ \tilde{FF} \end{pmatrix} = - \begin{pmatrix} \sum{}_a(\tilde{\mathbf{p}}) \\ \sum{}_b(\tilde{\mathbf{p}}) \\ \sum{}_c(\tilde{\mathbf{p}}) \end{pmatrix}, \tag{6.12}$$

where

$$\sum{}_a(\tilde{\mathbf{p}}) = \sum_{i=1}^{15} a_i \tilde{p}_i. \tag{6.13}$$

Table 6.13: *The last 4 of 18 principal components obtained from the correlation matrix* $\mathbf{R}$ *between production steps and* V_{oc}*,* J_{sc}*,* FF*. PCs 15-17 are used for the construction of a model for the optimisation of the production process. The PC 18 contains too little contribution of* V_{oc}*,* J_{sc} *and* FF*, i.e. the variables of interest (*$<10^{-8}$*). The full table can be found in the appendix on pages 196 and 197.*

	⋯	PC 15	PC 16	PC 17	PC 18
Δt_1=Δt[UV→PEDOT-SC]		-3.10E-2	3.69E-2	7.90E-5	3.96E-16
Δt_2=Δt[PEDOT-SC→Oven]		-1.35E-2	2.31E-2	6.06E-5	5.42E-16
OP=Order of PEDOT-SC		3.59E-2	-1.90E-1	3.48E-6	-2.38E-16
$t_d(P)$=Duration PEDOT Drying		1.11E-1	-6.23E-1	3.51E-4	-1.93E-15
Δt_3=Δt[Airlock→Absorber-SC]		-1.86E-1	6.68E-3	-3.29E-3	-1.81E-15
T_{SC}=Temp. during Absorber-SC		1.33E-1	-5.31E-2	-1.41E-4	1.01E-15
t_{sol}=Age of Absorber-Solution		-1.09E-1	-1.01E-1	7.83E-1	3.57E-13
Δt_4=Δt[Absorber-SC→Vacuum]		-1.72E-3	2.79E-4	1.25E-4	1.71E-16
$t_d(abs)$=Duration Absorber Drying	⋯	-7.13E-1	-5.38E-2	1.12E-3	4.24E-16
t_{evac}=Duration Evaporation Vacuum		-3.12E-1	-2.53E-1	-3.25E-1	6.20E-1
p_{base}=Evaporation Start Pressure		8.16E-2	-2.79E-1	-3.50E-1	-5.39E-1
p_{evap}=Evaporation Pressure		2.08E-2	3.44E-1	1.78E-1	-1.20E-1
$\frac{\Delta d_{5nm}}{\Delta t}$=Aluminium Rate $<$ 5nm		9.54E-2	2.83E-2	1.78E-1	4.05E-1
d_{evap}=Al-Layer Thickness		4.15E-1	-3.94E-1	1.90E-1	2.12E-1
t_{evap}=Duration of Evaporation		3.56E-1	3.76E-1	-2.44E-1	3.19E-1
V_{oc}		1.66E-2	-1.69E-2	5.01E-5	1.74E-16
J_{sc}		-5.10E-3	-5.47E-3	-4.87E-5	-1.02E-16
FF		1.01E-3	9.67E-3	1.45E-4	-1.42E-16
Eigenvalue λ_α		8.88E-5	2.62E-5	6.42E-9	1.74E-32
Variance / %	⋯	4.93E-4	1.45E-4	3.56E-8	9.65E-32
Cum. Variance /%		100.0	100.0	100.0	100.0
$\lvert V_{oc}\ \lambda_\alpha\rvert$		1.47E-6	4.41E-7	3.22E-13	3.02E-48
$\lvert J_{sc}\ \lambda_\alpha\rvert$	⋯	4.53E-7	1.43E-7	3.12E-13	1.78E-48
$\lvert FF\ \lambda_\alpha\rvert$		8.98E-8	2.53E-7	9.32E-13	2.46E-48

$\sum_b(\mathbf{p})$ and $\sum_c(\mathbf{p})$ are defined in the analogous way. Solving this set of linear equations leads to following equations for the normalised $\tilde{V}_{oc}$, $\tilde{J}_{sc}$ and $\tilde{FF}$:

$$\begin{aligned}\tilde{V}_{oc} \;=\; & \beta^{-1}\left(\textstyle\sum_a(\tilde{\mathbf{p}})(b_{18}c_{17}-b_{17}c_{18})+\right.\\ & \left.\textstyle\sum_b(\tilde{\mathbf{p}})(a_{17}c_{18}-a_{18}c_{17})+\sum_c(\tilde{\mathbf{p}})(a_{18}b_{17}-a_{17}b_{18})\right),\end{aligned} \tag{6.14a}$$

$$\begin{aligned}\tilde{J}_{sc} \;=\; & \beta^{-1}\left(\textstyle\sum_a(\tilde{\mathbf{p}})(b_{16}c_{18}-c_{18}c_{16})+\right.\\ & \left.\textstyle\sum_b(\tilde{\mathbf{p}})(a_{18}c_{16}-a_{16}c_{18})+\sum_c(\tilde{\mathbf{p}})(a_{16}b_{18}-a_{18}b_{16})\right),\end{aligned} \tag{6.14b}$$

$$\begin{aligned} \tilde{FF} &= \beta^{-1}\left(\sum{}_a(\tilde{\mathbf{p}})(b_{17}c_{16} - b_{16}c_{17}) + \right. \\ &\quad \left. \sum{}_b(\tilde{\mathbf{p}})(a_{16}c_{17} - a_{17}c_{16} + \sum{}_c(\tilde{\mathbf{p}})(a_{17}b_{16} - a_{16}b_{17})\right), \end{aligned} \tag{6.14c}$$

with

$$\beta = a_{16}(b_{17}c_{18} - b_{18}c_{17}) + a_{17}(b_{18}c_{16} - b_{16}c_{18}) + a_{18}(b_{16}c_{17} - b_{17}c_{16}) \tag{6.15}$$

Equation 6.10 is then used to arrive at the non-normalised solar cell parameters V_{oc}, J_{sc} and FF.

6.3.1 Cross-Validation

The question is, whether the linear model can only reproduce the data it has been constructed with or really capture the underlying physics affecting V_{oc}, J_{sc} and FF. Cross-validation, a testing practise in statistics, is thus used to check the quality of the model. During cross-validation the original data is partitioned and the data analysis and model development carried out on one subsample. The remaining subsamples are retained from this analysis and used later to test the model based on the initial analysis.

The model given by equations 6.14a, 6.14b and 6.14c is tested using the so-called "leave-one-out cross-validation". As the name suggests, one observation vector is left out when doing the PCA for the model and then the model's predictions are tested on the left-out observation vector. This procedure is then repeated for every single observation vector in the data. The data used for the construction of the model consists of 36 observation vectors, i.e. the data of 36 substrates. Thus the cross-validation is carried out 36 times. The summary of the results of the cross-validation is shown in tables 6.14 and 6.15. The full tables can be found in the appendix on pages 198 and 199. The predictions in the table are all based on a model with PCs 15 to 17, but the predictions for substrate S 439. When leaving out S 439 during cross-validation, PC 17 of the PCA on the remaining data had too little contribution ($<10^{-15}$) to V_{oc}, J_{sc} and FF, with a subsequent large error in the prediction. The values for S 439 thus validated with a model based on PCs 14 to 16.

The best predictions are obtained for V_{oc}, both when considering the deviations as percentage (table 6.14) and with respect to the standard deviation

Table 6.14: *This table summarises the results from the cross-validation by showing the quality of predictions in terms of a percentage deviation from the measured result per substrate. The total number of substrates is 36. n gives the number of substrates, the properties of which have been predicted better than the indicated percent. The values for the power conversion efficiency η are calculated from the predicted values of open circuit voltage V_{oc}, short circuit current density J_{sc} and fill factor FF. The predictions of V_{oc} are very good with all values lying within 10% of the measured values. The same data is shown in table 6.15 with deviations with respect to the standard deviations σ per substrate.*

	V_{oc}		J_{sc}		FF		η	
Percent	n	Cum%	n	Cum%	n	Cum%	n	Cum%
<2.5%	24	67%	4	11%	13	36%	4	11%
<5%	32	89%	11	31%	14	39%	6	17%
<10%	36	100%	22	61%	22	61%	15	42%
<15%	36	100%	29	81%	25	69%	18	50%
<20%	36	100%	30	83%	27	75%	23	64%
<30%	36	100%	33	92%	30	83%	27	75%
≥30%	0	100%	3	100%	6	100%	9	100%

Table 6.15: *This table summarises the results from the cross-validation by showing the quality of predictions in terms of the standard deviations of the measured values per substrate. The total number of substrates is 36. n gives the number of substrates, the properties of which have been predicted better than i times the standard deviation σ. The values for η are again calculated from the predicted values of V_{oc}, J_{sc} and FF. For 21 substrates, i.e. 58% of all, the predicted values for FF were within $2 \times \sigma$. The same data is shown in table 6.14 with deviations given in percent.*

	V_{oc}		J_{sc}		FF		η	
i	n	Cum%	n	Cum%	n	Cum%	n	Cum%
<1	20	56%	7	19%	14	39%	7	19%
<1.5	24	67%	9	25%	17	47%	11	31%
<2	26	72%	16	44%	21	58%	15	42%
<2.5	30	83%	19	53%	22	61%	17	47%
<3	32	89%	22	61%	23	64%	24	67%
<4	34	94%	27	75%	27	75%	25	69%
≥4	2	100%	9	100%	9	100%	11	100%

per substrate (table 6.15). All predicted values are within 10% of the measured values. However, because the standard deviations for the V_{oc} is always smaller than 5% (see table 6.5), the quality of predictions in terms of the standard deviation is lower. Still, predictions of V_{oc}, which are within 10% of the measured value for all OSCs, and 56%<1σ are very good, given the spread in the production data. This also indicates that the main parameters responsible for the variations in V_{oc} are included in the PCA.
The quality of the predictions for J_{sc} and FF is not as good as compared to the V_{oc} predictions when considering the percentage difference between predicted and measured value only. However, the standard deviations per substrate are larger than they are for the V_{oc} described by reasons in section 6.1.3. Assuming that the model reflects the underlying physics, there are most likely parameters, which were not included in the analysis, but have an effect on J_{sc} and FF. The necessity of including the parameter OP into the analysis shows that the variations in humidity during PEDOT:PSS spin-coating, which had not been monitored, might have an influence. Another parameter, which is known to have an influence on J_{sc} is the morphology of the absorber layer. It should largely depend on the production parameters, but is difficult to be assessed directly for every OSC. It is also currently not possible to parameterise the morphology, which would be necessary to include it into the analysis.
Not surprisingly, the predictions for the power conversion efficiency η which are calculated from V_{oc}, J_{sc} and FF, are deviating from the actual values, because the differences add up (see tables 6.14 and 6.15). Still the results are encouraging, not only if one considers that the model is based on just 36 substrates. Although 36 substrates are a large number comparing to what is typically published in literature, the experiments will need to continue to create a large data base.

Summary

- A linear model for V_{oc}, J_{sc} and FF was developed on basis of the PCA. It uses the fact that the last principal components have near zero variance, indicating a linear relationship between the variables.

- The cross-validation of the developed statistical model can reproduce the OSC properties well, given the small data set. Especially the pre-

dicted values for V_{oc} look promising as all are within 10% of the actual values. This suggesting that the main production parameters with an influence on V_{oc} are included in the model.

- The larger discrepancies between predicted and actual values for J_{sc} and FF (21 of 36 substrates predicted <10% from actual values) suggest that one or more underlying parameters, which leads to variations, have not yet been included in the PCA. Possible candidates are the humidity during PEDOT:PSS spin-coating, which will be monitored in future, and the morphology the absorber layer, which is difficult to parameterise and capture in the PCA.

- Removing substrates from the data base used for the model reduces the quality of predictions, suggesting that the number of substrates (36) is at the lower limit of substrates necessary to construct the statistical model.

- The quality of the model has to be verified with new experiments, which are currently being planned.

6.3.2 Outlook: Optimisation of the Production Process

Based on the model, a method for the optimisation of the production process is proposed. The model structure developed in section 6.3 gives linear equations for V_{oc}, J_{sc} and FF (equations 6.14a to 6.14c and equation 6.10). The power conversion efficiency η, i.e. the value which should be optimised, is given by

$$\eta = FF\frac{V_{oc}\ J_{sc}}{P_{ill}}, \tag{6.16}$$

where P_{ill} is the intensity of the incident light. Equation 6.16 has to be optimised subject to certain boundary conditions. The boundary conditions should be chosen such that the parameters can only move within the limits, in which the experiments were carried out (see table 6.2). Outside this range, the model will most likely fail. Furthermore the order of the PEDOT:PSS spin-coating should be fixed, because the detrimental effect of separating a batch into 2x4 substrates has been shown. Variations in this parameter can be avoided by using a different airlock for the second four substrates.

Using equations 6.14a, 6.14b and 6.14c and keeping in mind that $\sum_a(\mathbf{p})$, $\sum_b(\mathbf{p})$ and $\sum_c(\mathbf{p})$ are functions of $\mathbf{p}^T = (p_1, \ldots, p_{15})$

$$\arg\max_{\mathbf{p}} \eta(\mathbf{p}) = FF(\mathbf{p}) \frac{V_{oc}(\mathbf{p})\ J_{sc}(\mathbf{p})}{P_{ill}}, \tag{6.17}$$

has to be solved. This leads to a set of equations that has to be satisfied in order to arrive at an extremum

$$\frac{\partial \eta}{\partial p_i} = 0; \quad i = 1, \ldots, 15. \tag{6.18}$$

The equation 6.17, of which the maximum has to be found, describes a surface in a 15-dimensional space. The optimisation of equation 6.17, i.e. the search for a maximum, could be carried out with the Levenberg-Marquardt Algorithm (section 5.1.2). The boundaries are given by the range of the production parameters used during this experimental run, i.e. a solution is searched within the used parameter range. The optimisation should yield a set of production parameters, which will lead to an OSC with an optimised power conversion efficiency η.

Chapter 7

Outlook

During the course of this thesis the fundamental requirements for a sound statistical analysis of organic solar cells (OSCs) were developed. Furthermore the principal component analysis was presented as multivariate method to search for pattern in the data, with a particular focus on the correlations between production parameters and OSC properties.

Production Process

The structuring and standardisation of the OSC production process revealed more than 40 different production parameters, which are now routinely recorded for every substrate. Obtaining a standardised set of production parameters made a comparative OSC production possible. However, the PCA and the developed statistical model also showed that there are apparently influential parameters, which have not been monitored yet.
The PCA has identified the duration of the manual evaporation process as influential parameter, but the physical origin has yet to be determined. Although a first crude estimate of the heat transfer suggests little influence of the temperature, it should be at least monitored for some evaporation steps to have a direct access to this parameter. It should be possible to mount a small thermocouple inside the evaporation chamber at a similar distance to the source as the substrates are. Attaching the thermocouple directly to the substrates is as first evaluation difficult, because the substrates continuously rotate during evaporation. If however, the temperature is identified as important production parameter during a PCA, it would be advantageous to measure the temperature at the substrates. The other related process parameters, e.g. the evaporation pressure, are already monitored more closely.

However, in order to be eventually able to reproduce a good evaporation process it is suggested to replace the human factor in the evaporation process by an automated control of the evaporation process in the long run.
The second parameter, which might be responsible for some observed variations in OSC properties, especially in the fill factor FF, is the humidity during the spin-coating outside the glovebox. It is thought to be the cause of the detrimental effect seen in FF of the four substrates, which were spin-coated with PEDOT:PSS first and thus already had cooled down when they were exposed to ambient air. Thus a hygrometer has already been installed at the spin-coater used for the PEDOT:PSS spin-coating. The splitting of a batch of eight substrates into 2×4 substrates for the PEDOT:PSS spin-coating can be continued, but the exposure to ambient conditions of the already cooled down substrates has to be avoided by using a different airlock in future.
One issue, which has not received any attention during this thesis, but would be paramount is making different P3HT:PCBM absorber solutions comparable. The filtering of an absorber solution has become an integral part of the solution preparation process, because it removes particles otherwise deteriorating the quality of the absorber layer. However, during filtering, an unknown part of the P3HT and the PCBM is also held back by the filter, the amount of which varies. Even though two solutions were prepared from the same "master" solution, it was found that their absorption spectra differed in peak heights for the absorption peaks of P3HT and PCBM. This indicates a difference in the ratio between P3HT and PCBM. Developing a measure to account for these differences would make the two solutions comparable and thus the OSCs made from these solutions. This would to substantially increase the number of OSCs for which comparable production parameters can be recorded. Features of the absorption spectra, e.g. the relative peak height of the peaks of P3HT and PCBM, could be used as preliminary parameters. It received no attention in this thesis, because all OSCs which were presented were made from exactly the same absorber solution, which had been filtered once.

Automation of Measurement Methods

The automation of the measurement methods has been paramount for the reliable characterisation of the OSCs. The automated setup has been planned

and designed versatile from the beginning such that there is room for further extensions.

At the time of writing, the error in the spectral response (SR) measurement, which made the measured data only useful for qualitative comparison, has unfortunately not been found yet. Resolving this issue and reconciling the results for the short circuit density obtained from the SR measurement and the current-voltage measurement should receive the highest priority. The data of the SR measurement is very important, because it contains information about both the absorption and the charge carrier transport. Together with the absorption measurement and optical simulations, it would be possible to calculate the internal quantum efficiency (IQE), i.e. assessing efficiency of exciton dissociation and charge carrier transport.

The four-wire configuration ensures a high accuracy in the measured voltage across an OSC. In order to achieve a similar accuracy in the measured current densities, it is suggested to include an accurate checking of the photovoltaic area of each OSC. A visual inspection of every OSC is currently done, but it is not possible to quantify the loss in photovoltaic active area, if the misalignment of bottom and top electrode happens to be outside the built-in tolerances of the substrate layout. For an accurate measurement of the photovoltaic active area, it would be necessary to obtain a high resolution image of each OSC. Using a microscope is not practical due to several reasons, e.g. the substrate had to be removed from the glovebox and exposed to ambient conditions leading to a degradation of the OSCs. The most practical solution would be the integration of a small digital camera on the XY-table, which can obtain high resolution pictures of each substrate. The XY-table provides sufficient room and including the imaging into the LabView program should be straight forward due to the modular design of the program. With the help of imaging software, which could use the optical markers already present on the used substrates, it should be possible to obtain a very accurate value for the photovoltaic active area of each OSC. This then can be used to scale the measured current I to the current density J, an intensive OSC property. Furthermore, obtaining a picture of all substrates would be of great help in assessing the quality of the spin-coated layer and make data cleaning more reliable through a better categorisation of damaged solar cells.

Electronic Laboratory Notebook

The electronic laboratory notebook (ELN) unites production protocols and measurement data of all OSCs made in our lab, making an efficient access and linking of the data inside the ELN possible. The measured data is currently analysed for about 15 OSC properties. However, there is clearly more information in the measured data, the aggregation of which was not possible during the course of this thesis.

The log-plots of the representative dark IV-curves were shown during the analysis of the main physical phenomena observed during the analysis. Distinct changes can be observed going from non-annealed to annealed OSCs on the same substrate and between OSCs on different substrates. However, fitting a two diode model to the measured data did not yield acceptable fits. Thus until a suitable model is in place to describe the dark IV-curves, phenomenological characteristics, e.g. the slope before and after the change in slope around 0.3V, could be used. It would be especially interesting to investigate the behaviour of these characteristics upon annealing. Since there are no optically generated charge carriers in the device, the IV-curve should only be governed by the interfaces and the morphology of the absorber layer. During the analysis of the dark IV-curves, it became obvious that the OSCs all open in reverse bias in a way with can be fitted well with a simple exponential function with two parameters (p_1, p_2)

$$J = p_1 \left(exp(p_2 V) - 1\right) \quad \text{for } V < 0\text{V}. \tag{7.1}$$

However, the physical meaning of the parameters, the effect on the forward bias and their correlation with other OSC properties has yet to be determined. It is observed that IV-curves with a large opening in reverse bias generally have a reduced performance. The size of the opening in reverse changes upon annealing and J at -1V bias is typically reduced by about an order of magnitude, but it does not disappear.

Optical simulations of the absorption spectrum strongly indicate a linear relation between the position of the first absorption minimum between 320 and 540nm and the thickness of the absorber layer. First comparisons with values for the absorber layer thickness obtained by AFM measurements confirm this, but it requires more direct measurements of the absorber layer thickness, e.g. via AFM, to put the optical determination of the layer thickness on a solid base. As indicated in the PCA with OSC properties only, the extrema in the

absorber spectrum between 320 and 540nm exhibit a particular trend, which is apparently caused by changes in the absorber thickness. Using more than just the first absorption minimum for estimating the absorber layer thickness should make the method more reliable. Especially for absorber layers exceeding 160nm in thickness, an additional absorption minimum moves from below into the analysed region.

Data Analysis

The focus of the PCAs performed in this thesis was on attributing the variations seen in OSC properties to variations during the production process. During the first run of experiments all parameters which can be held fixed for all substrates were held fixed. This limited the variations to parameters, which unintentionally varied, yet were monitored. The analysis then showed the range of variations in OSC properties originating only from the "unintentional" variations during production, i.e. parameters which varied due the nature of the process.
It is suggested to conduct another experimental series with more OSC and in which it should be sought to minimise correlations between production parameters. Subsequently, the spin-coating speed of the absorber layer is suggested as first intentional variation in the production process. Variations between ω_{SC}=500 to 2000rpm in e.g. five steps should lead be a sensible coverage of the parameter range in order to assess the influence of ω_{SC} on OSC performance and its reproducibility.
The PCA with 15 production parameters and just one OSC property showed the large influence of the correlations between only the production parameters. During the interpretation of the PCA result, these correlations were taken into account as background correlations. However, often drawing firm conclusions was difficult. Therefore three solutions are suggested, which should be followed in parallel: (1) reducing the number of unintentional variations as much as possible, e.g. using a computer-controlled evaporation process, will lead to a reduction of possible correlations between unintentional parameter variations, thus leading to big improvements. However there are some variations, e.g. the time intervals between the production steps, which will always vary between the substrates of one batch and correlations between included parameters can still dominate the PCA. (2) Therefore as second measure a continuous assessment of the correlation between the production

parameters from batch to batch with the help of the PCA is suggested. Intentional parameter variation and unintentional ones, as far as possible, should be adjusted such that their correlations are reduced. (3) Finally, if there are still substantial correlations between the production parameters, it is necessary to develop a framework for the interpretation, which takes the background correlations into account. This would be best done with simulated data of known correlation. Then the changes in the principal component vectors caused by adding an extra variable to variables on which a PCA has already been carried out could be investigated.

The cross-validation of the model, which has been developed on the basis of the PCA shows promising results. Especially the predictions for the open circuit voltage V_{oc} are good, making the presented model the first model, which links production parameters and the V_{oc}. The predictions of the short circuit current density J_{sc} and the fill factor FF indicate that there are apparently parameters, which have not been included yet. Two parameters, which should be recorded during production in future are the humidity during PEDOT:PSS spin-coating and the temperature during evaporation. Still, with the present data, the model can be used to find optimised production parameters. Using the prediction of V_{oc}, J_{sc} and FF, the power conversion efficiency η can be obtained as function of the production parameters. However, neither the maximisation of the calculated η nor the testing of the proposed optimised production parameters could be carried out during the course of this thesis (see 6.3.2).

One parameter, which is difficult to quantify, but should soon receive a qualitative treatment is the effect of the morphology of the absorber layer. Although the morphology should be governed to a large extent by the production parameters, it is necessary to quantify the changes in morphology of the absorber layer in dependence of the production process. A fingerprint of the morphology could be obtained from the AFM images using specialised algorithms [98]. Interfaces to the ELN exist and thus these algorithms could be easily linked to the ELN.

Chapter 8

Conclusions

One of the major goals of research on organic solar cells (OSCs) is the improvement of the power conversion efficiency η. However, the large variety of organic semiconductors available and the many production parameters make a deterministic approach difficult. Statistical methods are required to analyse the performance of the materials and the reproducibility of OSCs made with them.
The focus of this thesis is both the development of an experimental platform to permit such a statistical analysis and to subsequently investigate – based on this platform – the influence of the production process on the OSC performance and reproducibility using principal component analysis (PCA). The model system used for the experiments is the currently most intensively investigated OSC system, i.e. devices based on P3HT:PCBM.
The platform consists of a standardised production process, an automated OSC characterisation setup and a flexible, yet efficient, data management infrastructure. This platform is necessary to acquire an adequate amount of well-documented OSC production and measurement records, i.e. the prerequisite for any statistical analysis.

Standardisation of the Production Process

To make the production of all OSCs comparable, the production process was structured and standardised. A set of more than 40 production parameters has been defined, which is now routinely recorded in a standardised way for every OSC made in our laboratory. With this data, the complete production history of an OSC can be traced.
The production parameters were divided into three groups: (1) parameters,

which can be controlled well and repeated for any substrate, such as the spin-coating speed for the organic layers; (2) time intervals, which vary from substrate to substrate within one batch due to the sequential spin-coating of each individual substrate; and (3) parameters, which vary due to human involvement and outside influences.
Previously only the six parameters of the cathode deposition process (2×pressure, layer thickness, rate and 2×duration) had been considered as causes for the variations in OSC properties, although they had not been investigated systematically. The remaining four parameters in (3), like the temperature during spin-coating, were initially assumed to be negligible, but did not turn out to be so at least for this parameter. The four time intervals of (2) had not been considered before and were found to have a significant influence on the OSC properties.

Automation of the OSC Characterisation

In addition to well-documented OSC production records, a corresponding large and consistent pool of measurement data is necessary for the many OSCs made. Therefore new substrates were developed and all common OSC characterisation methods were combined into a single multi-purpose automated measurement setup.
The new substrates are all based on a standardised contact pad structure, allowing the realisation of different layouts, e.g. for up to 10 OSCs, on the 25×25mm^2 substrate area. All substrates can be used in the new multiple mount, which can hold and contact up to nine substrates simultaneously. Substrates in the multiple mount can be characterised with current-voltage, spectral response and absorption measurements, which were all integrated into one automated setup. This combination allows reliable and versatile OSC characterisation with a high throughput. For example, the current-voltage characterisation of 90 OSCs at one light intensity can now be carried out within 90 minutes without any manual interaction, instead of requiring attention every minute. The automated setup additionally provides the flexibility for further extension.
The automation made the measurements less prone to human error and led to a standardised characterisation cycle. The successful automation of the main characterisation methods resolved a significant bottleneck in the experimental cycle, which would otherwise have made the reliable acquisition of

the required amount of characterisation data impossible.

Electronic Laboratory Notebook

The logging of more than 40 production parameters and the acquisition of large amounts of measurement data requires an efficient data management infrastructure for which an electronic laboratory notebook (ELN) and the corresponding computational tools were developed.
The ELN unites the data from two different sources – the user-friendly webinterface for the production protocol and the standardised output files from the automated characterisation – and stores them all in a hierarchical structure. The efficient access and linking of all data within the ELN creates the basis for the data analysis. The measurement data in the ELN is analysed and OSC properties are deduced, which are also stored in the ELN.
Parameterisation of the OSC characteristics is necessary to obtain scalar OSC properties, which can be used for the analysis. For the extraction of the properties splines have been used for all OSC. No equivalent circuit model could be found with parameters, which adequately fitted the current-voltage characteristics for fill factors FF below 0.4. This low FF is found in nearly 20% of the made OSCs and its physical origin currently subject to internal discussion.
Data quality has very high priority, which is ensured by a set of graded measures. The most important ones are syntax checks at the input stage, unit testing for the code, which handles the data, and keeping a continuous history tracking changes inside the ELN. As a result, none of the production records had to be excluded due to erroneous entries. However, it turned out that the final step of data preparation, i.e. the manual pruning of the measurement data for characteristics which can be explained by defects or artefacts rather than variations in production parameters, took more than 60% of the time necessary for the data analysis. Of the 360 OSCs made, 21% had to be sorted out. Automation or semi-automation of this process would therefore lead to a considerable time saving.

Experimental Results

36 substrates with a total of 360 OSCs were made. During production only the 15 parameter varied, which due to the nature of the production process always vary but had yet not been investigated systematically. This was done

to investigate the resulting variations in OSC properties, which need to be considered when assigning a significance to the effect of additional production parameters when varied intentionally.

Despite the standardised production process and keeping the majority of production parameters fixed, the measured OSC properties showed a wider spread than expected. For a reproducible production process, variations in η of $\pm 10\%$ around the mean, i.e. here $(2.0 \pm 0.2)\%$, would be reasonable, but a spread of nearly $\pm 50\%$ around the mean was obtained ($1.1\% \leq \eta \leq 2.8\%$). It was found that the spread in FF, which varied most between the substrates (0.29–0.50) was determining η. Already a focus on improving the FF from the obtained values to 0.6, which is often reported in literature, will lead to $\eta > 3.5\%$.

The only difference between the 360 OSCs was in production parameters, which are hardly mentioned in literature. This places the literature on P3HT:PCBM OSCs in a new light, where typically only the results of a few OSCs are presented without showing their significance. If our observations hold for the OSC production in other groups as well, both the production parameters have to be described in more detail and the significance of the results has to be shown in publications. Without this information the interpretation of the published results is difficult for the reader. However, assigning a significance to effects observed in OSC properties generally requires the investigation of a large number of OSCs. This proves the necessity of a systematic and statistical approach, the experimental tools of which were developed as part of the work on this thesis.

Principal Component Analysis

Principal component analysis (PCA) was used as a suitable method in the search for the production parameter or combination of parameters, which significantly contributed to the variations in the observed OSC properties. A PCA including the 15 production parameters, which varied, and η showed that the correlation between the production parameters only governed the behaviour of the largest principal component (PC). These correlations were taken into account as background correlations during the interpretation of the PCA results. Furthermore, it was found that the eigenvalue λ_α of a PC is not an adequate measure for the importance of a PC for η. λ_α alone does not reflect the contribution of the variable η to a PC. Therefore $|\eta\ \lambda_\alpha|$, i.e.

the weighting of λ_α with the contribution of the variable η to a PC, was introduced as a new measure of significance. This led to PC 2, PC 4 and PC 3 for the three most relevant PCs for η in decreasing order. PC 1 follows only ninth when ranked by $|\eta\ \lambda_\alpha|$.

The results of the PCA[1] suggest that – within the observed range (300-900s) – an extended duration of the Al-cathode deposition has a negative impact on η. This is indicated by a negative correlation between the duration of the vacuum deposition and η (PC 2) and a positive correlation between the pressure during evaporation (7-13·10^{-6}mbar) and η (PC 3). The latter parameter is typically higher for shorter deposition times. The results confirm experience from the laboratory, but the physical origin has yet to be found. A crude estimation of the heat transfer to the OSCs indicates that thermal stress is unlikely to be the cause.

The PCA also indicates that it is important to allow the absorber layer to dry slowly after spin-coating. A longer time interval between absorber spin-coating and drying of the absorber layer under vacuum (PC 4), and also a temperature during spin-coating (PC 3 and PC 4) at the lower end of the range (24-27°C), leave more time for the 2-phase system to relax to a more favourable morphology. This is in line with what is reported in the literature [61].

It was found that two parameters did not make any significant contributions to the first 7 PCs when ordered according to $|\eta\ \lambda_\alpha|$. The age of the absorber solution (3h to 22 days) and the duration of the PEDOT:PSS drying during the transfer into the glovebox (46-162min) both have negligible contributions up to PC 10 (seventh by $|\eta\ \lambda_\alpha|$). Hence they can receive less attention in future.

Although the set of data, which was used for the PCA, was large in term of what has previously been realised for OSCs in literature, it is at the lower limit of what is useful for the PCA, because correlations between production parameters still dominated the results. A new series of experiments should be planned which will involve more OSCs and in which it is sought to minimise correlations between production parameters.

On the basis of the PCA conducted, a statistical model was proposed and its quality tested via cross-validation. The model is used to predict the values of the open circuit voltage V_{oc}, the short circuit current density J_{sc} and FF (and

[1] The corresponding tables with all 18 PCs can be found on pages 194 and 195.

hence η), given the set of 15 production parameters which varied during the production process. The first results are promising, e.g. all values for V_{oc} are predicted within 10% of their measured values. However, the model cannot account for some variations seen in J_{sc} and FF, indicating that there are still parameters which have some influence on the OSC properties but have not yet been included in the analysis. Two additional parameters for the production protocol are proposed: the substrate temperature at the substrate during cathode deposition and the humidity during PEDOT:PSS spin-coating. The first is necessary to assess the thermal influence directly in order to narrow down the causes for the detrimental effect of an extended evaporation step. The second had been found to affect the OSC performance negatively when the cooled PEDOT:PSS layer was exposed to ambient conditions.
Numerical optimisation of the model, i.e. maximisation of the calculated η, should yield improved production parameters, but could not be carried out within time of this thesis.

To summarise, this work created a solid platform for the acquisition and management of well-documented OSC preparation and measurement records, the fundamental requirements for sound statistical analysis. PCA was established and used to search the data obtained for P3HT:PCBM OSCs for correlations, in order to explain the large observed spread in the measured OSC properties. It was found that variations in the evaporation process of the cathode have a significant influence on the OSC properties and it was confirmed that slow drying of the absorber layer leads to an improved OSC efficiency. Further links between production parameters and OSC properties were suggested and all necessary tools are in place to allow further investigations of the observed correlations and future material screening and OSC concept development. On the basis of the PCA, a statistical model was proposed, which can predict the main OSC properties given the production parameters. Thus, numerical optimisation of the predicted OSC properties should lead to improved production parameters, resulting in more reproducible OSCs with better performance.

Appendix A

Symbols and Constants

Symbol	Description	Units
α	exponential factor	
$\mathbf{\Gamma}$	PCA transformation matrix	
Δt_1	Δt[UV→PEDOT-SC]	s
Δt_2	Δt[PEDOT-SC→Oven]	s
Δt_3	Δt[Airlock→Absorber-SC]	s
Δt_4	Δt[Absorber-SC→Vacuum]	s
$\frac{\Delta d_{5nm}}{\Delta t}(i)$	rate of the first 5nm of the $t_{evap}(i)$ layer	ms^{-1}
$\frac{\Delta \omega_{SC}(i)}{\Delta t}$	ramp of spin-coating stage i	s^{-2}
ϵ_0	permittivity of free space	$\mathrm{AsV}^{-1}\mathrm{m}^{-1}$
ϵ_r	relative permittivity	
η	power conversion efficiency	%
λ	wavelength	m
$\mathbf{\Lambda}$	diagonal matrix	
μ	charge carrier mobility	$\mathrm{cm}^2\mathrm{V}^{-1}\mathrm{s}^{-1}$
μ_n	electron mobility	$\mathrm{cm}^2\mathrm{V}^{-1}\mathrm{s}^{-1}$
μ_p	hole mobility	$\mathrm{cm}^2\mathrm{V}^{-1}\mathrm{s}^{-1}$
ξ	damping factor (Levenberg-Marquardt Algorithm)	
σ	standard deviation	
σ_{SB}	Stefan-Boltzmann constant	$\mathrm{Wm}^{-2}\mathrm{K}^{-4}$
ϕ_B	potential barrier	eV
Φ_m	workfunction of metal	eV
$\omega_{SC}(i)$	speed of i^{th} spin-coating stage	s^{-1}
ω_0	transfer rate	s^{-1}
ω	angular frequency	s^{-1}
$\mathcal{E}$	energy	eV
$\mathcal{G}$.	generation rate	$\mathrm{cm}^{-3}\mathrm{s}^{-1}$
$\mathcal{R}$	recombination rate	$\mathrm{cm}^{-3}\mathrm{s}^{-1}$
$\mathbf{a}$	a column vector	
$\mathbf{a}^T$	the transpose of column vector $\mathbf{a}$	
$\mathbf{A}$	a matrix	

A	absorption	
A_{act}	absorption in the photovoltaic active layer	
c_A	concentration of electron acceptor	gl^{-1}
c_D	concentration of electron donor	gl^{-1}
$d_{evap}(i)$	duration of evaporation the i^{th} layer	s
$D_e(E)$	density of one-electron states	cm^{-3}
D	diffusion constant	$\mathrm{m}^2\mathrm{s}^{-1}$
e	elementary charge	As
$\hat{\mathbf{e}}$	a unit vector	
E_{eff}	effective electrical band gap	eV
$E_{AM1.5g}$	solar spectrum according to the AM1.5g standard	$\mathrm{Wm}^{-2}\mathrm{nm}^{-1}$
E_{ext}	external applied electric field	Vm^{-1}
$E_{F,C}$	quasi-Fermi energy for electrons	eV
$E_{F,V}$	quasi-Fermi energy for holes	eV
E_{HOMO}	energy at the edge of the HOMO	eV
E_{LUMO}	energy at the edge of the LUMO	eV
E_λ	energy for reorganisation	eV
E_C	energy at the conduction band edge	eV
E_F	Fermi energy	eV
E_G	band gap of semiconductor	eV
E_s	spectrum of a light source	$\mathrm{Wm}^{-2}\mathrm{nm}^{-1}$
E_V	energy at the valence band edge	eV
$E(x)$	electrical field due to redistribution of charges	Vm^{-1}
E	energy	eV
$evap_{src}(i)$	evaporation source for i^{th} layer	
$f_B(E)$	function of the Boltzmann distribution	
$f_F(E)$	function of the Fermi-Dirac distribution	
f''	the second derivative of a function f	
$f^{(k)}$	the k^{th} derivative of a function f	
FF	fill factor	
$\hbar$	Planck constant	eVs
$\mathbf{H}(\mathbf{p})$	Hessian matrix of vector $\mathbf{p}$	
i	index	
I	current	A
$\mathbf{I}$	identity matrix	
I_0	current of a reference solar cell at SRC	A
I_{01}	diode dark saturation current	A
$I_{evap}(i)$	current used for evaporation	A
I_p	ionisation potential	eV
I_{ph}	photocurrent	A
J	current density	Am^{-2}
$\mathbf{J}(\mathbf{p})$	Jacobian matrix of vector $\mathbf{p}$	
J_{1V}	current density at 1V forward bias	Am^{-2}
j_E	energy flux	Wm^{-2}

J_{mpp}	current density at the maximum power point	Am^{-2}
$J_n(x)$	electron current density	Am^{-2}
$J_p(x)$	hole current density	Am^{-2}
J_{sc}	short circuit current density	Am^{-2}
J_{sc}^{SR}	current density obtained via SR-measurement	Am^{-2}
J_{scl}	space charge limited current density	Am^{-2}
k_B	Boltzmann constant	$e\mathrm{VK}^{-1}$
M	spectral mismatch factor	
n_1	diode ideality factor	
N_C	effective density of states of the conduction band	m^{-3}
n_i	intrinsic charge carrier density	m^{-3}
N_V	effective density of states of the valence band	m^{-3}
n	electron density in the conduction band	m^{-3}
OP	parameter for the order of PEDOT:PSS spin-coating	
$p_{base}(i)$	base pressure of evaporation of layer i	Pa
P_{el}	electrical power	VA
$p_{evap}(i)$	pressure during evaporation of layer i	Pa
P_{ill}	illumination intensity	Wm^{-2}
P_{mpp}	electrical power at the maximum power point	VA
p_d	pressure of drying	Pa
p	hole density in the valence band	m^{-3}
r	recombination constant	$\mathrm{m}^3\mathrm{s}^{-1}$
R	reflectivity	
R_{1V}	resistance at 1V forward bias	Ω
r_B	Bohr radius	m
r_C	radius of Coulombic potential well at k_BT	m
$\mathbf{r}(\mathbf{p})$	residual vector of some function f with parameters $\mathbf{p}$	
$\mathbf{R}$	correlation matrix	
R_{dark}	reflectivity of the dark reference	
R_{ij}	distance between hopping sites i and j	m
R_{oc}	resistance at open circuit	Ω
R_p	parallel resistance	Ω
R_s	serial resistance	Ω
R_{sample}	reflectivity of the sample	
R_{sc}	resistance at short circuit	Ω
R_{white}	reflectivity of the white reference	
$\mathbf{S}$	covariance matrix	
SR_{ref}	spectral response of a reference solar cell	AW^{-1}
SR_{test}	spectral response of a test solar cell	AW^{-1}
SR	spectral response	AW^{-1}
T	temperature	K
$t_{bath}(i)$	duration of i^{th} cleaning bath	s
$T_{bath}(i)$	temperature of i^{th} cleaning bath	K
t_{evac}	duration of the vacuum of evaporation	s

T_{mix}	temperature at which solution is mixed	K
t_{pt}	duration of post-treatment	s
T_{pt}	temperature of post-treatment	K
$t_{SC}(i)$	dwell of spin-coating stage i	s
T_{SC}	temperature during the spin-coating process	K
t_{UV}	duration of UV-Ozone treatment	s
t_d	duration of drying	Pa
T_d	temperature of drying	K
t_{sol}	Age of Absorber-Solution	s
V_{bi}	built-in potential	V
V_{mpp}	voltage at the maximum power point	V
V_{oc}	open circuit voltage	V
V_{pt}	voltage bias during post-treatment	V
V_{sol}	volume of solution used for spin-coating	l
V_0	compensation voltage, V at $J_d - J_{ph} = 0$	V
V_d	vacuum level offset	eV
V	voltage	V
w_e	mean drift length of electrons	m
w_h	mean drift length of holes	m
$\mathbf{y}_{(i)}$	observation vector of variable i	
$\mathbf{y}_i$	observation vector of sample i	
$\bar{\mathbf{y}}$	mean of vector $\mathbf{y}$	
$\tilde{\mathbf{y}}$	normalised observation vector with $\bar{\tilde{\mathbf{y}}}$=0 and $\sigma_{\tilde{\mathbf{y}}}$=1	
$\mathbf{Y}$	observation matrix in terms of original variables	
$\mathbf{Z}$	observation matrix in terms of principal components	

Appendix B

List of Abbreviations

Abbreviation	Description
A	acceptor
AFM	atomic force microscopy
Al	aluminium
AM1.5g	air mass 1.5 global, the solar standard spectrum
an	annealed, i.e. with post-treatment
CB	conduction band
CCD	charged-coupled device
D	donor
DCB	o-dichlorobenzene
DI-water	deionised water
DMM	digital multi-meter
DRY	Don't repeat yourself
e	electron
ELB	electronic log base
ELN	electronic laboratory notebook
EQE	external quantum efficiency
FMF	Freiburg Materials Research Center
Fraunhofer ISE	Fraunhofer Institute for Solar Energy Systems
FWHM	full width at half maximum
GB	glovebox
GRP	glass-fibre re-enforced plastic
GUI	graphical user interface
h	hole
HDF5	Hierarchical Data Format, version 5
HOMO	highest occupied molecular orbital
ID	identifier
IPCE	incident photon to converted electron efficiency
IQE	internal quantum efficiency
ITO	indium-tin-oxide
IV	current-voltage

LF	laminar flow
LiF	lithiumfluoride
LMA	Levenberg-Marquardt Algorithm
LOTSDSC5	a calibrated reference solar cell
LCAO-MO	linear combination of atomic orbitals molecular orbitals
LUMO	lowest unoccupied molecular orbital
MDMO-PPV	poly(2-methoxy-5-(3,7-dimethyloctyloxy)- -1,4-phenylene vinylene)
MO	molecular orbital
mpp	maximum power point
MySQL	an open source database management system
n-QFL	electron quasi Fermi level
nan	non-annealed, i.e. without post-treatment
OFET	organic field effect transistor
OLED	organic light emitting diode
OSC	organic solar cell
p-QFL	hole quasi Fermi level
P3HT	poly(3-hexylthiophene)
PA	poly(acetylene)
PC	principal component
PCA	principal component analysis
PCV	principal component vector
PCBM	1-(3-methoxycarbonyl)-propyl-1-1-phenyl-(6,6)C_{61}
PEDOT	poly(3,4-ethylenedioxythiophene)
PL	photoluminescence
PSS	poly(styrene-sulfonate)
PT	post-treatment
QFL	quasi-Fermi level
rpm	rounds per minute
RR	regioregularity
RT	room temperature
S 419 p4	organic solar cell 9 on substrate S 419
SC	spin-coating
SR	spectral response
SRC	standard reporting conditions
UPS	ultraviolet photoelectron spectroscopy
UV	ultraviolet
VB	valence band
Xe	Xenon
XML	extended markup language

Appendix C

Tables

The tables on the following pages and the corresponding data, on which these tables are based, are available in electronic form from the Konstanzer Online-Publikations-System (KOPS).

Table C.1: *Summary of the OSC properties for batches 1 to 3 after pruning the measurement data. The first half of the table shows the substrate, the working number of OSCs on the substrate (OK) and the average values including standard deviation of the working OSCs for the open circuit voltage V_{oc}, the short circuit current density J_{sc}, the fill factor FF, the power conversion efficiency η and the position of the first minimum between 320 and 540nm in the absorption spectrum, a measure for the film thickness. The second half of the table gives the explanation on why particular OSCs on a substrate were excluded from the analysis. The abbreviations are as follows: NC=no/partial cover with absorber layer, B=defects caused by bubbles, SC=defects by scratches, P=particles, C=contact problems and U=unknown. The defect categorisation is described in section 5.3.1 on page 104.*

Substrate	Batch	OK	V_{oc} / V	J_{sc} / mA/cm^2	FF	η / %	1st Abs. Min / nm	NC	B	SC	P	C	U
S 408	1e1	10	0.58±0.00	9.6±0.4	0.48±0.02	2.7±0.2	355.7±0.5	-	-	-	-	-	-
S 410	1e1	7	0.57±0.03	8.6±0.2	0.41±0.02	2.0±0.1	357.8±1.2	-	1	1	-	1	-
S 411	1e1	6	0.56±0.01	9.1±0.3	0.43±0.01	2.2±0.1	358.4±1.1	-	-	3	1	-	-
S 413	1e1	8	0.55±0.02	8.8±0.3	0.41±0.04	2.0±0.1	353.8±1.1	1	-	1	-	-	-
S 407	1e2	8	0.50±0.01	8.7±0.5	0.42±0.03	1.8±0.2	356.7±2.2	1	-	-	1	-	-
S 409	1e2	6	0.50±0.01	8.1±0.5	0.39±0.02	1.6±0.1	357.5±0.8	1	2	-	-	1	-
S 412	1e2	8	0.51±0.02	8.5±0.4	0.39±0.03	1.7±0.1	357.6±1.6	-	-	-	-	2	-
S 414	1e2	8	0.50±0.01	8.7±0.3	0.42±0.02	1.8±0.1	356.0±1.1	-	-	2	-	-	-
S 416	2e1	9	0.56±0.01	9.4±0.2	0.43±0.02	2.3±0.1	355.3±0.7	-	-	-	1	-	-
S 417	2e1	7	0.56±0.01	9.4±0.2	0.45±0.01	2.3±0.1	356.5±0.6	-	-	-	1	2	-
S 419	2e1	6	0.56±0.01	10.1±0.6	0.50±0.01	2.8±0.1	362.7±0.6	1	-	-	1	2	-
S 421	2e1	10	0.55±0.01	9.5±0.2	0.50±0.01	2.7±0.1	356.3±0.6	-	-	-	-	-	-
S 423	3	8	0.50±0.01	9.1±0.4	0.37±0.02	1.7±0.2	359.5±0.6	-	-	1	1	-	-
S 424	3	8	0.51±0.02	9.1±0.3	0.40±0.05	1.8±0.1	355.2±1.8	-	-	1	1	-	-
S 425	3	9	0.50±0.01	9.1±0.4	0.40±0.03	1.9±0.2	353.4±0.7	-	-	-	1	-	-
S 426	3	7	0.48±0.01	9.1±0.3	0.43±0.03	1.9±0.1	356.7±0.7	-	-	1	-	1	1
S 427	3	6	0.48±0.01	10.0±0.4	0.44±0.01	2.1±0.1	358.1±0.8	-	-	1	-	3	-
S 428	3	9	0.49±0.00	9.2±0.3	0.42±0.01	1.9±0.1	362.5±0.5	-	-	-	-	-	1
S 429	3	9	0.48±0.01	9.3±0.3	0.46±0.01	2.0±0.1	358.0±1.1	-	-	-	-	1	-
S 430	3	8	0.47±0.01	9.4±0.3	0.45±0.02	2.0±0.1	359.3±0.8	-	-	1	1	-	-

Table C.2: *Summary of the OSC properties for batches 5 and 6 after pruning the measurement data. The first half of the table shows the substrate, the working number of OSCs on the substrate (OK) and the average values including standard deviation of the working OSCs for the open circuit voltage V_{oc}, the short circuit current density J_{sc}, the fill factor FF, the power conversion efficiency η and the position of the first minimum between 320 and 540nm in the absorption spectrum, a measure for the film thickness. The second half of the table gives the explanation on why particular OSCs on a substrate were excluded from the analysis. The abbreviations are as follows: NC=no/partial cover with absorber layer, B=defects caused by bubbles, SC=defects by scratches, P=particles, C=contact problems and U=unknown. The defect categorisation is described in section 5.3.1 on page 104.*

Substrate	Batch	OK	V_{oc} / V	J_{sc} / mA/cm^2	FF	η / %	1st Abs. Min / nm	NC	B	SC	P	C	U
S 439	5	7	0.50±0.01	9.0±0.2	0.36±0.01	1.6±0.1	356.0±0.7	-	-	-	1	1	1
S 440	5	8	0.47±0.01	8.4±0.3	0.29±0.01	1.1±0.1	357.7±0.9	-	-	-	1	-	1
S 441	5	9	0.49±0.01	9.0±0.3	0.35±0.03	1.6±0.1	356.2±0.7	-	-	-	1	-	-
S 442	5	9	0.46±0.01	8.6±0.6	0.31±0.02	1.2±0.1	354.8±1.0	-	-	-	-	1	-
S 443	5	8	0.47±0.01	9.9±0.4	0.45±0.01	2.1±0.1	361.5±1.4	-	-	1	-	1	-
S 444	5	8	0.49±0.01	9.5±0.2	0.44±0.04	2.1±0.2	356.1±1.2	-	-	1	-	1	-
S 445	5	4	0.48±0.02	9.1±0.6	0.45±0.03	1.9±0.1	356.2±0.3	-	-	-	-	6	-
S 446	5	10	0.48±0.01	9.7±0.2	0.47±0.01	2.2±0.1	359.3±1.1	-	-	-	-	-	-
S 447	6	7	0.54±0.01	8.9±0.3	0.48±0.01	2.3±0.1	356.3±1.5	-	-	-	2	-	1
S 448	6	10	0.52±0.01	8.9±0.3	0.43±0.02	2.0±0.1	356.1±0.9	-	-	-	-	-	-
S 449	6	7	0.51±0.01	8.7±0.4	0.41±0.03	1.8±0.2	353.1±0.9	-	-	-	3	-	-
S 450	6	10	0.50±0.00	9.1±0.3	0.46±0.01	2.1±0.1	355.3±1.4	-	-	-	-	-	-
S 451	6	9	0.49±0.01	8.9±0.5	0.48±0.00	2.1±0.1	354.0±0.6	-	-	-	-	1	-
S 452	6	7	0.50±0.01	8.7±0.6	0.49±0.00	2.1±0.2	357.6±1.1	2	1	-	-	-	-
S 453	6	8	0.48±0.01	8.8±0.2	0.47±0.02	2.0±0.1	356.0±1.0	-	-	1	1	-	-
S 454	6	8	0.48±0.01	9.0±0.3	0.48±0.01	2.1±0.1	355.1±1.8	-	1	-	-	1	-

Table C.3: *The first eight of 15 principal component vectors (PCVs) obtained from the correlation matrix* $\mathbf{R}$ *between the selected production parameters only. The last seven PCVs can be found in table C.4. A description of the parameters is given in 6.1.1.*

	PC 1	PC 2	PC 3	PC 4	PC 5	PC 6	PC 7	PC 8	⋯
Δt_1=Δt[UV→PEDOT-SC]	-0.19	0.15	0.54	-0.09	0.06	0.07	-0.01	0.40	
Δt_2=Δt[PEDOT-SC→Oven]	-0.11	0.06	-0.49	0.32	0.22	-0.10	-0.25	-0.40	
OP=Order of PEDOT-SC	0.05	-0.11	0.10	-0.43	-0.11	0.48	-0.64	-0.27	
$t_d(P)$=Duration of PEDOT Drying	-0.39	0.16	0.09	0.16	0.05	-0.34	-0.32	0.11	
Δt_3=Δt[Airlock→Absorber-SC]	0.01	-0.25	-0.26	-0.57	0.09	-0.12	0.08	0.08	
T_{SC}=Temp. during Absorber-SC	0.34	-0.13	0.14	-0.12	0.16	-0.50	-0.32	0.06	
t_{sol}=Age of Absorber-Solution	0.43	-0.01	0.12	0.14	0.26	0.03	-0.03	0.01	
Δt_4=Δt[Absorber-SC→Vacuum]	0.00	0.00	0.51	0.07	-0.22	-0.12	0.20	-0.72	
$t_d(abs)$=Duration Absorber Drying	-0.06	0.59	-0.02	-0.15	0.14	0.02	-0.03	-0.09	⋯
t_{evac}=Duration Evaporation Vacuum	0.41	-0.15	0.02	0.25	-0.22	0.04	-0.04	0.11	
p_{base}=Evaporation Base Pressure	0.38	0.10	0.02	0.22	0.23	0.37	0.07	0.07	
p_{evap}=Evaporation Pressure	0.07	0.25	-0.10	0.23	-0.60	0.04	-0.38	0.20	
$\frac{\Delta d_{5nm}}{\Delta t}$=Aluminium Rate < 5nm	-0.34	-0.13	0.03	0.20	0.30	0.45	0.00	0.04	
d_{evap}=Al-Layer Thickness	0.13	0.43	-0.25	-0.27	-0.26	0.09	0.33	-0.03	
t_{evap}=Duration of Evaporation	0.21	0.45	0.10	-0.11	0.38	-0.06	-0.16	-0.06	
Eigenvalue λ_α	4.38	2.56	2.12	1.75	1.55	1.12	0.71	0.57	
Variance / %	29.2	17.1	14.2	11.7	10.3	7.5	4.7	3.8	⋯
Cum. Variance / %	29.2	46.3	60.4	72.1	82.4	89.9	94.6	98.4	

Table C.4: *The last seven of 15 principal component vectors (PCVs) obtained from the correlation matrix* $\mathbf{R}$ *between the selected production parameters only. The first eight PCVs can be found in table C.3. A description of the parameters is given in 6.1.1.*

	⋯	PC 9	PC 10	PC 11	PC 12	PC 13	PC 14	PC 15
Δt_1=Δt[UV→PEDOT-SC]		-0.39	-0.56	-0.03	3.65E-02	2.07E-02	-1.06E-05	1.78E-17
Δt_2=Δt[PEDOT-SC→Oven]		-0.35	-0.49	-0.02	2.14E-02	1.65E-02	9.04E-06	-9.20E-17
OP=Order of PEDOT-SC		0.13	-0.11	-0.08	-9.12E-02	-1.63E-01	4.76E-05	-1.74E-17
$t_d(P)$=Duration of PEDOT Drying		-0.08	0.31	-0.24	-3.10E-01	-5.51E-01	-4.43E-05	-1.21E-16
Δt_3=Δt[Airlock→Absorber-SC]		-0.62	0.27	-0.10	1.80E-01	-5.37E-02	3.09E-03	-8.41E-16
T_{SC}=Temp. during Absorber-SC		0.03	-0.07	0.65	-1.41E-01	-1.25E-02	1.70E-04	8.68E-16
t_{sol}=Age of Absorber-Solution		-0.05	0.03	-0.26	7.34E-02	-1.27E-01	-7.83E-01	1.12E-13
Δt_4=Δt[Absorber-SC→Vacuum]		-0.30	0.14	0.06	3.23E-03	-1.47E-03	-1.21E-04	2.21E-17
$t_d(abs)$=Duration Absorber Drying	⋯	0.12	0.08	0.25	6.56E-01	-2.86E-01	-2.10E-03	-9.03E-17
t_{evac}=Duration Evaporation Vacuum		-0.12	-0.06	-0.10	2.10E-01	-3.43E-01	3.25E-01	6.20E-01
p_{base}=Evaporation Base Pressure		-0.25	0.15	0.11	-1.73E-01	-2.36E-01	3.50E-01	-5.39E-01
p_{evap}=Evaporation Pressure		-0.31	0.23	0.12	8.65E-02	3.28E-01	-1.78E-01	-1.20E-01
$\frac{\Delta d_{5nm}}{\Delta t}$=Aluminium Rate $<$ 5nm		-0.17	0.28	0.46	-9.11E-02	5.44E-02	-1.78E-01	4.05E-01
d_{evap}=Al-Layer Thickness		-0.07	-0.17	0.18	-5.24E-01	-2.35E-01	-1.90E-01	2.12E-01
t_{evap}=Duration of Evaporation		-0.04	0.20	-0.28	-2.03E-01	4.80E-01	2.44E-01	3.19E-01
Eigenvalue λ_α		0.21	0.02	0.00	1.25E-04	5.62E-05	8.92E-09	1.01E-32
Variance /%	⋯	1.4	0.2	0.0	0.0	0.0	0.0	0.0
Cum. Variance /%		99.8	100.0	100.0	100.0	100.0	100.0	100.0

Table C.5: *The first eight of 16 principal component vectors (PCVs) obtained from the correlation matrix* **R** *between OSC properties only. The second eight PCVs can be found in table C.6. The meaning of the parameters is described in section 5.3.2.*

	PC 1	PC 2	PC 3	PC 4	PC 5	PC 6	PC 7	PC 8	···
Radial Distance	-0.04	0.06	0.35	-0.43	0.72	-0.27	0.27	-0.02	
V_{oc}	0.18	-0.32	0.40	-0.29	-0.15	0.10	-0.38	-0.02	
J_{sc}	0.19	0.24	0.39	0.39	-0.12	-0.46	-0.17	0.15	
FF	0.35	0.06	-0.17	0.02	0.05	0.10	0.18	-0.22	
J_{1V} dark	0.29	0.09	-0.30	0.05	0.18	0.17	0.15	0.58	
R_{1V} dark	-0.33	0.00	0.23	0.06	-0.10	0.21	-0.02	0.14	
J_{1V} ill	0.33	-0.07	0.06	-0.02	0.05	0.18	0.00	0.54	
R_{1V} ill	-0.32	0.14	-0.04	0.13	-0.10	0.12	0.32	-0.06	···
V_{mpp}	0.33	-0.16	0.13	-0.16	-0.07	0.13	-0.19	-0.15	
J_{mpp}	0.31	0.17	0.17	0.25	-0.05	-0.24	0.09	-0.05	
R_{sc}	0.30	-0.13	0.09	-0.11	-0.13	0.34	0.35	-0.27	
R_{oc}	-0.33	-0.13	0.17	-0.14	-0.05	0.14	-0.10	0.37	
Absorption 1^{st} Min	0.02	0.42	0.22	-0.37	-0.42	0.01	0.22	0.14	
Absorption 1^{st} Max	0.03	0.54	0.13	-0.21	-0.13	0.19	0.04	-0.04	
Absorption 2^{nd} Min	0.04	0.30	-0.46	-0.42	-0.02	-0.21	-0.47	-0.04	
Absorption 2^{nd} Max	0.01	-0.39	-0.17	-0.28	-0.41	-0.54	0.39	0.16	
Eigenvalue λ_α	7.47	2.94	1.46	1.23	0.95	0.56	0.48	0.33	
Variance / %	46.7	18.4	9.1	7.7	5.9	3.5	3.0	2.1	···
Cum. Variance / %	46.7	65.0	74.1	81.8	87.7	91.3	94.3	96.3	

Table C.6: *The second eight of 16 principal component vectors (PCVs) obtained from the correlation matrix* **R** *between OSC properties only. The first eight PCVs can be found in table C.5. The meaning of the parameters is described in section 5.3.2.*

	···	PC 9	PC 10	PC 11	PC 12	PC 13	PC 14	PC 15	PC 16
Radial Distance		0.09	-0.05	0.05	0.05	0.00	-0.04	0.00	0.00
V_{oc}		-0.06	-0.39	-0.01	-0.05	-0.06	0.31	0.26	-0.35
J_{sc}		0.16	-0.12	-0.08	0.00	0.08	-0.45	-0.04	-0.26
FF		0.05	0.02	0.27	0.17	0.23	0.17	-0.47	-0.58
J_{1V} dark		-0.13	-0.43	-0.12	0.16	0.32	-0.04	0.24	0.02
R_{1V} dark		0.46	0.15	0.40	0.40	0.37	0.06	0.25	0.02
J_{1V} ill		0.24	0.34	0.27	-0.20	-0.51	0.01	-0.07	-0.04
R_{1V} ill	···	0.23	-0.65	0.22	-0.07	-0.43	-0.04	-0.10	-0.05
V_{mpp}		-0.09	-0.23	0.37	0.14	0.09	-0.37	-0.32	0.54
J_{mpp}		0.25	-0.10	-0.10	0.00	0.04	0.67	-0.09	0.43
R_{sc}		0.46	0.05	-0.48	-0.04	0.03	-0.27	0.15	0.01
R_{oc}		0.14	-0.07	-0.36	-0.17	0.24	0.06	-0.65	0.02
Absorption 1^{st} Min		-0.29	0.10	-0.14	0.47	-0.21	0.03	-0.08	-0.01
Absorption 1^{st} Max		-0.07	0.02	0.22	-0.65	0.31	0.00	0.12	0.01
Absorption 2^{nd} Min		0.47	-0.08	-0.07	0.09	-0.08	-0.03	-0.01	0.00
Absorption 2^{nd} Max		0.07	-0.01	0.20	-0.18	0.18	-0.02	0.06	0.01
Eigenvalue λ_α		0.25	0.13	0.07	0.04	0.04	0.02	0.01	0.00
Variance / %	···	1.6	0.8	0.5	0.3	0.3	0.1	0.1	0.0
Cum. Variance / %		97.9	98.8	99.2	99.5	99.8	99.9	100.0	100.0

Table C.7: *The first eight of 16 principal component vectors (PCVs) obtained from the correlation matrix* $\mathbf{R}$ *between production parameters and the average power conversion efficiency* η *per substrate. The second eight PCVs can be found in table C.8.*

	PC 1	PC 2	PC 3	PC 4	PC 5	PC 6	PC 7	PC 8	⋯
Δt_1=Δt[UV→PEDOT-SC]	-0.19	0.24	-0.43	-0.19	0.15	0.16	0.03	-0.40	
Δt_2=Δt[PEDOT-SC→Oven]	-0.11	0.00	0.42	0.20	-0.44	-0.02	0.24	0.41	
OP=Order of PEDOT-SC	0.05	-0.16	-0.07	-0.03	0.50	0.38	0.53	0.33	
$t_d(P)$=Duration of PEDOT Drying	-0.38	0.20	-0.06	-0.05	-0.17	-0.21	0.38	-0.11	
Δt_3=Δt[Airlock→Absorber-SC]	0.01	-0.20	0.07	0.53	0.39	-0.08	-0.06	-0.08	
T_{SC}=Temp. during Absorber-SC	0.34	0.00	-0.25	0.26	-0.01	-0.29	0.41	-0.07	
t_{sol}=Age of Absorber-Solution	0.43	0.05	-0.15	0.05	-0.21	0.17	0.04	-0.02	
Δt_4=Δt[Absorber-SC→Vacuum]	0.00	0.09	-0.43	-0.32	0.07	-0.19	-0.21	0.70	
$t_d(abs)$=Duration Absorber Drying	-0.06	0.53	0.21	-0.01	0.14	0.17	0.05	0.07	⋯
t_{evac}=Duration Evaporation Vacuum	0.41	-0.19	-0.01	-0.23	-0.14	-0.11	0.01	-0.10	
p_{base}=Evaporation Base Pressure	0.38	0.07	0.03	-0.09	-0.23	0.41	-0.11	-0.05	
p_{evap}=Evaporation Pressure	0.07	0.06	0.31	-0.53	0.07	-0.25	0.32	-0.16	
$\frac{\Delta d_{5nm}}{\Delta t}$=Aluminium Rate $<$ 5nm	-0.34	-0.12	-0.07	0.01	-0.25	0.49	-0.05	-0.02	
d_{evap}=Al-Layer Thickness	0.13	0.28	0.41	-0.07	0.36	-0.05	-0.35	0.02	
t_{evap}=Duration of Evaporation	0.21	0.48	0.00	0.14	-0.01	0.23	0.22	0.05	
η	-0.01	-0.42	0.21	-0.32	0.14	0.24	0.11	-0.05	
Eigenvalue λ_α	4.4	2.9	2.2	1.8	1.7	1.3	0.7	0.6	
Variance / %	27.4	17.9	13.8	11.5	10.8	8.1	4.5	3.5	⋯
Cum. Variance / %	27.4	45.3	59.1	70.5	81.4	89.5	94.0	97.5	
$\lvert\eta\ \lambda_\alpha\rvert$	0.05	1.20	0.47	0.59	0.23	0.31	0.08	0.03	⋯
Relative Order	9	1	3	2	5	4	8	10	

Table C.8: *The second eight of 16 principal component vectors (PCVs) obtained from the correlation matrix* $\mathbf{R}$ *between production parameters and the average power conversion efficiency* η *per substrate. The first eight PCVs can be found in table C.7.*

	⋯	PC 9	PC 10	PC 11	PC 12	PC 13	PC 14	PC 15	PC 16
Δt_1=Δt[UV→PEDOT-SC]		-0.34	0.16	-0.58	-0.05	0.03	-0.02	-2.23E-05	-3.79E-16
Δt_2=Δt[PEDOT-SC→Oven]		-0.30	0.12	-0.51	-0.03	0.01	-0.02	-6.16E-06	-2.19E-16
OP=Order of PEDOT-SC		-0.08	-0.37	-0.05	-0.06	-0.07	0.17	-2.24E-04	-2.92E-16
$t_d(P)$=Duration of PEDOT Drying		0.01	0.19	0.29	-0.21	-0.26	0.58	-1.03E-03	-1.69E-17
Δt_3=Δt[Airlock→Absorber-SC]		-0.50	0.38	0.24	-0.11	0.18	0.04	3.15E-03	1.96E-15
T_{SC}=Temp. during Absorber-SC		0.14	0.18	-0.11	0.65	-0.12	0.01	2.22E-04	-6.83E-16
t_{sol}=Age of Absorber-Solution		-0.01	0.08	0.03	-0.26	0.08	0.12	-7.83E-01	-3.71E-13
Δt_4=Δt[Absorber-SC→Vacuum]		-0.16	0.30	0.11	0.06	0.00	0.00	-1.09E-04	-1.02E-16
$t_d(abs)$=Duration Absorber Drying	⋯	0.19	0.10	0.05	0.23	0.69	0.22	-1.79E-03	-4.49E-16
t_{evac}=Duration Evaporation Vacuum		-0.18	-0.07	-0.04	-0.10	0.24	0.32	3.24E-01	-6.20E-01
p_{base}=Evaporation Base Pressure		-0.25	0.08	0.15	0.12	-0.14	0.25	3.49E-01	5.39E-01
p_{evap}=Evaporation Pressure		-0.40	-0.03	0.25	0.12	0.06	-0.34	-1.77E-01	1.20E-01
$\frac{\Delta d_{5nm}}{\Delta t}$=Aluminium Rate $<$ 5nm		-0.22	0.01	0.28	0.47	-0.08	-0.06	-1.78E-01	-4.05E-01
d_{evap}=Al-Layer Thickness		-0.06	0.02	-0.17	0.20	-0.49	0.28	-1.91E-01	-2.12E-01
t_{evap}=Duration of Evaporation		0.08	0.24	0.17	-0.29	-0.26	-0.45	2.45E-01	-3.19E-01
η		0.37	0.66	-0.12	-0.03	-0.01	0.01	-8.01E-05	-2.93E-16
Eigenvalue λ_α		0.2	0.1	0.0	0.0	0.0	0.0	7.91E-09	1.12E-32
Variance / %	⋯	1.5	0.8	0.1	0.0	0.0	0.0	0	0
Cum. Variance / %		99.1	99.9	100.0	100.0	100.0	100.0	100	100
$\lvert\eta\ \lambda_\alpha\rvert$	⋯	0.09	0.08	0.00	0.00	0.00	0.00	0.00	0.00
Relative Order		6	7	11	12	13	14	15	16

Table C.9: *The first nine of 18 principal component vectors (PCVs) obtained from the correlation matrix* $\mathbf{R}$ *between production parameters and the open circuit voltage* V_{oc}*, short circuit current density* J_{sc} *and the fill factor* FF*. The second nine PCVs are shown in table C.10.*

	PC 1	PC 2	PC 3	PC 4	PC 5	PC 6	PC 7	PC 8	PC 9	⋯
Δt_1=Δt[UV→PEDOT-SC]	-0.20	0.22	-0.34	-0.17	0.29	0.21	-0.04	0.38	-0.08	
Δt_2=Δt[PEDOT-SC→Oven]	-0.11	0.02	0.36	0.09	-0.48	-0.11	0.34	-0.31	-0.25	
OP=Order of PEDOT-SC	0.08	-0.18	-0.05	0.19	0.4	0.38	0.45	-0.1	-0.41	
$t_d(P)$=Duration of PEDOT Drying	-0.38	0.17	-0.06	-0.03	-0.05	-0.21	0.39	0.18	0.04	
Δt_3=Δt[Airlock→Absorber-SC]	0.05	-0.17	-0.07	0.58	-0.01	0.01	-0.26	0.16	-0.36	
T_{SC}=Temp. during Absorber-SC	0.34	0.03	-0.32	0.11	-0.12	-0.21	0.28	0.24	0.00	
t_{sol}=Age of Absorber-Solution	0.40	0.08	-0.10	-0.18	-0.19	0.15	0.05	0.04	0.04	
Δt_4=Δt[Absorber-SC→Vacuum]	-0.02	0.08	-0.37	-0.28	0.27	-0.12	-0.03	-0.72	-0.13	
$t_d(abs)$=Duration Absorber Drying	-0.05	0.45	0.25	0.12	0.20	0.09	0.12	-0.05	0.23	⋯
t_{evac}=Duration Evaporation Vacuum	0.37	-0.16	0.02	-0.32	-0.05	-0.13	-0.04	0.09	-0.18	
p_{base}=Evaporation Base Pressure	0.34	0.10	0.13	-0.27	-0.16	0.33	-0.07	0.02	-0.05	
p_{evap}=Evaporation Pressure	0.04	0.00	0.36	-0.30	0.31	-0.35	0.24	0.23	-0.38	
$\frac{\Delta d_{5nm}}{\Delta t}$=Aluminium Rate $<$ 5nm	-0.34	-0.09	0.00	-0.10	-0.22	0.46	0.04	-0.03	-0.05	
d_{evap}=Al-Layer Thickness	0.13	0.21	0.40	0.17	0.33	-0.11	-0.36	-0.10	0.03	
t_{evap}=Duration of Evaporation	0.21	0.44	0.04	0.07	0.01	0.18	0.24	0.05	0.16	
V_{oc}	-0.27	-0.24	0.17	-0.37	0.04	0.04	-0.16	0.20	0.03	
J_{sc}	0.09	-0.42	-0.06	0.10	0.19	-0.21	0.26	-0.04	0.54	
FF	0.11	-0.35	0.30	-0.02	0.19	0.35	0.15	-0.04	0.25	
Eigenvalue λ_α	4.77	3.37	2.31	2.09	1.84	1.53	0.81	0.61	0.35	
Variance / %	26.5	18.7	12.8	11.6	10.2	8.5	4.5	3.4	2.0	⋯
Cum. Variance / %	26.5	45.2	58.0	69.7	79.9	88.4	92.9	96.2	98.2	
$\lvert V_{oc}\ \lambda_\alpha\rvert$	1.30	0.82	0.40	0.76	0.07	0.06	0.13	0.12	0.01	
$\lvert J_{sc}\ \lambda_\alpha\rvert$	0.41	1.42	0.14	0.21	0.35	0.31	0.21	0.02	0.19	⋯
$\lvert FF\ \lambda_\alpha\rvert$	0.54	1.16	0.70	0.05	0.35	0.53	0.12	0.02	0.09	

Table C.10: *The second nine of 18 principal component vectors (PCVs) obtained from the correlation matrix* $\mathbf{R}$ *between production parameters and the open circuit voltage* V_{oc}*, short circuit current density* J_{sc} *and the fill factor* FF*. The first nine PCVs are shown in table C.9.*

	⋯	PC 10	PC 11	PC 12	PC 13	PC 14	PC 15	PC 16	PC 17	PC 18
Δt_1=Δt[UV→PEDOT-SC]		-0.29	-0.14	-0.17	0.60	5.73E-02	-3.10E-02	3.69E-02	7.90E-05	3.96E-16
Δt_2=Δt[PEDOT-SC→Oven]		-0.30	-0.09	0.08	0.49	3.64E-02	-1.35E-02	2.31E-02	6.06E-05	5.42E-16
OP=Order of PEDOT-SC		0.2	-0.21	0.32	-0.04	6.53E-02	3.59E-02	-1.90E-01	3.48E-06	-2.38E-16
$t_d(P)$=Duration of PEDOT Drying		-0.07	0.23	-0.18	-0.23	2.28E-01	1.11E-01	-6.23E-01	3.51E-04	-1.93E-15
Δt_3=Δt[Airlock→Absorber-SC]		-0.51	0.22	-0.10	-0.20	1.02E-01	-1.86E-01	6.68E-03	-3.29E-03	-1.81E-15
T_{SC}=Temp. during Absorber-SC		-0.03	0.29	0.20	0.13	-6.49E-01	1.33E-01	-5.31E-02	-1.41E-04	1.01E-15
t_{sol}=Age of Absorber-Solution		-0.12	0.01	0.06	-0.04	2.61E-01	-1.09E-01	-1.01E-01	7.83E-01	3.57E-13
Δt_4=Δt[Absorber-SC→Vacuum]		-0.29	0.25	-0.04	-0.06	-6.02E-02	-1.72E-03	2.79E-04	1.25E-04	1.71E-16
$t_d(abs)$=Duration Absorber Drying	⋯	-0.07	0.02	0.13	-0.08	-2.43E-01	-7.13E-01	-5.38E-02	1.12E-03	4.24E-16
t_{evac}=Duration Evaporation Vacuum		0.00	-0.06	-0.08	0.05	1.03E-01	-3.12E-01	-2.53E-01	-3.25E-01	6.20E-01
p_{base}=Evaporation Base Pressure		-0.27	-0.16	-0.12	-0.16	-1.14E-01	8.16E-02	-2.79E-01	-3.50E-01	-5.39E-01
p_{evap}=Evaporation Pressure		-0.09	-0.03	-0.26	-0.21	-1.23E-01	2.08E-02	3.44E-01	1.78E-01	-1.20E-01
$\frac{\Delta d_{5nm}}{\Delta t}$=Aluminium Rate $<$ 5nm		-0.15	-0.16	-0.24	-0.27	-4.72E-01	9.54E-02	2.83E-02	1.78E-01	4.05E-01
d_{evap}=Al-Layer Thickness		-0.10	-0.10	0.03	0.16	-1.85E-01	4.15E-01	-3.94E-01	1.90E-01	2.12E-01
t_{evap}=Duration of Evaporation		-0.24	0.11	0.13	-0.20	2.83E-01	3.56E-01	3.76E-01	-2.44E-01	3.19E-01
V_{oc}		-0.30	0.21	0.70	-0.06	-7.15E-04	1.66E-02	-1.69E-02	5.01E-05	1.74E-16
J_{sc}		-0.41	-0.43	-0.05	-0.05	6.18E-03	-5.10E-03	-5.47E-03	-4.87E-05	-1.02E-16
FF		0.03	0.61	-0.31	0.25	2.11E-02	1.01E-03	9.67E-03	1.45E-04	-1.42E-16
Eigenvalue λ_α		0.18	0.07	0.05	0.02	1.20E-03	8.88E-05	2.62E-05	6.42E-09	1.74E-32
Variance / %	⋯	1.0	0.4	0.3	0.1	0.0	4.93E-04	1.45E-04	3.56E-08	9.65E-32
Cum. Variance / %		99.2	99.6	99.9	100.0	100.0	100.0	100.0	100.0	100.0
$\lvert V_{oc}\ \lambda_\alpha\rvert$		0.05	0.01	0.04	0.00	8.57E-07	1.47E-06	4.41E-07	3.22E-13	3.02E-48
$\lvert J_{sc}\ \lambda_\alpha\rvert$	⋯	0.08	0.03	0.00	0.00	7.41E-06	4.53E-07	1.43E-07	3.12E-13	1.78E-48
$\lvert FF\ \lambda_\alpha\rvert$		0.01	0.04	0.02	0.00	2.53E-05	8.98E-08	2.53E-07	9.32E-13	2.46E-48

Table C.11: *The results from the cross-validation (part 1). The table shows the measured values and the standard deviation σ in percent of the open circuit voltage V_{oc} and the short circuit current density J_{sc} as well as the values predicted during cross-validation and the percentage deviations from the measured value. The statistical model is using PCVs 15-17 of table C.10 for all substrate but for S 439, for which PCVs 14-17 are used. The prediction for the fill factor FF and the power conversion efficiency η, which is calculated with the predicted values, are found in table C.12.*

	V_{oc}				J_{sc}			
	meas	σ	pred	Δ	meas	σ	pred	Δ
	V	%	V	%	mA/cm^2	%	mA/cm^2	%
S 408	0.58	0.8%	0.57	-0.8%	9.60	4.2%	8.94	-6.9%
S 410	0.57	4.5%	0.58	1.8%	8.62	1.9%	9.44	9.5%
S 411	0.56	1.2%	0.56	-0.5%	9.09	3.3%	8.20	-9.8%
S 413	0.55	3.3%	0.54	-0.4%	8.78	3.7%	9.64	9.9%
S 407	0.50	2.7%	0.49	-2.4%	8.67	5.4%	7.62	-12.1%
S 409	0.50	2.5%	0.49	-0.6%	8.14	6.4%	7.65	-6.0%
S 412	0.51	3.9%	0.50	-0.8%	8.47	4.2%	10.24	20.8%
S 414	0.50	1.4%	0.53	4.5%	8.72	3.4%	8.39	-3.7%
S 416	0.56	1.9%	0.56	-0.9%	9.37	2.4%	11.55	23.3%
S 417	0.56	1.2%	0.55	-1.8%	9.42	1.9%	13.44	42.7%
S 419	0.56	1.3%	0.55	-0.2%	10.06	6.4%	7.60	-24.5%
S 421	0.55	1.0%	0.58	4.4%	9.52	2.4%	5.14	-46.0%
S 423	0.50	2.8%	0.50	-0.8%	9.12	3.9%	10.20	11.8%
S 424	0.51	4.3%	0.51	0.8%	9.14	2.9%	7.88	-13.8%
S 425	0.50	1.5%	0.50	-0.8%	9.13	4.5%	9.58	5.0%
S 426	0.48	1.2%	0.50	3.0%	9.12	3.0%	8.68	-4.9%
S 427	0.48	1.4%	0.48	-0.9%	10.01	4.0%	9.39	-6.2%
S 428	0.49	1.0%	0.49	0.7%	9.20	3.0%	8.39	-8.8%
S 429	0.48	1.2%	0.47	-1.9%	9.29	3.0%	10.31	10.9%
S 430	0.47	1.7%	0.48	2.2%	9.38	3.1%	9.23	-1.6%
S 439	0.50	1.5%	0.52	3.2%	8.98	2.3%	8.00	-10.9%
S 440	0.47	1.5%	0.45	-5.8%	8.43	3.5%	7.33	-13.1%
S 441	0.49	2.3%	0.47	-3.7%	9.00	3.5%	7.29	-19.0%
S 442	0.46	1.4%	0.46	-0.7%	8.63	7.3%	7.45	-13.7%
S 443	0.47	1.7%	0.45	-4.2%	9.85	3.8%	13.83	40.4%
S 444	0.49	1.6%	0.48	-2.0%	9.47	1.9%	10.05	6.1%
S 445	0.48	4.9%	0.51	6.7%	9.12	6.9%	9.08	-0.5%
S 446	0.48	1.1%	0.48	0.6%	9.74	2.3%	9.94	2.0%
S 447	0.54	1.9%	0.52	-4.4%	8.92	3.3%	8.21	-8.0%
S 448	0.52	1.3%	0.52	-0.8%	8.91	3.1%	9.57	7.4%
S 449	0.51	2.4%	0.54	6.6%	8.67	4.6%	8.39	-3.2%
S 450	0.50	0.9%	0.53	4.4%	9.11	3.0%	9.54	4.7%
S 451	0.49	1.0%	0.48	-0.8%	8.94	5.3%	8.18	-8.5%
S 452	0.50	2.7%	0.47	-5.5%	8.71	6.8%	9.06	4.1%
S 453	0.48	1.7%	0.48	0.3%	8.82	1.7%	9.12	3.4%
S 454	0.48	2.2%	0.48	-0.1%	8.95	3.8%	8.96	0.1%

Table C.12: *The results from the cross-validation (part 2). The table shows the measured values and the standard deviation σ in percent of the fill factor FF as well as the values predicted during cross-validation and the percentage deviations from the measured value. The statistical model is using PCVs 15-17 of table C.10 for all substrate but for S 439, for which PCVs 14-17 are used. The power conversion efficiency η is calculated from the predicted values of open circuit voltage V_{oc}, short circuit current density J_{sc} (see table C.11) and the FF.*

	FF				η			
	meas	σ	pred	Δ	meas	σ	calc	Δ
	-	%	-	%	%	%	%	%
S 408	0.48	3.4%	0.43	-9.9%	2.66	5.8%	2.21	-16.7%
S 410	0.41	4.4%	0.47	14.2%	2.03	6.1%	2.59	27.4%
S 411	0.43	2.7%	0.39	-9.4%	2.19	3.3%	1.78	-18.7%
S 413	0.41	9.0%	0.45	9.1%	1.96	6.9%	2.35	19.6%
S 407	0.42	8.3%	0.36	-12.9%	1.81	11.0%	1.36	-25.3%
S 409	0.39	5.2%	0.38	-1.9%	1.56	8.2%	1.43	-8.3%
S 412	0.39	8.5%	0.46	17.7%	1.68	3.6%	2.38	41.6%
S 414	0.42	4.4%	0.41	-2.4%	1.83	5.2%	1.79	-1.9%
S 416	0.43	4.1%	0.58	34.4%	2.28	4.2%	3.74	64.2%
S 417	0.45	2.2%	0.63	40.6%	2.34	2.9%	4.60	97.0%
S 419	0.50	1.6%	0.39	-22.5%	2.81	5.1%	1.65	-41.5%
S 421	0.50	2.1%	0.23	-53.6%	2.67	3.0%	0.70	-73.8%
S 423	0.37	6.5%	0.40	7.2%	1.71	11.3%	2.03	18.5%
S 424	0.40	13.3%	0.35	-11.4%	1.85	8.0%	1.43	-22.6%
S 425	0.40	7.6%	0.40	-2.1%	1.86	12.0%	1.89	1.6%
S 426	0.43	6.5%	0.52	22.0%	1.89	7.7%	2.26	19.5%
S 427	0.44	3.2%	0.43	-2.3%	2.11	4.9%	1.91	-9.1%
S 428	0.42	3.4%	0.40	-6.0%	1.90	4.8%	1.64	-13.7%
S 429	0.46	2.4%	0.45	-2.4%	2.04	3.8%	2.17	6.2%
S 430	0.45	3.9%	0.48	7.0%	1.96	7.6%	2.10	7.5%
S 439	0.36	4.0%	0.36	-1.7%	1.64	3.6%	1.48	-9.5%
S 440	0.29	3.6%	0.20	-30.7%	1.14	5.8%	0.65	-43.3%
S 441	0.35	7.5%	0.22	-39.0%	1.56	8.5%	0.74	-52.4%
S 442	0.31	6.5%	0.23	-25.0%	1.23	12.2%	0.79	-35.8%
S 443	0.45	1.3%	0.64	43.2%	2.06	4.5%	3.96	92.5%
S 444	0.44	8.2%	0.47	7.4%	2.06	9.1%	2.30	11.6%
S 445	0.45	7.0%	0.44	-0.8%	1.93	5.0%	2.04	5.7%
S 446	0.47	3.1%	0.47	1.1%	2.19	5.8%	2.27	3.7%
S 447	0.48	2.4%	0.41	-15.1%	2.32	5.8%	1.73	-25.4%
S 448	0.43	4.0%	0.46	7.0%	2.00	4.6%	2.29	14.1%
S 449	0.41	7.3%	0.42	1.7%	1.83	11.7%	1.91	4.7%
S 450	0.46	1.6%	0.45	-1.5%	2.09	3.5%	2.25	7.7%
S 451	0.48	0.6%	0.48	-0.1%	2.11	5.7%	1.92	-9.4%
S 452	0.49	0.9%	0.51	3.9%	2.12	7.1%	2.17	2.2%
S 453	0.47	3.3%	0.48	2.2%	2.01	5.2%	2.13	5.9%
S 454	0.48	1.8%	0.49	0.3%	2.08	4.9%	2.09	0.3%

Appendix D

Publications

Papers

M. Glatthaar, M. Niggemann, B. Zimmermann, P. Lewer, M. Riede, A. Hinsch, J. Luther. Organic solar cells using inverted layer sequence. *Thin Solid Films*, 491 (1-2), 298–300, 2005

B. Zimmermann, M. Glatthaar, M. Niggemann, M. Riede, A. Hinsch. Electroabsorption studies of organic bulk-heterojunction solar cells. *Thin Solid Films*, 493 (1-2), 170–174, 2005

M. Glatthaar, M. Riede, N. Keegan, K. Sylvester-Hvid, B. Zimmermann, M. Niggemann, A. Hinsch, A. Gombert. Efficiency limiting factors of organic bulk hetero-junction solar cells identified by electrical impedance spectroscopy. Accepted in *Solar Energy Materials and Solar Cells*. June 2006

B. Zimmermann, M. Glatthaar, M. Niggemann, M. K. Riede, A. Hinsch, A. Gombert. ITO-free anode wrap through organic solar cells – a module concept for cost efficient reel to reel production. Accepted in *Solar Energy Materials and Solar Cells*. June 2006

Presentations and Conference Proceedings

M. Riede, M. Glatthaar, M. Niggemann, B. Zimmermann, A. Hinsch, J. Luther. Untersuchung von photovoltaisch aktiven Grenzflächen zwischen organischen und anorganischen Leitern. *12. FMF-Kolloquium*, Titisee-Neustadt, Germany, 10.10.–11.10.2003

M. Riede, M. Glatthaar, M. Niggemann, B. Zimmermann, A. Hinsch. Interface Studies in Organic Solar Cells. *EuroSun 2004*, Freiburg, Germany, 20.6.–23.6.2004

M. Riede, A.W. Liehr, R. Kern, M. Glatthaar, M. Niggemann, B. van der Wiel, T. Ziegler, B. Zimmermann, G. Willeke, A. Gombert, J. Luther. Analyse der Schlüsselparameter in Organischen Solarzellen mittels Datamining. *14. FMF-Kolloquium*, Titisee-Neustadt, Germany, 6.10.–7.10.2005

M. Riede, A.W. Liehr, M. Glatthaar, M. Niggemann, B. Zimmermann, T.Ziegler, A.Gombert, G. Willeke. Datamining and analysis of the key parameters in organic solar cells. *SPIE Photonics Europe*, Strasbourg, France, 3.4.–6.4.2006

Appendix E

Zusammenfassung

Die Forschung auf dem Gebiet der organischen Halbleiter hat in den vergangenen Jahren viel Interesse angezogen. Organische Halbleiter, d.h. auf Kohlenstoff basierende Materialien mit Halbleiter-Eigenschaften, haben besondere Eigenschaften, welche sowohl für die Grundlagenforschung als auch bereits für industriell gefertigte Produkte interessant sind.

Der wissenschaftliche Fokus richtet sich auf die speziellen elektronischen Eigenschaften organischer Halbleiter, welche neuartige Phänomene zeigen und ein spannendes System für die Grundlagenforschung darstellen. Das Potential einer kostengünstigen Verarbeitung, z.B. aus Lösungen, und die mögliche mechanische Flexibilität von Geräten mit organischen Halbleitern machen diese Materialien attraktiv für die Industrie.

Während Geräte (z.B. Mobiltelefone) mit organischen Leuchtdioden (OLEDs) bereits auf dem Markt erhältlich sind, gibt es organische Solarzellen (OSZ) noch nicht zu kaufen. Neben niedrigen Herstellungskosten ($<$€$1/\mathrm{W_p}$) und einer hohen Lebensdauer ($>$5 Jahre) ist die Effizienz $>$5% eine der wichtigsten Voraussetzungen für die Kommerzialisierung von OSZ [1]. Jedoch werden diese Voraussetzungen von den bisher untersuchten Materialien und OSZ-Konzepten noch nicht alle gleichzeitig erfüllt. Dafür sind weitere grundlegende Forschungsarbeiten auf dem Gebiet der OSZ notwendig.

Bei der Suche nach neuen Materialien und der Optimierung von OSZ erweist sich ein deterministischer Ansatz als nur schwer durchführbar: bereits ohne extra Materialvariationen gibt es während der Herstellung eine große Anzahl von freien Parametern mit einem möglichen Einfluss auf die OSZ Eigenschaften und es variieren immer mehrere Parameter gleichzeitig zwischen den hergestellten OSZ. Die Variationen mehrerer Parameter und ihre

Auswirkungen müssen gleichzeitig untersucht werden, da das OSZ-System ein komplexes und empfindliches Verhalten zeigt. Es bedarf daher statistischer Methoden, um den Einfluss der Herstellungsparameter, bzw. die Kombinationen von Herstellungsparametern zu untersuchen, das Potential neuer Materialien abzuschätzen und die OSZ zu optimieren.
Gegenstand dieser Doktorarbeit ist sowohl die Entwicklung einer experimentellen Infrastruktur, auf deren Basis eine stichhaltige statistische Analyse der Eigenschaften von OSZ durchgeführt werden kann, als auch die Einführung der Hauptkomponentenanalyse (englisch: principal component analysis, PCA) für die statistische Analyse der Daten.
Als Modell-System diente das derzeit am meisten untersuchte OSZ-System, in welchem die photovoltaisch aktive Schicht aus einer Mischung von P3HT und PCBM besteht.
Eine statistische Analyse erfordert eine solide Datenbasis. Die Grundvoraussetzungen für die Schaffung einer solchen Datenbasis gliedern sich in dieser Arbeit folgendermaßen: (1.) ein strukturierter und vergleichbarer OSZ-Herstellungsprozess, (2.) die Automatisierung der wichtigsten Charakterisierungsmethoden und (3.) das entsprechende Datenmanagement in Form eines elektronischen Laborbuchs (englisch: electronic laboratory notebook, ELN).

Strukturierung des Herstellungsprozesses

Die untersuchten OSZ sind auf einem mit transparentem Indium-Zinn-Oxid (ITO) beschichteten Glas-Substrat aufgebaut. Auf diesem Substrat werden nacheinander eine transparente Schicht von PEDOT:PSS und die photovoltaisch aktive Absorberschicht (eine Mischung aus P3HT und PCBM) aus Lösung aufgeschleudert. Abschließend wird die Kathode per thermischen Verdampfens von Aluminium auf die Absorberschicht abgeschieden.
Der Herstellungsprozess der OSZ wurde für den Labormaßstab untersucht und strukturiert, um eine vergleichbare Herstellung zu ermöglichen. Dabei wurden über 40 Herstellungsparameter definiert, die seitdem routinemäßig über ein dazu entwickeltes Webinterface in standardisierter Form protokolliert werden. Mit diesen Daten kann die komplette Herstellungsgeschichte für jede OSZ nachvollzogen werden.
Die Herstellungsparameter wurden in drei Kategorien eingeteilt: (1) Herstellungsparameter, die sehr gut kontrollierbar sind und für jedes hergestellte Substrat gleich eingestellt werden können, wie z.B. die Spin-Coating-Ge-

schwindigkeit für die organischen Schichten. (2) Zeitintervalle, die von Substrat zu Substrat innerhalb einer Charge auf Grund des Spin-Coating-Prozesses, bei dem die Substrate nur einzeln bearbeitet werden können, variieren. (3) Parameter, die durch manuelle Vorgänge und äußere Einflüsse schwanken.
Bisher wurden nur sechs Parameter des Aufdampfprozesses (2×Druck, Schichtdicke, Rate und 2×Dauer) als Ursachen für die Variationen der OSZ-Eigenschaften berücksichtigt. Jedoch wurden sie nicht systematisch untersucht. Der Einfluss der weiteren vier Parameter aus Kategorie (3), wie z.B. die Temperatur während des Spin-Coatings, wurde bisher als vernachlässigbar eingeschätzt. Es zeigte sich zumindest bei diesem Parameter, dass er einen Einfluss auf die OSZ-Eigenschaften hat. Parameter der Kategorie (2) wurden bisher nicht berücksichtigt, es stellte sich aber heraus, dass sie Variationen in den OSZ-Eigenschaften erklären können.

Automatisierung der Charakterisierungsmethoden

Für einen aussagekräftigen Datensatz werden zusätzlich zu einer gut dokumentierten Herstellungsgeschichte ein entsprechend großer und konsistenter Datensatz an Messdaten benötigt. Um dieses zu ermöglichen wurden alle wichtigen Charakterisierungsmethoden (Strom-Spannungs-Kennlinie, Spektrale Empfindlichkeit und Absorptionsmessung) in einen vielseitigen automatisierten Aufbau kombiniert.
Die Komponenten dieses Aufbaus sind eine standardisierte Kontaktstruktur für die Substrate, ein Vielfach-Substrathalter, ein XY-Tisch mit integriertem optischen Tisch und ein LabView Programm, welches alle Hardware-Komponenten steuert. Um die Flexibilität des Aufbaus in Bezug auf neue Messobjekte und Messmethoden trotz einer Standardisierung nicht einzuschränken, wurden die Komponenten möglichst vielseitig ausgelegt. Die Standardisierung der Substrate gibt nur eine Kontaktstruktur am Rande einer 25×25mm^2 großen Substrat-Fläche vor, auf dieser dann verschiedene Layouts, z.B. für bis zu 10 OSZ pro Substrat, realisiert werden können. Auf Grund der standardisierten Kontaktstruktur lassen sich alle Substrate in einem Vielfachhalter, der gleichzeitig bis zu neun Substrate aufnehmen und kontaktieren kann, mit den Standardmethoden vermessen. Diese Kombination erlaubt eine zuverlässige OSZ Charakterisierung mit hohem Durchsatz. Beispielsweise kann nun die Strom-Spannungs-Messung an 90 OSZ innerhalb von 90 Minuten und ohne manuellen Eingriff durchgeführt werden, der vorher

jedoch minütig notwendig war. Der automatisierte Aufbau bietet zudem noch die Möglichkeiten für die Integration weiterer Messmethoden.
Die Automatisierung macht die Messungen weniger anfällig für menschliche Fehler und führte zu einem standardisierten Charakterisierung-Zyklus. Ohne die Automatisierung der wichtigsten Charakterisierungmethoden wäre die zuverlässige Erfassung der benötigten Messdaten unmöglich gewesen.

Elektronisches Laborbuch

Die Protokollierung von mehr als 40 Herstellungsparametern und die Erfassung einer großen Menge an Messdaten erfordert ein effizientes Datenmanagement, für welches ein elektronisches Laborbuch (ELN) und die dafür notwendigen Programme entwickelt wurden.
Das ELN bündelt die Daten der zwei wichtigsten Quellen – einem benutzerfreundlichen Webinterface für die Herstellungsprotokolle und den standardisierten Ausgabedateien des automatisierten Messaufbaus – und speichert sie in einer hierarchischen Struktur. Der effiziente Zugriff und die Verknüpfung der Daten in dem ELN schaffen die Basis für die Datenanalyse. Die Messdaten werden sowohl in dem ELN analysiert, als auch die ermittelten OSZ-Eigenschaften im ELN gespeichert.
Eine Parametrisierung der OSZ-Messdaten ist notwendig um skalare OSZ-Eigenschaften zu erhalten, welche für die Datenanalyse verwendet werden können. Für die Extraktion der Eigenschaften wurden Splines für alle OSZ verwendet. Ein Ersatzschaltbild, mit dem sich die Strom-Spannungskennlinien, welche einen Füll Faktor (FF) von unter 0.4 hatten, anpassen ließen, wurde nicht gefunden. Dieser niedrige FF tauchte in fast 20% der hergestellten OSZ auf und sein Ursprung ist Thema interner Diskussionen.
Die Qualität der Daten spielt eine sehr große Rolle und wird durch eine Reihe von Maßnahmen sichergestellt. Die wichtigsten Maßnahmen sind Syntax-Checks bei der Eingabe der Daten, Unit-Tests für die Programme, mit welchen die Daten verwaltet werden, und eine Änderungsverfolgung im ELN. Dadurch wurde erreicht, dass kein Datensatz aus der Herstellung wegen falschen Angaben, z.B. inkonsistenten Zeiten, von der Analyse ausgeschlossen werden musste. Jedoch stellte sich heraus, dass die manuelle Aussortierung von Messdaten, deren ungewöhnliche Charakteristika durch Defekte oder Mess-Artefakte und nicht durch Variationen im Herstellungsprozess erklärt werden können, mehr als 60% der Zeit für die Datenanalyse in Anspruch nahm. Von

den 360 hergestellten OSZ mussten 21% aussortiert werden. Eine Automatisierung oder Halb-Automatisierung dieses Prozesses würde daher zu einer erheblichen Zeitersparnis führen.

Ergebnisse der Experimente

36 Substrate mit insgesamt 360 OSZ wurden hergestellt. Während der Herstellung variierten nur die 15 Parameter, die auf Grund der Beschaffenheit unseres Herstellungsprozesses immer variieren, aber bisher nicht systematisch untersucht worden waren. Deshalb wurden diese Parameter auf ihre Auswirkungen auf die OSZ-Eigenschaften untersucht. Diese Variationen müssen berücksichtigt werden, um Effekten, die durch zusätzliche gezielte Variation verursacht werden, eine Signifikanz zuweisen zu können.

Trotz des standardisierten Herstellungsprozesses und der Fixierung der Mehrzahl der Herstellungsparameter, zeigten die OSZ-Eigenschaften eine breitere Streuung als erwartet. Für einen reproduzierbaren Herstellungsprozess wären Variationen im Wirkungsgrad η von $\pm 10\%$ um den Mittelwert erwartet worden, d.h. für die hergestellten OSZ $\eta = (2.0 \pm 0.2)\%$. Jedoch lag die Streuung bei fast $\pm 50\%$ um den Mittelwert von 2.0% ($1.1\% \leq \eta \leq 2.8\%$). Dabei stellte sich heraus, dass der FF, welcher am meisten zwischen den hergestellten Substraten streute (0.29–0.50), η bestimmt. Bereits die Fokussierung auf eine Verbesserung des FF von den erhaltenen auf die in der Literatur erwähnten Werte (0.6) wird zu $\eta > 3.5\%$ führen.

Der einzige Unterschied zwischen den 360 OSZ waren Herstellungsparameter, welche kaum in der Literatur erwähnt werden. Diese Tatsache stellt die Literatur zu P3HT:PCBM basierten OSZ, in denen gewöhnlich nur die Ergebnisse einiger weniger OSZ gezeigt werden, in ein neues Licht. Falls sich unsere Ergebnisse auf den OSZ Herstellungsprozess anderer Gruppen übertragen lassen, müssen sowohl die Herstellungsparameter in den Veröffentlichungen genauer beschrieben werden, als auch eine Signifikanz für die Ergebnisse ausgewiesen werden. Ohne diese Angaben ist eine Interpretation für den Leser nur schwer möglich. Um jedoch einem Ergebnis eine Signifikanz zuweisen zu können bedarf es im Allgemeinen der Untersuchung einer großen Anzahl von OSZ. Dieses beweist die Notwendigkeit eines systematischen und statistischen Ansatzes, für den die experimentellen Voraussetzungen im Rahmen dieser Arbeit entwickelt wurden.

Hauptkomponentenanalyse

Die Hauptkomponentenanalyse eignet sich für die Suche nach den Herstellungsparametern, welche maßgeblich zu den beobachteten Variationen in den OSZ-Eigenschaften beitragen. Die PCA zeigt Korrelationen in den verwendeten Datensätzen auf. Ziel ist es, anhand dieser Korrelationen in dem komplizierten OSZ-System die Parameter zu identifizieren, welche einen signifikanten Einfluss auf die OSZ-Eigenschaften haben. Dabei kann nicht nur der Einfluss einzelner Parameter, sondern auch die Auswirkungen mehrerer Parameter gleichzeitig erfasst werden. Anschließend ist es möglich die physikalischen Ursachen für die gefundenen Korrelationen genauer zu untersuchen. Die PCA[1] mit den 15 oben erwähnten Herstellungsparametern und η zeigte, dass die Korrelationen zwischen den Herstellungsparametern das Verhalten der ersten Hauptkomponente (englisch: principal component, PC) dominiert. Die Korrelationen, welche alleine durch die Herstellungsparameter verursacht wurden, wurden bei der Interpretation der PCA Ergebnisse berücksichtigt. Außerdem stellte sich heraus, dass der Eigenwert λ_α, der einer PC zugeordnet wird, kein angemessener Maßstab für die Relevanz einer PC hinsichtlich der Variablen η ist. λ_α alleine berücksichtigt nicht den Beitrag der Variablen η zu einer PC. Daher wurde $|\eta\ \lambda_\alpha|$, d.h. die Gewichtung von λ_α mit dem Beitrag von η zu einer PC, als neuer Maßstab für die Relevanz einer PC eingeführt. Daraus ergab sich die Reihenfolge von PC 2, PC 4 und PC 3 als die drei für η wichtigsten PCs. PC 1 folgt nach diesem Kriterium erst auf Platz 9.

Die Ergebnisse der PCA legen nahe, dass – im beobachteten Intervall (300-900s) – ein langer Prozess zum Abscheiden der Aluminium-Kathode einen negativen Einfluss auf η hat. Dies zeigte sich durch eine negative Korrelation zwischen der Dauer des Aufdampfprozesses und η (PC 2) und einer positiven Korrelation zwischen dem Druck während des Aufdampfprozesses (7-13$\cdot 10^{-6}$mbar) und η (PC 3). Der zweite Parameter ist üblicherweise höher für einen kürzeren Abscheidungsprozess. Diese Ergebnisse bestätigen die Erfahrung aus dem Labor, wobei der physikalische Ursprung noch nicht geklärt ist. Eine erste Abschätzung des Wärmeübertrags auf die OSZ deutet an, dass eine thermische Belastung als Ursache unwahrscheinlich ist.

Die PCA deutet weiterhin an, dass es wichtig ist, die Absorberschicht nach dem Spin-Coating langsam trocknen zu lassen. Ein längeres Zeitintervall zwi-

[1] Die Tabellen mit allen 16 Hauptkomponenten befinden sich auf Seite 194 und 195.

schen dem Absorber Spin-Coating und dem Trocknen der Schicht im Vakuum (PC 4) und auch eine Temperatur während des Spin-Coating am unteren Ende der beobachteten Skala (24-27°C) gibt dem 2-Phasen-Gemisch von P3HT und PCBM mehr Zeit, um in eine günstigere Morphologie zu relaxieren. Dies ist im Einklang mit Ergebnissen aus der Literatur [61].

Weiterhin stellte sich heraus, dass zwei Herstellungsparameter keinen signifikanten Einfluss auf die ersten sieben PCs (nach $|\eta\ \lambda_\alpha|$ sortiert) haben. Das Alter der Absorberlösung (3h bis 22 Tage) und die Dauer des PEDOT:PSS Trockenprozesses während des Transfers der Substrate in die Glovebox (46-162min), haben auf diesen PCs beide einen vernachlässigbaren Einfluss. Diesen Parametern kann in Zukunft weniger Beachtung geschenkt werden.

Die für die PCA verwendete Datenbasis ist groß im Vergleich zu den bisher in der Literatur realisierten Experimenten. Jedoch ist sie am unteren Limit von dem, was notwendig für die PCA ist, denn die Korrelationen zwischen den Herstellungsparametern dominieren immer noch die Ergebnisse. Es wäre sinnvoll, eine neue Serie von Experimenten zu planen, welche mehr OSZ beinhalten sollte und während der versucht werden sollte, die Korrelationen zwischen den Herstellungsparametern zu minimieren.

Auf Basis der durchgeführten PCA wurde ein statistisches Modell vorgeschlagen und dessen Qualität per Kreuz-Validierung überprüft. Das Modell kann anhand der 15 Herstellungsparametern, die während den Experimenten variierten, die Werte für die offene Klemmspannung V_{oc}, den Kurzschluss-Strom J_{sc} und den FF (und damit auch η) vorhersagen. Die ersten Ergebnisse sind vielversprechend, z.B. werden alle Werte für V_{oc} mit weniger als 10% Abweichung vom tatsächlichen Wert vorhergesagt. Jedoch kann das Modell einige Variationen, die in J_{sc} und FF beobachtet werden, nicht erklären. Diese Tatsache deutet darauf hin, dass nicht alle Herstellungsparameter, die einen Einfluss auf die OSZ-Eigenschaften haben, für die PCA erfasst wurden. Zwei zusätzliche Parameter werden für das Herstellungsprotokoll vorgeschlagen: die Substrat-Temperatur während des Aufdampfprozesses und die Feuchtigkeit während des PEDOT:PSS Spin-Coating. Mit dem ersten Parameter ließe sich die thermische Belastung der OSZ direkt erfassen, um die Ursachen für den negativen Effekt eines langandauernden Aufdampfprozesses eingrenzen zu können. Der zweite Parameter ist wahrscheinlich ausschlaggebend für die negativen Auswirkungen auf η, die beobachtet wurden, wenn eine bereits abgekühlte PEDOT:PSS Schicht der Umgebungsluft

ausgesetzt wurde.
Eine numerische Optimierung des Modells, d.h. eine Maximierung des berechneten η, sollte verbesserte Herstellungsparameter ergeben, konnte aber im Zeitrahmen dieser Arbeit nicht mehr ausgeführt werden.

Zusammenfassend kann gesagt werden, dass diese Arbeit eine solide Basis für die Erfassung und Verwaltung von gut dokumentierten OSZ Herstellungs- und Charakterisierungs-Datensätzen geschaffen hat, welche die Grundvoraussetzung für eine stichhaltige statistische Analyse sind. Als statistische Methode wurde die PCA eingeführt und dazu verwendet, die Daten von P3HT:PCBM basierten OSZ nach Korrelationen zu untersuchen um die große beobachtete Streuung in den OSZ-Eigenschaften zu erklären. Dabei stellte sich heraus, dass Variationen im Aufdampfprozess der Kathode einen signifikanten Einfluss auf die OSZ-Eigenschaften haben, und es bestätigte sich, dass ein langsameres Trocknen der Absorberschicht zu einem verbesserten Wirkungsgrad führt. Weitere Zusammenhänge zwischen Herstellungsparametern und OSZ-Eigenschaften wurden vorgeschlagen. Die notwendige Infrastruktur für weitere Untersuchungen dieser Zusammenhänge ist nun vorhanden und erlaubt es, in Zukunft auch neue Materialien und OSZ-Konzepte zu testen. Auf Grundlage der PCA wurde ein statistisches Modell vorgeschlagen, welches ausgehend von den Herstellungsparametern, die Hauptcharakteristika einer OSZ vorhersagen kann. Eine numerische Optimierung dieser vorhergesagten OSZ-Eigenschaften sollte daher zu verbesserten Herstellungsparametern führen und somit zu reproduzierbareren und leistungsfähigeren OSZ.

Bibliography

[1] C. J. Brabec. Organic photovoltaics: technology and market. *Solar Energy Materials and Solar Cells*, 83(2-3):273–292, 2004.

[2] A. J. Heeger. Semiconducting and metallic polymers: The fourth generation of polymeric materials. *Journal of Physical Chemistry B*, 105(36):8475–8491, 2001.

[3] N. S. Sariciftci, L. Smilowitz, A. J. Heeger, and F. Wudl. Photoinduced electron-transfer from a conducting polymer to buckminsterfullerene. *Science*, 258(5087):1474–1476, 1992.

[4] M. C. Scharber, D. Mühlbacher, M. Koppe, P. Denk, C. Waldauf, A. J. Heeger, and C. J. Brabec. Design rules for donors in bulk-heterojunction solar cells – towards 10% energy-conversion efficiency. *Advanced Materials*, 18:789–794, 2006.

[5] M. A. Green, K. Emery, D. L. King, Y. Hisikawa, and W. Warta. Solar cell efficiency tables (version 28). *Progress in Photovoltaics*, 14:455–461, 2006.

[6] P. Würfel. *Physik der Solarzellen.* Spektrum Akad. Verl., Heidelberg, 2000.

[7] S. M. Sze. *Physics of semiconductor devices.* Wiley, New York, N.Y., 1981.

[8] B. Zimmermann. *Aufbau eines Elektroabsorptionsspektroskopie-Messplatzes.* Diplomarbeit, Universität Hamburg, Fakultät für Physik, 2004.

[9] A. J. Heeger, S. Kivelson, J. R. Schrieffer, and W. P. Su. Solitons in conducting polymers. *Reviews of Modern Physics*, 60(3):781–850, 1988.

[10] G. Hadziioannou and P. F. van Hutten. Opto-electronic properties of polymers. Lecture Notes, University Louis Pasteur, Strasbourg, 2003.

[11] R. E. Peierls. *Quantum Theory of Solids*. Clarendon, Oxford, UK, 1955.

[12] C. J. Brabec, V. Dyakonov, J. Parisi, and N. S. Sariciftci. *Organic Photovoltaics. Concepts and Realization*. Springer, Berlin, 1 edition, 2003.

[13] S. E. Gledhill, B. Scott, and B. A. Gregg. Organic and nano-structured composite photovoltaics: An overview. *Journal of Materials Research*, 20(12):3167–3179, 2005.

[14] V. D. Mihailetchi, H. X. Xie, B. de Boer, L. J. A. Koster, and P. W. M. Blom. Charge transport and photocurrent generation in poly (3-hexylthiophene): Methanofullerene bulk-heterojunction solar cells. *Advanced Functional Materials*, 16(5):699–708, 2006.

[15] A. Miller and E. Abrahams. Impurity conduction at low concentrations. *Physical Review*, 120(3):745–755, 1960.

[16] R. A. Marcus. Nonadiabatic processes involving quantum-like and classical- like coordinates with applications to nonadiabatic electron transfers. *Journal of Chemical Physics*, 81(10):4494–4500, 1984.

[17] J. Stephan, S. Schrader, and L. Brehmer. Monte carlo simulations of charge transport in molecular solids: a modified Miller Abrahams type jump rate approach. *Synthetic Metals*, 111:353–357, 2000.

[18] U. Wolf, V. I. Arkhipov, and H. Bassler. Current injection from a metal to a disordered hopping system. I. Monte Carlo simulation. *Physical Review B*, 59(11):7507–7513, 1999.

[19] Y. Kim, S. Cook, S. M. Tuladhar, S. A. Choulis, J. Nelson, J. R. Durrant, D. D. C. Bradley, M. Giles, I. Mcculloch, C. S. Ha, and M. Ree. A strong regioregularity effect in self-organizing conjugated polymer films and high-efficiency polythiophene: fullerene solar cells. *Nature Materials*, 5(3):197–203, 2006.

[20] C. J. Brabec, A. Cravino, D. Meissner, N. S. Sariciftci, M. T. Rispens, L. Sanchez, J. C. Hummelen, and T. Fromherz. The influence of materials work function on the open circuit voltage of plastic solar cells. *Thin Solid Films*, 403:368–372, 2002.

[21] G. Zerza, C. J. Brabec, G. Cerullo, S. De Silvestri, and N. S. Sariciftci. Ultrafast charge transfer in conjugated polymer-fullerene composites. *Synthetic Metals*, 119(1-3):637–638, 2001.

[22] S. S. Sun. Optimal energy offsets for organic solar cells containing a donor/acceptor pair. *Solar Energy Materials and Solar Cells*, 85(2):261–267, 2005.

[23] C. W. Tang. 2-layer organic photovoltaic cell. *Applied Physics Letters*, 48(2):183–185, 1986.

[24] J. Rostalski and D. Meissner. Photocurrent spectroscopy for the investigation of charge carrier generation and transport mechanisms in organic p/n- junction solar cells. *Solar Energy Materials and Solar Cells*, 63(1):37–47, 2000.

[25] C. J. Brabec, N. S. Sariciftci, and J. C. Hummelen. Plastic solar cells. *Advanced Functional Materials*, 11(1):15–26, 2001.

[26] Y. Cao, G. Yu, C. Zhang, R. Menon, and A. J. Heeger. Polymer light-emitting diodes with polyethylene dioxythiophene-polystyrene sulfonate as the transparent anode. *Synthetic Metals*, 87:171–174, 1997.

[27] H. Hoppe, N. S. Sariciftci, and D. Meissner. Optical constants of conjugated polymer/fullerene based bulk-heterojunction organic solar cells. *Molecular Crystals and Liquid Crystals*, 385:233–239, 2002.

[28] P. J. Brown, D. S. Thomas, A. Köhler, J. S. Wilson, J. S. Kim, C. M. Ramsdale, H. Sirringhaus, and R. H. Friend. Effect of interchain interactions on the absorption and emission of poly(3-hexylthiophene). *Physical Review B*, 67(6):064203–1–064203–16, 2003.

[29] V. D. Mihailetchi, L. J. A. Koster, P. W. M. Blom, C. Melzer, and B. de Boer. Compositional dependence of the performance of poly(p-phenylene vinylene):methanofullerene bulk-heterojunction solar cells. *Advanced Functional Materials*, 15(5):795–801, 2005.

[30] H. Hoppe, M. Niggemann, C. Winder, J. Kraut, R. Hiesgen, A. Hinsch, D. Meissner, and N. S. Sariciftci. Nanoscale morphology of conjugated polymer/fullerene-based bulk-heterojunction solar cells. *Advanced Functional Materials*, 14(10):1005–1011, 2004.

[31] W. L. Ma, C. Y. Yang, X. Gong, K. Lee, and A. J. Heeger. Thermally stable, efficient polymer solar cells with nanoscale control of the interpenetrating network morphology. *Advanced Functional Materials*, 15(10):1617–1622, 2005.

[32] M. Glatthaar, N. Mingirulli, B. Zimmermann, T. Ziegler, R. Kern, M. Niggemann, A. Hinsch, and A. Gombert. Impedance spectroscopy on organic bulk-heterojunction solar cells. *Physica Status Solidi A-Applications and Materials Science*, 202(11):R125–R127, 2005.

[33] W. Fahlman and W. R. Salaneck. Surfaces and interfaces in polymer-based electronics. *Surface Science*, 500(1-3):904–922, 2002.

[34] H. Ishii, K. Sugiyama, E. Ito, and K. Seki. Energy level alignment and interfacial electronic structures at organic/metal and organic/organic interfaces. *Advanced Materials*, 11(12):972–972, 1999.

[35] T. Kugler, W. R. Salaneck, H. Rost, and A. B. Holmes. Polymer band alignment at the interface with indium tin oxide: consequences for light emitting devices. *Chemical Physics Letters*, 310(5-6):391–396, 1999.

[36] J. S. Huang, P. F. Miller, J. S. Wilson, A. J. de Mello, J. C. de Mello, and D. D. C. Bradley. Investigation of the effects of doping and post-deposition treatments on the conductivity, morphology, and work function of poly (3,4-ethylenedioxythiophene)/poly (styrene sulfonate) films. *Advanced Functional Materials*, 15(2):290–296, 2005.

[37] H. Frohne, S. E. Shaheen, C. J. Brabec, D. C. Müller, N. S. Sariciftci, and K. Meerholz. Influence of the anodic work function on the performance of organic solar cells. *Chemphyschem*, 3(9):795–799, 2002.

[38] J. Huang, P. F. Miller, J. C. de Mello, A. J. de Mello, and D. D. C. Bradley. Influence of thermal treatment on the conductivity and morphology of PEDOT/PSS films. *Synthetic Metals*, 139(3):569–572, 2003.

[39] V. D. Mihailetchi, P. W. M. Blom, J. C. Hummelen, and M. T. Rispens. Cathode dependence of the open-circuit voltage of polymer : fullerene bulk heterojunction solar cells. *Journal of Applied Physics*, 94(10):6849–6854, 2003.

[40] J. Nelson. Diffusion-limited recombination in polymer-fullerene blends and its influence on photocurrent collection. *Physical Review B*, 67(15):155209–1–155209–10, 2003.

[41] A. F. Nogueira, I. Montanari, J. Nelson, J. R. Durrant, C. Winder, and N. S. Sariciftci. Charge recombination in conjugated polymer/fullerene blended films studied by transient absorption spectroscopy. *Journal of Physical Chemistry B*, 107(7):1567–1573, 2003.

[42] M. Niggemann. *Fundamental Investigations on Periodic Nano- and Microstructured Organic Solar Cells.* Dissertation, Albert-Ludwigs-Universität, Freiburg im Breisgau, Fakultät für Angewandte Wissenschaften, 2005.

[43] M. Glatthaar. *Experimentelle Untersuchung und Modellierung organischer Solarzellen auf der Basis interpenetrierender Donator/Akzeptor-Netzwerke.* Diplomarbeit, Eberhardt-Karls-Universität Tübingen, Fakultät für Mathematik und Physik, 2003.

[44] L. J. A. Koster, E. C. P. Smits, V. D. Mihailetchi, and P. W. M. Blom. Device model for the operation of polymer/fullerene bulk heterojunction solar cells. *Physical Review B*, 72(8):085205–1–085205–9, 2005.

[45] L. J. A. Koster, V. D. Mihailetchi, R. Ramaker, and P. W. M. Blom. Light intensity dependence of open-circuit voltage of polymer : fullerene solar cells. *Applied Physics Letters*, 86(12), 2005.

[46] C. Waldauff, P. Schilinsky, J. Hauch, and C. J. Brabec. Material and device concepts for organic photovoltaics: towards competitive efficiencies. *Thin Solid Films*, 451-52:503–507, 2004.

[47] M. A. Green. *Solar Cells: Operating Principles, Technology, and System Applications.* Prentice Hall, 1 edition, 1981.

[48] T. Aernouts, W. Geens, J. Poortmans, P. Heremans, S. Borghs, and R. Mertens. Extraction of bulk and contact components of the series resistance in organic bulk donor-acceptor-heterojunctions. *Thin Solid Films*, 403:297–301, 2002.

[49] P. Schilinsky, C. Waldauf, J. Hauch, and C. J. Brabec. Simulation of light intensity dependent current characteristics of polymer solar cells. *Journal of Applied Physics*, 95(5):2816–2819, 2004.

[50] J. Merten, J. M. Asensi, C. Voz, A. V. Shah, R. Platz, and J. Andreu. Improved equivalent circuit and analytical model for amorphous silicon solar cells and modules. *IEEE Transactions on Electron Devices*, 45(2):423–429, 1998.

[51] S. S. Hegedus. Current-Voltage Analysis of a-Si and a-SiGe Solar Cells Including voltage-dependent Photocurrent Collection. *Progress in Photovoltaics*, 5(3):151–168, 1997.

[52] S. Yoo, B. Domercq, and B. Kippelen. Intensity-dependent equivalent circuit parameters of organic solar cells based on pentacene and C_{60}. *Journal of Applied Physics*, 97:103706–1–103706–9, 2005.

[53] J. G. Xue, S. Uchida, B. P. Rand, and S. R. Forrest. 4.2% efficient organic photovoltaic cells with low series resistances. *Applied Physics Letters*, 84(16):3013–3015, 2004.

[54] B. Maennig, J. Drechsel, D. Gebeyehu, P. Simon, F. Kozlowski, A. Werner, F. Li, S. Grundmann, S. Sonntag, M. Koch, K. Leo, M. Pfeiffer, H. Hoppe, D. Meissner, N. S. Sariciftci, I. Riedel, V. Dyakonov, and J. Parisi. Organic p-i-n solar cells. *Applied Physics A-Materials Science & Processing*, 79(1):1–14, 2004.

[55] M. Granström, K. Petritsch, A. C. Arias, A. Lux, M. R. Andersson, and R. H. Friend. Laminated fabrication of polymeric photovoltaic diodes. *Nature*, 395(6699):257–260, 1998.

[56] H. J. Snaith, A. C. Arias, A. C. Morteani, C. Silva, and R. H. Friend. Charge generation kinetics and transport mechanisms in blended polyfluorene photovoltaic devices. *Nano Letters*, 2(12):1353–1357, 2002.

[57] J. S. Kim, M. Granström, R. H. Friend, N. Johansson, W. R. Salaneck, R. Daik, W. J. Feast, and F. Cacialli. Indium-tin oxide treatments for single- and double-layer polymeric light-emitting diodes: The relation between the anode physical, chemical, and morphological properties and the device performance. *Journal of Applied Physics*, 84(12):6859–6870, 1998.

[58] M. Al Ibrahim, O. Ambacher, S. Sensfuss, and G. Gobsch. Effects of solvent and annealing on the improved performance of solar cells based on poly(3-hexylthiophene): Fullerene. *Applied Physics Letters*, 86(20), 2005.

[59] D. Meyerhofer. Characteristics of resist films produced by spinning. *Journal of Applied Physics*, 49(7):3993–3997, 1978.

[60] S. E. Shaheen, R. Radspinner, N. Peyghambarian, and G. E. Jabbour. Fabrication of bulk heterojunction plastic solar cells by screen printing. *Applied Physics Letters*, 79(18):2996–2998, 2001.

[61] G. Li, V. Shrotriya, J. S. Huang, Y. Yao, T. Moriarty, K. Emery, and Y. Yang. High-efficiency solution processable polymer photovoltaic cells by self-organization of polymer blends. *Nature Materials*, 4(11):864–868, 2005.

[62] H.C. Starck Homepage. http://www.baytron.com. [Online; accessed 15-July-2006].

[63] C. H. Seaman. Calibration of solar cells by the reference cell method - the spectral mismatch problem. *Solar Energy*, 29(4):291–298, 1982.

[64] P. J. Brown, D. S. Thomas, A. Köhler, J. S. Wilson, J. S. Kim, C. M. Ramsdale, H. Sirringhaus, and R. H. Friend. Effect of interchain interactions on the absorption and emission of poly(3-hexylthiophene). *Physical Review B*, 67(6):064203–1–064203–16, 2003.

[65] T. Ziegler. *Optische Spektroskopie an organischen Solarzellen*. Diplomarbeit, Albert-Ludwigs-Universität, Freiburg im Breisgau, Fakultät für Mathematik und Physik, 2006.

[66] J. Rostalski and D. Meissner. Monochromatic versus solar efficiencies of organic solar cells. *Solar Energy Materials and Solar Cells*, 61(1):87–95, 2000.

[67] Wikipedia. Atomic force microscope — wikipedia, the free encyclopedia. http://en.wikipedia.org/wiki/Atomic_force_microscope, 2006. [Online; accessed 15-July-2006].

[68] Wikipedia. Ellipsometry — wikipedia, the free encyclopedia. http://en.wikipedia.org/wiki/Ellipsometry, 2006. [Online; accessed 15-July-2006].

[69] F. Jäger. *Automatisierung der spektralen Kennlinienmessung an organischen Solarzellen.* Technikerarbeit, Richard-Fehrenbach Gewerbeschule, Freiburg im Breisgau, 2004.

[70] F. Clement. *Untersuchung des Transportmechanismus in organischen Solarzellen mittels Messungen an organischen Feldeffekttransistoren (OFETs).* Diplomarbeit, Albert-Ludwigs-Universität, Freiburg im Breisgau, Fakultät für Mathematik und Physik, 2005.

[71] M. Glatthaar, M. Niggemann, B. Zimmermann, P. Lewer, M. Riede, A. Hinsch, and J. Luther. Organic solar cells using inverted layer sequence. *Thin Solid Films*, 491(1-2):298–300, 2005.

[72] J. Honerkamp. *Stochastic Dynamical Systems.* Jon Wiley & Sons, New York, 1 edition, 1993.

[73] M. Unser. Splines - a perfect fit for signal and image processing. *IEEE Signal Processing Magazine*, 16(6):22–38, 1999.

[74] W. H. Press, S. A. Teukolsky, W. V. Vetterling, and B. P. Flannery. *Numerical Recipes in C/C++.* Cambridge University Press, Cambridge, UK, 1 edition, 2001.

[75] K. Levenberg. A method for the solution of certain non-linear problems in least squares. *Quarterly Applied Mathematics*, 2:164–168, 1944.

[76] D. W. Marquardt. An algorithm for least-squares estimation of nonlinear parameters. *Journal of the Society for Industrial and Applied Mathematics*, 11(2):431–441, 1963.

[77] A. Ranganathan. The Levenberg-Marquardt Algorithm. http://citeseer.ist.psu.edu/638988.html, 2004. [Online; accessed 15-July-2006].

[78] K. Pearson. On lines and planes of closest fits to systems to points in space. *Philosophical Magazine*, 2(6):559–572, 1901.

[79] A. C. Rencher. *Multivariate Statistical Inference and Applications*. John Wiley & Sons, New York, 1998.

[80] R. Dyer. *MySQL in a Nutshell*. O'Reilly, 1 edition, 2005.

[81] B. A. Tate and C Hibbs. *Ruby on Rails: Up and Running*. O'Reilly, 1 edition, 2006.

[82] E. R. Harold and W. S. Means. *XML in a Nutshell*. O'Reilly, 3 edition, 2004.

[83] The National Center for Supercomputing Applications (NCSA). HDF5. http://hdf.ncsa.uiuc.edu/HDF5/. [Online; accessed 15-July-2006].

[84] H. P. Langtangen. *Python Scripting for Computational Science*. Texts in Computational Science and Engineering. Springer, Berlin Heidelberg New York, 2 edition, 2005.

[85] F. Altet. Pytables. http://www.pytables.org. [Online; accessed 15-July-2006].

[86] T. E. Oliphant. Scipy.org. http://www.scipy.org. [Online; accessed 15-July-2006].

[87] J. Kitchin. Graceplot. http://graceplot.sourceforge.net. [Online; accessed 15-July-2006].

[88] E. Stambulchik. Grace. http://plasma-gate.weizmann.ac.il/Grace/. [Online; accessed 15-July-2006].

[89] M. Rivers. mpfit. http://cars9.uchicago.edu/software/python/mpfit.html. [Online; accessed 15-July-2006].

[90] S. Schmerler. mpfit. http://aspn.activestate.com/ASPN/Mail/Message/2723412. [Online; accessed 15-July-2006].

[91] Wikipedia. Unit test — wikipedia, the free encyclopedia. http://en.wikipedia.org/wiki/Unit_test, 2006. [Online; accessed 15-July-2006].

[92] CollabNet. Subversion. http://subversion.tigris.org. [Online; accessed 15-July-2006].

[93] V. D. Mihailetchi, J. Wildeman, and P. W. M. Blom. Space-charge limited photocurrent. *Physical Review Letters*, 94(12), 2005.

[94] M. Glatthaar, M. Riede, N. Keegan, K. Sylvester-Hvid, B. Zimmermann, M. Niggemann, A. Hinsch, and A. Gombert. Efficiency limiting factors of organic bulk hetero-junction solar cells identified by electrical impedance spectroscopy. Submitted to Solar Energy Materials and Solar Cells, 6 2006.

[95] G. Li, V. Shrotriya, Y. Yao, and Y. Yang. Investigation of annealing effects and film thickness dependence of polymer solar cells based on poly(3-hexylthiophene). *Journal of Applied Physics*, 98(4):043704–1–043704–5, 2005.

[96] T. Yamanari, T Taima, K Hara, and K Saito. Investigation of optimum conditions for high-efficiency organic thin-film solar cells based on polymer blends. *Journal of Photochemistry and Photobiology A-Chemistry*, In Press, Corrected Proof, 2006.

[97] M. Glatthaar. Personal Communication after a visit to another research group, 5 2006.

[98] K. Zimmermann, L. Quack, and A. W. Liehr. Pyphant - a python framework for modelling reusable data processing tasks. http://tinyurl.com/r4rdz, 2006. [Online; accessed 15-July-2006].